ENERGY TRANSFER AND DISSIPATION IN STRUCTURES WITH DISCRETE NONLINEARITIES

by

George Lertin Sarver III
B.S., Massachusetts Institute of Technology (1980)
S.M., Massachusetts Institute of Technology (1982)

SUBMITTED TO THE DEPARTMENT OF
AERONAUTICS AND ASTRONAUTICS IN PARTIAL FULFILLMENT OF THE
REQUIREMENTS FOR THE DEGREE OF
DOCTOR OF PHILOSOPHY
at the
MASSACHUSETTS INSTITUTE OF TECHNOLOGY
February 1988

Signature of Author _____
Department of Aeronautics and Astronautics, November 30, 1987

Certified by _____
Professor Edward F. Crawley
Thesis Supervisor, Professor of Aeronautics and Astronautics

Certified by _____
Professor James W. Mar
Professor of Aeronautics and Astronautics

Certified by _____
Professor T.H.H. Pian
Professor of Aeronautics and Astronautics

Accepted by _____
Professor Harold Y. Wachman
Chairman, Department Graduate Committee

ENERGY TRANSFER AND DISSIPATION IN STRUCTURES WITH DISCRETE NONLINEARITIES

by
George Lertin Sarver III

Submitted to the Department of Aeronautics and Astronautics in partial fulfillment of the requirements of the Degree of Doctor of Philosophy at the Massachusetts Institute of Technology
February 1988

Abstract

The dynamics of space structures with discrete, non-hysteretic, nonlinear, joints are analytically and experimentally investigated. The structures are modeled as long thin beams with a single discontinuous joint at its center. The joints are piecewise linear in nature and represent joints of asymmetric stiffness and joints with dead-band. The nonlinear joint causes energy to be transferred among structural modes. The apparent damping of the modes can therefore change. The beam's damping due to modal coupling is calculated as a function of the beam and joint parameters. An experiment is developed which measures damping while jointed beams are lofted in vacuum to simulate weightlessness and the vacuum of space. The experiments are designed to confirm the analytical model.

An analytic model is developed to model space structures as continuous, damped, engineering beams and a piecewise linear joint. The use of continuous models eliminates the possibility of trapping energy in the lower modes of a system due to finite degrees of freedom. Proportional strain rate damping is assumed in the model and is shown to decouple the mode's amplitudes and energy. Independent equations are used to model individual modes and assign modal damping rates. The transfer and dissipation of energy is calculated on a mode by mode basis. The effective damping rate of the beams is calculated for a variety of joint configurations and beam internal damping rates.

Experiments with structures similar to the jointed beams used in the analysis were conducted to correlate with the analysis. The experiments were performed in the MIT ASTROVAC where vacuum and weightlessness can be simulated for up to 1.75 seconds. Each structure was lofted from the bottom of a vacuum chamber, resulting in free-fall from the time it left the launcher to the

time it landed. The accelerations the structure underwent during launch were used to initially excite the motions of the structure. Strain gauge data from the structure was retrieved via thin wires stretched between the structure and a follower system, which acted to reduce the influence of the wires on the structure. The correlation between the analysis and the experiments was generally good.

The models used to examine damping due to modal coupling are relatively simple but some inferences are established which may, with some careful consideration of the limits of this analysis, be applied to more complex structures. The inferences indicate that damping due to modal coupling is not important unless the modal coupling is dominant and the damping rates in the coupled modes are greater than the damping rate of the primary mode in oscillation. It is also indicated that beating between modes is also a function of the relative damping rates of the modes.

Thesis Supervisor: Professor Edward F. Crawley

Title: Associate Professor of Aeronautics and Astronautics

Acknowledgments

I wish to thank everyone that helped and supported me in completing this paper. I especially thank Mr. Sam Venneri with NASA Headquarters for their funding, contract number # NAGW-21, and Dr. A. Amos, with the United States Air Force for funding the experimental facility which was built in conjunction with this research, AFOSR 83-0352. I especially thank the members of my thesis committee, Professor Crawley, Professor Mar, and Professor Pian for their efforts and support. I also thank Professor Dugundji for his help and Professor Akin for the use of his computers. I especially thank my unofficial committee member, Mary Bowden, for the invaluable proof reading. I also extend my thanks to Laurie for putting up with me for so long, and all the gang in 407 for not kicking me out because of my repetitive " anything going on?" questions. Last but not least I wish to thank my family for their support and encouragement, but I'm a little tired of school for an MBA right now, dad!

Thanks

Table of Contents

Experiment

Chapter 6 Experimental Method and Apparatus

Chapter 7 Analysis of Experimental Data

Chapter 8 Conclusions and Recommendations

Appendix

Appendix A Engineering Beam Equations

Appendix C List of Simulations

List of Figures

List of Tables

Nomenclature

Symbols	Definitions
a	Complex shape factor.
A	Complex modal amplitude
A_{DB}	Amplitude of first mode where dead-band first engages.
$Amp(t_1)$	Peak amplitude of oscillation at time t_1.
A_{M1}	Amplitude of first mode.
b	Complex shape factor, initial system.
B	Complex coefficient.
c	Complex shape coefficient.
C	Damping coefficient, N sec. m^{-2}, assumed to be a real constant for a beam section.
C_S	Rotational spring damping constant, N m sec.
d	Complex shape coefficient, initial system.
DBR	Dead-band amplitude ratio, normalized amplitude.
DR	Modal damping rate, sec^{-1}, exponential decay term.
DR_{1int}	Internal damping rate of sub-system first modes.
$DR_{2\text{-}7}$	Internal damping rate of the upper sub-system modes, 2-7.
δ_{mn}	Delta function.
ΔDR_1	Difference between the internal and effective damping rates of the first structural mode.
ΔDR_{1Eff}	Effective damping rate of the first mode of the structure.
ΔDR_M	Difference in the internal damping rates of the first and the upper sub-system modes.
$\Delta Z_1\%$	Normalized difference between the internal and effective damping rates of the first structural mode.

$\Delta Z_M\%$	Normalized difference in the internal damping rates of the first and the upper sub-system modes.
E	Modulous of elasticity, N m^{-2}, assumed to be a real constant for a beam section.
$\underline{E}$	Structural energy, a real function, J.
f(x,t)	External forces applied to beam, a real function of x and t.
Φ	Complex mode shape function.
i	Imaginary unit, $\sqrt{-1}$.
I	Moment of inertia, m^4, assumed to be a real constant for a beam section.
K	System proportionality constant.
K_1	Rotational spring stiffness of flexible spring, (K_L), real, N m.
K_2	Rotational spring stiffness of stiff spring, ($K_L + K_{NL}$), real, N m.
K_L	Rotational spring stiffness of linear spring, real, N m.
K_{NL}	Rotational spring stiffness of nonlinear (on-off) spring, real, N m.
K_S	Rotational spring stiffness of spring S, real, N m.
K_W	Linear spring stiffness, real, N m^{-1}.
l	Beam length
l_S	Wire bracing moment arm (stand off) length, m.
m	Mass per unit length, kg m^{-1}, assumed to be a real constant for a beam section.
M	Point mass mass, kg.
μ_{j*k}	Complex modal mass, a function of two modes, j and k, complex conjugate notation.
μ_{mn}	Complex modal mass, a function of two complex modes m and n.

ν_{nm}	Complex orthogonality coefficient, a function of two complex mode frequencies and shapes n and m.
SSQ	Sum of least squares residuals.
t	Time, real.
τ_{mn}	Transfer coefficient, a function of two complex mode frequencies and shapes of two systems.
u	Assumed complex beam solution.
v	Complex displacement, initial structure.
V	Beam displacement, initial system, m, a real function of x and t.
w	Complex displacement.
W	Beam displacement, m, a real function of x and t.
W_H	Homogeneous portion of beam displacement solution, real.
W_P	Particular portion of beam displacement solution, real.
ω	Complex frequency, initial system.
$\underline{\omega}$	Complex portion of complex frequency Ω.
Ω	Complex frequency.
Ω_{NL}	The natural frequency of the first mode of the structure including nonlinear effects.
x	Position along x axis, real.
Y	Complex time function.
ψ	Complex mode shape function, initial system.
Z	Complex time function, initial system.
Z %	Normalized modal damping rate, equivalent to damping ratio of mode if $\Omega_{NL} = \underline{\omega}_n$.
ζ	Modal critical damping ratio

Sub-Super-Scripts	Definitions
$( )_B$	Subscript A, B, C, or D indicates the beam section, B is the general beam section symbol.
$( )^B$	Superscript A, B, C, or D indicates the beam section, B is the general beam section symbol.
$( )_j$	Subscript j or k indicates the complex mode number.
$( )_L$	Subscript L or R indicates the left or right end of the beam section.
$( )_M$	Subscript M indicates the point mass or the beam section where it is located.
$( )_n$	Subscript n or m indicates the real mode number.
$( )_R$	Subscript L or R indicates the left or right end of the beam section.
$( )_S$	Subscript S indicates the rotational spring or the beam section where it is located.
$( )_T$	Subscript T indicates the time of sub-system transfer.

Operators	Definitions
$( )^*$	Superscript *, indicates complex conjugate.
$\dot{( )}$	Superscript dot, differentiation with respect to time, t.
$\ddot{( )}$	Double superscript dot, twice differentiation with respect to time, t.
$( )'$	Superscript prime, differentiation with respect to space, x.
$( )''$	Double superscript prime, twice differentiation with respect to space, x.
$\frac{d}{dt}( )$	Differentiation with respect to time, t.
$\frac{d^2}{d^2 t}( )$	Twice differentiation with respect to time, t.
$\frac{d}{dx}( )$	Differentiation with respect to space, x.

$\frac{d^2}{d^2 x}(\ )$	Twice differentiation with respect to space, x.
$e^{(\ )}$	Natural exponent of ( ).
$\ln(\ )$	Natural log of ( ).
$\boldsymbol{L}(\ )$	Indicates operator of ( ).
$(\ )\|_t$	Evaluated at time t.
$\{\ \}\|_x$	Evaluated at position x.

Chapter 1

Introduction

1.0 Summary

The design requirements of large structures in space are very different from those of similar structures on earth. The space environment, the lack of gravity, and the high cost of transporting the structure into space, changes the importance of various design considerations. The differences can be summarized by the three points:

- The dominant loads in large space structure will be oscillatory,
- The natural frequencies of a large space structure will be closely packed and overlap the load frequencies,
- The damping mechanisms present in earth based structures will not be present in space.

Earth based structures are commonly designed for applied oscillatory loads but the gravity loads usually dominate the design. In space there is no gravity so a large space structure is primarily designed for oscillatory loadings.

The size and nature of large space structures imply that the natural frequencies of these structures will be low compared to current spacecraft. Since space structures undergo mostly oscillatory loading it is postulated that large space structures will be forced at or near their resonance frequencies. The amplitude of the resultant motions will depend on the inherent damping in the structure. If these motions and the induced loads within the structure dominate the design of the structure then the level of inherent damping becomes increasingly important.

Structures on earth can dissipate energy into their environment. The atmosphere and the attachments to the earth contribute greatly to the damping observed in earth based structures. These phenomena are not present in the space based structure. Earth based experience with damping of large structures becomes of limited usefulness. A new body of information relating to the damping properties of large space structures is necessary.

Difficulties with simulating the space environment limits experimental measurement of the damping of a large space structure on earth. An analytical approach is necessary for the prediction and enhancement of damping of large

space structures. To investigate damping in space structures a simple idealized space structure is envisioned.

Such a structure would commonly have a complex nonlinear joint. As an illustrative example, consider the idealized, 2-D, jointed space structure shown in figure 1.1.

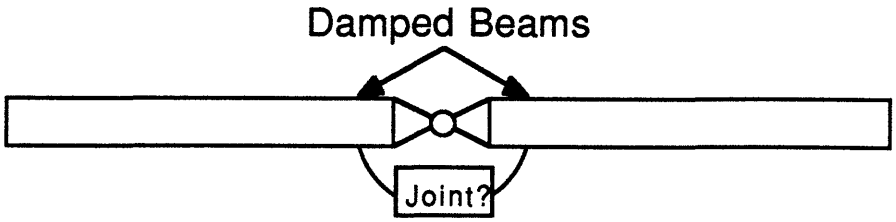

Idealized Jointed Space Structure
Figure 1.1

It consists of two long beam like sections connected together by a joint. In order to concentrate on the joint of the structure, the beam sections are assumed to have linear properties in both stiffness and damping. The beam damping will be modeled as strain rate or strain velocity damping. It is possible that the joint may have linear properties or nonlinear properties, and may be damped or undamped. The jointed beam can, therefore, be separated into four categories: linear undamped, linear damped, non-hysteretic nonlinear, and hysteretic nonlinear, (see figure 1.2).

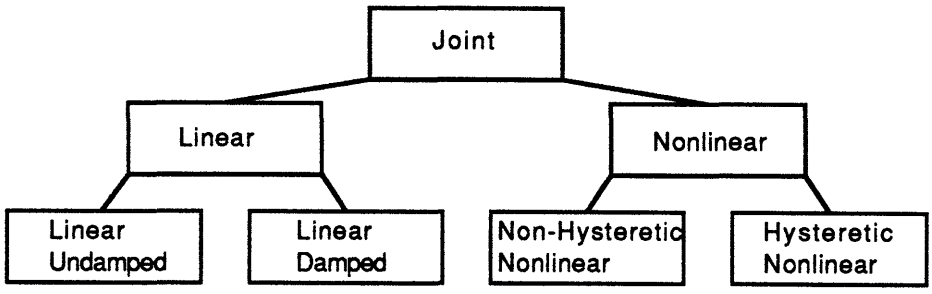

Joint Categories
Figure 1.2

If the joint of the structure is modeled as a linear undamped joint then the dissipation of vibration energy from the structure can only occur in the beam sections. If the joint of the structure is modeled as a linear damped joint then the joint will dissipate energy as well. The modeling of the joint as linear along

with the linear beam sections allows the structure to be modeled with classical structural modes. Two types of modes of a structure are defined in this report. A real mode of a structure occurs when there is no damping or proportional damping is present in the structure. A real mode is a mode which has a constant mode shape throughout the cycle. It also has the property that the energy of the structure can be divided into independent modal components. A complex mode occurs when there is non-proportional damping in the structure. A complex mode does not have a constant mode shape and the energy of the structure can not be divided into modal energy components.

A joint which is nonlinear and is modeled as such can fall into two categories, non-hysteretic and hysteretic. A non-hysteretic nonlinear joint is one where the joint behaves in a nonlinear manner but does not dissipate energy. An example of this is an asymmetrically stiff joint where the stiffness of the joint changes at a given deflection. No energy is dissipated in the joint due to the nonlinearity. A nonlinear joint, such as the asymmetrically stiff joint, will, however, couple the modes of the structure. Energy is allowed to pass between the modes due to the nonlinearity. If energy is passed from one mode to another then the effective damping rate of the first mode will increase and the effective damping rate of the second mode will decrease. Modal coupling can, therefore, cause apparent changes in the modal damping rates of a structure due to the energy transfer between the modes. A hysteretic nonlinear joint will cause modal coupling and will also dissipate energy.

Energy dissipation can, therefore, occur in three different ways in the jointed space structure shown in figure 1.1:

- Linear damping,
- Nonlinear hysteretic joint damping,
- Damping due to modal coupling.

Damping due to modal coupling caused by nonlinear non-hysteretic joints is the focus of this study. The objective is to develop a method to determine when damping due to modal coupling is important to a structural analysis and how to use it to improve the damping characteristics of a large space structure.

The method chosen to analyze damping due to modal coupling is to create a model composed of proportionally damped, continuous beam sections joined by piecewise linear joints. The joints are non-hysteretic but proportional linear damping is included. An experiment is also performed in which

structures, representative of those analyzed, are tested in vacuum and zero-g. The experiment is used to verify the analytical model developed.

The results of the analysis show a correlation between the amount of damping induced by the modal coupling and the relative internal decay rates of the coupled modes. The increase in damping due to modal coupling is limited by the amount of coupling the structure exhibits. A technique is developed to estimate the maximum amount of damping due to modal coupling.

This chapter introduces the study by first discussing the motivation and scope of the problem. Previous research and analytical approaches are then presented. The analytical approach and the experimental procedure used in this study follow.

1.1 Problem Motivation

The design requirements of space structures are different than those of earth based structures [1,2]. These differences are do to the absence of gravity, of environmental damping, and of a ground attachment in space.

Gravity is a primary load in any large earth-based structure. As a result, this constant load tends to dominate the design, and oscillatory loads are usually small in comparison. Without gravity, oscillatory loads dominate the load spectrum, to which a large space structure is exposed. For example, oscillatory loads can be caused by attitude control jets, moment gyros, gravitational variations, etc. Loads of these types dominate the design of large space structures.

The size and nature of large space structures causes the structure to have low frequency modes which place the modal frequencies of the structure in the same range as the frequencies of the loads. This can cause the structure to be forced at or near a resonance. The frequencies of modal vibration may be within the control band-width of the attitude control system. This can cause coupling between the structural vibration and the attitude control system. The active control of structural vibration modes may become necessary if not desirable to reduce the cost of the structure [3].

Design of manned vehicles, such as the space station, must also consider the length of time oscillations persist since the vehicle may become too uncomfortable for habitation. It would be undesirable to have any vibratory motions noticeable to the station occupants for any great length of time, for

example, after a shuttle docking, even though this motion may not be detrimental to the structure.

The amplitude of the resultant motion to the dynamic loads will depend on the level of damping in the structure. Damping is, therefore, a key parameter in the design of a large space structure. The more common damping mechanisms found on earth are not available to space structures. The absence of an atmosphere in space eliminates the predominant environmental damping mechanism present in earth-based structures.

When air is present, damping occurs by air acting against motions, or by squeeze damping in joints. Squeeze damping occurs when air is trapped in gaps within a joint. When the joint is worked, the air is squeezed out, dissipating energy. A large body of work exists quantifying the damping attributed to aerodynamic effects [4,5]. Space structures will not have these forms of damping; however, the atmosphere may be present when ground tests of a space structure occur. This will cause the damping present in ground tested structures to be greater than for the same structure in space.

The atmosphere also inhibits cold welding [6], allowing friction to continue to occur in joints and fasteners. Friction in joints and fasteners causes energy dissipation when surfaces of the joints slide against one another as the joint flexes under load. An oxide layer on the surfaces prevent them from cold welding. In the presence of air the oxide layer is continuously replenished, preventing the welding. In space, the absence of the atmosphere will allow the motion of the surfaces to wear away the oxide layer and cold welding of the joints may occur.

The absence of a ground attachment eliminates another common source of energy dissipation. Structures built into the ground transmit energy into it, causing apparent damping [4,7,8]. This type of dissipation will not be present on spacecraft. This can add another source of error to the ground measurement of the damping of a space structure. Attachments or suspension mechanisms can cause the dissipation of energy in ground tested space structures which will not be present in space.

Loss factors of earth-based structures [4] similar to large space structures are typically of the order of 1 - 3%. The damping mechanisms include those mentioned above. Material damping [4,9,10] typically accounts for only 0.1 - 0.3%. The material damping of a structure may deteriorate at low frequencies, such as those found in large space structures. An example of this is the drop in the

damping ratio of a metal beam in flexural vibration predicted by the Zener damping theory [9]. The Zener damping theory describes the dissipation mechanism in metal beams in flexure due to the differential heating induced across the beam. For example a thin aluminum beam will have a peak critical damping ratio of approximately 0.1%(zeta) at a frequency defined by the beams geometric and material properties. For frequencies below the peak damping frequency, the damping decreases roughly proportionally as the frequency decreases. It also decreases above the peak damping frequency, roughly inversely proportional to the increasing frequency. It is apparent that if all but material damping mechanisms were eliminated damping factors could drop an order of magnitude as compared to earth-based structures. Prediction and understanding of damping in a space structure becomes increasingly important.

1.2 Analytical Approach

Several analytical approaches are used to solve the problem of estimating the structural damping of a space structure. The most common is to ignore any joint nonlinearities since they are difficult to model and usually small. Damping of the structure are then estimated by empirical rules or experimentally determined. Interpolation of earth measured damping data may not be practical. In order to build a linear structure, very tight or welded joints can be used [5,11,12]. This may reduce the damping of the structure to that of material damping. Since the structural design will be sensitive to the structural damping, this may not be acceptable.

It may be possible to include highly dissipative materials in the structure to increase the structural damping to acceptable levels. Much work has been performed in this direction. Allowing joint nonlinearities may be an alternative way to enhance damping in large space structures. Using a more complex nonlinear model of a large space structure to represent and predict the structural damping then becomes necessary [5,13].

Nonlinear mechanisms within an otherwise linear structure, such as friction and dead-band in joints, local buckling of the structure, and large displacements and rotations, affect many of the dynamic properties of the structure, only one of which is damping. In general, nonlinear mechanisms completely couple the dynamics of a multi-degree of freedom system. The damping caused by these nonlinear mechanisms does not occur in the classic

form of linear damping even though it is often modeled as such. In the case of small nonlinearities present in an otherwise linear structure the nonlinearities can manifest themselves as apparent changes in damping. If the apparent damping can be experimentally determined then a linear analysis may be successfully used. Experimentally determining the damping of a large space structure may be impractical, limiting the usefulness of this approach.

Joint nonlinearities can dissipate energy causing direct nonlinear damping but it can also cause energy to transfer between modes of the structure, commonly referred to as modal coupling. The effective damping rate of a mode of a structure will reflect the damping due to the direct damping in the joints and the energy transferred to other modes of the structure. A common method of calculating the energy dissipation caused by nonlinear joints is to measure or calculate the hysteresis curves of a joint undergoing a oscillatory loading. The hysteresis curves can be used to determine the energy dissipation in the joint. This can be used to estimate the damping of the structure by modeling the joint dissipation as an amplitude dependent linear viscous damping. This type of method does not account for the modal coupling caused by the nonlinear joints.

The term modes as related to a nonlinear system is not a precisely correct term. The concept of modes comes from a linear analysis. Nonlinear systems may or may not exhibit modal behavior, however, since these systems are modeled as linear systems, or perturbed linear systems, the concept of modes is carried over [14]. Modal coupling is a result of this concept in that linear systems have orthogonal modes. Orthogonal modes do not allow excitation of one mode by another mode. Nonlinear systems couple these modes allowing inter-modal excitation.

It is postulated that modal coupling can cause a change in the apparent modal damping of the system. This would occur because the internal damping rate of different modes typically differs from one mode to the next in a structure. If a vibration mode with a low internal damping rate excites a mode with a high internal damping rate the energy of the system will be dissipated faster. The apparent damping of the first mode will be higher than if there was no modal coupling and the apparent damping of the other mode will be lower.

Energy dissipation of a vibrating structure with small nonlinearities can, therefore, be grouped into three classifications: linear internal damping, nonlinear hysteretic damping, and damping due to modal coupling. Material

damping is typically assumed to be linear internal damping. Hysteretic nonlinear damping is that portion of a nonlinear mechanism within a structure that directly dissipates energy from the system, such as the heat generated by friction. In the case of friction this energy dissipation can be measured via hysteresis curves generated by applying pseudo-static loads. Damping due to modal coupling is a result of energy transfer between the modes caused by the nonlinear mechanisms of the system. When a vibration mode excites other modes via modal coupling, energy is transferred to the other modes of the system. The energy may be dissipated from that mode via linear damping, hysteretic nonlinear damping, or by transferring energy to another mode, including the original mode the energy came from. Noting that damping rates for modes are typically different from one another, the effective damping rate of a given oscillation may be higher or lower than that predicted using only linear and hysteretic nonlinear damping.

1.3 Previous Research

Most of the work on nonlinear systems is limited to single-degree of freedom systems. Numerous techniques are available for analyzing this type of system [15,16]. While these systems are useful in the research of the dynamics of nonlinear systems they can not demonstrate modal coupling. In a single degree of freedom system the hysteresis caused by the nonlinearity and any linear damping assumed in the model are the only mechanisms for dissipating energy. This type of analysis is commonly extended to multi-degree of freedom systems by limiting the analysis to a single mode of oscillation [17,18]. An analysis which is limited to a single mode of oscillation is essentially reducing the multi-degree of freedom system to a single degree of freedom system. If modal coupling, caused by the nonlinearity, is ignored, the energy associated with modal coupling may be trapped in this single mode.

Modal coupling is described in some work on multi-degree of freedom nonlinear systems [19,20,21,22]. These systems typically have dominant nonlinear behavior and significant modal coupling [23,24,25,26]. The energy associated with modal coupling is discussed but is rarely associated directly with damping [27]. Coupled nonlinear damping has been discussed briefly in regard to the measurement of damping in beams, plates and trusses [28,29,30]. When measuring small parameters such as material damping, damping induced by

nonlinearities becomes important and can easily dominate the measurement. Studies investigating joint dominated structures have also noted damping due to modal coupling. Chapman, Shaw, and Russell [31] describe a recent investigation of how joint nonlinearities affect the dynamics of a space structure. Modal coupling is evident and damping of the structure is apparently affected by the modal coupling.

1.4 Research Approach

An investigation of damping due to modal coupling requires an analytically modeled structure with the following properties:

- many degrees of freedom, preferably a continuous structure,
- linear or internal damping in all modes,
- some nonlinearity which causes modal coupling, preferably without introducing hysteretic damping of its own.

There are very few exact solutions to nonlinear continuous structures, especially with damping included. There are solutions to linear continuous structures. Uniform, continuous, beams can be coupled with piecewise linear joints to form a continuous nonlinear structure. The model chosen in this analysis is that of long thin beams, modeled as damped engineering beams, linked together by rotational spring-dampers acting as joints. The joints are piecewise linear in time, which means that during an oscillation they can assume only a few different linear configurations, each with a different stiffness. A set of linear sub-systems representing all the different permutations of the joints, is generated where each sub-system is only valid when it is in a particular joint state defined by its joint properties. The structure can be modeled by one sub-system at a time. The structure is nonlinear because as the structure vibrates the joint state changes causing an abrupt transfer from the current linear sub-system to another linear sub-system. This type of nonlinearity can effectively model joint dead-band, asymmetrically stiff joint, and local buckling of portions of the structure. Each of these nonlinearities is piecewise linear in the sense that it is composed of a set of linear states which the structure transfers among, subject to some structural parameter.

The joint's dynamics enter the model as boundary conditions applied to the beam segments. The beams are modeled as damped engineering beams so a system of equations, given a single joint configuration of the nonlinear

joints, is derived [32]. This results in a transcendental equation which is solved iteratively for mode frequencies and shapes. Initial conditions are applied and a time marching routine is used to monitor the nonlinear parameters and iteratively determine when the nonlinear structure transfers from one linear sub-system to another. The final state of the current linear sub-system is used as the initial condition of the new linear sub-system. Orthogonality equations derived from the engineering beam equations are used to solve the initial condition problem of the sub-system transfer.

The damping of the engineering beam is accomplished by including a strain velocity or strain rate damping term in the beam equations. The resulting damping ratio for each mode is defined by the damping coefficient in the strain rate damping term. The modal damping ratio increases linearly as the modal frequency increases. As a result, the damping rate, the real portion of the complex eigenvalue describing the beam's motion, increases rapidly with the modal frequency. This analysis requires different damping ratios for the modes in order to examine the relationship of the modal damping rates to the damping due to modal coupling. To accomplish this the special case of proportionally damped engineering beam equations is used. In a proportionally damped system the mode shapes are equivalent to those of the undamped engineering beam. The mode shapes and the orthogonality equations become independent of the damping term and the energy of the proportional system de-couples into modal form. This allows separate equations, the same beam equation with different damping coefficients, to represent each individual mode and still maintain orthogonality between the modes. The modal damping can then be set to any desired ratio. The special case of proportional damping is limited, however, since it requires that damping be proportionally distributed over the beam.

This model has a number of advantages for examining nonlinear coupled damping. The most useful is the preservation of modes. The structure is made up of linear models for each linear sub-system, so linear modes can be used. This allows the tracking of modal amplitudes as the structure transfers from linear sub-system to linear sub-system. The model is also a continuous structure, so an infinite number of modes are implicitly included and there is no possibility of energy being trapped due to limited degrees of freedom. When a mode shape is calculated, except for computational limits, the calculated shape is exact and orthogonal to all other sub-system modes even though all modes

may not be, calculated. Only a limited number of modes are calculated, but the coupling to uncalculated modes is implicitly included in the model. This is an improvement over a finite element model where unmodeled modes, due to a finite number of degrees of freedom, can not contribute to the coupling, so the energy is effectively trapped within the model.

Coupling of unmodeled modes is consistently accounted for. Energy transferred to an unmodeled modes is assumed to be dissipated quickly. This allows the estimation of the maximum amount of damping due to modal coupling from the simulation of the structure by including only one mode in the model. The nonlinear structure modeled in this paper only allows energy to exit a mode by coupling to another mode and by linear internal modal damping. The joints have little or no hysteretic damping of their own. By modeling only a single mode the energy transferred to coupled modes is assumed to be lost and will represent the maximum amount of energy dissipation possible via modal coupling. This allows the investigation of the influence of coupled nonlinear damping with a minimum of computation.

In any analysis it is always important to compare theory with experiment to confirm that there are no significant unmodeled dynamics or inaccuracies in the analysis. The requirements of an experiment examining damping due to modal coupling are similar to those discussed for large space structures, namely the lack of atmosphere, gravity, and support interaction must be simulated. These requirements are met by testing in the ASTROVAC facility at MIT. The ASTROVAC is a fourteen foot tall, ten foot diameter vacuum chamber with a lofting system at its base. Specimens, such as the long thin beams described above, are lofted, in vacuum, to the top of the chamber. During the 1.5 seconds it takes the specimen to travel from the bottom to the top and back again, it is in free-fall and isolated from all external forces. Strain gauges mounted on the specimen transmit their signal over very thin signal wires connecting the specimen to a follower system. The follower system carries shielded wires from the chamber wall to near the specimen as it follows its flight path. The thin signal wires travel only the short distance between the specimen and the follower, and remain slack throughout the flight, in order to impart little or no influence on the specimen. At the end of its flight the specimen lands in a net, most of the time surviving the impact. This system has been used to measure material damping ratios in the past with great accuracy [9].

1.5 Outline

Chapter 2 establishes the models and analytical method to be used. Chapter 3 derives the equations necessary in the analysis. Chapter 4 establishes the computational techniques used in the analysis. Chapter 5 describes the theoretical analysis and presents results of the computational model. Chapter 6 presents an experiment utilizing the ASTROVAC. Chapter 7 correlates the theoretical model and the experimental data and investigates coupled nonlinear damping and nonlinear dynamics of the experimental specimens. Chapter 8 summarizes the results and conclusions of this work.

ANALYSIS

Chapter 2

Analytical Method

2.0 Overview of Analysis

The focus of this report is to develop an understanding of the energy dissipation due to modal coupling and the transfer of energy between modes. To eliminate the possibility of artificially restricting the energy transfer between modes due to the limited degrees of freedom of discrete models, the nonlinear structures chosen for analysis are continuous engineering beams. The beam sections include internal damping and are linked together by nonlinear joints. The nonlinear joints are piecewise linear and non-hysteretic. Exact modal solutions can be calculated during piecewise intervals of time. The objectives of the analysis section is to present an analytical method for the examination of energy dissipation in such nonlinear structures. More specifically this will include the following:

- Chapter 2 describes the analytical models, piecewise linear engineering beams linked by rotational springs, outlines the analytical approach used in the analysis, and describes the derivations necessary for the analysis. The advantages of the approach, its more general application, and its limitations are also discussed.
- Chapter 3 derives and solves the equations of motion of the engineering beams used in the analysis. The initial condition problem is solved with the use of orthogonality equations derived from the equation of motion. A structural energy equation is generated and conditions of modal de-coupling of the energy are derived. Independent modelling of structural modes is described and justified with the use of the energy equations.
- Chapter 4 describes the computational approach used in the analysis. The structure and logic of the programs used are discussed. Limits of the software and the hardware used are described and tests for errors and accuracy are presented.
- Chapter 5 presents the results of the analysis. The procedure used for the analysis is described. Results and conclusions about how and where energy is dissipated in the sample structures are presented.

2.1 Problem Statement

The objective of the analysis is to model the dynamics of a structure which has nonlinear, non-dissipative joints. The focus of the analysis is the transfer of energy between modes, as well as where and how energy is dissipated within the structure. This requires that the model chosen have sufficient degrees of freedom that modal coupling can occur and that uncoupled internal damping be present.

Real structures have unlimited degrees of freedom so that any coupling of the modes that occurs can, in effect, couple an unlimited number of modes. In principle energy can transfer between all of the modes. If a model of a real system has limited degrees of freedom, energy transfer can only occur between those modes modeled. To eliminate this potential problem, the modeled structures are long, thin, uniform, continuous engineering beams joined at their ends. The nonlinearities are incorporated into the structure by designing the joints as piecewise linear rotational springs.

The piecewise linear nature of the joints and the uniformity of the beam sections allows the model to be analyzed directly in a piecewise linear fashion. The structure is divided into separate linear sub-systems which represent the structure during a specified structural state. The modes of the linear sub-systems of the structure are determined independently. When the structure transfers from being represented by one sub-system to another sub-system the energy transfer between the modes can be calculated. Obviously not all modes are calculated. An estimate of the total energy transferred to uncalculated modes can be calculated by subtracting the total energy of the modeled modes of the second sub-system from the total energy of the first sub-system, assuming that the first sub-system's uncalculated modes have zero amplitude. At the next sub-system transfer the implicit assumption is that the uncalculated modes have zero amplitude. The implicit assumption in this analysis is that the energy transferred to uncalculated modes is dissipated in those modes.

The internal or material damping of real structures occurs in a complex manner. Some assumptions of internal damping are made in this analysis. Internal damping is assumed to be small, to cause exponential decay, to be decoupled between the modes, and to vary as a function of frequency according to some unknown but experimentally determinable function. A damping term is added to the engineering beam equation which simulates

strain rate or strain velocity damping within the beams. A damping term is also added to the rotational springs at the joints. For the modes in this model to decouple with respect to amplitude and energy the damping must be proportional. A proportionally damped beam has the identical mode shapes as the same beam with any other proportional damping value or no damping at all. This property is used to separate the damped system equation into a set of independent modal equations. Each mode is assigned its own damping factor.

2.2 Analytic Models

The models chosen for this analysis consist of long thin damped engineering beams joined at their ends by piecewise linear rotational spring dampers. The characteristics of the piecewise linear joints can be varied to simulate an asymmetric stiffness, dead-band, or any combinations of on-off springs. The on-off spring is the principal mechanism used in this analysis to simulate a discrete nonlinearity. An idealized asymmetrically stiff joint is shown in figure 2.1. To simplify the illustrations the dampers associated with the rotational springs are not shown.

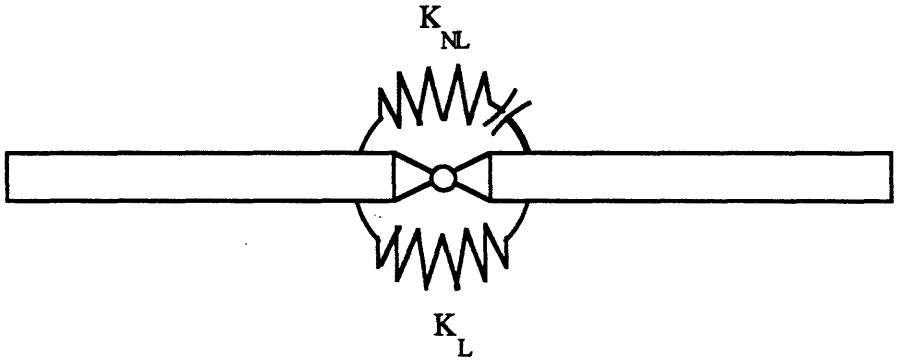

Idealized Asymmetrically Stiff Joint
Figure 2.1

The linear rotational spring with the stiffness designated as K_L, represents the linear portion of the joint. The rotational spring with the stiffness designated as K_{NL} is an on-off spring representing the piecewise linear portion of the joint. The on-off spring is only active when it is in compression. The asymmetrically stiff joint can be separated into two linear sub-joints. The two sub-joint configurations are shown in figures 2.2 and 2.3.

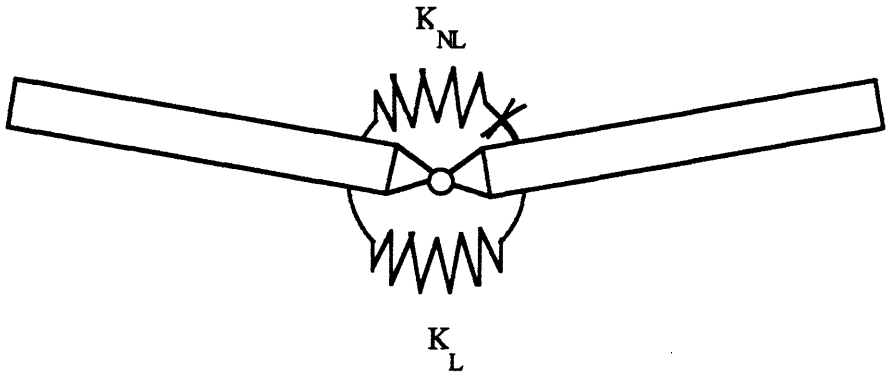

Asymmetrically Stiff Joint
Stiff Sub-Joint Configuration
Joint Stiffness = $K_{NL} + K_L$
Figure 2.2

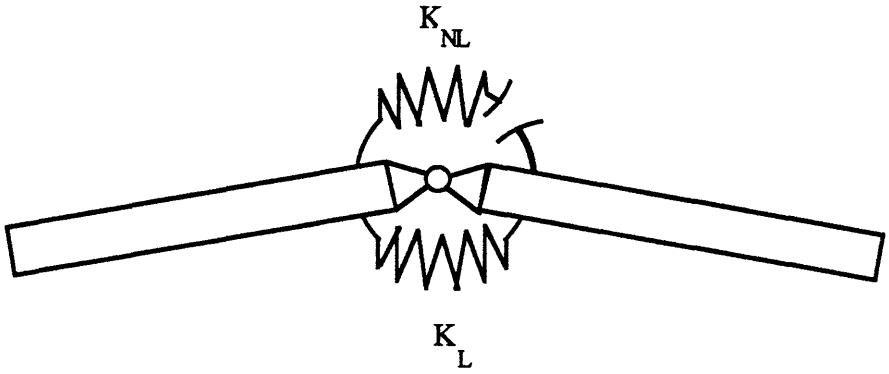

Asymmetrically Stiff Joint
Flexible Sub-Joint Configuration
Joint Stiffness = K_L
Figure 2.3

The point when the joint transfers between the two sub-joint configurations is determined by the characteristics of the on-off spring. When the moment provided by the on-off rotational spring reaches zero the spring disengages. The spring does not re-engage until the joint rotates back to the spring's rest position. If there is no damping included in the joint the point of zero moment and the rest position of the spring are the same. When damping is included the moment and position transfers occur at different points. The moment-rotation plot of the on-off spring is shown in figure 2.4.

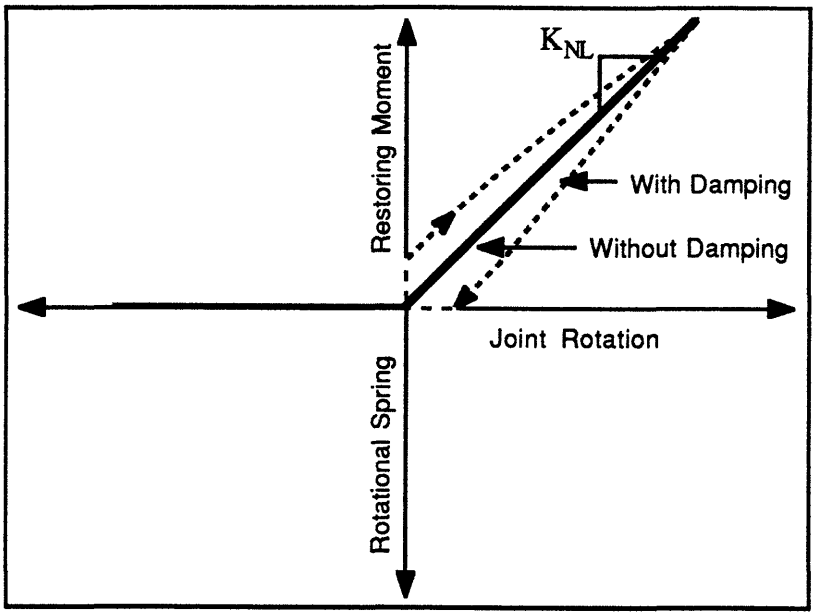

Moment-Rotation Plot for On-Off Rotational Spring-Damper
Figure 2.4

The linear rotational spring moments are added to the on-off spring moments to obtain the overall joint moments of the asymmetrically stiff joint, figure 2.5.

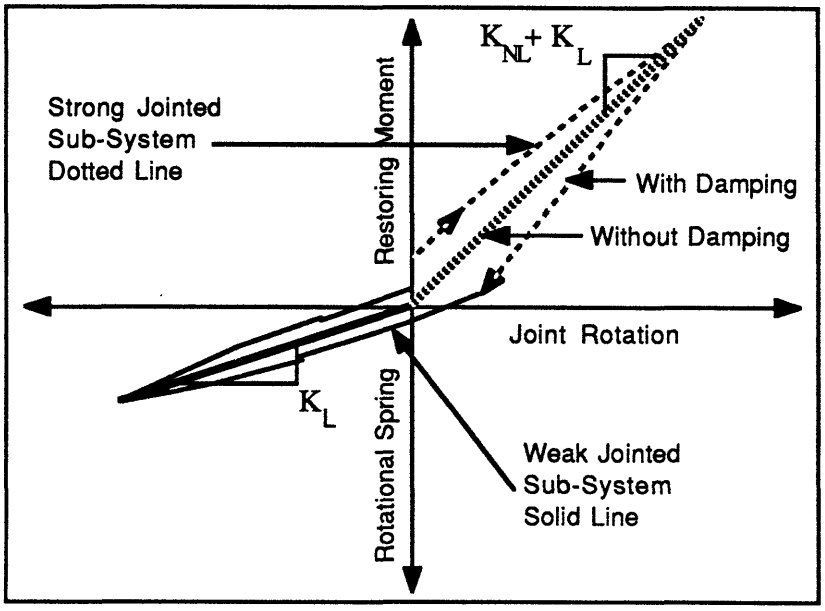

Moment-Rotation Plot of Asymmetrically Stiff Joint
Figure 2.5

The sub-joint transfer points are determined from the the on-off spring moments only. The rotation at which the on-off spring engages can be adjusted by applying an offset to the on-off rotational spring. This is done by applying a constant, balanced moment to the joint. No applied moments are necessary if the transfer is located at zero rotation of the joint.

Three specific models are examined: a two section beam joined by a piecewise linear, asymmetrically stiff, rotational spring; a long thin beam with a piecewise linear, asymmetrically stiff, rotational spring, linking the one-third points; and a two section beam joined by piecewise linear, rotational springs, with a dead-band. These systems of beams and joints are assumed to be in an unconstrained free-free state. The systems are set in motion via a given initial condition and allowed to decay. No external forces are applied.

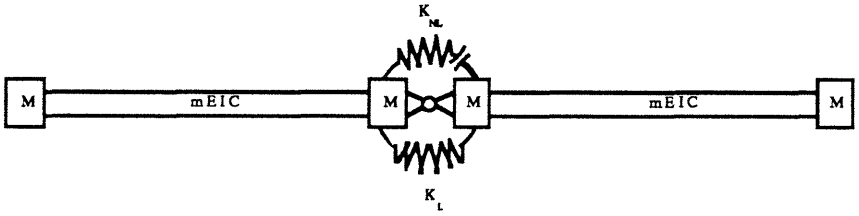

Two Beam Section System
with Asymmetrically Stiff Joint and Point Masses
Figure 2.6

The first system analyzed, shown in figure 2.6, consists of two beam sections jointed in the middle by a asymmetrically stiff joint, figure 2.1. This is intended to be a rough simulation of a structure with structural joints which are stiffer in one direction than another. This system of beams and a joint is separated into two different sub-systems, coinciding with all the possible joint configurations the system can assume, figures 2.2 and 2.3. The two sub-systems of the asymmetrically stiff jointed beam are illustrated in figures 2.7 and 2.8. The sub-system transfer points are obtained from figure 2.5.

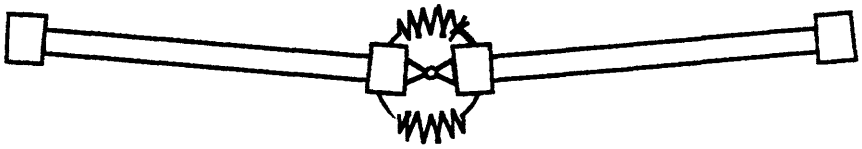

Asymmetrically Stiff Jointed Beam
Stiff Jointed Sub-System
Figure 2.7

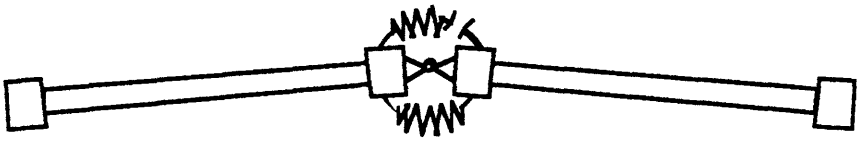

Asymmetrically Stiff Jointed Beam
Flexible Jointed Sub-System
Figure 2.8

The second system, shown in figure 2.9, is a long thin beam made up of three beam sections rigidly coupled together with a spring damper coupling the rotation of the ends of the middle section together. It is schematically shown with a linear spring connected to two lever arms located at the one third points of the beam. The linear force of the spring is transmitted to the beam via the lever arms and couples the rotational motion of these positions on the beam. Damping is included in the linear spring but, for clarity, is not shown in the figures. Extensional and compressive loads applied to the beam by the linear spring are ignored. This type of system roughly simulates a wire braced structure.

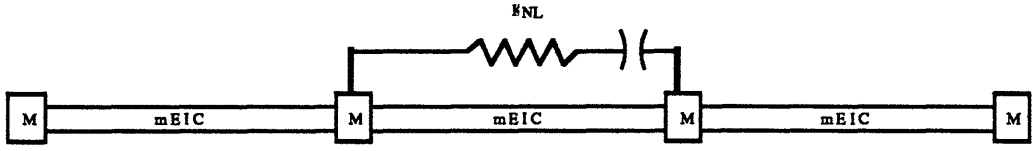

Three Beam Section System with Asymmetrically Stiff Spring Coupling
the One-Third Positions and Point Masses
Figure 2.9

The wire braced structure is separated into two linear sub-systems. The transfer between the sub-systems is determined by the difference in the rotations of the

one third points of the beam. The sub-systems are illustrated in figures 2.10 and 2.11.

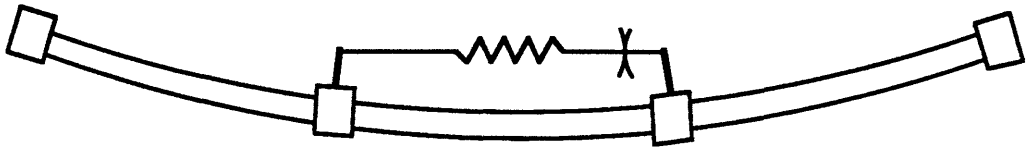

Three Beam Section System with Asymmetrically Stiff Spring Coupling
the One-Third Positions and Point Masses
Stiff Sub-System
Figure 2.10

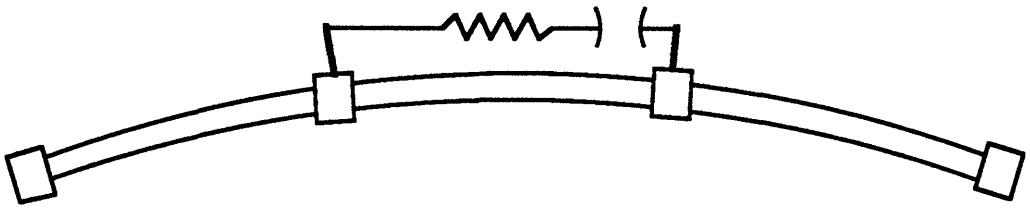

Three Beam Section System with Asymmetrically Stiff Spring Coupling
the One-Third Positions and Point Masses
Flexible Sub-System
Figure 2.11

The rotational coupling of the one third points of the beam takes the form of a more generalized asymmetrically stiff joint. The same formulations are used but the rotations and moments of the joint are at different positions on the beam.

The third system is a two section beam joined in the middle by a joint which has a dead-band section in it, figure 2.12. This is intended to be a rough simulation of a structure with loose joints. A dead-band joint is assumed to be a rotational spring damper where the spring has a small stiffness when it is centered and a much higher stiffness when the joint is rotated to ether side of the center position. Damping is included in the joint simulations but, for clarity, is not included in the figures.

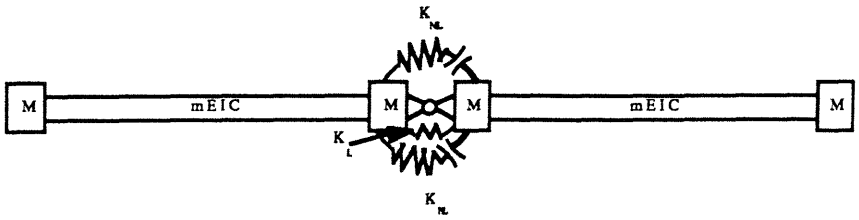

Two Beam Section System
with Dead-Band Joint and Point Masses
Center Sub-System
Figure 2.12

The dead-band jointed structure has two on-off rotational springs and is, therefore, separated into three separate sub-systems. The center position sub-system is illustrated in figure 2.12. The joint stiffness, when the joint is in the centered sub-system, is designated K_L. Both of the on-off rotational springs are not engaged in this sub-system. The other two sub-systems are illustrated in figures 2.13 and 2.14. A single on-off rotational spring engages when the joint reaches a given rotation. The dead-band joint is assumed to be symmetric. The two on-off springs have the same stiffness and engage at the same but opposite rotations.

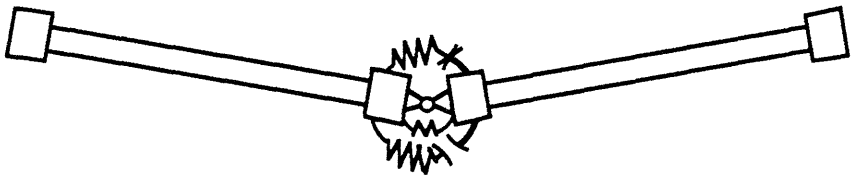

Two Beam Section System
with Dead-Band Joint and Point Masses
Second Sub-System
Figure 2.13

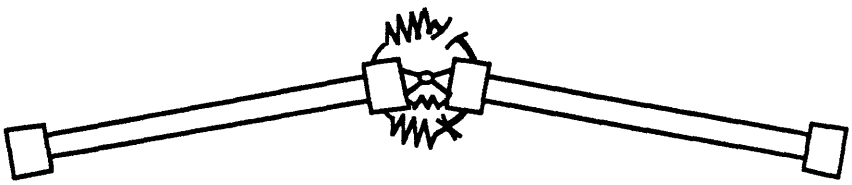

Two Beam Section System
with Dead-Band Joint and Point Masses
Third Sub-System
Figure 2.14

The asymmetrically stiff joint, present in the first and second systems, are designed so that no steady state forces are required to simulate it. The systems are, therefore, amplitude independent, simplifying the analysis. The dead-band joint requires steady state moments at the joint. The system is amplitude dependent and requires a slightly different analysis.

2.3 Outline of Analytical Procedure

The analytical approach used to examine energy dissipation in structures with non-hysteretic, piecewise linear, joints is to divide the resultant nonlinear structure into a number of linear sub-systems. The sub-systems are structural simulations which represent the entire structure with the piecewise linear joints of the structure in a single sub-joint configuration. Each sub-system represents the nonlinear structure only over an interval defined by a set of structural state requirements on the system variables. The structural state requirements used in this analysis are the angular rotations and rotation rates of the joints. There are as many linear sub-systems as there are permutations of the sub-joints.

The nonlinear structure is set in motion in one of its linear sub-systems by giving it an initial condition which causes the structure to be within desired structural state limits. As the structure vibrates in its linear sub-system, the structural state eventually exceeds the limits associated with that linear sub-system. The time the structural state reaches its limits is determined and the final structural state of the current sub-system is used as the initial condition for the new sub-system. This process is repeated resulting in a string of sub-systems each with initial times and modal amplitudes.

The string of sub-system parameters is used to calculate the energy of each mode as a function of time. The energy plots are used to examine the transfer of energy between modes, and where and how energy is dissipated. Simulated strain gauge data is generated and used to calculate a log decrement damping ratio and to compare with experimental data directly. The calculated damping ratio is, in general, different from the linear modal damping ratios set in the original definition of the model because it includes damping effects due to energy transfer between modes.

The justification for using these systems and this type of analysis centers around their ability to be modeled as a continuous, damped system. This characteristic eliminates the possibility of trapping energy in a system due to limited degrees of freedom. The piecewise linear rotational spring-dampers linking the ends of the beams are chosen because they allow a solution to a continuous system with nonlinear joints which are non-hysteretic and therefore, provides no damping themselves. The damping of the structure comes from the uncoupled linear damping assumed in the model. The nonlinear joints couple the modes of the structure allowing energy transfer between the modes. Since the structure is separated into linear sub-systems, modes and modal characteristics are preserved in the analysis. This way energy can be calculated on a mode by mode basis. How the structural energy is distributed among the modes and where it is actually dissipated is calculable with these systems.

The analysis can be used to establish a technique which is also useful in the estimation of the maximum energy dissipation due to modal coupling. This is done by only including the primary modes in the analysis, allowing the energy transfer to the uncalculated modes to be lost, assuming it to be dissipated in the uncalculated modes. The techniques used in this analysis are also useful in discrete systems if a sufficient number of degrees of freedom are present.

2.4 Outline of Derivations

The first step in the analysis is defining the equations of motion of damped engineering beams linked together by damped rotational springs. The equations of motion are used to model the linear sub-systems of the piecewise linear structure. The derivations and solutions of the linear sub-systems are

based on a general, non-proportional system of equations. A special case of proportionally damped systems is used to model individual modes of the sub-systems by similar and independent equations. This allows the setting of individual modal damping rates and the calculation of modal energy.

The second step in the analysis is solving each of the linear sub-systems for their modal frequencies, shapes, and any forced displacements. A general beam equation is solved, the solutions taking the form of complex exponentials for the homogeneous case and polynomials for the particular case. Solutions for modal frequencies and shapes are derived from the boundary conditions of the sub-system. Typical boundary conditions of the structures analyzed are listed.

The third step in the analysis is the calculation of the transfer between sub-systems when the state limits are exceeded. This is accomplished by first deriving a set of orthogonality equations which are in turn used to derive a system transfer equation. The system transfer equation is based on transfer coefficients calculated from an equation very similar to the orthogonality equations.

The fourth step in the analysis is the calculation of the energy of the structure and the simulated output of a strain gauge over the time of the simulation. The energy equation is derived and the conditions of proportionality are discussed. Modal energy and identical modes are established for similar proportional systems and are used as a basis for separate, similar equations modeling the individual modes of the sub-systems. The method of simulating strain gauge data is also discussed.

Chapter 3

Engineering Beam Derivations

3.0 Overview

The objective of chapter 3 is the development and derivation of all mathematical tools necessary for the analysis of continuous, damped, engineering beams with piecewise linear joints. The procedure is to start with the equations of motion of a jointed, damped, engineering beam and develop the general solution to its motion and the equations necessary to calculate its modal amplitudes and energy properties from its initial conditions. The general solution is then used, with the conditions of proportional damping, to establish independent but similar equations for each mode of the system so that modal damping can be set individually.

3.1 Damped Engineering Beam Equations

The sub-systems of the beam structure are made up of beam sections which are modelled by the engineering beam equation with strain rate damping included [33]. Each beam section is assumed to be long and thin such that the engineering beam assumptions apply. It is also assumed that the beam sections are uniform over their entire length with respect to their mass/length (m), moment of inertia (I), modulus of elasticity (E), and damping coefficient (C). The local displacements are defined by W(x) and the external loads are defined as f(x,t). The equation of motion for a single beam section takes the form

$$m\ddot{W} + (EIW'' + CI\dot{W}'')'' = f(x,t) \qquad (3.1)$$

The dot superscripts signify differentiation with respect to time (t), the prime superscripts signify differentiation with respect to space (x). All terms are real and the solution for the displacements, W, must remain real. Each beam section has its own equation with its own material properties. (Please turn to appendix A for a more detailed explanation of the analysis.)

The solution for displacements is divided into homogeneous and particular parts.

$$W = W_H + W_P \tag{3.2}$$

While no external forces are allowed, f(x,t) may still be non-zero since internal moments arising from joint offsets can exist. The homogeneous solution will be examined first.

3.2 Homogeneous Solution

The homogeneous portion of equation (3.1) is:

$$m\ddot{W} + (EI\acute{W} + CI\dot{\acute{W}})\acute{} = 0 \tag{3.3}$$

An assumed solution of the form

$$W = Be^{\Omega t + ax} + B^{*}e^{\Omega^{*} t + a^{*} x} = u + u^{*} \tag{3.4}$$

is applied. Here Ω is the complex frequency, a is the complex shape factor, and B is a complex coefficient. The superscript * indicate the complex conjugate. This solution has the complex conjugate form to insure that the displacements W are always real quantities. Inputting equation (3.4) into equation (3.3) and noting that the beam properties of a single beam section are assumed to be constant, results in a characteristic equation of the form

$$u[m\Omega^{2} + a^{4}(EI + CI\Omega)] + u^{*}[m\Omega^{*2} + a^{*4}(EI + CI\Omega^{*})] = 0 \tag{3.5}$$

Since the two exponential terms, u and u* are not zero the two terms in the brackets must go to zero independently. A relationship between Ω and a is derived.

$$m\Omega^2 + a^4 (EI + CI\Omega) = 0 \tag{3.6}$$

or equivalently

$$a = \sqrt[4]{\frac{-m\Omega^2}{EI + CI\Omega}} \tag{3.7}$$

The equivalent complex conjugate equations are not shown. For each solution Ω, there are four corresponding values of a, (ia, -ia, a, -a). Combining this with their complex conjugates a total of eight terms are needed to describe each possible solution of equation (3.3).

$$W = B_1 e^{\Omega t + iax} + B_2 e^{\Omega t - iax} + B_3 e^{\Omega t + ax} + B_4 e^{\Omega t - ax} + B_1^* e^{\Omega^* t + ia^* x} + B_2^* e^{\Omega^* t - ia^* x} + B_3^* e^{\Omega^* t + a^* x} + B_4^* e^{\Omega^* t - a^* x} \tag{3.8}$$

These terms can be separated into time (Y), and spatial (ϕ), components.

$$W = \phi\, Y + \phi^*\, Y^* \tag{3.9}$$

where

$$\phi = c_1\, e^{ia\,x} + c_2\, e^{-ia\,x} + c_3\, e^{a\,x} + c_4\, e^{-a\,x} \tag{3.10}$$

$$Y = A\, e^{\Omega\, t} \tag{3.11}$$

To this point no specific solution for Ω or a has been found nor shown to exist. It is possible, however, that multiple solutions exist so the subscript j is used to distinguish between them. These are referred to as modes. The entire solution to equation (3.3) takes the form

$$W_H = \sum_j W_j \tag{3.12}$$

where there are an unspecified number of solutions or modes represented in the sum. The modal displacements can be separated into their complex conjugate parts or complex conjugate pair modes.

$$W_j = w_j + w_j^* \tag{3.13}$$

The complex modes, w and w*, insure that the solution remains real. The complex modes behave in the analysis much like conventional real modes. It is found later in the analysis to be computationally advantageous to consider the complex conjugates separate modes. There are two types of notation used in this analysis, complex conjugate notation and complex mode notation. The indication of the notation type is by the subscript variables. Complex conjugate notation uses j and k as subscript variables while complex mode notation uses n and m as subscript variables. Complex conjugate notation is illustrated in equation (3.13). The complex conjugate pair modes are given the same mode number and the same subscript variable, j or k. The complex mode notation designates the complex conjugate pair modes as even and odd and has different subscripts, n or m, identifying the complex conjugate modes. There are twice as many complex modes as there are real modes or solutions.

$$W_H = \sum_j (w_j + w_j^*) = \sum_{2\,n} (w_n + w_{n+1}^*) \Rightarrow \sum_n w_n \tag{3.14}$$

The individual modes, including complex conjugate pairs, can be separated into their spatial (mode shape), and time components.

$$w_n = \phi_n Y_n \tag{3.15}$$

The spatial components are written as

$$\phi_n = c_{1n} e^{i a_n x} + c_{2n} e^{-i a_n x} + c_{3n} e^{a_n x} + c_{4n} e^{-a_n x} \tag{3.16}$$

and the time components are written as

$$Y_n = A_n e^{\Omega_n t} \tag{3.17}$$

In general the complex frequency (Ω) is fully complex. The imaginary portion represents the sinusoidal motion of the system and the real portion represents the decay rate of that motion. The amplitude of the motion is represented by the coefficient (A). The real portion of the complex frequency is related directly to the damping coefficient (C). In the special case of C=0 (assuming a single beam section) the complex frequency becomes only imaginary. Noting that (a) is in units of 1/length (l), equation (3.7) reduces to the familiar form of the frequency equation for a beam.

$$\Omega \propto i\sqrt{\frac{EI}{m l^4}} \tag{3.18}$$

The shape function (ϕ) is also in general complex. The complex shape coefficients (c) are usually normalized. The shape factor (a) is also, in general, complex. In the special cases of C=0 (assuming a single beam section) or if the interactions with connected beam sections form a system with proportional damping the shape factor becomes either purely real or purely imaginary. In both cases the shape function (ϕ) becomes a real function and represents the

mode shape. If the shape function (ϕ) is complex then the mode shape is represented, but there are phase components present as well.

3.3 Boundary Conditions and the Transcendental Matrix Equation

Determination of the valid modal frequencies arises from the boundary condition applied to the beam sections. Each equation describing a beam section requires four boundary conditions in order to be solved. The boundary conditions at the location where the beam sections are joined together are defined by the joint properties. Five different types of boundary conditions are used in this analysis: a free end, an attached mass, the direct coupling of two beam sections, a hinged joint, and the rotational spring coupling of two beam sections. The five different types of boundary conditions are illustrated below.

Free End:

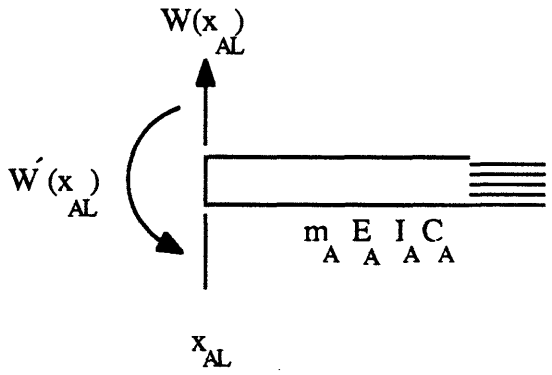

Free End Boundary Condition
Figure 3.1

The free end boundary condition sets the moment loads and the shear forces at the end of the beam section to zero.

$$E_A I_A \ddot{W}_A(x_{AL}) + C_A I_A \dot{W}_A''(x_{AL}) = 0 \tag{3.19}$$

$$[E_A I_A \ddot{W}_A'(x_{AL}) + C_A I_A \dot{W}_A'(x_{AL})]' = 0 \tag{3.20}$$

Attached Mass:

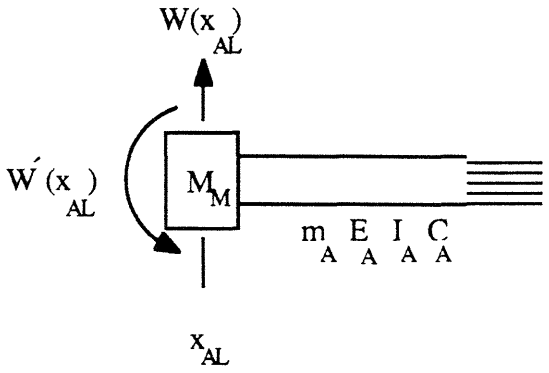

Attached Mass Boundary Condition
Figure 3.2

The attached mass boundary condition sets the shear force at the beam section boundary equal to that of the inertial loading of the attached mass (M), which is attached to the beam and undergoes any motion it does. In the example shown in figure 3.2 the moment loads are the same as in the free end case, equation (3.19).

$$[E_A I_A W_A''(x_{AL}) + C_A I_A \dot{W}_A''(x_{AL})]' = M \ddot{W}_A(x_{AL}) \qquad (3.21)$$

Direct Coupling:

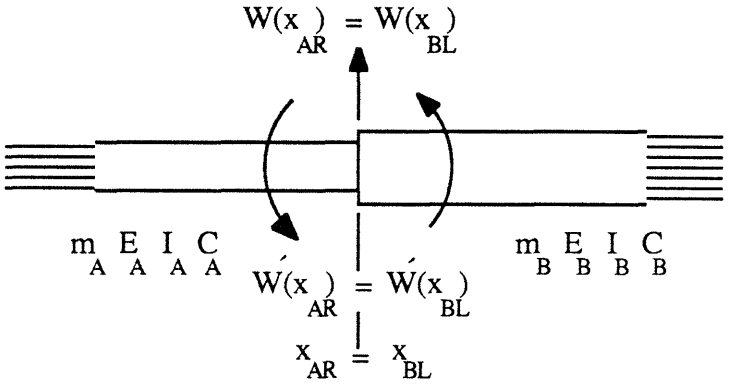

Direct Coupling Boundary Conditions
Figure 3.3

The direct coupling of two beam sections is accomplished by setting the displacements, rotations, shear forces, and moment loadings at the boundaries of the two beams equal to one another.

$$W_A(x_{AR}) = W_B(x_{BL}) \tag{3.22}$$

$$W_A'(x_{AR}) = W_B'(x_{BL}) \tag{3.23}$$

$$E_A I_A W_A''(x_{AR}) + C_A I_A \dot{W}_A'(x_{AR}) = E_B I_B W_B''(x_{BL}) + C_B I_B \dot{W}_B'(x_{BL}) \tag{3.24}$$

$$[E_A I_A W_A''(x_{AR}) + C_A I_A \dot{W}_A'(x_{AR})]' = [E_B I_B W_B''(x_{BL}) + C_B I_B \dot{W}_B'(x_{BL})]' \tag{3.25}$$

Hinged Joint:

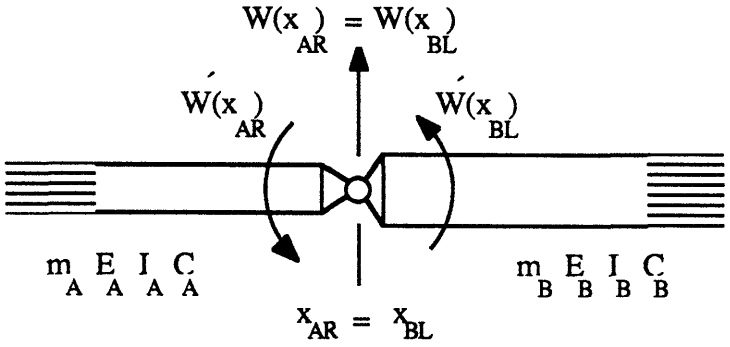

Hinged Joint Boundary Conditions
Figure 3.4

The hinged joining of two beam sections is accomplished by setting the displacements and the shear forces equal to one another and by setting the moments at the boundaries equal to zero.

$$W_A(x_{AR}) = W_B(x_{BL}) \tag{3.26}$$

$$[E_A I_A W_A''(x_{AR}) + C_A I_A \dot{W}_A'(x_{AR})]' = [E_B I_B W_B''(x_{BL}) + C_B I_B \dot{W}_B'(x_{BL})]' \tag{3.27}$$

Rotational Spring Damper:

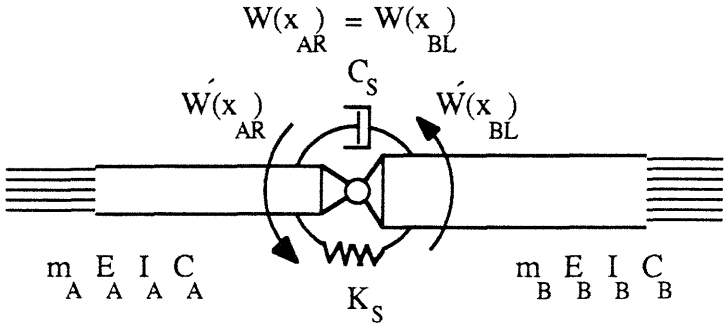

Rotational Spring Damper Boundary Condition
Figure 3.5

The rotational spring-damper coupling of two beam sections is done by setting the moment loads at the boundaries equal to one another. The moment loads at the boundaries are also equal to the moment load provided by the rotational spring-damper. The rotational spring damper provides a moment as a function of the difference between the angular and angular rate motions of the two boundaries. The rotational spring constant (K_S) and the damping factor (C_S) define the joint properties.

$$W_A(x_{AR}) = W_B(x_{BL}) \tag{3.28}$$

$$E_A I_A W_A''(x_{AR}) + C_A I_A \dot{W}_A''(x_{AR}) = E_B I_B W_B''(x_{BL}) + C_B I_B \dot{W}_B''(x_{BL}) \tag{3.29}$$

$$[E_A I_A W_A''(x_{AR}) + C_A I_A \dot{W}_A''(x_{AR})]' = [E_B I_B W_B''(x_{BL}) + C_B I_B \dot{W}_B''(x_{BL})]' \tag{3.30}$$

$$K_S [W_B'(x_{BL}) - W_A'(x_{AR})] + C_S [\dot{W}_B'(x_{BL}) - \dot{W}_A'(x_{AR})] = E_B I_B W_B''(x_{BL}) + C_B I_B \dot{W}_B''(x_{BL}) \tag{3.31}$$

The boundary conditions are used alone and in combination with each other. The systems used in this analysis provide two boundary conditions for each beam section boundary and no unconstrained degrees of freedom, except for rigid body displacements.

The boundary conditions are used to solve for the complex modal frequencies and shape coefficients. A single complex mode solution is inputted into the boundary condition equations and the equations solved simultaneously. The equations are written in matrix form. An example matrix equation is shown in equation (3.32). This matrix equation represents the modal solution of a uniform free-free beam.

$$A_n e^{\Omega_n t}(E_A I_A+\Omega_n C_A I_A)\begin{bmatrix} -a_n^{A2} e^{i a_n^A x_{AL}} & -a_n^{A2} e^{-i a_n^A x_{AL}} & a_n^{A2} e^{a_n^A x_{AL}} & a_n^{A2} e^{-a_n^A x_{AL}} \\ -i a_n^{A3} e^{i a_n^A x_{AL}} & i a_n^{A3} e^{-i a_n^A x_{AL}} & a_n^{A3} e^{a_n^A x_{AL}} & -a_n^{A3} e^{-a_n^A x_{AL}} \\ -a_n^{A2} e^{i a_n^A x_{AR}} & -a_n^{A2} e^{-i a_n^A x_{AR}} & a_n^{A2} e^{a_n^A x_{AR}} & a_n^{A2} e^{-a_n^A x_{AR}} \\ -i a_n^{A3} e^{i a_n^A x_{AR}} & i a_n^{A3} e^{-i a_n^A x_{AR}} & a_n^{A3} e^{a_n^A x_{AR}} & -a_n^{A3} e^{-a_n^A x_{AR}} \end{bmatrix}\begin{bmatrix} c_{1n}^A \\ c_{2n}^A \\ c_{3n}^A \\ c_{4n}^A \end{bmatrix}$$

$$= [0] \qquad (3.32)$$

The time (t) terms and the beam section shape coefficients ($c_\alpha{}^A{}_n$) are brought out of the matrix leaving terms with the complex frequency (Ω_n), complex shape factors ($a^A{}_n$), and the boundary condition limits ($x_{A(R \text{ or } L)}$). The superscript A on the beam section shape coefficients and the complex shape factor indicates which beam section the shape coefficients apply. There is only one beam section in this example but the jointed beams analyzed in this report include multiple beam sections. The shape coefficients and shape factors of the beam sections are, in general, not the same. The complex frequency and the complex shape factors are related to each other through equation (3.6). In the example of a uniform free-free beam the beam properties and the complex frequency can also be separated from the matrix, ($E_A I_A + \Omega_n C_A I_A$). This is not the case when there are multiple beam sections in the model with different properties. The solution of this matrix equation occurs when the determinant of the matrix goes to zero. The matrix equation is, in general, transcendental and multiple solution exist. Each solution to the transcendental matrix equation represents a complex mode.

3.4 Particular Solution

The particular solution to the equation of motion involves the forcing function f(x,t). In this analysis no external loads are allowed. However, constant internal moments caused by offsets in the joints does create the need for a particular solution. A joint offset allows the on-off spring to transfer between sub-joints at a rotation other than zero. For the moments to be balanced at the transfer rotation there must be a biasing moment present in the joint. The only joint examined in this analysis which exhibits an offset is the dead-band joint. The sub-system representing the joint when it is in-between the discontinuous springs, figure 2.12, has no offset and no particular solution. When the transfer to a sub-system which includes a discontinuous spring is made, figures 2.13 or 2.14, the moment applied by the discontinuous spring is zero when the joint has rotated away from the neutral position. A constant, balanced moment is applied at the joint.

The particular solution is calculated in much the same way as the homogeneous solution. The boundary conditions, which contain the moments applied at the joints, are placed into matrix form and solved simultaneously. There is no time dependence so the solution can be written in the form of a cubic polynomial.

$$W_P = c_{10}^A x^3 + c_{20}^A x^2 + c_{30}^A x + c_{40}^A \tag{3.33}$$

The subscript P of the displacement W_P indicates the particular solution. The superscript A indicates the beam section the solution represents. In this analysis there is only one particular solution for each system. Since the homogeneous solution has multiple solutions designated as modes starting at one, the second subscript zero on the coefficients represents the particular solution or the zero-th mode. The matrix determined by the boundary conditions is degenerate since the model chosen is free-free and rigid body modes are included. To remedy this it is noted that no external loads are applied, only internal moments. The ends of the model can be pinned to restrict translation without affecting the particular solution. The coefficients of the particular solution for each of the beam sections can now be calculated using

the same techniques as in the homogeneous solution but no row-column reduction is necessary.

This solution will cause the center of gravity of the model to move and rotate. The shape is correct, but the model has moved. To correct this the particular solution is translated and rotated back to its original orientation defined by its center of mass. This particular solution is stored as the zero-th mode. It is kept separate from the homogeneous solutions because it has a different form and therefore uses different formulations.

3.5 Orthogonality Equations

The orthogonality equations are derived from the homogeneous equations of motion of the beam sections. The orthogonality equations are useful in a number of operations because they can be used to define modal quantities: an orthogonality relationship between two eigenvalue solutions will produce a complex number if the two solutions are the same, and zero if not.

The operator defining the homogeneous equation of motion of a beam section, equation (3.3), is

$$L(u) = m\frac{d^2}{dt^2}(u) + \frac{d^2}{dx^2}\left(EI\frac{d^2}{dx^2}(u) + CI\frac{d^3}{dx^2\,dt}(u) \right) = 0 \tag{3.34}$$

The orthogonality equations are derived by placing a single complex mode into the operator, L, multiplying by a different complex mode, and integrating the entire equation. This yields equation (3.35).

$$\int_{x_1}^{x_2} w_m L(w_n)\,dx = 0 \tag{3.35}$$

A similar equation can be written by switching the modes:

$$\int_{x_1}^{x_2} w_n \boldsymbol{L}\,(w_m)\,dx = 0 \tag{3.36}$$

Subtracting equation (3.36) from (3.35), an integral operator is defined by the equation;

$$\int_{x_1}^{x_2} \{ w_m \boldsymbol{L}\,(w_n) - w_n \boldsymbol{L}\,(w_m) \}\,dx = 0 \tag{3.37}$$

Each beam section contributes a similar equation to form an equation representing the entire system of beam sections. The boundary conditions describing the system joints and point masses are included, and after integration and some manipulation, the first orthogonality equation is derived (see Appendix A, section A.4.6).

$$\sum_{B}^{\text{all beams}} \left\{ \int_{x_{BL}}^{x_{BR}} \left\{ (\Omega_m + \Omega_n)\,\phi_{Bm}\phi_{Bn}\,m_B + \phi''_{Bm}\phi''_{Bn}\,C_B I_B \right\} dx \right\}$$

$$+ \sum_{M}^{\text{all masses}} \left\{ \left\{ M_M\,(\Omega_m + \Omega_n)\,\phi_{Mm}(x_M)\,\phi_{Mn}(x_M) \right\} \right\}$$

$$+ \sum_{S}^{\text{all springs}} \left\{ C_S\,[\phi'_{SRm}(x_{SR}) - \phi'_{SLm}(x_{SL})]\,[\phi'_{SRn}(x_{SR}) - \phi'_{SLn}(x_{SL})] \right\} = \delta_{mn}\,\nu_{mn} \tag{3.38}$$

The orthogonality equation involves any two solutions or modes of the system designated m and n. A subscript m or n of a variable indicates that the particular variable originates from that complex mode. The subscript B indicates which beam the variable originated from. The subscript of BL indicates the left end of beam B. Similarly the subscript BR indicates the right end of beam B. The subscript M indicates reference to the mass M, the subscript S indicates reference to the rotational spring-damper S, the subscript SL indicates the left end of the rotational spring-damper and subscript SR indicates the right end of the rotational spring damper. The right hand side of equation (3.38) indicates that the orthogonality equation is zero when the modes m and n are different, and equal to the complex coefficient (ν) when they are identical.

A second orthogonality equation can be generated by placing the first orthogonality equation back into a modified form of the equation of motion (see Appendix A, section A.4.7).

$$\sum_{B}^{\text{all beams}} \int_{x_{BL}}^{x_{BR}} \{ -\Omega_n \Omega_m m_B \phi_{Bn} \phi_{Bm} + E_B I_B \phi''_{Bn} \phi''_{Bm} \}$$

$$+ \sum_{M}^{\text{all masses}} \{ -\Omega_n \Omega_m M_M \phi_{Mn}(x_M) \phi_{Mm}(x_M) \}$$

$$+ \sum_{S}^{\text{all springs}} \{ K_S [\phi'_{SRm}(x_{SR}) - \phi'_{SLm}(x_{SL})][\phi'_{SRn}(x_{SR}) - \phi'_{SLn}(x_{SL})] \} = -\Omega_n \delta_{mn} \nu_{mn} \tag{3.39}$$

These orthogonality equations are used in three ways. First, they are used to normalize the complex mode shape coefficients. This is accomplished by dividing each complex mode shape coefficient ($c_{\alpha n}$) by the complex orthogonality coefficient (ν_{nn}). The double subscript n indicates that the same complex mode was used for both modes in the orthogonality equation. Placing the normalized complex shape coefficients into the orthogonality equations the new complex orthogonality coefficients become one (real) or zero. The second use of the orthogonality equations is as a check on the solutions of the eigenvalues. When a mode is placed into the orthogonality equation with itself, the result should be a real one. When it is placed into the orthogonality

equation with another mode, the result should be zero. If these conditions are not met then mode orthogonality is not achieved. The third use is the separation of modes in the solution of the initial condition problem and the energy equation.

3.6 Initial Condition Problem and System Transfer

As the structure is allowed to vibrate the states of the piecewise linear joints change and the system jumps from one linear system to another. The final shape and velocity of the current linear sub-system are used as the initial conditions for the new linear sub-system. Determining the amplitudes of the individual modes as a function of some initial shape and motion derives from the first orthogonality condition. The orthogonality equations play a significant role by decoupling the equation and allowing the the individual calculation of modal amplitudes. After some manipulation the general initial condition equation for the engineering beam equations used in this analysis becomes

$$\frac{e^{-\Omega_m t_T}}{\nu_{m\,m}} \left\{ \sum_{B}^{\text{all beams}} \left\{ \int_{x_{BL}}^{x_{BR}} \left\{ \Omega_m \phi_{Bm} W_{B_T} m_B + \phi_{Bm} \dot{W}_{B_T} m_B + \phi''_{Bm} W''_{B_T} C_B I_B \right\} dx \right\} \right.$$

$$+ \sum_{M}^{\text{all masses}} \left\{ \left\{ M_M (\Omega_m \phi_{Mm} W_{M_T} + \phi_{Mm} \dot{W}_{M_T}) \right\} \Big|_{x_M} \right\}$$

$$\left. + \sum_{S}^{\text{all springs}} \left\{ C_S \left[\phi'_{SR_m}(x_{SR}) - \phi'_{SL_m}(x_{SL}) \right] \left[W'_{SR_T}(x_{SR}) - W'_{SL_T}(x_{SL}) \right] \right\} \right\} = A_m \tag{3.40}$$

The subscript T on the displacements, W, and the time, t, indicates the time of the initial condition or transfer. The complex amplitude of the complex mode is represented by the variable A, see equation (3.17). The subscript m indicates the mode which is being calculated.

Equation (3.40) allows the calculation of modal amplitudes given a general initial shape and motion, which are in this analysis, the final state of the previous sub-system at the time of transfer between the sub-systems. In this

analysis, the dimensions and mass distributions of the sub-systems making up the nonlinear beam system are assumed to be the same. The only parameters allowed to change from sub-system to sub-system are the stiffness and damping of the beam sections and joints. This allows considerable simplification of the transfer equation.

Compatibility requires that at the time of transfer between two sub-systems, the shape and velocity of the two sub-systems must be the same.

$$V(t_T) = W(t_T) \tag{3.41}$$

$$\dot{V}(t_T) = \dot{W}(t_T) \tag{3.42}$$

The displacement of the previous sub-system is designated as V, the new sub-system is W. Since the previous sub-system's motions are described in the same modal form as the new sub-system, equations (3.41) and (3.42) can take the form

$$V_0 + \sum_m V_m = W_0 + \sum_n W_n \tag{3.43}$$

$$\sum_m \dot{V}_m = \sum_n \dot{W}_n \tag{3.44}$$

The subscript 0 on the displacements V and W indicates the particular solution of the systems and the subscripts m and n indicate complex modes of the respective systems. The solution is divided into two parts, the particular solution and the homogeneous solution. The particular solution of the new system is already determined and is subtracted from the particular solution of the previous system. The particular solution in this analysis is not time dependent and therefore does not appear in the rate equation.

$$(V_0 - W_0) + \sum_m V_m = \sum_n W_n \tag{3.45}$$

Each term of the left side of equations (3.43) and (3.44) will in principle contribute to the amplitude of every term of the right side of the equations. The amplitude of mode n will be, in general, the sum of the contributions from all of the terms on the left side of both equations.

Particular Solution Transfer:

The particular portion of the left side of equation (3.45) is in the form of a cubic polynomial and has the same dimension as the exponential functions on the right side. It is placed into equation (3.40) and the initial condition equation takes the form of a transfer equation

$$\frac{e^{-\Omega_m t_T}}{\nu_{m\,m}} \left\{ \sum_{B}^{\text{all beams}} \left\{ \int_{x_{BL}}^{x_{BR}} \left\{ \Omega_m \phi_{Bm} (V_{B_0} - W_{B_0}) m_B + \phi''_{Bm} (V_{B_0} - W_{B_0})'' C_B I_B \right\} dx \right\} \right.$$

$$+ \sum_{M}^{\text{all masses}} \left\{ M_M \; \Omega_m \phi_{Mm} (V_{M_0} - W_{M_0}) \; \Big|_{x_M} \right\}$$

$$\left. + \sum_{S}^{\text{all springs}} \left\{ C_S \; [\phi'_{SR_m}(x_{SR}) - \phi'_{SL_m}(x_{SL})] [V'_{SR_0}(x_{SR}) - V'_{SL_0}(x_{SL}) - \right. \right.$$

$$\left. \left. W'_{SR_0}(x_{SR}) + W'_{SL_0}(x_{SL})] \right\} \right\} = A_{m0} \qquad (3.46)$$

where the subscript m indicates the mode to which this complex amplitude contributes. The subscript 0 on the amplitude A indicates that this contribution originates from the particular solutions. If the particular solutions of the two systems are identical then the contribution is zero. The term inside the parentheses is designated as the particular transfer coefficient, τ, where

$$\left\{ \sum_{B}^{\text{all beams}} \left\{ \int_{x_{BL}}^{x_{BR}} \{ \Omega_m \phi_{Bm}(V_{B_0}-W_{B_0})\ m_B + \phi''_{Bm}(V_{B_0}-W_{B_0})''\ C_B I_B \}\, dx \right\} \right.$$

$$+ \sum_{M}^{\text{all masses}} \{ M_M\ \Omega_m \phi_{Mm}(V_{M_0} - W_{M_0}) \Big|_{x_M} \}$$

$$\left. + \sum_{S}^{\text{all springs}} \{ C_S [\phi'_{SR_m}(x_{SR}) - \phi'_{SL_m}(x_{SL})] [V'_{SR_0}(x_{SR}) - V'_{SL_0}(x_{SL}) - W'_{SR_0}(x_{SR}) + W'_{SL_0}(x_{SL})] \} \right\} = \tau_{m0}$$

(3.47)

Homogeneous Solution Transfer:

The homogeneous terms on the left side of equations (3.43) and (3.44) have the same exponential form and dimension as the right side. Placing them into equation (3.40) results in an equation very similar to the orthogonality equation

$$\sum_{n} \left[B_n \frac{e^{(\omega_n-\Omega_m)t_T}}{\nu_{mm}} \left\{ \sum_{B}^{\text{all beams}} \left\{ \int_{x_{BL}}^{x_{BR}} \{ (\Omega_m + \omega_n)\, \phi_{Bm} \psi_{Bn} m_B + \phi''_{Bm} \psi''_{Bn} C_B I_B \}\, dx \right\} \right.\right.$$

$$+ \sum_{M}^{\text{all masses}} \{ \{ M_M(\Omega_m + \omega_n)\ \phi_{Mm}\ \psi_{Mn} \} \Big|_{x_M} \}$$

$$\left.\left. + \sum_{S}^{\text{all springs}} \{ C_S [\phi'_{SR_m}(x_{SR}) - \phi'_{SL_m}(x_{SL})] [\psi'_{SR_n}(x_{SR}) - \psi'_{SL_n}(x_{SL})] \} \right\} \right] = A_m$$

(3.48)

The modal frequencies and shapes of the previous solution are designated as ω, ψ, and the subscript n indicates the mode. The beam parameters m, C, I, and M are those of the new system and the mode frequencies and shapes of the new system are designated Ω and ϕ. The subscript m indicates the mode. The

terms inside the parentheses are identical to the orthogonality equation, equation (3.38), with the exception that the frequencies and modes are of different systems. The modal transfer coefficient, τ, is defined as a more general form of the orthogonality coefficient, ν, and takes the form

$$\left\{ \sum_{B}^{\text{all beams}} \left\{ \int_{x_{BL}}^{x_{BR}} \left\{ (\Omega_m + \omega_n)\, \phi_{Bm} \psi_{Bn}\, m_B + \phi''_{Bm} \psi''_{Bn} C_B\, I_B \right\} dx \right\} \right.$$

$$+ \sum_{M}^{\text{all masses}} \left\{ \left\{ M_M (\Omega_m + \omega_n)\, \phi_{Mm}\, \psi_{Mn} \right\} \Big|_{x_M} \right\}$$

$$\left. + \sum_{S}^{\text{all springs}} \left\{ C_S \left[\phi'_{SRm}(x_{SR}) - \phi'_{SLm}(x_{SL}) \right] \left[\psi'_{SRn}(x_{SR}) - \psi'_{SLn}(x_{SL}) \right] \right\} \right\} = \tau_{mn} \tag{3.49}$$

The transfer coefficient, τ, is, in general, not one or zero, as is the case with the normalized orthogonality coefficient, ν. Inputting equation (3.49) into equation (3.48) and equation (3.47) into equation (3.46), the transfer equation takes the form

$$\sum_{n=0}^{\infty} \left\{ B_n e^{(\omega_n - \Omega_m) t_T} \frac{\tau_{mn}}{\nu_{mm}} \right\} = A_m \tag{3.50}$$

The second subscript, n, of the modal transfer coefficient, τ, indicates the mode of the previous system contributing to the new systems mode, indicated by the first subscript, m. The particular solution enters as the zero-th mode, the frequency of the particular solution in this analysis is set as zero and the amplitude of the particular solution is set as one. This is a very compact equation and the principle reason why the complex conjugate pairs were considered separate modes.

The ratio of the modal transfer coefficient to the orthogonality coefficient of the new system is a constant and is the characteristic term which defines the modal transfer. In this analysis the orthogonality coefficients of all modes in all

systems are normalized to one, therefore, the modal transfer coefficient is the characteristic transfer term. The exponential term in equation (3.50) takes account of the differences in time scales and decay rates and also applies a phase relationship to the transfer. The transfer coefficient is, in general, complex. The amplitude of the new system will depend on the amplitudes of the previous system and the time the transfer between systems takes place. For example, if the two systems being transferred between are the same, the transfer equation reduces to the orthogonality equation. In the case of identical modes the modal transfer coefficient is one, indicating identical amplitudes in those modes. Orthogonal modes produce a modal transfer coefficient of zero, indicating no coupling of orthogonal modes. When the systems are not orthogonal the transfer coefficients are generally complex and non-zero.

3.7 System Energy

The energy of the engineering beam structures used in this analysis is defined as the sum of the potential energy (strain energy) and the kinetic energy.

$$\underline{E} = \int_{x_1}^{x_2} \frac{1}{2} m \dot{W}^2 + \frac{1}{2} E I W''^2 \, dx \tag{3.51}$$

Inputting the beam section limits, boundary conditions, and defining the modal mass, μ, as

$$\mu_{mn} = \left[\sum_{B}^{\text{all beams}} \int_{x_{BL}}^{x_{BR}} \{ m_B \phi_{Bm} \phi_{Bn} \} \, dx + \sum_{M}^{\text{all masses}} \{ M_M \phi_{Mm}(x_M) \phi_{Mn}(x_M) \} \right] \tag{3.52}$$

The energy equation reduces to

$$\underline{E} = \sum_m \sum_n Y_m Y_n \, \Omega_n \left[\Omega_m \mu_{mn} - \frac{1}{2} \delta_{mn} \nu_{mn} \right] \tag{3.53}$$

Energy terms involving different modes are present. In general the energy equation does not decouple into modal form. Transforming equation (3.53) into complex conjugate notation and separating the like and unlike terms the energy equation takes the form

$$\begin{aligned} \underline{E} = \sum_j \Big[& Y_j^2 \, \Omega_j \left\{ \Omega_j \mu_{jj} - \frac{1}{2} \nu_{jj} \right\} \\ & + Y_j^* Y_j \, \Omega_j^* \Omega_j \mu_{j^*j} + \text{c. c.} \Big] \\ + \sum_{j \neq k} \sum \Big[& Y_j Y_k \, \Omega_j \, \Omega_k \mu_{jk} \\ & + Y_j^* Y_k \, \Omega_j^* \Omega_k \mu_{j^*k} + \text{c. c.} \Big] \end{aligned} \tag{3.54}$$

The first summation in equation (3.54) consists of complex energy terms which involve a single mode only. These terms are referred to as the modal energy terms. There are two types of modal energy terms present, oscillatory terms and non-oscillatory terms. The square of the time function, Y^2, causes the oscillatory terms to oscillate at twice the frequency, and decay at twice the rate, of the relevant modal amplitudes. The non-oscillatory terms are always real and decay at twice the rate at which the relevant modal amplitude decays.

The second summation in equation (3.54) consists of terms which are dependent on two separate modes and represent modal coupling of the energy equation. These terms are referred to as the coupled complex energy terms. Generally the coupled energy terms are non-zero and are oscillatory with frequencies and decay rates which are combinations of frequencies and decay rates of pairs of modes. There are special cases where energy does decouple into modal form, and the coupled complex energy terms become zero. The two

special cases examined in this analysis are the cases of undamped beams and of proportionally damped beams. The proportionally damped beam is examined first because equations for the undamped beam can all be derived from the proportionally damped case.

3.8 Proportional Damping

The special case of proportional damping is used extensively in this analysis. The proportionality constraint is defined here as

$$\frac{C_B}{E_B} = \frac{C_S}{K_S} = \text{Constant} \tag{3.55}$$

where C / E represents the proportionality factor of any beam and C / K the proportionality factor of any spring. This is a very useful and interesting case because the mode shapes of a single assemblage of beam equations reduce exactly to those obtained when damping is not included. The mode shapes are real because the imaginary components become zero and therefore, the mode shapes do not change as a function of phase. These real modes, obtained for undamped or proportionally damped systems, can be used to separate the individual modes of the single assemblage of beam equations into separate but similar assemblages of beam equations, each equation representing a mode of the system. The damping rate for each modal equation can be set, without changing either mode shape or orthogonality. This allows the modal damping ratios of the system to be set to fit any requirements of the analysis. For example, the damping ratio of a beam in vibration can be assumed to be ruled by the Zener damping curve where damping is a function of frequency. The modal damping ratios of a proportional system can be set to match that of the Zener curve thus providing a model which simulates the measured modal damping of higher modes.

3.9 Modal Energy of Proportional Systems

The first and second orthogonality equations, equations (3.38) and (3.39), can be combined with the conditions of proportionality to show modal

energy decoupling of a proportionally damped system. This is accomplished by multiplying the second orthogonality equation, equation (3.39), by the proportionality coefficient, (K), and subtracting it from the first orthogonality equation, equation (3.38). After some manipulation the energy equation can be reduced to a decoupled sum of modal energy terms.

$$\underline{E} = \sum_{m} \Big[Y_m^2 \, \Omega_m \, \{\Omega_m \mu_{mm} - \frac{1}{2} \nu_{mm}\} + Y_m^* Y_m \, \Omega_m^* \Omega_m \mu_{m^* m} + \text{c. c.} \Big] \tag{3.56}$$

Equation (3.56) shows that the energy of a proportionally damped system is decoupled. The energy of a known mode can therefore be calculated without prior knowledge of other modes of the structure. The energy of an undamped beam reduces equation (3.56) to a single term for each mode where the modal energy term is always real, constant and uncoupled.

$$\underline{E} = \sum_{j} 2 \, \underline{\omega}_j^2 \, \mu_{j^* j} \tag{3.57}$$

Where $\underline{\omega}$ is the imaginary portion of the complex frequency, Ω.

3.10 Non-Proportional Models

A proportionally damped system does have its limitations. All of the joints, beam sections, wires, etc. must have the same ratio of stiffness to damping. In most structures, damping is small and any variations can be ignored. However, if a component of the structure has a significant variation from the proportionality condition, a single equation, non-proportional solution may have to be used to model changes in the dynamics of the system due to the non-proportional damping.

The non-proportional solution has the damping defined on a component by component basis. The modal damping is therefore defined for all modes by the strain rate damping assumption included in the model, a single damped

engineering beam equation. Strain rate damping typically increases as mode number increases. This is due to the higher strain rate from the mode shapes and the higher frequency of the modes. As a result, non-proportional systems typically have very highly damped upper modes.

The non-proportional solution also, in general, results in complex modes, modes which change shape as a function of phase. These modes are different from modes of the undamped system in shape and character. Modes of undamped or proportional systems have a constant shape, only varying amplitude as a function of time. Non-proportional systems can have complex modes which have a phase component, a term which changes the mode shape as a function of time. Mathematically there is no difference in how the mode is handled, it is just more difficult to envision. For example, if the displacement of a point on a proportional system vibrating in a single mode is monitored, the resulting signal would be a damped sine wave. If a second point on the same system were monitored the displacement would, in general, have a different amplitude but the frequency, phase, and damping rates would be the same. When the same exercise is performed on a non-proportional system the signals will, in general, not have the same phase.

Insight into the complex behavior of the phase dependent modes of a non-proportional system can be obtained by examining the energy equation of a non-proportional system. In general the energy equation is coupled between all of the modes. This indicates that the damping term in the non-proportionally damped engineering beam is coupling the modes of the undamped beam. The damping term in the damped beam equations is therefore a form of coupled damping which causes the modes of the system to take on a phase dependent behavior.

3.11 Summery

Chapter 3 has derived and established all of the solutions and equations necessary for the analysis of damped engineering beam equations. This paper uses the technique of separate proportionally damped beam equations to model the beam structure's modes for three reasons. First, the damping mechanism being modeled is that of internal or material damping which is assumed to follow a frequency distribution different than that of strain rate damping. Second, it is assumed that the material damping is small, uncoupled

and induces exponential decay. Third, it is required of the analysis that the beam's energy be uncoupled and calculable.

Chapter 4

Computational Techniques

4.0 Overview

The objective of chapter 4 is to develop the computational solution techniques, computer programs using the equations developed in chapter 3, which are used in the analysis of the nonlinear models described of this paper. The programs developed for this analysis consist of programs for the following tasks: computation of solutions of the sub-systems, calculation and storage of the transfer coefficients, time stepping and iteration routine for determination of sub-system state factors, calculation of modal energy, estimation of maximum energy dissipation due to modal coupling, and simulation of strain gauges affixed to the beam. The procedure used to solve for the motion of a piecewise linear jointed beam is shown in figure 4.1.

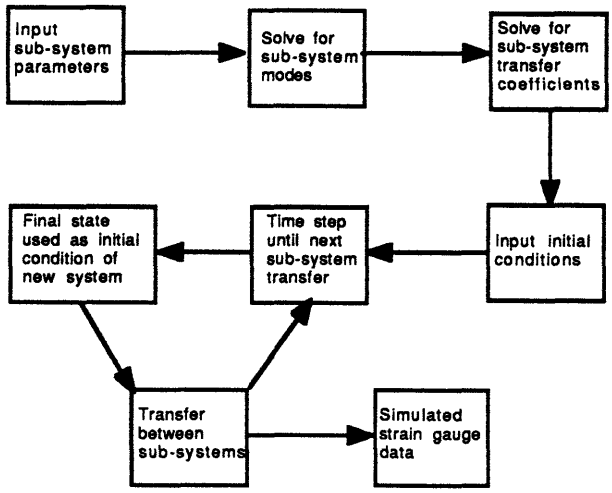

Computational Procedure
Figure 4.1

The following chapter sections describe in detail each of the procedural steps and the computational processes used.

4.1 Establishment of Linear Systems and States of Validity

The non-linear structures used in this analysis are engineering beams linked by piece-wise linear rotational springs. Linear sub-systems are obtained by setting the joints to the configuration of a single linear sub-joint and setting the boundaries of the of the joint states, rotation and rotation rate, to the condition for which the sub-joint is valid. For example, a single joint consisting of an asymmetrically stiff rotational spring is considered as two linear sub-joints, a sub-joint where the rotational spring has one stiffness and a sub-joint where rotational spring has another stiffness. The first sub-system is the structure with a linear joint that has the first stiffness and the second sub-system is the same structure with a joint that has the second stiffness (see chapter 2, section 2.2).

The limits set for joint states can be specific joint rotations; for example, to one side of a given joint rotation (angle > 0) the first sub-system describes the structure's dynamics, and to the other side of the joint rotation (angle <0) the second sub-system describes the structure's dynamics. The rotational moments of the on-off rotational spring in the joint must be zero at the transfer between the systems. If the angle at which system transfers is not at zero then the sub-systems are designed with a balanced static moment applied at the joint so that at the transfer the on-off spring with the applied moment will be zero. When damping is included in the model the point of transfer will not always occur at a given rotation angle due to rotation rate moments in the joint. The rotational moment of the on-off spring must still be zero at the transfer point (see figure 2.4). Joint transfer moments are also set and stored with the set joint rotation angles and the beam parameters. The input of the sub-system parameters and their conditions of validity take place in a program written for this analysis and are stored in a separate data file for each sub-system.

4.2 Calculation of Homogeneous Solutions

The beam parameters of a structural sub-system are used to generate the transcendental matrix equation. A different matrix equation is generated for each mode of the sub-system by inputting the desired damping proportionality factor. The determinant of this matrix is usually a transcendental equation which allows for an infinite number of zeros or eigenvalues. The inputted damping factor is valid for only one of the eigenvalues.

The eigenvalue of the matrix is solved for by iteration using a steepest rate of descent routine. This routine starts with a guess of the appropriate complex eigenfrequency (Ω), restricted to have a positive imaginary component. A modal solution is assumed so the eigenfrequencies of all the beam sections are assumed to be equal. The complex shape factor (a) for each beam section is calculated via equation (3.7) using the assumed complex eigenfrequency. The complex shape factors are in general not equal to one another. The eigenfrequency and all the complex shape factors are inputted into the complex matrix equation defined by the boundary conditions. The determinate is then calculated using a Gaussian elimination routine.

Double precision complex variables are used in the fortran code which calculates the determinant. The steepest rate of descent routine changes the guessed complex eigen frequency slightly in the real direction and a new determinant is calculated. The original guessed complex eigen frequency is changed slightly in the imaginary direction and a new determinant value is calculated. Using the three points calculated the slope of the complex determinant surface is then defined and the vector corresponding to the steepest descent is calculated. The magnitude of the vector is initially set at a relatively large value. Using this, a new guess at the complex eigen frequency is calculated. If the determinant of the new guess is larger than the previous one then the magnitude of the vector of steepest descent is lowered and a new guess obtained. This process proceeds until a minimum magnitude of the descent vector is reached. The minimum value of the descent vector used in this analysis solves for the complex eigen frequency to approximately the 12th significant digit.

The general surface of the determinant, a surface over the real and imaginary plane of complex frequencies is in the shape of a exponential to roughly the power of the dimension of the matrix times the magnitude of the complex frequency. The eigenvalues appear as steep depressions or holes in this surface, lowering it to zero. Because of the shape of this surface the minimization routine could skip over or go around a zero. If all zeros were missed the minimization routine would end up at the origin, a zero representing the rigid body modes. The initial guess of the complex frequency needs to be fairly close to the desired eigen frequency in order for the minimization routine to fall into it. This necessitated a fairly rigorous search of the complex space to insure that all of the eigen frequencies of interest are found.

The steepness of the determinant surface walls gave very high values of the determinant when the complex frequency was of any size. The limit found for the standard fortran double precision code and a three beam section solution (matrix dimension of 12X12) was approximately the 10th mode. This proved to be a sufficient number of modes for the analysis. When the minimization routine found an eigen frequency and started down its determinant surface the walls of the surface became very steep: the higher the eigen frequency was the steeper the walls. This resulted in very high values of the determinant even though the eigen frequency was accurate to the 12th significant digit. The high determinant values did not affect later calculations.

The beam section shape coefficients are solved for by placing the complex eigen frequency back into the matrix equation and solving for the shape coefficients. The matrix is singular so one of the coefficients is set to one and its row and a column are eliminated. The residual terms are transported to the right hand side of the equation. Gaussian elimination is utilized to solve for the coefficients. This technique is not infallible in that the choice of which rows and columns are chosen affects the solution of the coefficients.

To insure that the best possible solution is found all possible combinations of rows and columns are tested. The resulting coefficients are placed back into the matrix equation before the row column reduction. The right hand vector is then calculated and its magnitude determined. This vector should be zero but round-off errors and matrix singularity problems will yield a nonzero value. The solution which has the minimum error is chosen. The error of the chosen solution was typically on the order of the round-off error of the machine.

The complex shape coefficients are then normalized by the orthogonality coefficient. The orthogonality coefficient (ν) is defined by the orthogonality equations, equations (3.38) and (3.39). This solution, including all coefficients, frequencies, and factors, is designated the odd complex conjugate pair mode. The complex conjugate mode is calculated by taking the complex conjugate of the odd mode's coefficients, frequencies, and factors and designating it the even mode. All modal solutions are stored in the same file as the sub-system's beam parameters.

4.3 Calculation of Particular Solution

The particular solution is calculated in a manner similar to the calculation of the oscillatory modes. The beam parameters of the sub-system are input into a program written for this analysis along with the balanced applied joint moments. Since the moments are balanced so that no rigid body motions will occur a matrix equation, which assumes pinned ends of the beam assembly, is generated. These moments are not functions of time and the matrix has a real determinant. The particular solution to the sub-system is solved for directly. Due to the pinned ends the beam assembly may translate and rotate away from its inertially correct position. The solution is translated and rotated back to a position corresponding to a beam assembly with no constraints. The particular solution is stored in the same file as the beam parameters and oscillatory modes and is labeled the zero-th mode.

4.4 Calculation of Sub-System Transfer Matrix

The solutions of all sub-systems are input into a transfer program written for this analysis. The transfer coefficients between the sub-systems are calculated for every mode transfer in every sub-system to every other mode in every other sub-system and stored in transfer files. This is done to keep from recalculating the same coefficients over and over as the structure transfers back and forth between the same sub-systems. The accuracy of the modal transfer coefficients, using double precision complex variables, was on the order of the 5th significant digit. This is considered sufficient for this analysis since this represents an error in the structures critical damping ratio of approximately 0.001% (zeta). The accuracy of the transfer coefficient is limited by the accuracy of the mode shapes and in turn the accuracy of the eigen-frequencies which are machine limited. More complex structures using this analysis will need higher precision than complex*16.

4.5 Time Stepping Routine and System Transfer Logic

With the solutions of the individual sub-systems and the transfer coefficients between them stored in files a time stepping routine designed for this analysis was run. The time stepping routine, given an initial sub-system

with initial conditions and a start time, marches through time looking for the next transfer between sub-systems. The size of the initial time step is determined from the frequency of the highest mode of the sub-system modeled. Twelve time steps are necessary to pass through a complete cycle of the highest mode. This insures that no transfer will be missed.

The time stepping routine steps through time calculating the state of the stepwise linear joints as it proceeds. The state of the joints are determined by calculating the difference in slope across a joint and the rotational spring moment provided by the joint. In the case of an asymmetrically stiff joint, figure 2.6, the joint has two rotational springs and two possible joint configurations. The transfer point between the sub-systems is determined by the moments and rotations of the on-off spring used in the joint, figure 2.4. The strong jointed sub-system involves the joint configuration where the joint has the spring engaged, figure 2.7. The weak jointed sub-system involves the joint configuration where the joint does not have the on-off spring engaged, figure 2.8. The moment-rotation plot of the asymmetrically stiff joint is shown in figure 2.5.

If damping in the joint is zero, the moment provided by the on-off spring is zero when the joint rotation passes through zero. The moment state is redundant in the determination of the sub-system transfer point. However, when the damping is not zero, the moment provided by the joint is rate dependent and will go to zero before the joint rotation passes through zero. The transfer occurs at this point and the strain energy left in the on-off spring is assumed to be dissipated within the spring. This discontinuity causes some nonlinear hysteretic damping in the joint but it is small compared to the linear damping of the joint.

When the transfer from one sub-system to another is indicated the time stepping routine iterates around the point where the joint condition changes to find the exact time for the transfer. A minimum time-step of 1/10000 of the initial time-step is used to signal that the transfer time has been found to a sufficient accuracy.

The new sub-system is determined and the transfer from the current sub-system to the new sub-system is performed. The transfer coefficients are used to calculate the new sub-system's complex modal amplitudes from the old sub-system's complex modal amplitudes. The new sub-system should be in the new joint condition, but, since there are only a limited number of modes used and the accuracy of the modes is limited, some error is expected. To alleviate

this discrepancy the first time step in the new sub-system is taken before the joint condition is tested. If the error is not large and the new sub-system has the proper joint condition, the time stepping routine continues on to the next transfer.

If the new sub-system does not have the correct joint condition then the routine shrinks the time step and tries again. If the minimum time step is reached and the sub-system has still not found the correct joint state then a search is started with a pre-set time step and a limit of one half of one cycle of the lowest mode. If the correct joint condition has still not been found then an error message is sent and the routine halted. The experience with the models analyzed was that the sub-system almost always found the correct joint condition on the first transfer. The program ended when a time limit or a transfer limit was reached. The transfer times, sub-system number, and the modal amplitudes were stored in a file for later analysis.

4.6 Calculation of Modal Energy

Energy, in this analysis, is a modal quantity. The energy equations of the linear sub-systems are uncoupled. The energy of each mode of each sub-system is calculated in a program written for this analysis, by using the amplitude information which resulted from the time-stepping routine. The modal coupling present in the nonlinear structures allows energy to transfer between modes of the system. At a sub-system transfer the difference in the total energy of the first sub-system and the second sub-system indicates the energy lost to modes not calculated in the model. Energy transferred to modes not calculated in the model is implicitly assumed to be dissipated before the next sub-system transfer.

Since this analysis solves for the modal frequencies and shapes independently of the other modes of the sub-system, the transfer coefficient, used to calculate the new modal amplitudes, takes into account all infinite modes, to the accuracy of the calculation. This technique essentially assumes that the modes not calculated and not used in the model have very high damping ratios. It is this property of this analysis which makes it unique from a finite degree of freedom model which does not allow energy transfer to any mode not modeled. Essentially a finite degree of freedom system traps the energy in the system. Any unmodeled modes can not contribute to the energy

dissipation of the system. It may be possible to approximate the analysis with a finite degree of freedom model if enough degrees of freedom are included.

It was found that the energy lost to uncalculated modes was negligible when seven modes were calculated and included in the models. When less modes were used the energy loss to uncalculated modes became significant.

4.7 Single Mode Technique

With the treatment of uncalculated modes used in this analysis, it is possible to estimate the maximum energy dissipation due to modal coupling by modeling just one mode. Any excitation of other modes is assumed to be dissipated before the next sub-system transfer. The transfer equation reduces to the contributions from the particular solution and the two complex conjugate modes of the primary mode in oscillation.

$$\sum_{n=0}^{2} \left\{ B_n e^{(\omega_n - \Omega_m) t_T} \frac{\tau_{mn}}{\nu_{mm}} \right\} = A_m \qquad (4.1)$$

This iteration scheme is used to determine the maximum dissipation due to modal coupling. The single mode technique ignores any dynamics of the coupled modes and assumes that the sub-system transfer is determined by the single mode only.

4.8 Calculation of Simulated Strain Gauge Data

A strain gauge simulation program, written for this analysis, was used to analyze the results. This program used the time stepping output and the solutions of the systems equations to simulate a strain gauge mounted at a given position on the beam. A digital output similar to the output provided by experimental strain gauges was created and stored in standard data format. The strain gauge set-up measures beam curvature at the point where the strain gauges are affixed, the center of the beam sections. Beam curvature is proportional to the modal amplitudes of the beam but different proportionality constants exist for each mode. From simulated strain gauge data direct

comparisons between theoretical models and experimental data were made. The output of this program could be manipulated to show the contribution of each mode of the system individually. The amplitudes of individual modes were compared to illustrate the coupling between the modes and to show relative changes in modal damping rates. The effective damping rates were calculated using a log decrement estimation on the modal amplitude plots.

4.9 Summary

This modeling technique, although limited to very simple structures, allows very accurate calculation of modes and mode shapes of a continuous nonlinear system. The inclusion of three or four modes performs well, the addition of higher modes not affecting the output very much. The first seven modes of the system were calculated and used in the analysis. This technique also allows the estimation of the maximum dissipation due to the coupling of modes by calculating and using a single mode of the system.

Chapter 5

Analysis of Damping Due to Modal Coupling

5.0 Overview

The objective of chapter 5 is to examine the effect of non-dissipative, piecewise linear joints on the effective damping of structures. The effective damping of a structure is defined in this paper as the apparent decay rate of a structure when set in motion in a single mode. The piecewise linear nature of the joints allows the structure to be divided into sub-systems where a sub-system models the structure while the structure is within predetermined state limits.

A transfer of energy from mode to mode occurs when the structure transfers from one sub-system to another. A modal energy tree can be created establishing how the energy moves between the modes within the structure. The energy transfer between modes combined with the internal decay rates of the individual modes is used to model the effective decay rate of a structure. A structure is set in motion in a single mode and its decay rate calculated. The decay of the mode represents a loss of energy which is due to internal damping and the transfer of energy to other modes. The energy transferred to other modes could be dissipated in those modes, transferred to more modes or transferred back to the original mode.

Three example structures are examined, a beam with a asymmetrically stiff joint, a beam which is wire braced at its one-third points, and a beam with a dead-band joint. The effective damping of structures with different internal damping rates and joint parameters are calculated. The results of the analysis are used to draw conclusions about how damping due to modal coupling occurs, how it can be estimated, and when it is most likely to be important in a structure.

The section 5.1 describes the specific objectives of chapter 5. Section 5.2 discuses the nature of the nonlinear jointed beams and energy transfer between modes. Section 5.3 discuses the effective decay rate of a structure and how it is calculated. Section 5.4 describes the procedure for analyzing the structures. Section 5.5 analyses the asymmetrically stiff jointed beam. Section 5.6 analysis the wire braced beam. Section 5.7 analysis the dead-band jointed

beam. Section 5.8 summarizes the analysis of the three beams and the nature of damping due to modal coupling.

5.1 Objective of Analysis

The focus of this analysis is the calculation of damping due to modal coupling. The three structures analyzed have piecewise linear, non-dissipative joints. The joints cause modal coupling within the structure without generating damping of there own. The modal coupling causes the transfer of energy between the modes of the structure. The transfer of energy can contribute to the effective damping of the structure by transferring energy to modes were the internal damping is more advantageous. The models and analytical techniques developed in this paper are designed to track energy as it transfers between modes and dissipates within the modes. The increase in damping due to modal coupling can be calculated directly from the simulation.

By varying the internal damping parameters and the joint parameters of a structure the relative magnitude of the contribution of modal coupling to the structure's effective damping and its sensitivity to the structures parameters can be determined. The relationship between the structure's parameters and the damping due to modal coupling provides insight into how energy is dissipated in real structures, when this phenomenon is important to the modeling of a structure, and how damping can be enhanced if modal coupling is present. The objective of chapter 5 is, therefore, to examine the contribution of non-dissipative, piecewise linear joints to the effective damping and to determine its sensitivity to the joint and beam parameters.

5.2 Energy Transfer

The nature of the nonlinear joints used in this analysis are that modal coupling occurs only when the structure transfers from one linear sub-system to another. In-between transfers the modes are orthogonal and the modal oscillations decay at their own internal damping rates. At the transfer a discontinuity occurs, the amplitudes of the modes change instantaneously.

The linear sub-systems may have very different modes and mode shapes but in this analysis the first mode of a sub-system is associated with the first mode of every other sub-system of a structure, the second mode with the

second mode of every other sub-system, etc. The first mode of a structure is therefore the first mode of all the sub-systems of the structure. This causes a semi-sinusoidal oscillation of the individual modal contributions to the motion of the structure. Discontinuities occur at the transfers between the sub-systems especially in the higher modes. The discontinuities represent the excitation or the de-excitation of modes due to the sudden discontinuity in the joint.

The discontinuity can also be described as the transfer of energy between modes. Figure 5.1 illustrates how energy can be distributed throughout the modes of a structure. The structure is set in motion with energy in the first mode only. When the structure transfers from sub-system 1 to sub-system 2 most of the energy transfers to the first mode of the new sub-system but some energy is allowed to transfer to other modes of the sub-system. At the next sub-system transfer the same transfer pattern occurs for all the modes of the sub-system. Energy transferred to uncalculated modes of the sub-systems are assumed to be completely dissipated before the next sub-system transfer.

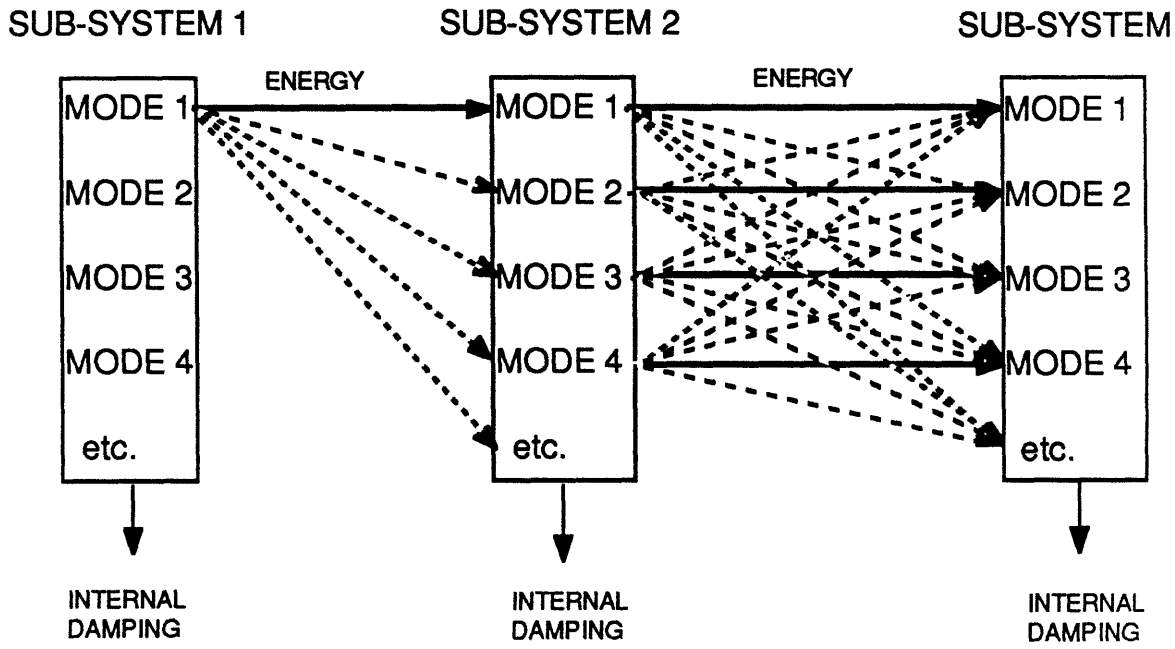

Energy Transfer Between Structural Sub-Systems
Figure 5.1

Between sub-system transfers the amplitudes of vibration in sub-system modes decay according to their own internal modal damping rate. If the damping rates

of the coupled modes, modes 2-4 in figure 5.1, are higher than the primary mode in vibration, mode 1 in figure 5.1, then the dissipation of energy will increase due to energy transfer between the modes. Modal coupling will cause an apparent increase in damping of the first mode.

Energy can also transfer back and forth between modes causing an oscillation or beating of the modal amplitudes. Modal beating is observed in all three beam models when the relative internal damping is not to high. The energy transfer between modes can be shown by calculating the energy of the individual modes as the simulation proceeds. Figure 5.2 shows the modal energy of a asymmetrically stiff jointed beam during a simulation run. Energy is primarily transferred between the first and third modes with the fifth mode playing a small role. The structure is symmetric such that only the odd modes will be coupled.

Beating of the modes is not persistent in the example shown in figure 5.2 because the relative modal damping rates of the upper modes are quite high even though the damping ratios of the modes are similar. The dotted line shows the envelope of the first mode's oscillation had no modal coupling been present. It is apparent that the decay of the first mode is enhanced due to the modal coupling of the system. Figure 5.3 shows an example where the upper modal damping rates are zero. The beating of the first and third modes are illustrated by showing the first and third modal components separately. A portion of the energy of the first mode is transferred to the third mode then transferred back to the first mode, over a period of approximately six cycles.

5.3 Effective Damping

There are two ways of describing the damping of a structure used in this analysis. The more common method is the damping ratio, zeta, which is the rate of decay of the structure normalized by the frequency of the structure. The second is the damping rate, the real portion of the complex frequency which relates directly to the time rate of decay of the structure's oscillations. The difficulty in using the damping ratio is that there are many frequencies present in this analysis. The different linear sub-systems describing the structure, in general, have different frequencies, the different modes have different frequencies, and the joint nonlinearities may cause the structural frequencies to change. In this analysis it is undesirable to have the damping change due to

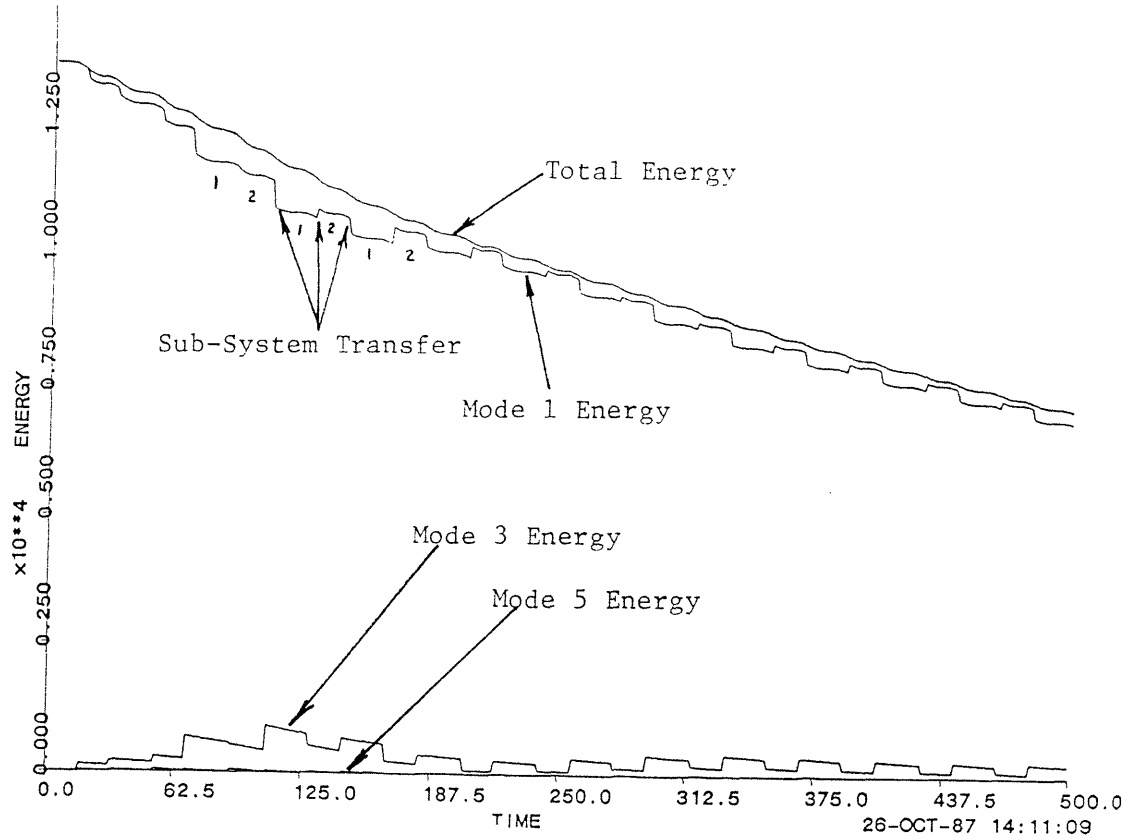

Structural Energy
Figure 5.2

Table 5.1
Simulation Beam Parameters
$K_N = .033$, $K_S = 26$

Mode	Sub-System 1		Sub-System 2	
Number	Internal Damping Rate	Frequency (rd/sec)	Internal Damping Rate	Frequency (rd/sec)
1	0.5	139	0.5	213
2	2.2	659	2.2	659
3	4.4	938	6.9	1174
4	24	2195	24	2195
5	32	2542	44	2994

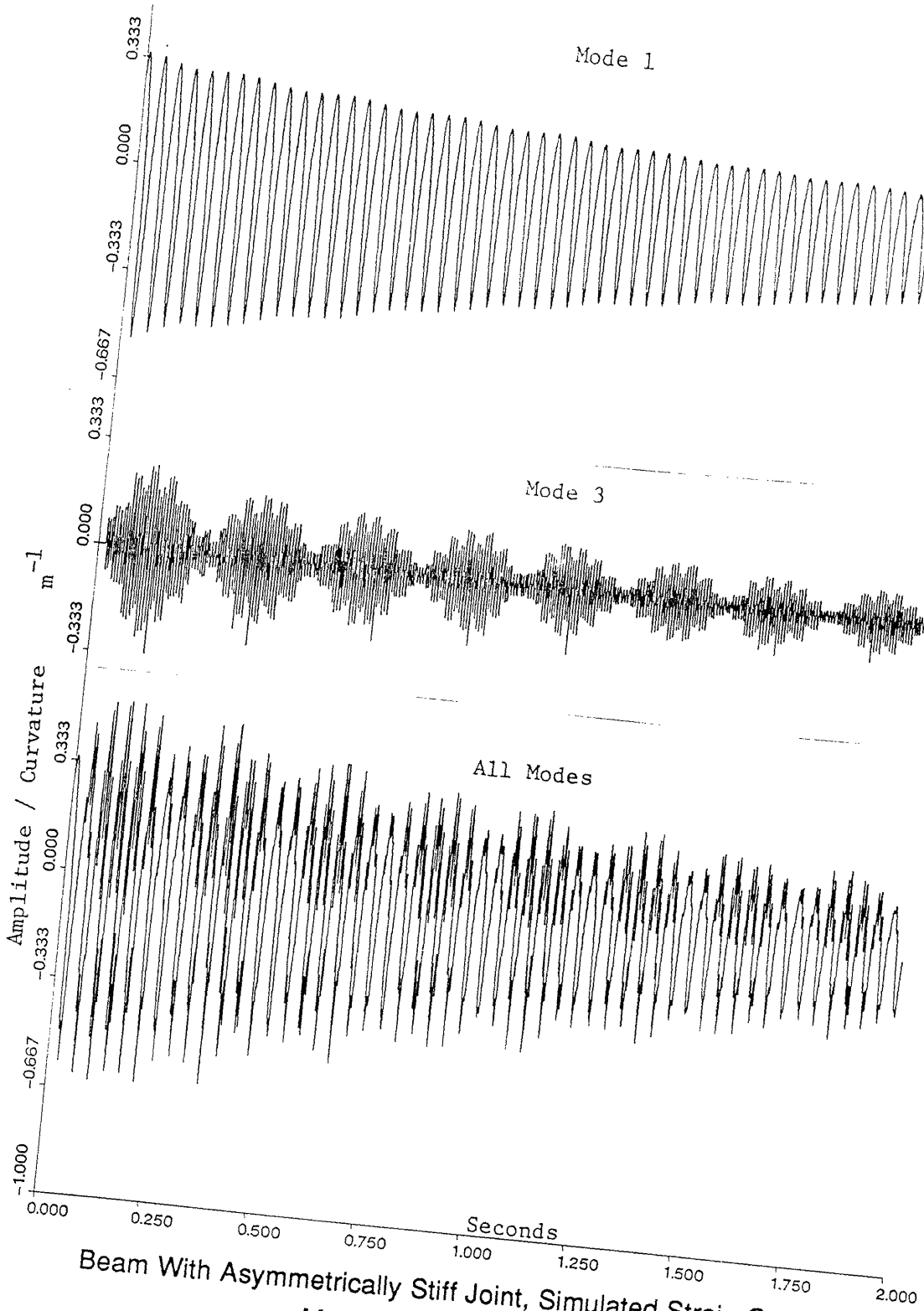

Beam With Asymmetrically Stiff Joint, Simulated Strain Gauge Data
Modal Amplitudes / Curvature
$DR_{1int} = 0.5$, $DR_{2\text{-}7} = 0.0$, $\Delta DR_M = -0.5$, $K_N = .033$, $K_S = 26$
Figure 5.3

frequency changes in the structure. To this end the damping rate is used throughout the analysis. This way the damping of all modes and sub-systems can be calculated directly on a time rate of decay basis.

The damping rate is labelled DR. In order to relate the results of this analysis to more conventional damping data, the damping rate is also normalized by the nonlinear systems fundamental frequency at the time of calculation. Since the structure is nonlinear, as the amplitude of the structure's modes change, so may the frequency. In most of the cases analyzed the fundamental frequency does not change greatly with amplitude and could be considered a constant, the dead-band joint being the exception. The damping ratio in this analysis is defined by

$$Z\,\% = \frac{DR}{\Omega_{NL}}\,100 \tag{5.1}$$

Where Z % is the damping ratio shown in percent. The frequency of the fundamental mode of the nonlinear system, Ω_{NL}, is in radians. The structures damping rate and frequency is a weighted average of the component sub-systems damping and frequencies and are calculated directly from the simulation.

The damping rate of the individual sub-systems can be derived directly from their solutions and in this analysis is set as a parameter of the structure. The effective damping rate, the damping rate of a mode of the structure due to internal damping as well as energy transfer must be calculated from the structural simulations.

The structures modelled are nonlinear in nature and the internal damping is assumed to be small, less than 1.0%. The modeling technique used in this analysis divides the motion of the structure into a series of linear sub-systems. The linear sub-systems can be very different from one another and the resulting motion of the structure may be quite different from that of a linear structure. In order to visualize the motion of the structure, simulated output of strain gauges placed on the structure are generated. Figure 5.3 is an example of the simulation output. Care was used to insure that all modes are observable by the simulation. The simulated strain gauge output also allowed a direct comparison with experimental data described in chapter 6.

The calculation of the damping of the different modes proved to be difficult using curve fitting routines. The curve fitting routines fit the simulated strain gauge output to a decaying sine wave. The motion of the structures were generally not close enough to a decaying sine wave to allow this type of analysis. Filtering of the simulated strain gauge signal was considered since this is the method used in identifying the modes of the experiments described in chapter 6, but was not used because this caused modal information to be lost. For example, the discontinuities in the coupled modes would be smoothed over giving the impression that they are continuously excited when they are actually excited only when a sub-system transfer occurs.

The method of log decrement was used since it was not sensitive to the detailed motion of the structure, but instead depends only on the peak amplitudes at the beginning and end of the data window. The log decrement method uses the peak to peak amplitude of the simulated strain gauge output at a point near the beginning of the simulation and another point near the end of the simulation. These amplitudes and the time between them is input into equation (5.2).

$$DR = \frac{\ln (\text{Amp}(t_1) - \text{Amp}(t_2))}{(t_2 - t_1)} \qquad (5.2)$$

Equation (5.2) estimates the effective damping rate but is subject to some error. The decay of nonlinear structures, such as those analyzed in this paper, do not necessarily follow a simple exponential decay pattern which is the assumption in the log decrement estimation. This tends to generate some scatter in the damping rate calculations. The extent of the scatter depends on the nature of the structure in question. The dotted line in figure 5.3 represents the fitted decay envelope.

5.4 Analytic Procedures

Two analysis procedures were used to analyze the structures. The first procedure models multiple modes of the structure and keeps track of the modal energy as it moves from mode to mode. Each of the component linear sub-

systems of the structures were solved for the first seven modes. The internal damping rate of the first mode was set to be the same for all linear sub-systems and was labelled DR_{1int}. The internal damping rate of the other six modes of each sub-system were set to the same value and labelled $DR_{2\text{-}7}$. In this way, the internal damping rate of the individual modes would not change due to system transfer. The internal damping rate of the structure remains constant no matter which sub-system the structure is in or how long it is in a particular sub-system.

The method used to analyze modal coupling and its associated damping is to set the system in motion in its first mode only. As the system vibrates the higher modes are excited. The system is allowed to vibrate for approximately 50 cycles and a simulated strain gauge output and its modal components are created. The decay rate of the first mode is calculated using the log decrement method. This procedure is useful in measuring the effect of the modal damping rates and the joint parameters on the damping of a single mode due to modal coupling.

The second procedure was used to calculate the maximum damping due to coupling for a given structure. The higher modes of the systems were excluded from the model leaving only the first mode, figure 5.4.

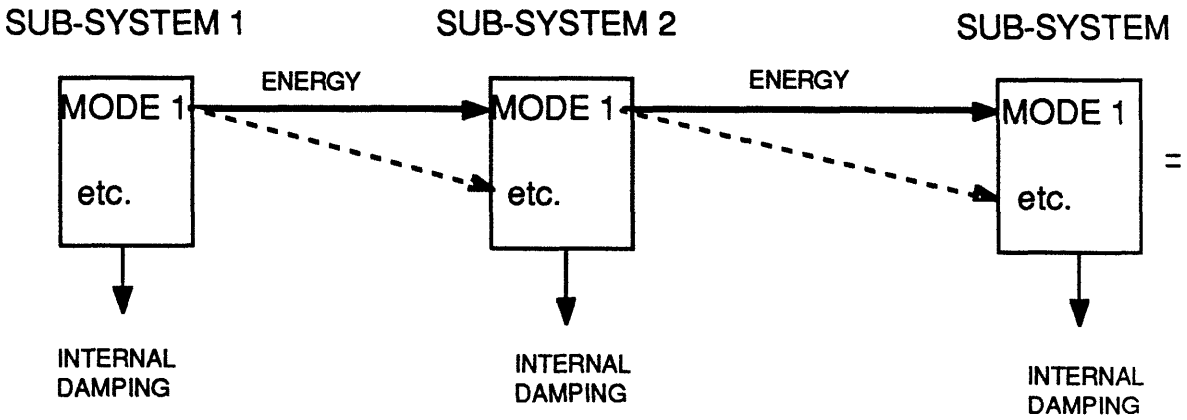

Single Mode Calculation
Figure 5.4

This assumes that oscillations of the upper modes caused by modal coupling at a sub-system transfer are dissipated completely before the next transfer can occur. The system is allowed to vibrate for approximately 50 cycles and a simulated strain gauge output is created. The decay rate of the structure is

calculated using the log decrement method. The calculated damping rate of the first mode represents the maximum effective damping of the structure's first mode including damping due to modal coupling. This procedure is useful in the investigation of the variation of the nonlinear joint parameters, showing the maximum effect the nonlinearities have on the damping of the first modes, without including the upper modes and their damping rates.

The relationship between the damping due to modal coupling and the internal damping rates of the systems centers around the difference in damping rates. This occurs not only in the difference between the internal damping rate of the first mode and the effective damping rate including modal coupling but also in the relationship between the internal damping rates of the first mode compared to the internal damping rate of the upper modes. This is due to two observations:

The maximum increase in damping due to modal coupling is a function of the nonlinearity of the joints only, since it is the nonlinearity which allows the transfer of energy between the modes. The internal modal damping rates may be any value but the maximum added damping due to modal coupling will be a constant. This indicates that the difference between the internal damping rate and the effective damping rate is the appropriate measure of damping due to modal coupling.

Differencing between the internal modal damping rate of the first mode and the coupled modes comes from the observation that the increase in damping due to modal coupling is the same for similar systems with different internal damping rates as long as the difference between the internal modal damping rates is the same. This is due to the direct dependence of the structural energy dissipation on the internal modal damping rates. The difference in the internal modal damping rates is labeled as ΔDR_M.

$$\Delta DR_M = (DR_{2\text{-}7}) - (DR_{1int}) \tag{5.3}$$

The effective damping rate of the first mode is labeled DR_{1Eff}. The difference between the first modes effective damping rate and the first modes internal damping rate is the damping due to modal coupling and is labeled ΔDR_1.

$$\Delta DR_1 = (DR_{1Eff}) - (DR_{1int}) \tag{5.4}$$

The damping rates can be normalized by the frequency of the structures first mode. The frequency of the first mode is determined from the simulation. It is a weighted average of the first mode frequencies of the individual sub-systems. The normalized damping rates take the form

$$\Delta Z_M\% = \frac{\Delta DR_M}{\Omega_{NL}} 100 \tag{5.5}$$

$$\Delta Z_1\% = \frac{\Delta DR_1}{\Omega_{NL}} 100 \tag{5.6}$$

The structures described in chapter 2, were modeled with seven modes. The beam model parameters, transfer coefficients, and data from the analysis are listed in Appendix C. The upper modal damping rate of 1000 signifies a simulation with only the first mode retained in the model.

5.5 Asymmetrically Stiff Jointed beam

The nonlinear joint characteristics are represented by the relative stiffnesses of the on-off springs which make up the joint. The asymmetrically stiff joint, figure 2.6, has two torsional springs and consists of two linear sub-joints. The first linear sub-joint is where the stiffness of the joint is represented by the linear spring stiffness

$$K_L = K_1 \tag{5.7}$$

The second linear sub-joint defines the joint stiffness as the sum of two springs

$$K_L + K_{NL} = K_2 \tag{5.8}$$

The two parameters used to describe the nonlinearity of this joint are the ratio of the stiffnesses, K_1 and K_2, and the relative stiffness of the joint to the beam's rigidity, K_S

$$\frac{K_1}{K_2} = K_N \quad \text{and} \quad \frac{K_2}{(EI/l)} = K_S \tag{5.9}$$

Where E, I and l are the modulous of elasticity, the moment of inertia, and the structures length respectively. The ratio of K_1 and K_2 indicates the degree of nonlinearity in the joint. Assuming that K_1 is always less than K_2, as K_N approaches unity the joint approaches being linear. In the limit as K_1 goes to zero the joint approaches a pinned joint and the system becomes undefined, having another rigid body mode. The joint stiffness ratio, K_S, indicates the relative stiffness of the joint.

In the asymmetrically stiff jointed beam the joint parameters K_N and K_S are held constant at 0.033 and 26 respectively, these values represent experimentally tested structures. Different values of damping rates are applied to the first mode and the upper modes. The first mode damping rates vary from 0.1 to 100 and the upper mode damping rates vary from 0.01 to infinity (labeled 1000). The difference between the damping rates of the first and upper modes are calculated and the difference between the internal damping rates of the first mode and the effective damping rates are calculated (Appendix C). The results are shown in figure 5.5. The extrapolated curve asymptotically approaches the upper limit in damping calculated by the single mode test and shown as a horizontal line. The damping rates are normalized by the frequency of the first mode of the system and shown in figure 5.6.

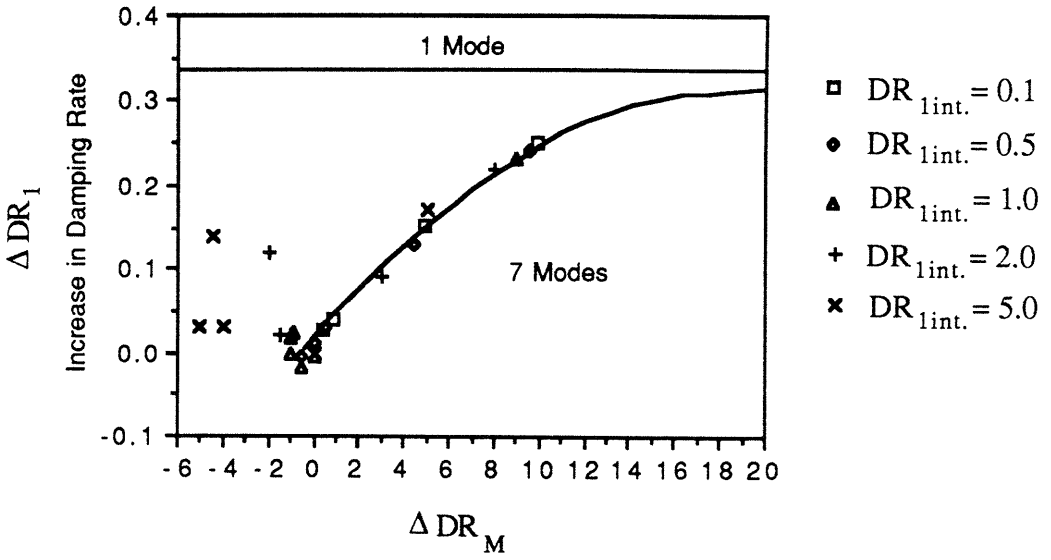

Asymmetrically Stiff Jointed Beam
Increase in First Mode Damping Rate Due to Modal Coupling
vs Difference in Modal Damping Rates
$DR_{1int} = 0.1, 0.5, 1.0, 2.0, 5.0$ $K_N = 0.033$ $K_S = 26$
Figure 5.5

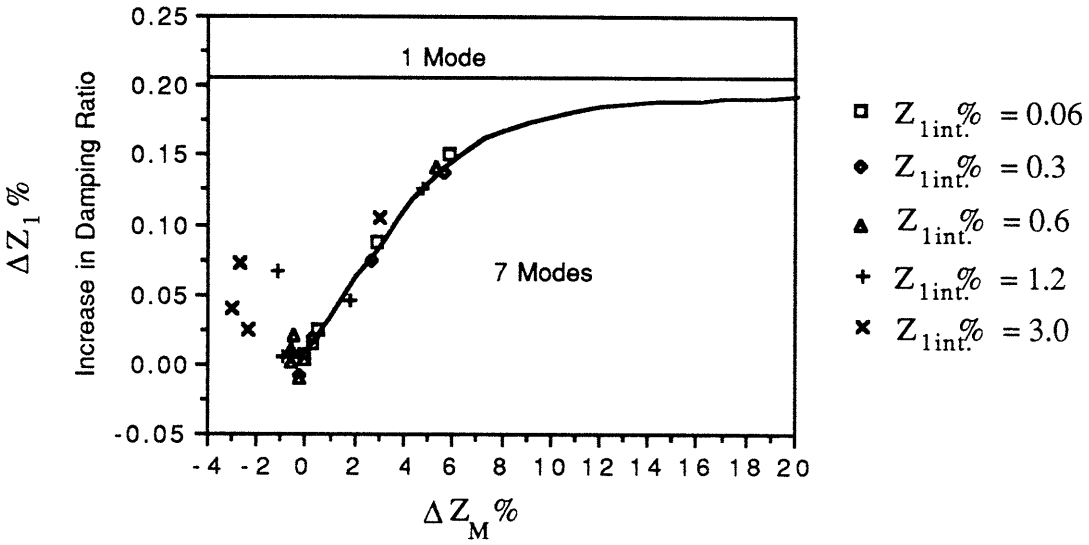

Asymmetrically Stiff Jointed Beam
Increase in First Mode Damping Ratio Due to Modal Coupling
vs Normalized Difference in Modal Damping Rates
$Z_{1int}\% = 0.06, 0.3, 0.6, 1.2, 3.0$ $K_N = .033$ $K_S = 26$
Figure 5.6

Three regions are identified in these figures, ΔDR_M is greater than zero, ΔDR_M is near zero, and ΔDR_M is less than zero. The slight scatter in the data is primarily due to errors incurred by using the log decrement method of calculating the damping rate. The largest contributor to the scatter was the nonlinear behavior of the structure, especially when the upper modal damping rates were lower than the damping rate of the first mode.

When ΔDR_M is greater than zero, there is a dissipation advantage in the upper modes and the effective damping of the first mode increases. As the relative damping of the upper modes increases the effective damping of the first mode increases. An asymptotic limit is reached which coincides with the single mode simulation. Different values of the first mode damping rates, DR_{1int}, are assumed in the model but lie on the same line. The simulated strain gauge data of a simulation with ΔDR_M greater than zero is shown in figure 5.7. The third mode is initially excited by the coupling of the first mode but very quickly settles into a steady oscillation. The envelope representing the decay of the first mode had no modal coupling been present is shown as a dotted line.

When ΔDR_M is zero, the damping rates of all the modes of the system are the same. In this case, when a higher mode is excited by the first mode, there is not any relative increase in the first mode's effective damping rate since there is no dissipation advantage in the upper modes. The simulated strain gauge data of a simulation with ΔDR_M equal to zero is shown in figure 5.8. The third mode is initially exited by the coupling with the first mode and starts a beating phenomenon where energy transfers back and forth between the first and the third modes. Higher modes are involved but the third mode dominates the inter-modal energy transfers. After a few beating cycles the beating starts to transform to a steady state oscillation. The indications are that the point where beating starts to play a significant role in the dynamics of the structure is when the damping rates of the coupled modes are the same.

When ΔDR_M is less than zero, the damping rates of the upper modes of the system are less than the damping rate of the first mode. In this case the beating of the first and third modes becomes persistent, lasting throughout the simulation. Figures 5.3 and 5.9 show the simulated strain gauge data of a system with ΔDR_M less than zero. This indicates that the beating phenomenon may be an instability in the dynamics of the structure. The increase in damping due to modal coupling is unclear due to the scatter in the calculation. It is

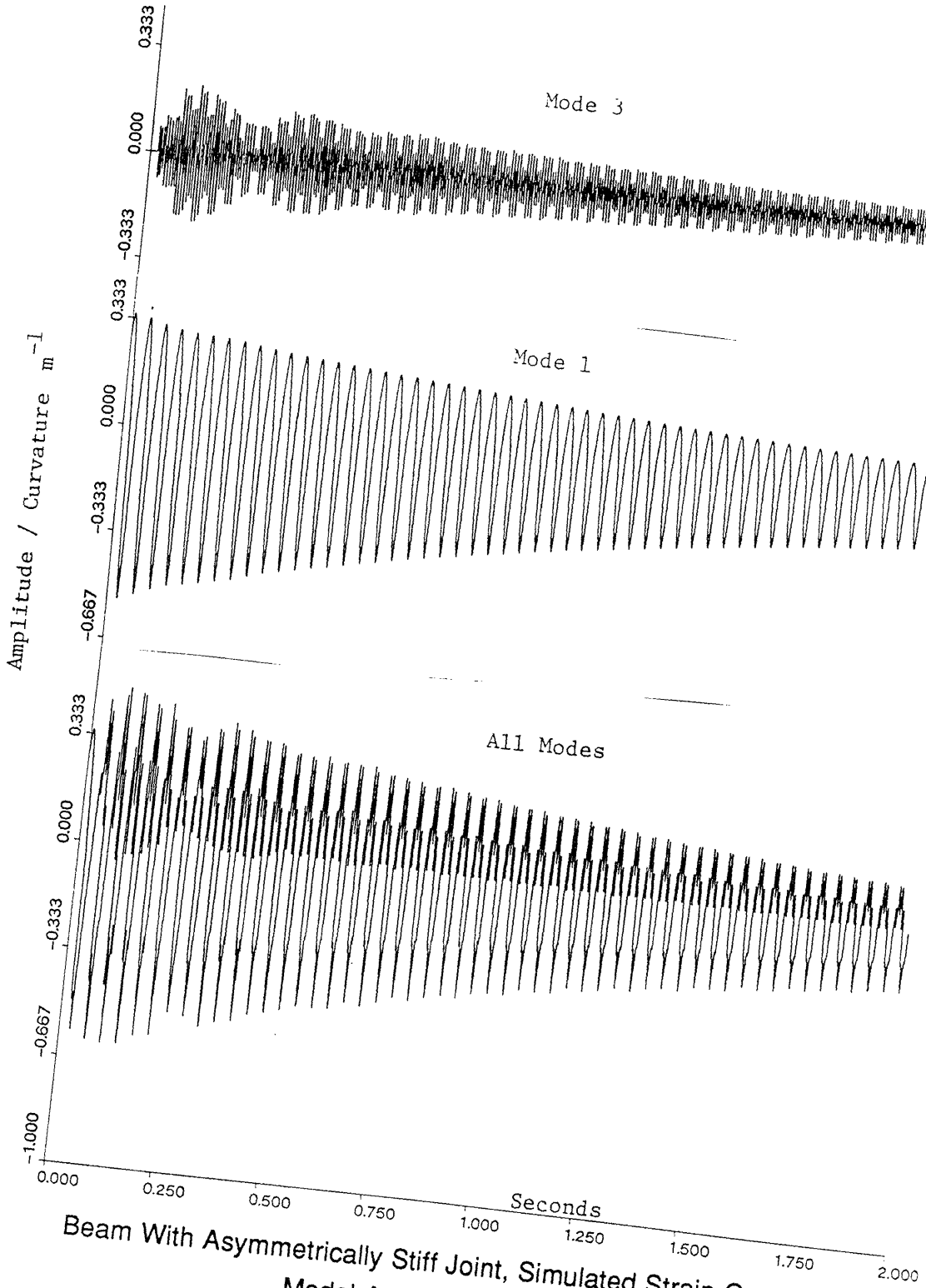

Beam With Asymmetrically Stiff Joint, Simulated Strain Gauge Data
Modal Amplitudes / Curvature
$DR_{1int} = 0.5$, $DR_{2\text{-}7} = 5.0$, $\Delta DR_M = 4.5$, $K_N = .033$, $K_S = 26$
Figure 5.7

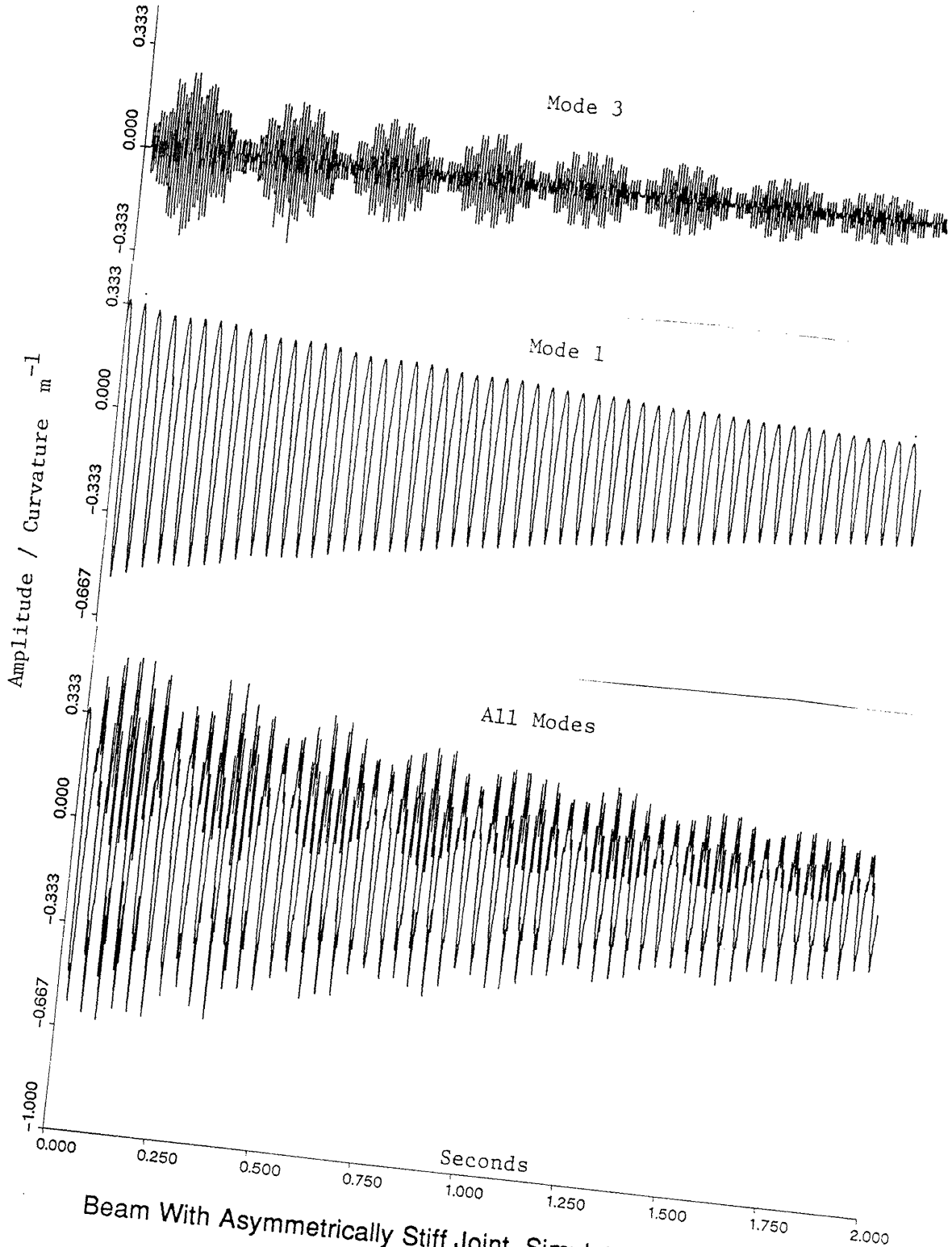

Beam With Asymmetrically Stiff Joint, Simulated Strain Gauge Data
Modal Amplitudes / Curvature
$DR_{1int} = 0.5$, $DR_{2\text{-}7} = 0.5$, $\Delta DR_M = 0.0$, $K_N = .033$, $K_S = 26$
Figure 5.8

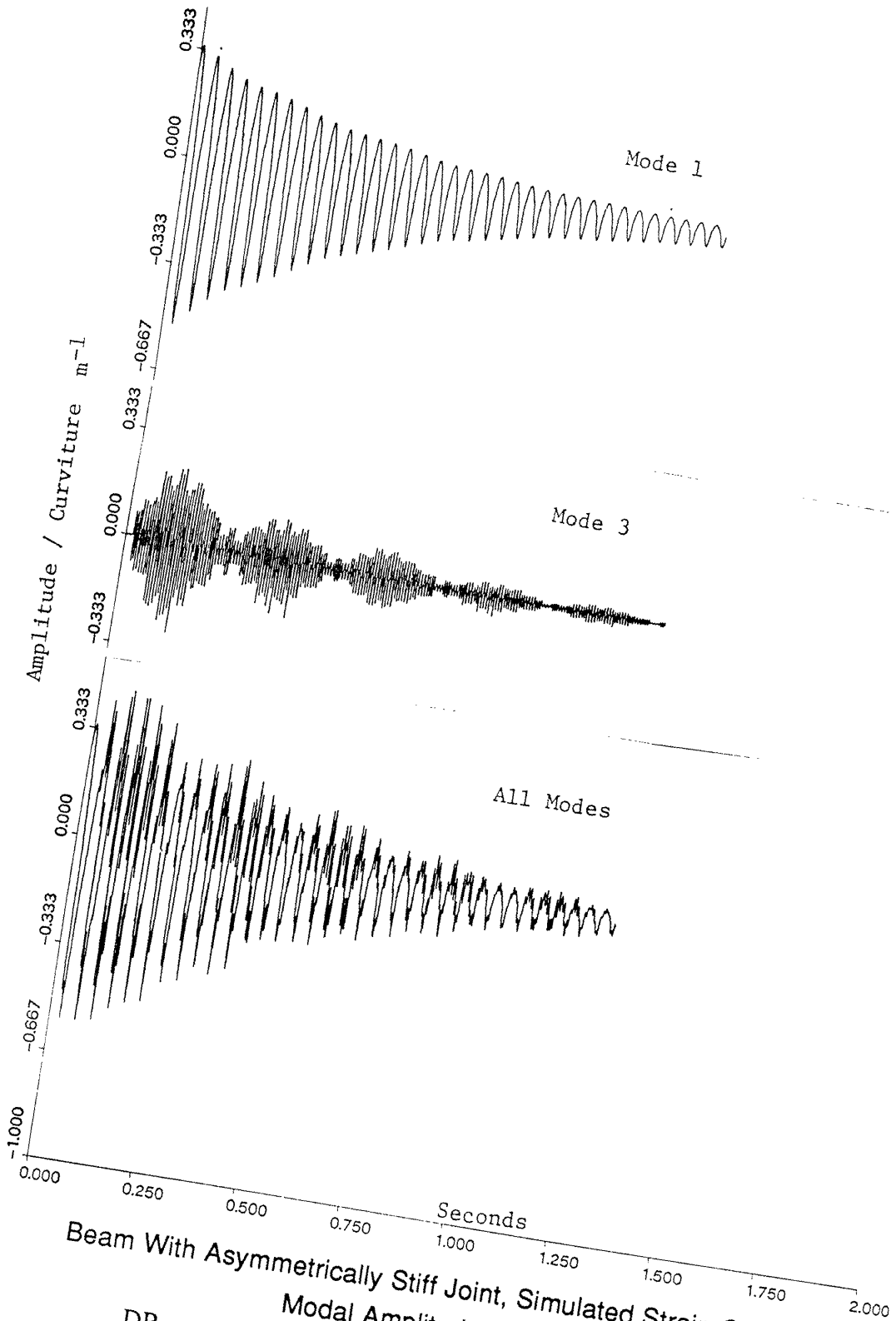

Beam With Asymmetrically Stiff Joint, Simulated Strain Gauge Data
Modal Amplitudes / Curvature
$DR_{1int} = 2.0$, $DR_{2\text{-}7} = 0.5$, $\Delta DR_M = -1.5$, $K_N = .033$, $K_S = 26$
Figure 5.9

possible that the relatively high amplitudes of the third mode couple with higher modes to dissipate energy but no clear pattern is noticeable. The scatter in the damping data is possibly a result of the modal beating effecting the log decrement calculation. This is especially true of systems with ΔDR_M much less than zero because it forces the damping rate of the first mode up, making damping calculations more sensitive to modal beating.

Since the variation of the first modes modal damping reduces to the same representative curve in ΔDR_M and $\Delta Z_M\%$ the variation of the nonlinear joint parameters could be conducted with the single mode test to observe the maximum damping including modal coupling. This greatly reduced the number of computer simulations required. This test gives the limit of very high damping in the upper modes, the asymptotic limit as ΔDR_M goes to infinity. The results for the asymmetrically stiff jointed beam for three values of K_S, 2.6, 13, 26, are illustrated figure 5.10. The same data normalized by the frequency of the systems first mode is shown in figure 5.11.

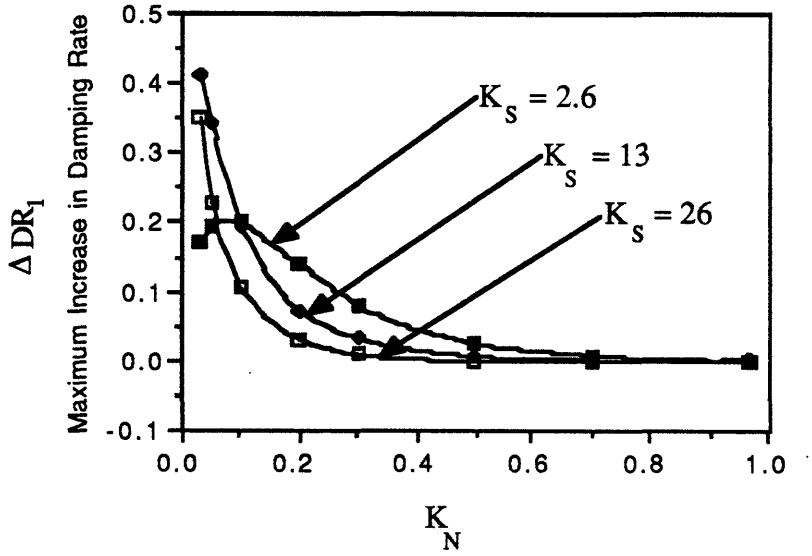

Asymmetrically Stiff Jointed Beam
Maximum Increase in First Mode Damping Rate Due to Modal Coupling
vs Joint Stiffness Ratio (K_N) and Joint Stiffness Parameter (K_S)
Single Mode Simulation
DR_{1int} = .5
Figure 5.10

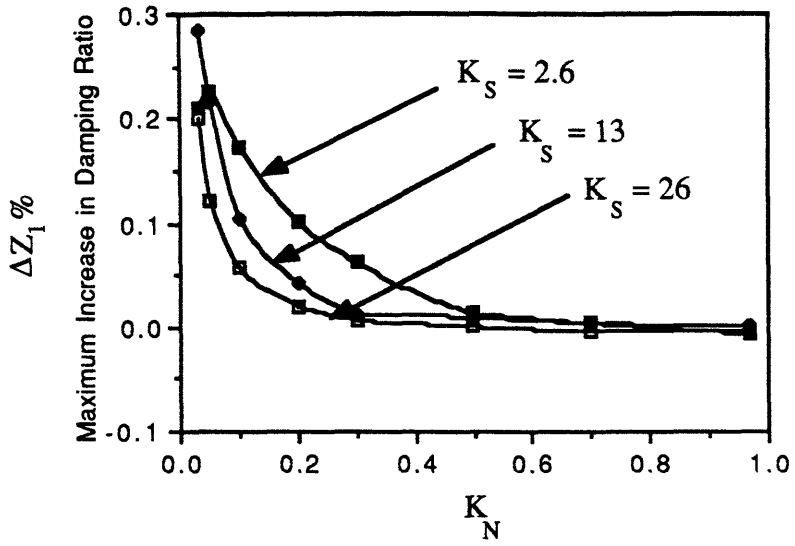

Asymmetrically Stiff Jointed Beam
Maximum Increase in First Mode Damping Ratio Due to Modal Coupling
vs Joint Stiffness Ratio (K_N) and Joint Stiffness Parameter (K_S)
Single Mode Simulation
$Z_{1int}\% = 0.3$
Figure 5.11

The figures show that the nonlinearity must be fairly large before any significant damping can occur. Figure 5.12 shows the simulated strain gauge data of a jointed beam with a mildly nonlinear joint. The data trace is mostly sinusoidal and little damping due to modal coupling is possible. Figure 5.13 shows the simulated strain gauge data of a jointed beam with a strongly nonlinear joint. The data trace is not sinusoidal and exhibits strong nonlinear behavior. The maximum possible damping caused by the nonlinearity is determined by the nonlinearity alone and only contributes, in the examples used in this analysis, less than 1.0% damping. The peak damping provided by the modal coupling decreases as the joint stiffness, K_S, decreases but the increase in damping starts at a earlier point in K_N.

5.6 Wire Braced Beam

In the system simulating a wire braced beam by coupling the one third points of the beam, figure 2.9, there is only the one joint parameter considered since the beam properties are assumed to be constant.

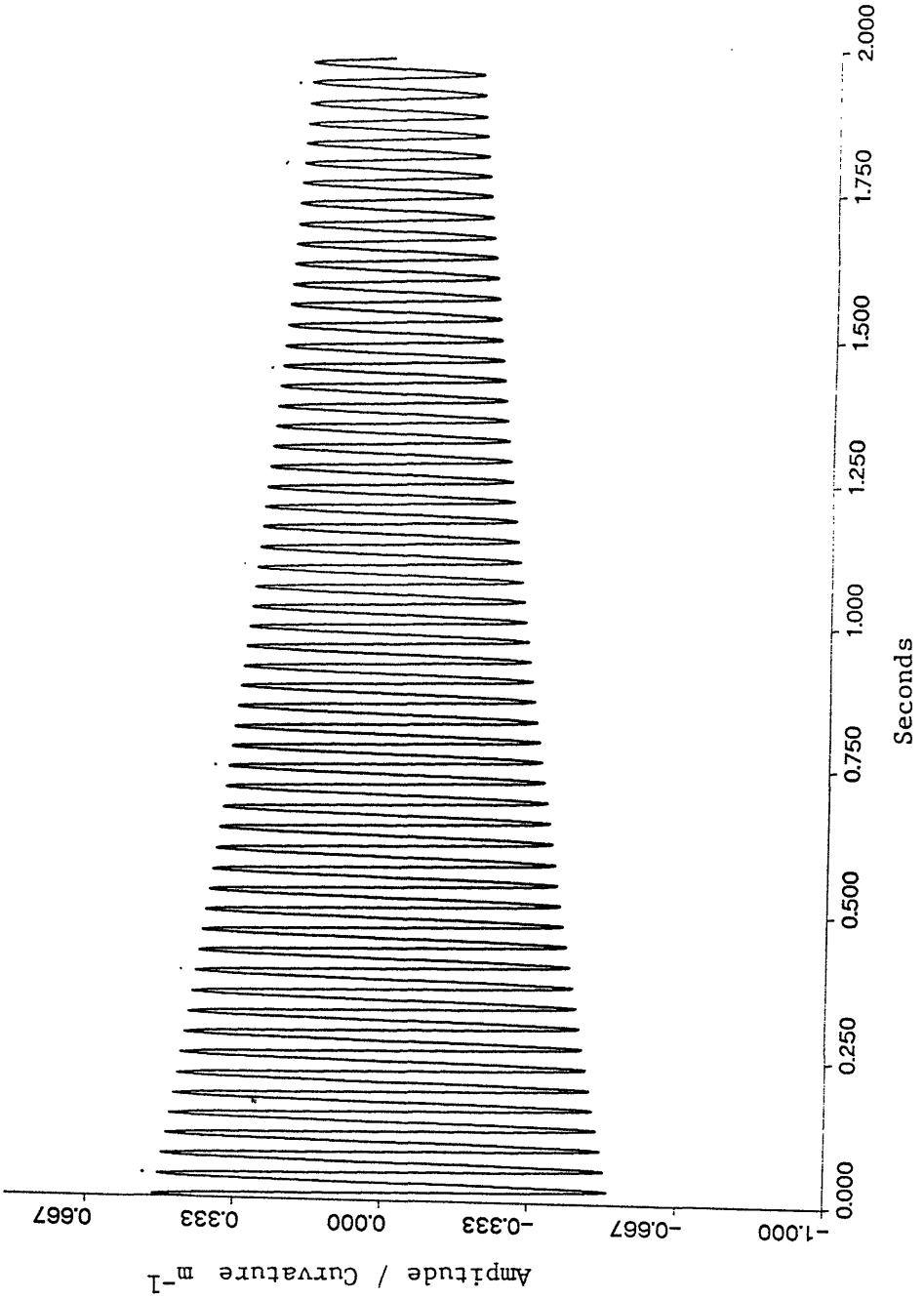

Beam With Asymmetrically Stiff Joint, Simulated Strain Gauge Data
Amplitude / Curvature, Single Mode Simulation
$K_N = 0.97$, $K_S = 2.6$, $DR_{1int} = .5$
Figure 5.12

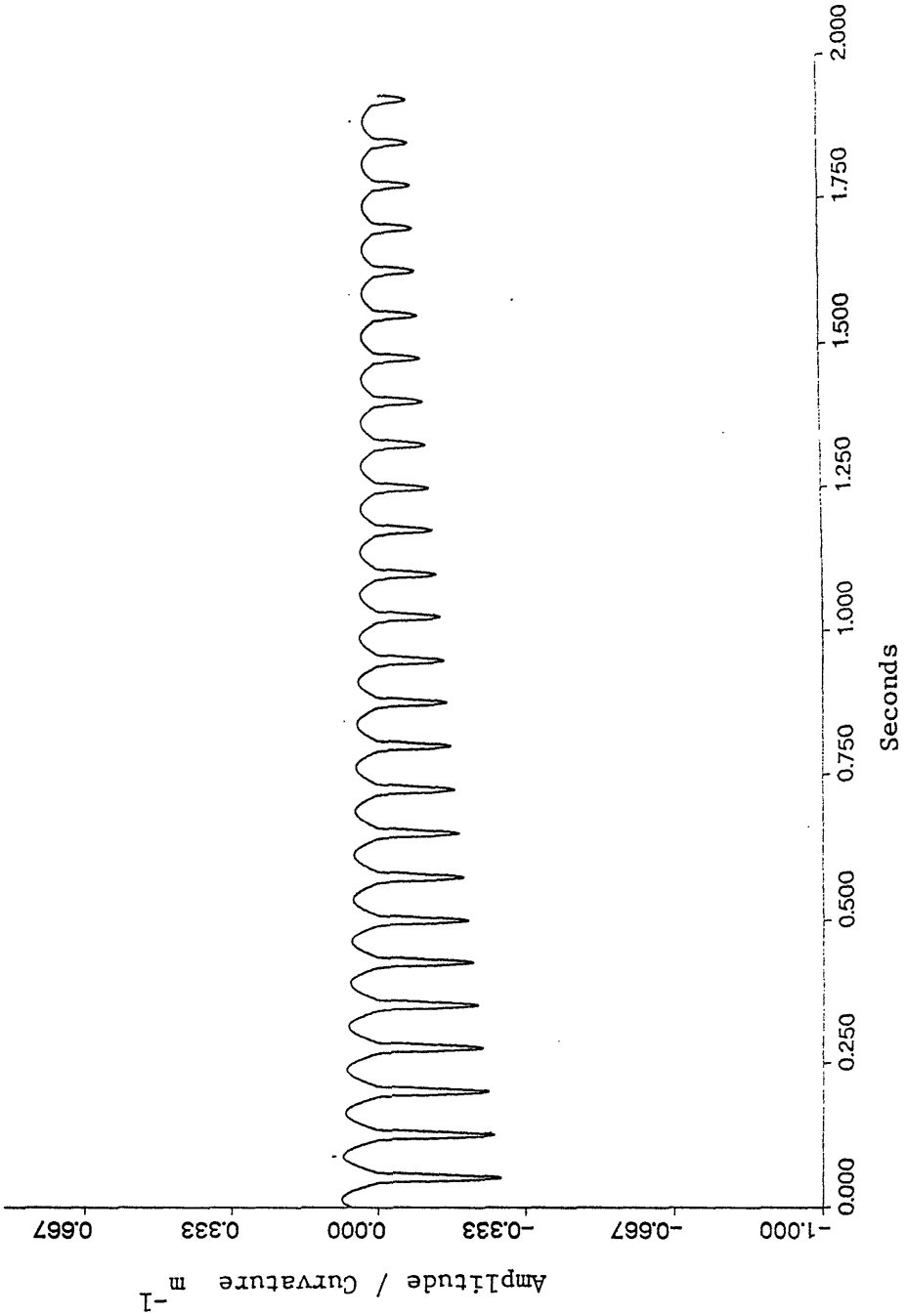

Beam With Asymmetrically Stiff Joint, Simulated Strain Gauge Data
Amplitude / Curvature, Single Mode Simulation
$K_N = 0.033$, $K_S = 2.6$, $DR_{1int} = .5$
Figure 5.13

$$\frac{(\frac{EI}{l})}{K_2+(\frac{EI}{l})} = K_N \qquad (5.10)$$

As before, K_N is a measure of the nonlinearity of the system.

An analysis similar to that of the asymmetrically stiff jointed beam produces similar graphs. The structure where the one third points of the beam are coupled by a piecewise linear spring is an extension of the above analysis. The potential for nonlinear coupling is greater in this example and shows that large nonlinearities may cause significant damping due to modal coupling. The figure 5.14 shows the effect of damping rates on the damping due to modal coupling for a particular value of K_N. It is very similar to figure 5.6 but does not approach the asymptotic limit as quickly.

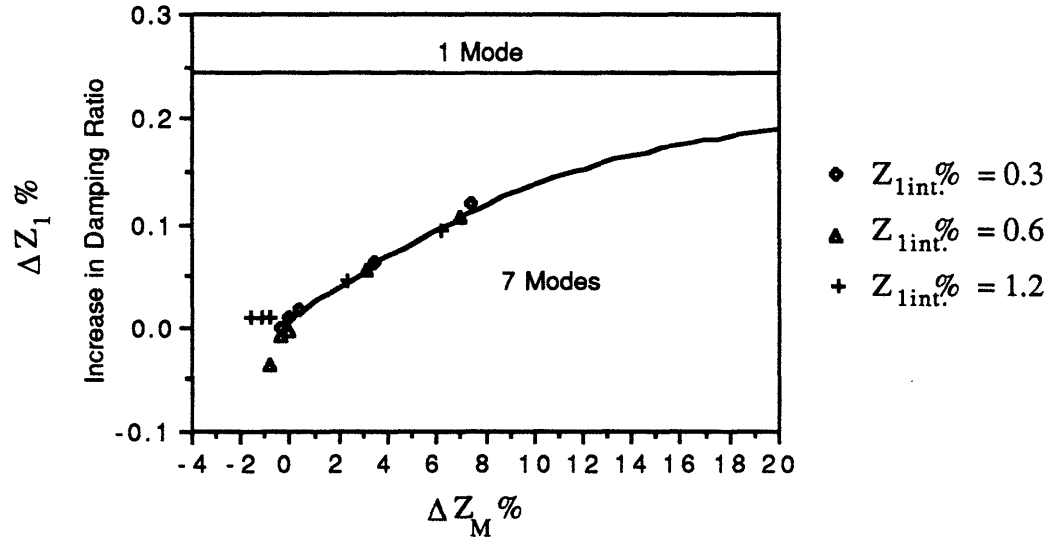

Wire Braced Structure
Increase in First Mode Damping Ratio Due to Modal Coupling
vs Normalized Difference in Modal Damping Rates
K_N =0.8
Figure 5.14

The single mode test is performed with different values of K_N and shown in figure 5.15. As can be seen the nonlinearities, again, must be fairly large in order to cause significant damping due to modal coupling.

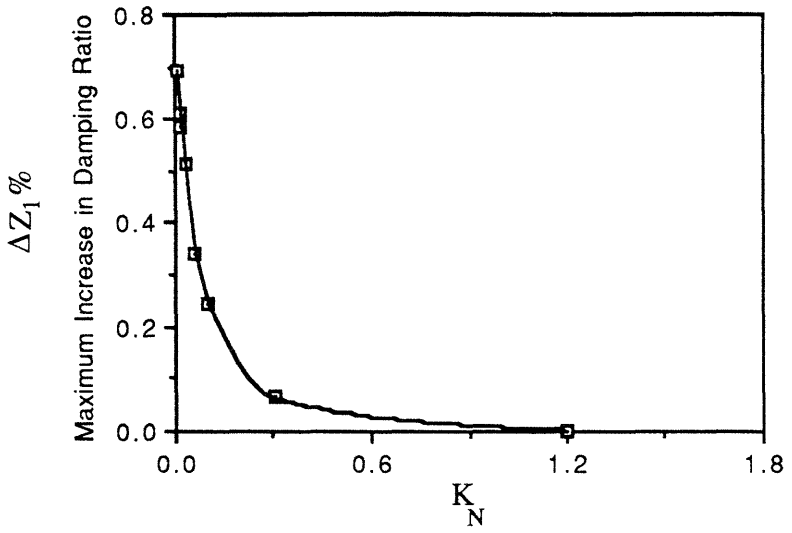

Wire Braced Beam
Maximum Increase in First Mode Damping Ratio Due to Modal Coupling
vs Joint Stiffness Ratio (K_N)
Single Mode Simulation
Figure 5.15

5.7 Dead-Band Jointed Beam

The dead-band joint is assumed to have relatively rigid springs with a relatively weak spring representing the dead-band, figure 2.12. In this analysis the angle the joint must rotate to pass through the center weak spring, is held constant and the amplitude of the first mode varied. The effect the dead-band has on the structure changes as the amplitude decays. Since the dead-band is assumed to be centered in the sense that when the structure is at rest the joint is centered in the weak spring region, there is an amplitude of the first mode the joint just starts to exit the center region and contact the outer springs. This amplitude is labelled A_{DB}, and is defined as the amplitude of the first mode where the onset of dead-band nonlinearities occurs. The measure of the amount of the nonlinearities is defined as the ratio of the amplitude of the first mode and the amplitude of the first mode where dead-band onset occurs.

$$\frac{A_{M1}}{A_{DB}} = DBR \tag{5.11}$$

When the normalized amplitude, DBR, is equal to or less than one then the system is linear. When DBR is greater than one then nonlinear behavior occurs. When DBR is much greater than one then the dead-band becomes small compared to the dynamics of the structure and will approach a linear structure in the limit as DBR goes to infinity.

The dead-band jointed beam is a slightly different case than the two structures examined above. The amplitude dependence is examined by setting the system in motion in its first mode and calculating the log decrement damping for each cycle. The damping rate of the upper modes is set at 100 where the damping rate of the first mode is set at 0.5. The simulated strain gauge data of a dead-band jointed beam is shown in figure 5.17. The single mode test proved ineffective in this example because as the dead-band was small compared to the motion of the beam, more than the first mode was needed to model the transition. The amplitude of the system as it decays is shown in figure 5.16. It is very close to a linear line.

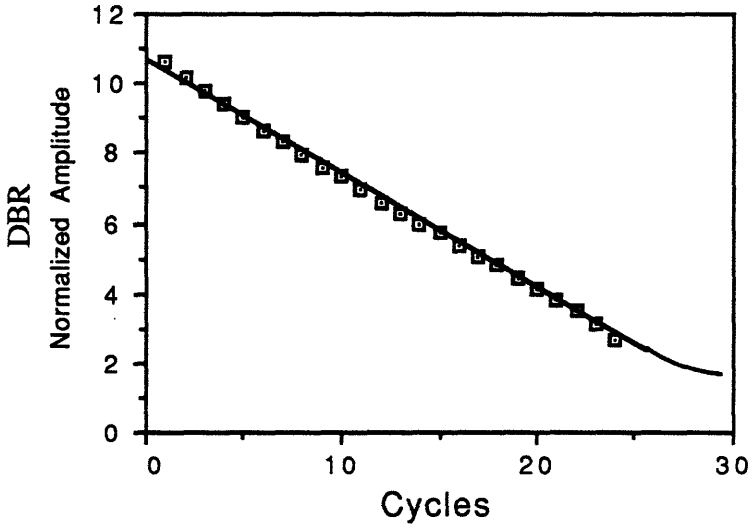

Dead Band Jointed Beam
Amplitude Ratio vs Cycles
Figure 5.16

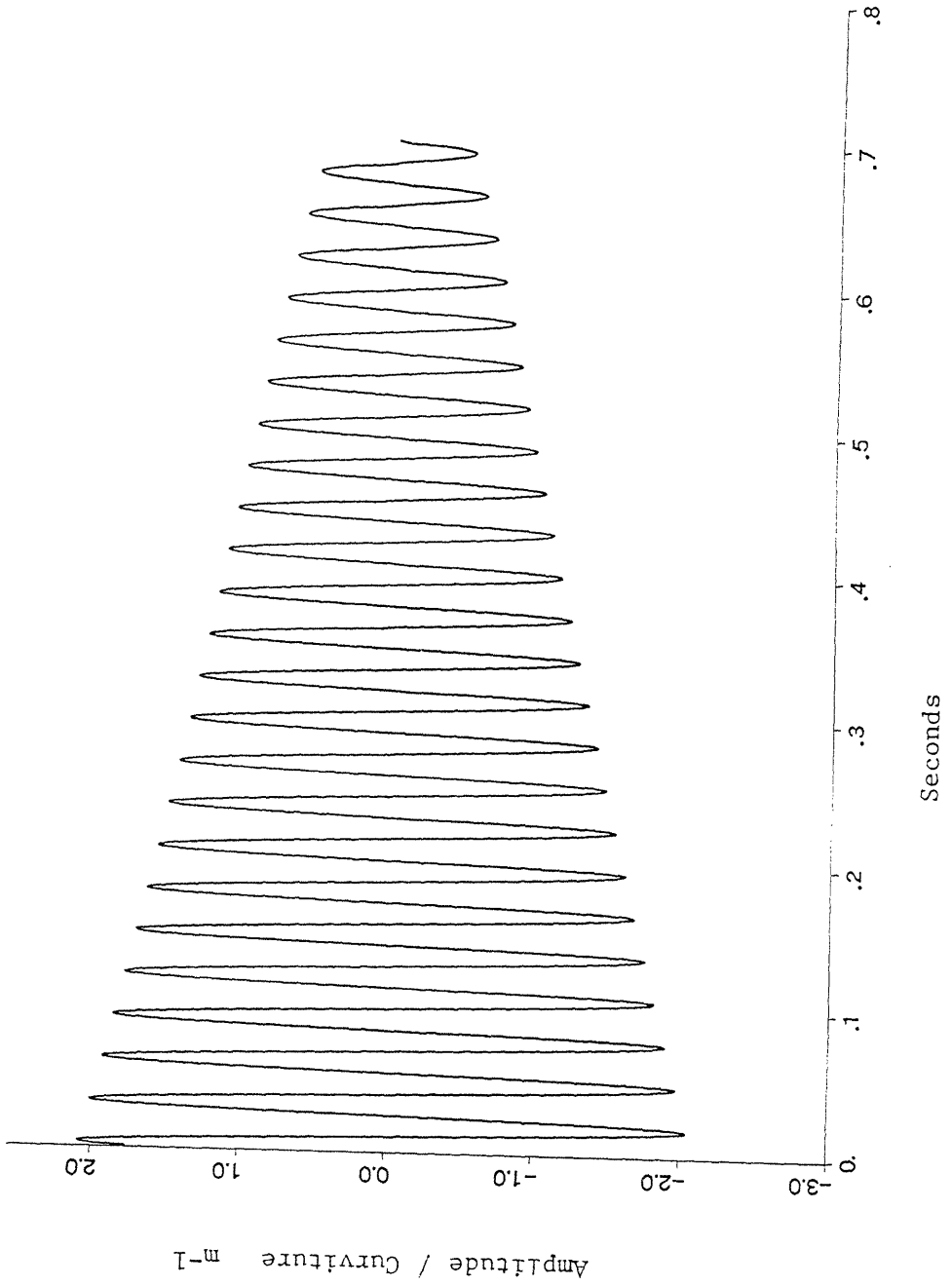

Beam With Dead Joint, Simulated Strain Gauge Data
Amplitudes / Curvature, Mode 1
$DR_{1int} = 1.0$, $DR_{2\text{-}7} = 100$, $\Delta DR_M = 99$, $K_N = 0.033$, $K_S = 26$
Figure 5.17

When the oscillations drop below the point where the dead-band is effective the structure becomes linear and the curve in figure 5.16 flattens out. The damping associated with modal coupling is illustrated in figure 5.18. At high amplitude the damping due to modal coupling is near zero. As the amplitude ratio approaches unity, the point where the structure becomes linear, the damping contributed by the modal coupling increases to near 2% before it starts to fall again. This is with a very high upper modal damping rate. Lower damping rates reduce the damping in a similar manner as in the previous structures.

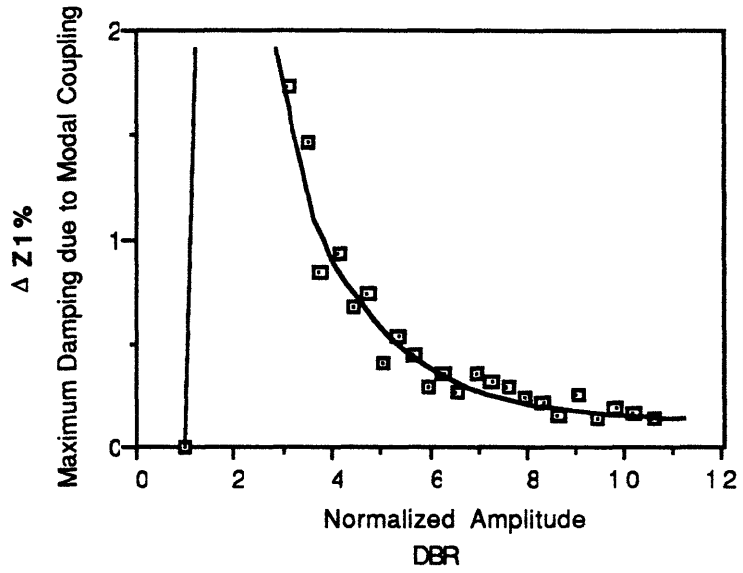

Dead Band Jointed Beam
Maximum Increase in First Mode Damping Ratio Due to Modal Coupling
vs Normalized Amplitude
Figure 5.18

To complete the analysis the structure coupled at its one third points was set in motion with its third mode only. This is in an effort to determine if coupling from higher modes to lower modes was significant. In this case very little excitation of the of the first mode by the third was observed. This seams to be because the nonlinear joint is causing the structure to transfer between sub-systems at the rate of the third mode and this tends to not excite the first mode significantly. However, the third mode excited the fifth mode in exactly the same method as the first excited the third, exhibiting damping due to modal coupling and beating between the modes. This indicates, at least for this structure and

on-off nonlinearities, that the modes above the excited mode are the most important. This is not surprising given the nature of the on-off springs since the sudden jump in stiffness will mostly contribute higher frequency disturbances to the structure.

5.8 Summary

The conclusion from this analysis is that damping due to modal coupling will contribute significantly only if,

1) The internal damping ratio of the fundamental mode is small so as to not overwhelm the the damping due to modal coupling which is limited by the modal coupling caused by the discrete nonlinearities.
2) The nonlinearities are large, causing significant coupling, without causing significant hysteretic damping to violate condition 1.
3) The damping rate of the coupled modes must be significantly higher than the fundamental mode in order to increased its effective damping.

This analysis is limited to the three examples described but some references of more complex structures may be made. Damping due to modal coupling will be directly related to the degree of nonlinearity present in the system. Structures with only small nonlinearities will most likely not have significant damping due to modal coupling because the excitation of the coupled modes will be small. This is especially true if the same nonlinearities which couple the modes also causes hysteretic damping. Hysteretic damping can dissipate energy which would dominate the damping of the structure.

In structures where the nonlinear joints or mechanisms are significant but not hysteretic and the internal damping of the system is small, the damping due to modal coupling may be significant. It is dependent on the relative damping rates of the coupled modes. If the damping rates of the coupled modes are high then an increase in damping is expected. However, if the damping rate of the coupled modes are the same or lower than the fundamental mode then little or no increase in damping is expected but a dynamic coupling of the modes will occur where the amplitude of the modes beat out of phase with one another. In a system with significant coupling between the modes, the stresses caused by the modal excitation may be significant.

The analytical methods used in this analysis can be used for more complex structures but a continuous model will most likely not be advantageous. A sufficient number of degrees of freedom must be included in the model to insure that energy will not be trapped in the system.

EXPERIMENT

Chapter 6

Experimental Method and Apparatus

6.0 Overview

The objective of chapter 6 is to describe the experimental method and the facility used to perform the experiments. The experiment performed was designed to verify and observe damping due to modal coupling of a simulated space structure in a simulated space environment. The technique used was to design the test structures, or specimens, to resemble the theoretical models described in chapter 2 so comparisons could be made between experiment and theory. Both linear and nonlinear specimens were tested in order to measure material damping parameters and to make direct comparisons between. The specimens were tested in free-fall and vacuum to isolate them from environmental and support influences. The dynamics of the specimens were monitored via strain gauges placed on the specimens.

6.1 Experimental Method

As was discussed in chapter one it is important to isolate the experimental space structure from any phenomenon which could affect or mask the intended measurement. The effects caused by the absence in space of an atmosphere and gravity are the two most difficult to simulate. The procedure chosen for this analysis places an experimental specimen in vacuum and free-fall. The vacuum environment is provided by a large vacuum chamber which the experiment is performed in, figure 6.1. The state of free-fall is accomplished by lofting the specimen upwards in the chamber allowing it to free-fall to the top of the chamber and back down. The time the specimen is in free-fall is brief, less than two seconds. This limits the types of experiments using this technique to those of relatively short duration. The initial lofting of the specimen is used to excite the dynamics of the structure. The specimen vibrates as it free-falls straight up and back down, landing in a net stretched across the bottom of the chamber. Strain gauges mounted on the specimen transmit their signal via very fine wires to a follower system. The follower system carries shielded data lines

to close to the specimen, following it as it travels up and down. The strain gauge data is then stored for later use.

This type of experiment causes the specimen to undergo an initial impulse loading then to freely vibrate with no external forces acting on it until it lands in the net. The free decay data received from the strain gauges can then be analyzed for decay rates, modal coupling, and joint dynamics.

6.2 ASTROVAC Facility

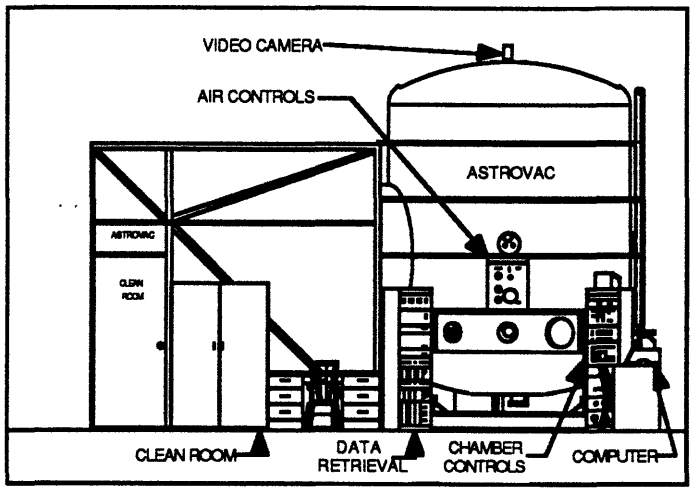

MIT ASTROVAC Facility
Figure 6.1

The MIT ASTROVAC (Apparatus for Structural Testing and Research on On-orbit Vibration And Control) facility was used to provide the necessary isolation and space simulation necessary to perform these measurements. The structure is lofted upward so that it free-falls up to the top of the chamber and back down. The ASTROVAC chamber is 10 foot in diameter and 14 foot tall with a 6 foot diameter door. This can accommodate up to 3 meter structures placed into free-fall for approximately 1.75 seconds. The chamber has two vacuum pumps connected to it. The primary or roughing pump is located on the floor below and connected to the chamber via a 6 inch diameter pipe. The second pump is a cryo-pump mounted on the back of the chamber. The two stage 350 cfm roughing pump is designed to pump the chamber to approximately 0.001 torr. where the cross-over to the cryo-pump occurs. The

cryo-pump is a helium refrigerator which freezes the atmosphere remaining in the chamber to its condenser coils. The facility is capable of pressures between 10^{-6} and 10^{-8} torr., however, the vacuum chamber was typically evacuated to only 0.1 torr for these experiments, sufficient to eliminate any atmospheric damping effects. The roughing pump could pump the chamber down to .1 torr in approximately half of an hour. The turn-around time between loft tests was roughly one hour. A pressurized room connected to the chamber provides a clean environment for personnel to work in.

6.3 Launch Platform

The launching of specimens is done by a pneumatically powered device called the TELM (Tunable Excitation Launch Mechanism), figure 6.2. The launch, the sudden acceleration of the structure from rest to its takeoff speed, places the structure under stress. By supporting the structure in certain ways an initial excitation of the structure is also performed. This initial excitation is adjusted by changing the launch platform, the support structure, or changing the acceleration rate of the launch. A shaker system is used for long duration and forced oscillation tests and was not used in these experiments.

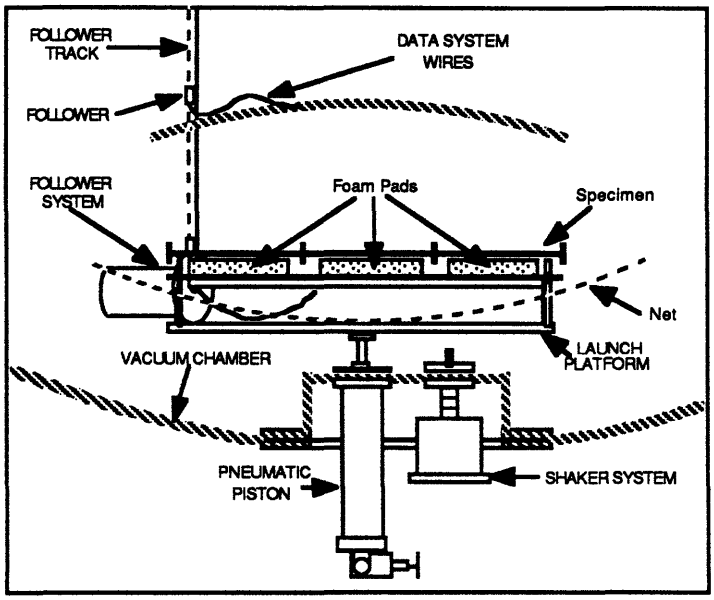

TELM System
Figure 6.2

The TELM consists of a pneumatic piston assembly, with a 5 inch diameter and a 18 inch stroke, located under the vacuum chamber. The piston assembly, figure 6.3, consists of upper and lower chambers in the cylinder separated by the piston. The piston can be forced either up or down. The shaft of the piston passes through a hole in a brass plate mounted on the chamber floor. The hole and shaft are sealed with dual o-rings and grooves located in the copper plate. This seal has proven effective even at very low pressures. The piston assembly is supplied by a two inch diameter,100 psi air line which passes through a series of valves before entering the piston assembly. A flow regulation valve is located at the base of the piston assembly. This valve regulates the flow of air into the lower chamber of the cylinder and controls the launch platform accelerations during launch. A soft launch is obtained by restricting the flow of air into the cylinder by partially closing the flow regulation valve. If a faster launch or a heavy specimen is used then the flow regulation valve is opened more.

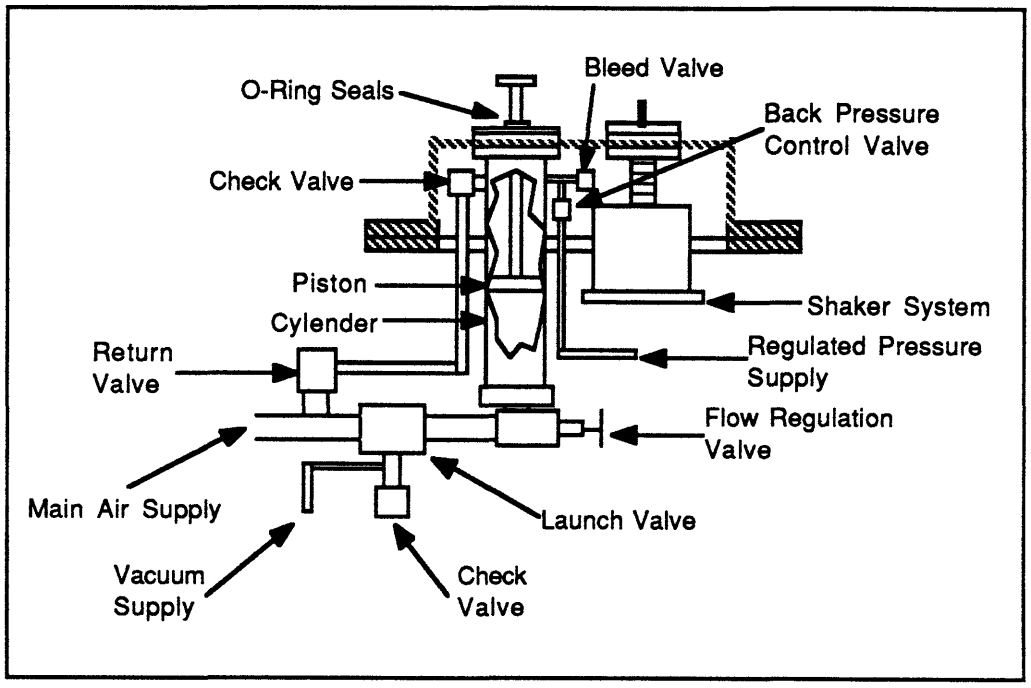

TELM Piston Assembly
Figure 6.3

The launch valve is located just before the flow regulation valve and controls the launch. The valve is a two position valve. When it is closed the

lower chamber of the cylinder is connected to a check valve to atmosphere and a vacuum valve to the second stage of the roughing pump. When the piston is ready to be fired the launch valve is closed, the check valve is closed and the vacuum valve is open pulling a vacuum on the lower chamber of the cylinder. This vacuum is necessary to keep the piston from being pulled into the chamber due to the difference in pressure across the piston shaft entering the chamber. The pressure in the upper chamber of the cylinder is regulated through two valves located at the top of the piston assembly. The pressure in the upper chamber of the cylinder is used to regulate the altitude of the launched specimen. It is desired to have the specimen launched to near the top of the chamber. The flow valve is used to regulate how fast the specimen accelerates and the air in the upper chamber of the cylinder is used to regulate the stroke and therefore the altitude of the loft. A return valve connects the upper chamber of the cylinder, through a check valve, to a 1 inch diameter, 100 psi air line to force the piston back down after a launch has occurred.

Before a launch, the flow valve is set and vacuum supplied to the lower chamber of the cylinder. The upper chamber of the cylinder pressure is then set and the TELM is ready to be fired. When the computer signals for a launch, the vacuum valve is closed, the valves at the top of the piston assembly are closed and the launch valve is opened simultaneously. The 100 psi air passes through the flow valve into the lower chamber of the cylinder forcing the piston to rise, accelerating the specimen upward. The air in the upper chamber of the cylinder is trapped due to the closed valves at the top of the piston assembly. As the piston rises in cylinder, the air in the upper chamber of the cylinder compresses, slowing and eventually stopping the piston. This action shortens the stroke and prevents the piston from striking the top of the cylinder. The specimen leaves the platform and continues to the top of the chamber. Approximately 0.3 seconds after launch has been initiated the computer signals for the launch valve to close and the return valve to open. The vacuum valve has already been closed and the air accumulated in the lower chamber of the cylinder exhausts through the check valve to atmosphere. The return valve supplies pressure to the upper chamber of the cylinder forcing the piston back down. The check valve in the return line prevents the piston from being accidentally re-launched until the system has been reset.

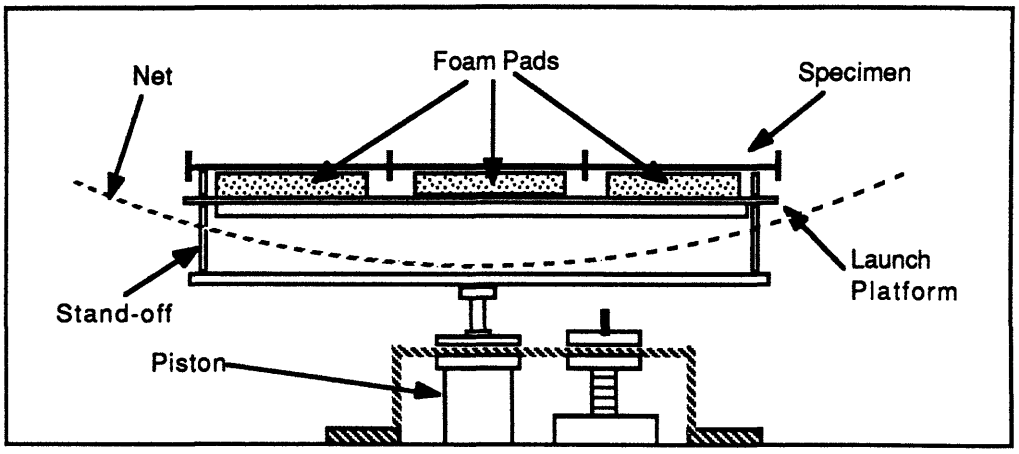

Launch Platform
Figure 6.4

Two types of launch platforms were used in these experiments. The structures were long slender beams from 2 foot to 3 foot long. The first launch platform had two supports located at the ends of the beams. The beam was free to bend between them as lofting occurred, figure 6.2. The induced stresses of this system proved to be too high causing excessively high geometric displacements and forces. The more successful launch platform was one where foam was placed on a rigid platform, figure 6.4. End supports were placed at the ends of the beam roughly level with the foam. During loft, the beam, sitting on the foam, would compress the foam as it deformed. This provided a smaller initial deflection. The deflection could also be adjusted by changing the relative height of the end supports and the type of foam used.

6.4 Data Retrieval System

All experimental data was from strain gauges mounted no the specimens and transmitted from the specimen via small gauge wires (50 ga.) connecting the specimen to a follower mechanism. The follower mechanism is a track riding device which roughly follows the path of the free-falling specimen. Its purpose is to carry shielded wiring to close to the specimen and connect to the specimen through very thin wires. The thin wires are very light and short and do not effect the dynamics of the free-falling specimen. Experiments measuring the material damping of metals has shown that the wires induce little or no

influence on the specimens. Damping ratios (zeta) less than .03% have been successfully measured with no discernable error caused by the wires. However, the wires must remain slack. If the wires are pulled tight for any reason during the test they will have a large influence on the specimen.

Heavier shielded wiring carries the data signals from the follower, see figure 6.2, out of the chamber to a computerized data retrieval system. A motor, located at the base of the follower track, drives a pulley system which causes the follower to run up and down the track. The follower motor is contained inside its own pressure vessel to isolate it from the vacuum and the data system from the electrical noise it generates. The follower system is driven open loop by the same computer that runs the TELM system. Approximately 0.1 seconds before a launch the follower is commanded to accelerate upwards. This lead time is necessary to allow the follower to get up to speed. When the launch occurs the specimen very quickly catches up to the follower and passes it. The specimen is, however, decelerating and the follower keeps pace with it to the top of the chamber. Near the top of the follower's track the computer commands the follower to reverse direction. The follower motor is not powerful enough to decelerate at the rate the specimen is so rubber stops are placed at the top of the track. The stops help turn the follower around and send it back down the track. When the specimen lands in the net the follower is just behind. The computer signals to the follower to stop and rubber stops at the bottom of the track insure that it does. The follower track is roughly 2 foot from the specimen and a 4 foot length wire between the specimen and the follower proved to be sufficient. Most experiments used a 5 foot length wire and no discernible differences where found.

A test takes place in less than 2 seconds and is completely computer controlled. The strain gauges were connected to a 4 volt half bridge, amplified (x 1000), and filtered through a Bessel filter with a corner frequency of approximately 2500 Hz. The signal was digitized at a rate of 5000 samples per second and stored on an IBM-PC. The noise levels were measured at approximately 2 mv. p.t.p. where the signal was around 2 to 4 volts. A video camera, looking through a port on the top of the chamber, records the actual flight path. The launching force set on the TELM is determined through a computer model of the TELM and by trial and error, mostly trial and error. If the flight path was too low the data wires would be pulled tight. If the flight path was

too high the specimen would hit the top of the chamber. A camera at the top of the chamber was used to determine the success of the test flights.

At the end of the test, the specimen lands in a net stretched across the bottom of the chamber. This prevents damage to the structure but some repairs were necessary. Most damage would occur when the specimen would land on the launch platform.

6.5 Experimental Specimens

Experiments were performed on five different types of structures. They all are made up of long thin beams joined together by joints. The challenge of this experiment was to design nonlinear joints which can be modelled as piecewise linear. Three different nonlinear joints were devised.

The first structure, designated Beam 2, consisted of a 3 foot long 1 inch wide by 1/8 inch thick aluminum 6061-T6 bar with 1/2 inch standoffs at the ends and the one foot marks. The entire structure is machined out of a single piece of metal to eliminate any joining effects, see figure 6.5.

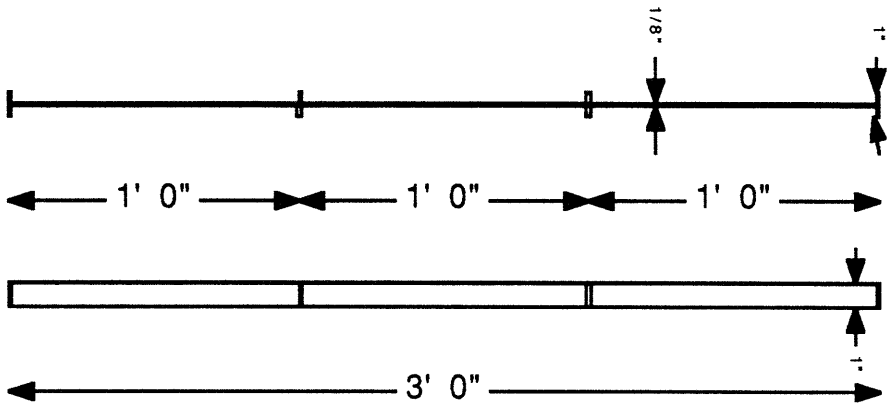

Experimental Specimen Beam 2A
Figure 6.5

The specimen was tested, designated Beam 2A, in order to measure material damping. A thin stainless steel plate, 0.001 inch thick, 1 foot long, and 1 inch wide was then bolted and glued to two inner standoffs. As the structure flexes, the thin plate would go tight then loose depending on the angles of the beam at

the standoffs. The thin plate was attached to the stand-off by punching three holes in the stainless steel which matched three bolt assemblies on the top of the stand-offs. The plate was glued and bolted to the top of the stand-off with a metal bar between the bolt heads and the plate, figure 6.6. The plate was attached in such a way as to be just tight when the specimen was at rest.

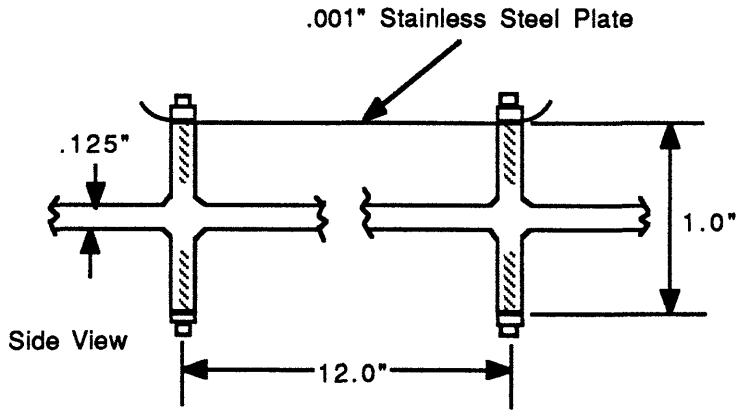

Wire Braced Beam Assembly
Figure 6.6

Since the thin plate was only .001 inch thick, it had negligible compressive strength and acted as a discontinuous spring linking the standoffs. This specimen was designated Beam 2B. Strain gauges were placed at the middle of each beam section and on each standoff to measure beam deformation and plate loading. A second test, designated Beam 2C, attached two plates to opposite sides of the same beam section. A third test, designated Beam 2D, was made by attaching three plates to the three beam sections on alternating sides of the beam. This test was intended to increase the nonlinearity of the specimen. The configurations tested and their designation symbol are shown in Appendix C. An example is shown in figure 6.7. The specimen is designated Beam 2B. It has a single thin plate attached across the middle section of the beam. The designation symbol illustrates this by including a line between the two inner standoffs.

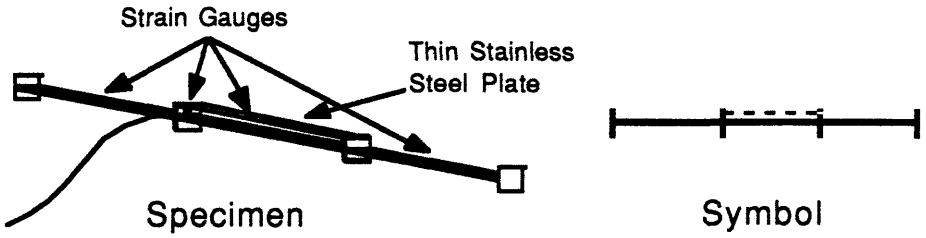

Experimental Specimen Beam 2B
Figure 6.7

The second type of specimen tested incorporated flexible joints. Three one foot long beam sections with standoffs at each end were made, figure 6.8.

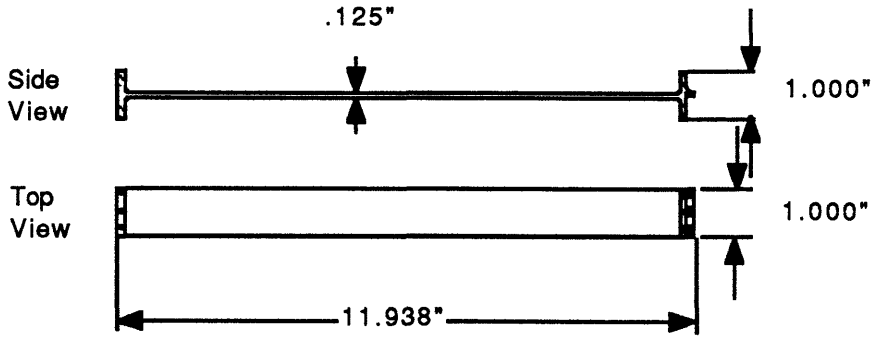

Beam Section of Specimen Beam 3/4
Figure 6.8

A joint was made between the beam sections by bolting and gluing a thin stainless steel plate between them, see figure 6.9. The thicknesses of the joining plate was 0.02 inch. The length of the joint was approximately 1/8 inch and provided for a flexible linear joint. The joint was made nonlinear by again fastening 0.001 inch thick stainless steel plates between the ends of the standoffs. The joint could be made to have an asymmetric stiffness by attaching a thin plate on one side of the joint. When the deflection of the joint put the thin plate in compression, the plate would buckle, the stiffness of the joint being only that provided by the 0.02 inch thick joining plate. When the thin plate is in tension it contributes to the stiffness of the joint. The thin plate was attached such that it just went tight when the joint was in its unloaded position, figure 6.9.

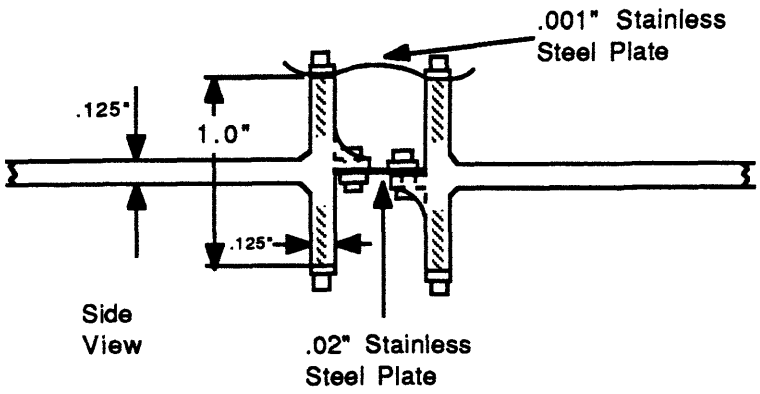

Asymmetrically Stiff Joint Assembly
Figure 6.9

A dead-band joint was made by placing a thin plate on both sides of the joint. The plates were given a measured amount of slack so that as the joint flexed it would be stiff then flexible then stiff again, see figure 6.10.

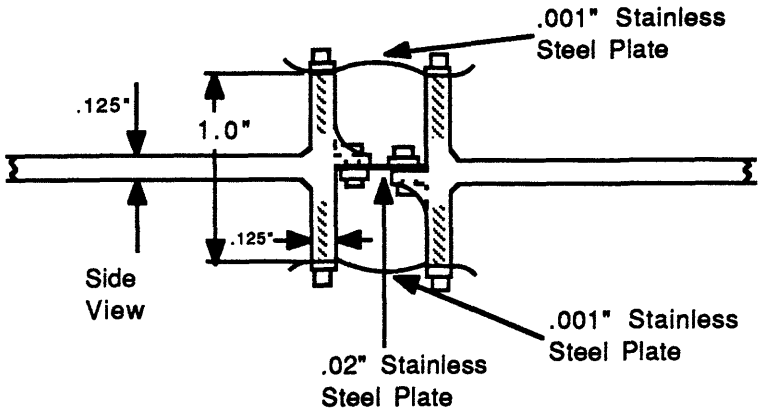

Dead-Band Joint Assembly
Figure 6.10

It was discovered that the thin stainless steel plate could deform in such a way as to be able to support a small amount of compressive load, the shims were only 1/2 inch long. By smoothing the plate with a narrow rod this could be eliminated. This property proved useful because damping data of the stiffened joint system could be obtained. Tests of specimens with two beam sections, designated Beam 3, and with three beam sections, designated Beam 4, were performed. Asymmetrically stiff, dead-band, and joints without a thin plates were tested. Tests without thin plates were made in order to measure the

internal damping of the jointed beam systems. The three beam section specimens were intended to increase the nonlinearity of the specimens. The configurations tested are shown in Appendix C. An example is shown in figure 6.11. The specimen designated Beam 4D is a three section beam joined by dead band joints. The configuration symbol illustrates this by showing lines between the inner standoffs representing the joints. The lines are on both sides of the joint indicating a dead-band joint. An asymmetrically stiff joint has a line on only one side. The lines represent the thin plates attached to the standoffs and which side the line appears indicates which side the plate is attached to the beam.

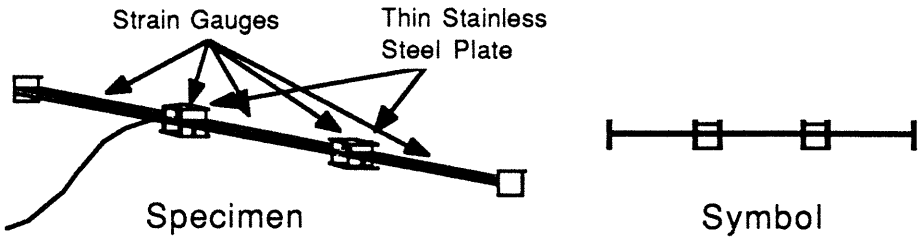

Experimental Specimen Beam 4D
Figure 6.11

6.6 Experimental Procedure

The procedure for testing a specimen started with setup of the launch platform. The support placements and height over the foam were set depending on the level of initial oscillation desired in the specimen. A dummy specimen was then placed on the platform and launched in air to test the TELM settings. Once the TELM was adjusted the experimental specimen was placed on the platform and the wires coming from the strain gauges connected to the follower. The ASTROVAC chamber was then sealed and pumped to approximately 0.1 torr. The TELM system was then readied for launch and the chamber valves closed. The video tape recorder was then started, the follower power turned on, and the launch control safety interlocks switched off. The computer was then given the signal to proceed and the launch would take place. The data which was stored in the computer was transferred to diskette.

The tests conducted are listed in Appendix C along with comments on the tests. The strain gauge data was stored in files labeled by the date of the

test and identified the strain gauge being recorded. For example a data file is identified with a eight digit code, for example, AP250101. The first four digits indicate the month and date the test occurred in, in the example, April 25th. The fifth and sixth digits indicate which test of the day, in the example, the first test of the day. The last two digits identifies the strain gauge, in the example, strain gauge 1. Video recordings of each launch were also examined and comments from the recording are listed with each test. Some minor damage to the specimens was suffered when a bad loft occurred or the structure had an awkward landing. The thin stainless steel plate proved to be quite rugged and only rarely broke. A simple of the data taken and how it is illustrated is shown in figure 6.12.

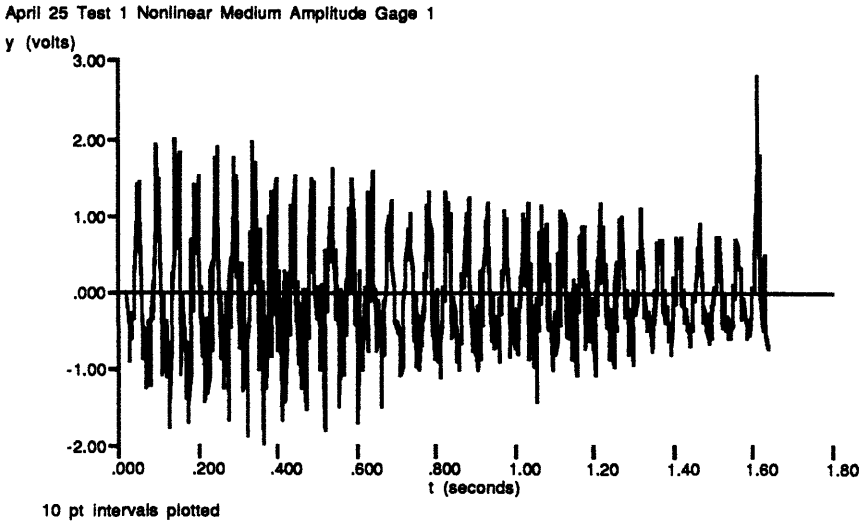

Test AP250101
Sample Strain Gauge Data
Figure 6.12

The data shown is the strain gauge signal from a strain gauge located at the center of the first beam section of specimen Beam 2B, a long slender beam with a single thin plate linking its one third points. The first oscillation of the data is the specimen is being launched. The large oscillation at the end of the data is caused by the landing of the specimen.

Chapter 7

Analysis of Experimental Data

7.0 Overview

The objective of chapter 7 is to experimentally validate the theoretical analysis by measuring the modal amplitudes and effective modal damping rates of experimental specimens in free-free oscillation and compare them to analytic models developed and simulated in chapters 2 through 5. Two types of experimental specimens were tested, linear and nonlinear. The linear specimens were tested to determine the internal material damping of the specimens. The three analytic models used in the analytic chapters were modeled after the three nonlinear specimens tested in the experiments. A wire braced beam, an asymmetrically stiff jointed beam, and a dead-band jointed beam, were tested. The nonlinear specimens had piecewise linear joints described in chapter 6, section 6.5. The objective of these tests were to observe the structural dynamics associated with this type of nonlinear joint, in particular, modal coupling and damping due to modal coupling. A set of multiply jointed beams were also tested to observe how more complex jointed structures effect the structural response.

In order to generate the analytical simulations with which to compare to the experimental specimen tests the internal or material damping rates of the experimental specimens are required. It is possible to experimentally measure the internal material damping of the specimens by testing the individual sub-system structures. The nonlinear structures, both simulated and experimental, can be divided into sub-systems where a sub-system consists of the entire structure with the joint in one of two configurations, (see chapter 2, section 2.2). The joint configurations, or sub-joints, consist of a stiff sub-joint and a flexible sub-joint. The stiff sub-joint represents the joint when a stainless steel plate is in tension and restricts joint rotation, (see chapter 6, section 6.5). The flexible sub-joint represents the joint when the thin plate is under compression and buckles. The plate is very thin, 0.001 inches, and buckles under very low load. The linear sub-joints are created, for example, by removing the thin plate which buckles under load. The resulting experimental sub-system is tested and its

damping ratio determined. A technique can be found to test most but not all of the sub-systems.

After the experimentally determined internal damping rates and initial conditions are established they are input into the analytical model and the simulation run. The simulations are then compared to the experimental tests of the nonlinear structures. Several characteristics are looked for in the comparisons. Modal frequencies and modal coupling, the excitation of modes by other modes, are the most observable phenomena. In particular the beating phenomenon, which occurs in the coupled modes under certain conditions, is used as a critical comparison for the verification of the analytical model. Since the internal modal damping rates are not adjustable and somewhat variable in the experiments, the damping due to modal coupling is more difficult to observe. The correlation of the damping data, particularly in the asymmetrically stiff jointed beam and the dead-band jointed beam, are also used to justify the analytical model but the damping measurement error does become significant.

Section 7.1 describes the analytical procedure used to reduce the experimental data. Section 7.2 analyzes the wire braced structure. Section 7.3 analyzes the asymmetrically stiff jointed beam. Section 7.4 analyzes the dead-band jointed beam. Section 7.5 summarizes the analysis of the experiments.

7.1 Analysis Procedure

The first step in the analysis is to experimentally determine the internal damping rates of the experimental structures. As in the theoretical analysis the nonlinear joints used in the experimental specimens are piecewise linear and can be separated into their individual components. A physical structure can be developed to represent the sub-system, the structure with a single component or sub-joint of the original piecewise linear joint. For example the asymmetrically stiff jointed beam has two sub-systems, one where the thin plate in the joint has buckled and the other when it has pulled tight. A sub-system for the buckled case can be developed by removing the thin plate. The sub-system for the unbuckled case can be developed for special cases and is discused in section 7.3.

The internal damping rate of each constituent sub-systems was experimentally determined by lofting the specimen with single components of the piecewise linear joints and measuring the damping rate of the different

modes. The modes were identified by performing an FFT on the data and observing the modal frequencies. The data retrieved from a sample linear specimen is shown in figure 7.1. The portions of the data which correspond to launch, landing, or any mishaps, such as a collision with the chamber roof, are excluded from the FFT. The FFT of the test shown in figure 7.1 is shown in figure 7.2. As can be seen the first few modes are excited. How the structure is excited is primarily determined by the launch platform configuration. The launch platform is described in chapter four and is designed to primarily excite the first mode.

The individual modes were isolated by digitally filtering the strain gauge data so that only one mode is retained in the data, (see figure 7.3). A ten pole Butterworth sine band-pass filter with the center of the band-pass at the modal frequency and a band-pass width of ten hertz was applied to each identified mode. The Butterworth sine filter has the characteristic of preserving the amplitude information well but loosing phase information. This filter was considered the best choice of a variety of filters since the damping is determined by the amplitude information, not the phase information. Curves representing the response of the individual modes were generated and stored. Figures 7.4 and 7.5 show the individual modal responses of the first and third modes of the test shown in figure 7.1.

The modal damping rates were determined by performing a least squares curve fit of the filtered data to a damped sinusoid. Information on how the damping rate changed as the oscillation continued was desired so the curve fitting routine was applied to a window of the data 0.2 seconds long or one thousand data points, the data sampling rate being 5000 samples per second. The curve was fit and the data window's fitted parameters; median time, average amplitude (of beam curvature), frequency, damping rate, etc., were stored. The window was then moved approximately 0.1 seconds down the response curve and the fitting routine repeated. An overlap of 0.1 seconds is maintained for all of the windows over the entire modal response. The fitted parameters of all three strain gauges, (G1, G2, G3), are shown.

Each structure has a number of strain gauges mounted on it. The data obtained from each is curve fit as described. The damping ratios of the first and third modes of the above data are shown in figures 7.6 and 7.7 respectively. Each data point represents the damping ratio of a fitted window. The fitted

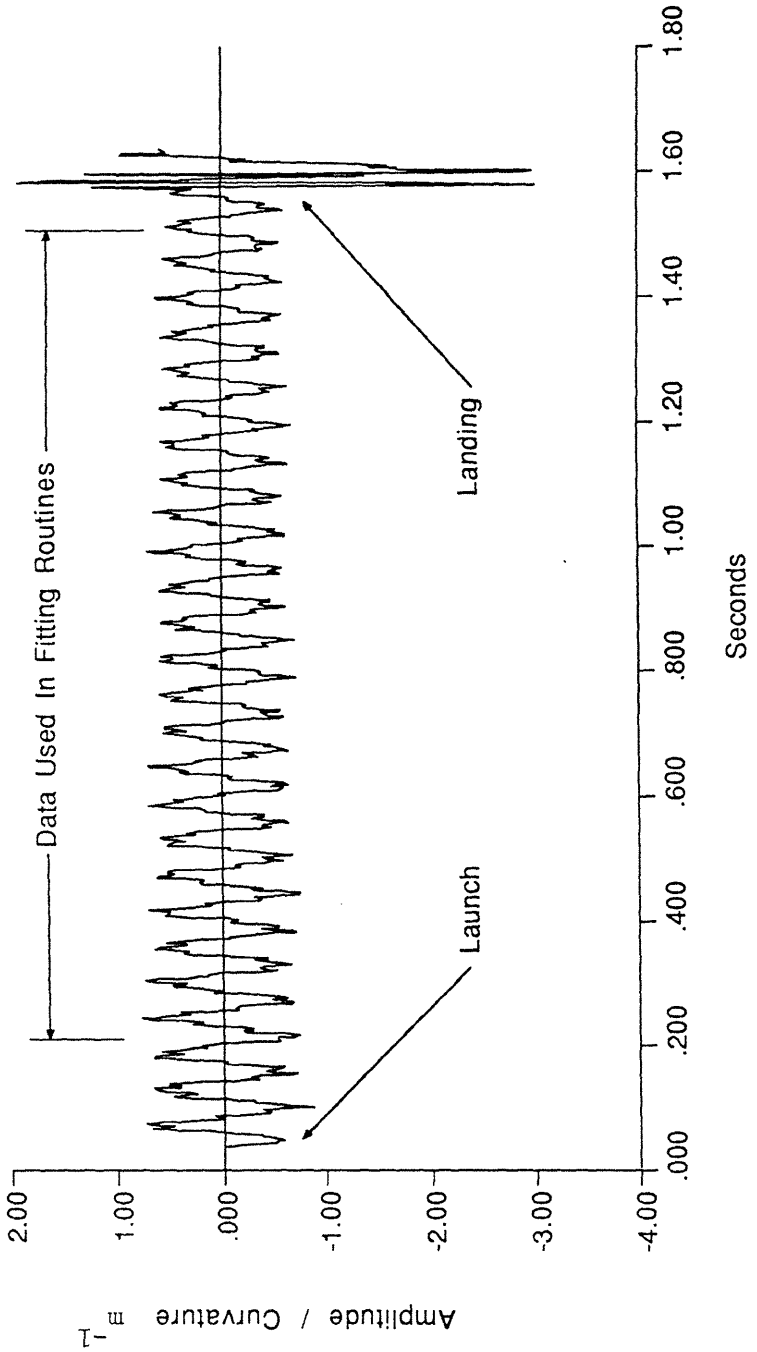

Experimental Strain Gauge Data, Amplitude / Curvature
Continuous Unjointed Beam, Beam 2A, Test AP2401 Gauge 1
Figure 7.1

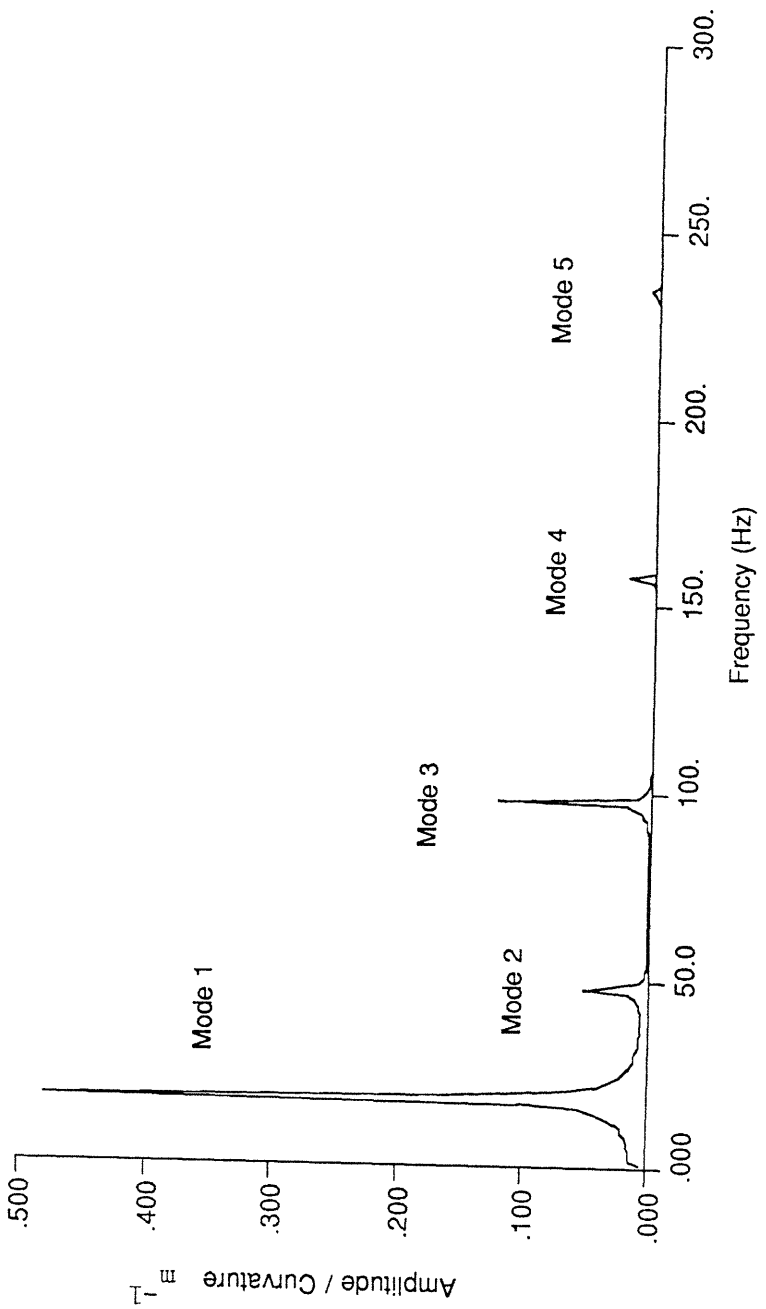

FFT of Experimental Strain Gauge Data
Amplitude / Curvature vs Frequency
Continuous Unjointed Beam, Beam 2A, Test AP2401 Gauge 1
Figure 7.2

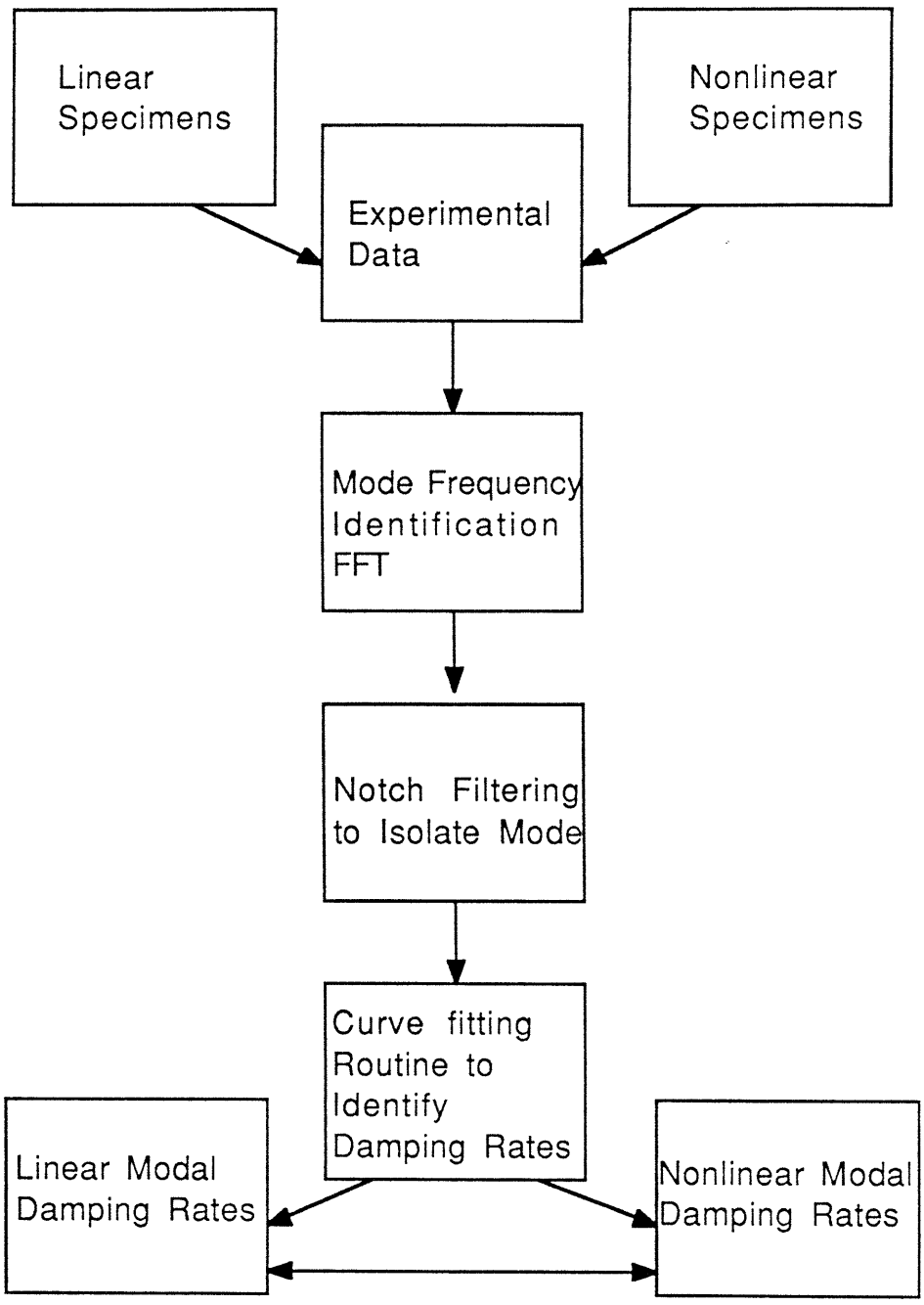

Experimental Data Reduction Procedure

Figure 7.3

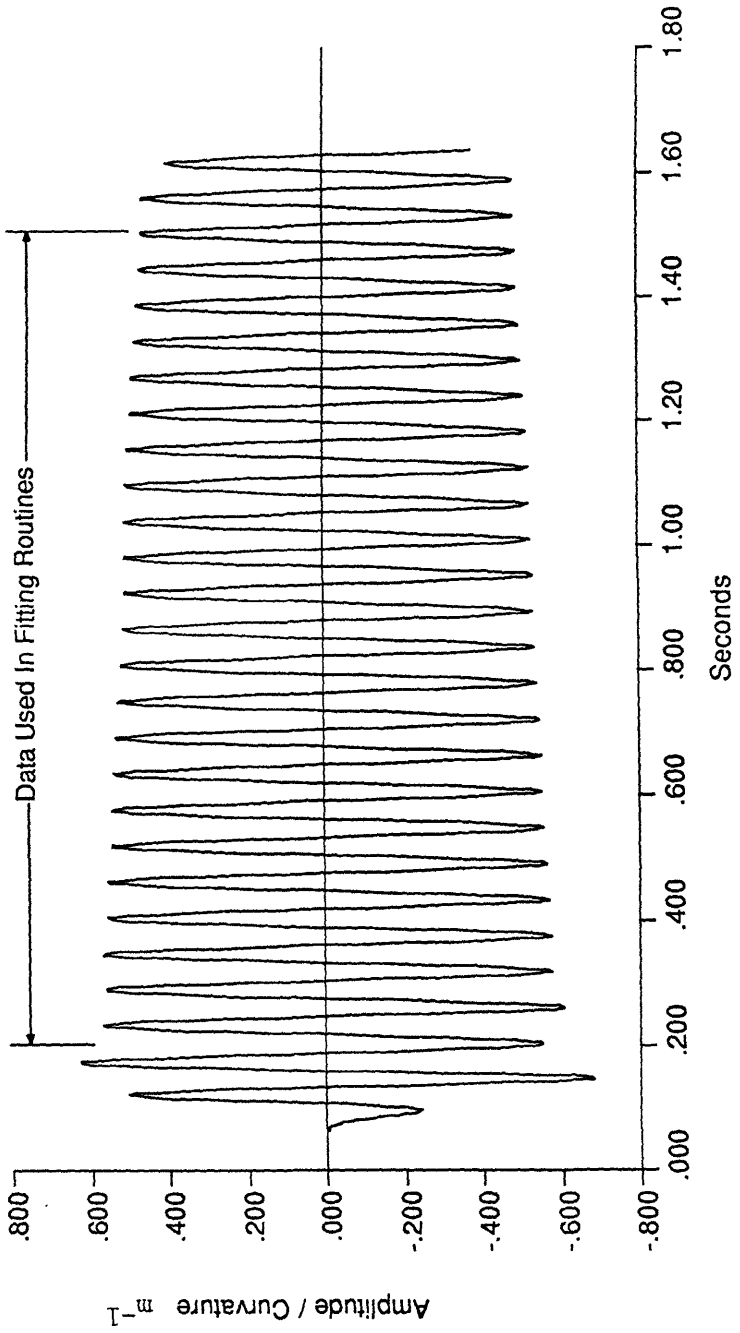

Mode 1 of Experimental Strain Gauge Data, Amplitude / Curvature
Filtered With Band-Pass Filter, Center = 18 Hz, Width = 10 Hz
Continuous Unjointed Beam, Beam 2A, Test AP2401 Gauge 1
Figure 7.4

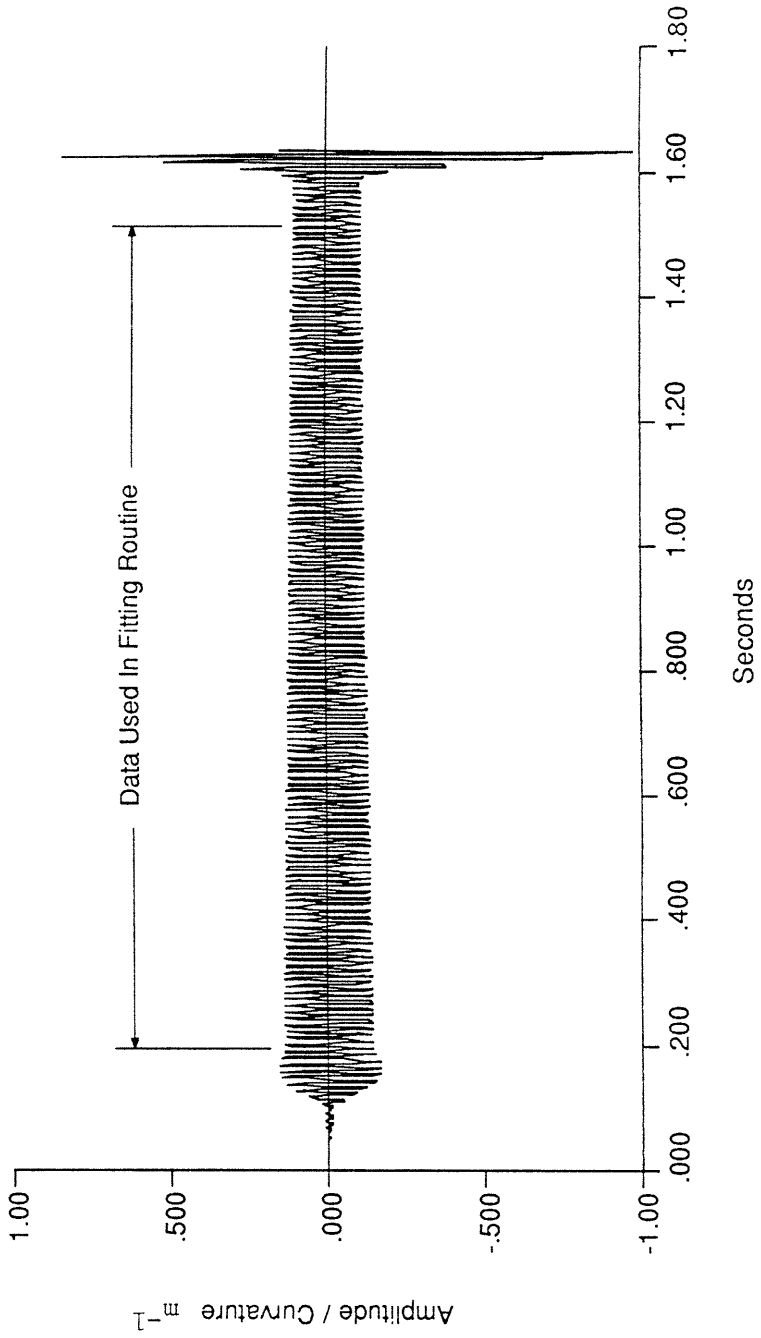

Mode 3 of Experimental Strain Gauge Data, Amplitude / Curvature
Filtered With Band-Pass Filter, Center = 97 Hz, Width = 10 Hz
Continuous Unjointed Beam, Beam 2A, Test AP2401 Gauge 1
Figure 7.5

parameters of the two outer strain gauges (G1 and G3) are used since the amplitude of the first mode is greatly reduced at these positions.

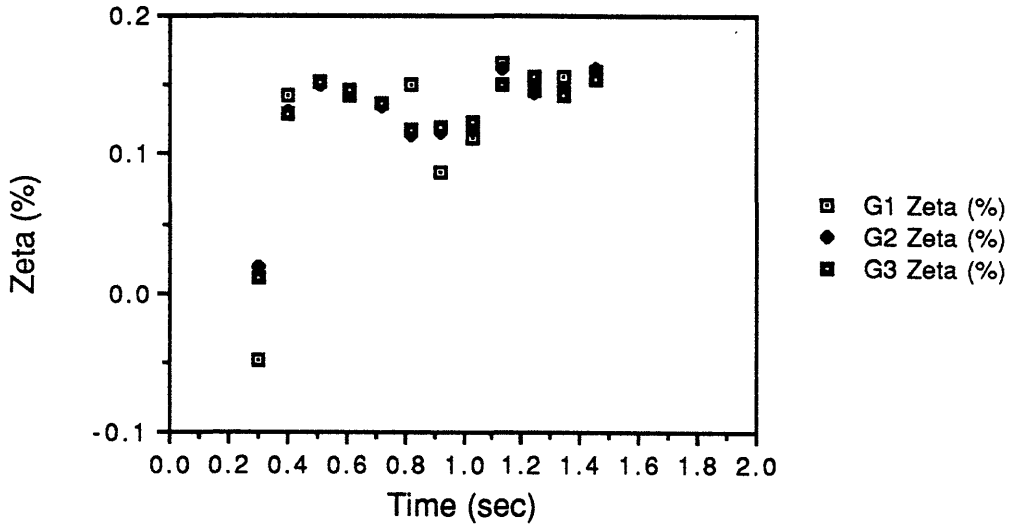

Fitted Damping Ratio vs Median Time
Continuous Unjointed Beam, Beam 2A, First Mode of Test AP2401
Figure 7.6

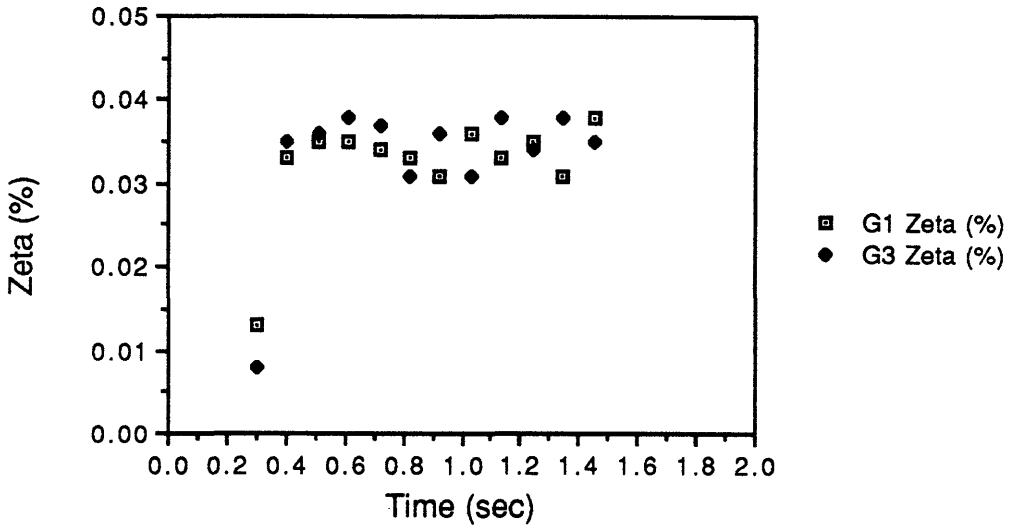

Fitted Damping Ratio vs Median Time
Continuous Unjointed Beam, Beam 2A, Third Mode of Test AP2401
Figure 7.7

In each of the graphs showing the damping data there are stray points. Points such as these can occur any time a disturbance of the structure takes place; in

this case, it occurs at the beginning, indicating that the specimen has not settled down from the launch.

Disturbances typically occur when the specimen lands in the net or if the specimen strikes anything, such as the chamber roof. These disturbances cause the specimen to vibrate in a more complex manner and this causes the residuals of the least squares fitting routine to increase. Figures 7.8 and 7.9 show the residuals of the fitting routine versus the fitted damping ratio. The stray points identified above as possibly being influenced by the launch show a significant increase in their residuals (SSQ). A relative increase in the residuals does not guarantee that the measurement is incorrect but is used as an indication of when the specimen effectively left the launcher and when it has hit something. In the test above, it is surmised that the first window is still under the influence of the launch and is therefore removed from the results.

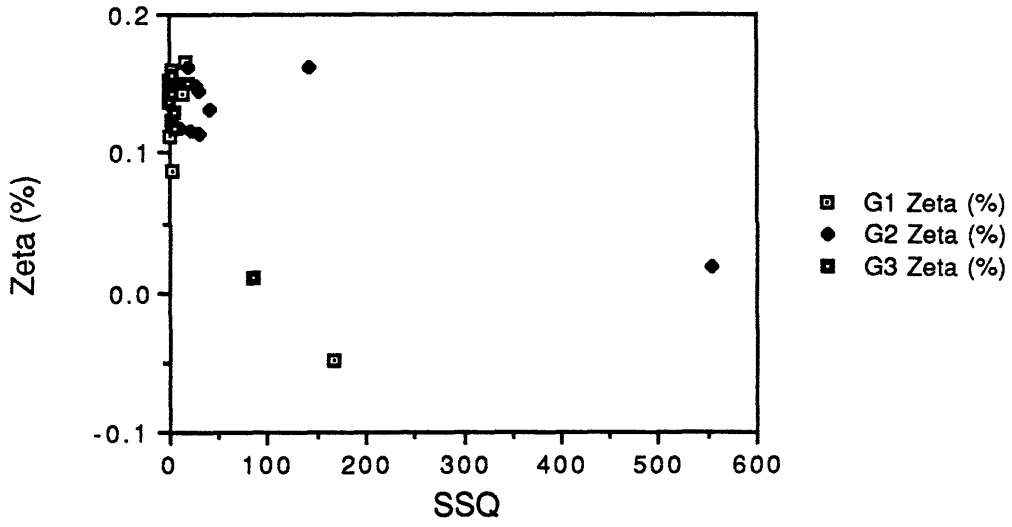

Fitted Damping Ratio vs Least Squares Residuals
Continuous Unjointed Beam, Beam 2A, First Mode of Test AP2401
Figure 7.8

Note in figure 7.9, there are several points with high residuals but they are not significantly different from points with low residuals. These points occur when the specimen is near the top of the chamber. This could be caused by the specimen slightly tapping the chamber roof but is more likely signal noise caused by the follower bouncing off its stops at the top of its track. There are connectors on the follower and the sudden impact of the follower jars these

connectors and changes the resistance across them very slightly. A fourth strain gauge was included on the specimen, monitoring the strain in an upright (see figure 6.6). The upright was not connected to a thin plate and only experienced inertial loads. Its signal was recorded during the launch and is shown in figure 7.10. A sudden, permanent shift occurs at 0.8 seconds, the time the follower strikes the top of its track. The shift is on the order of one-hundredth of the signal being generated by the strain gauges but this is enough to increase the residuals of the curve fitting routine. The shift does not appreciably affect the damping parameters primarily because the digital filtering used to isolate the modes tends to minimize its effect.

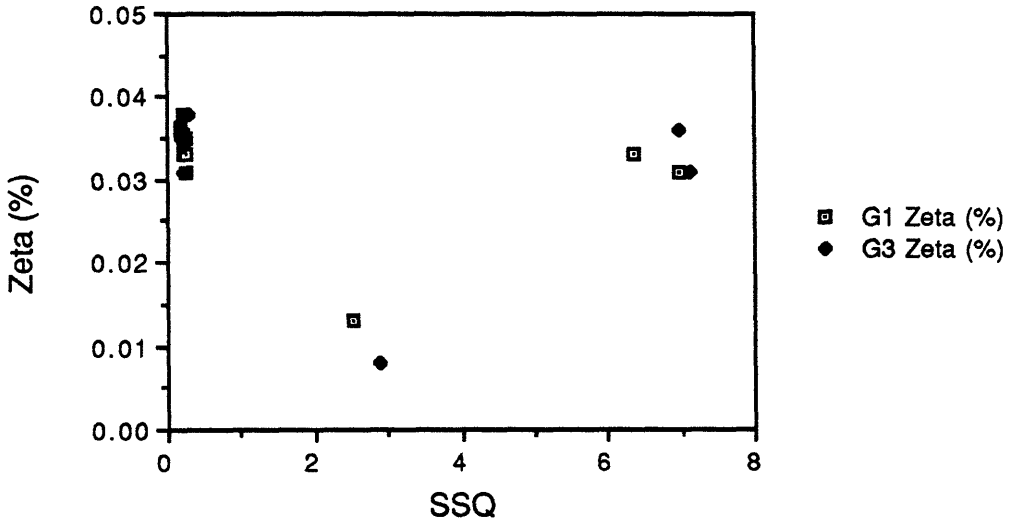

Fitted Damping Ratio vs Least Squares Residuals
Continuous Unjointed Beam, Beam 2A, Third Mode of Test AP2401
Figure 7.9

On launch, an individual mode may or may not be excited by the launch's configuration. Typically only the first and third modes were excited to any great extent. Estimates of the other modal damping rates were obtained when the loft was too high and the specimen inadvertently tapped the top of the vacuum chamber. The impact with the chamber excited all of the modes of the specimen and damping data was obtained during the return to the ground. The curve fitting routine did not perform well above the fourth mode, due primarily to the increasing number of cycles included in the window being fit. The log decrement technique was used to estimate the damping of these modes.

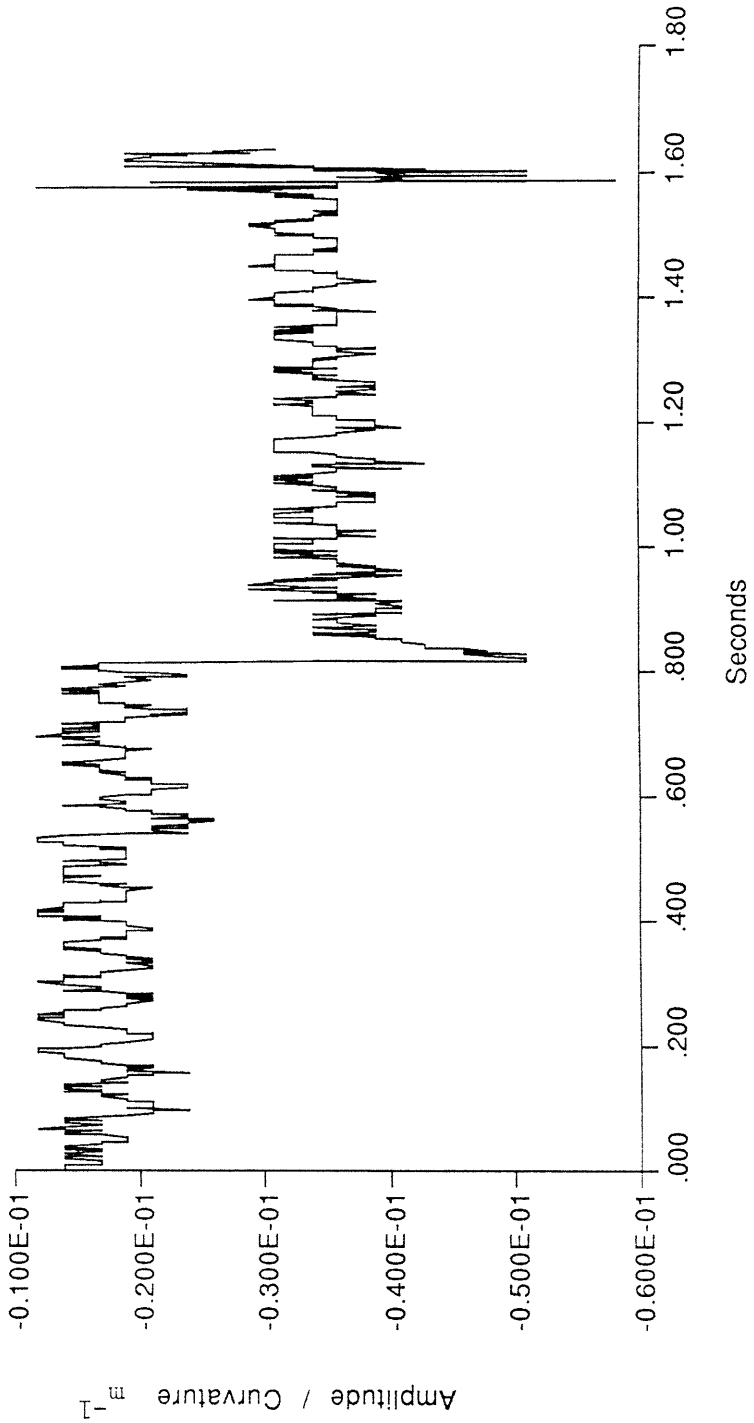

Experimental Strain Gauge Data, Amplitude / Curvature of Free Upright Continuous Unjointed Beam, Beam 2A, Test AP2401 Gauge 4

Figure 7.10

Tests of nonlinear beams with asymmetrically stiff joints, asymmetrically stiff linking of the one third points and dead-band joints were also conducted. The modal amplitudes and modal damping rates were determined using the same process as in the sub-system tests. The nonlinear nature of the structures caused the FFT to not show the modes as distinctly as in the sub-system tests but the first few modes could always be identified. The same digital filter was applied to the data to isolate the modes. The curve fitting routine could usually be used on the first mode only due to the beating phenomenon in the upper modes. The residuals of the curve fitting process could still be used for error analysis but the inherent nonlinear oscillations of the structures caused the residuals to be much greater than in the sub-system tests.

Simulations of the experiments, using the experimentally established internal damping parameters were also conducted. These simulations are described in chapters two and three. The three different simulations conducted relate directly to three of the specimens tested. Direct comparisons are made between the experimental strain gauge data and the simulated strain gauge data generated from the simulations. Three comparisons are made between the experimental tests and the simulations: the modal frequencies; the increase in damping of the first mode due to nonlinear effects; and the form of dynamic coupling of the upper modes with the first mode.

7.2 Wire Braced Beam

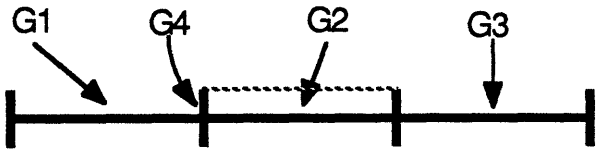

Schematic Wire Braced Beam, Beam 2B
Figure 7.11

Linear Tests:

The wire braced beam, Beam 2B (figure 7.11), can be divided into two sub-systems, one in which the thin plate is pulled tight, and one in which the thin plate has buckled. A structure representing the sub-system where the thin plate has buckled is created by removing the thin plate, Beam 2A (figure 7.12).

No structure was possible for the sub-system where the thin plate is pulled tight due to the length and flexibility of the thin plate.

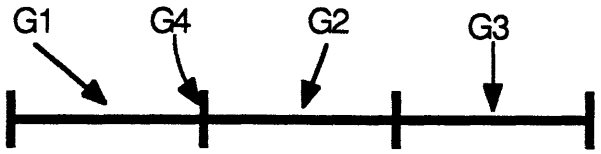

Schematic Beam, No Wire Bracing, Beam 2A
Figure 7.12

For the specimens where no thin plate was present, Beam 2A, the modal damping was found to coincide well with the experimentally determined data for aluminum in reference 4. The difference between this experiment and the previous experiments is that the damping data of the previous experiments was all obtained from the first mode of different specimens. The modal frequency was changed by altering the length and thickness of the specimens, which were long thin beams. These experiments used a single beam and measured the damping rates of all of its excited modes. The modal damping rates for the six valid low amplitude tests of the linear continuous beam, Beam 2A, are shown in figure 7.13 and table 7.1. The high amplitude tests caused large deflection effects to occur in the beam so the analysis was limited to low amplitude tests.

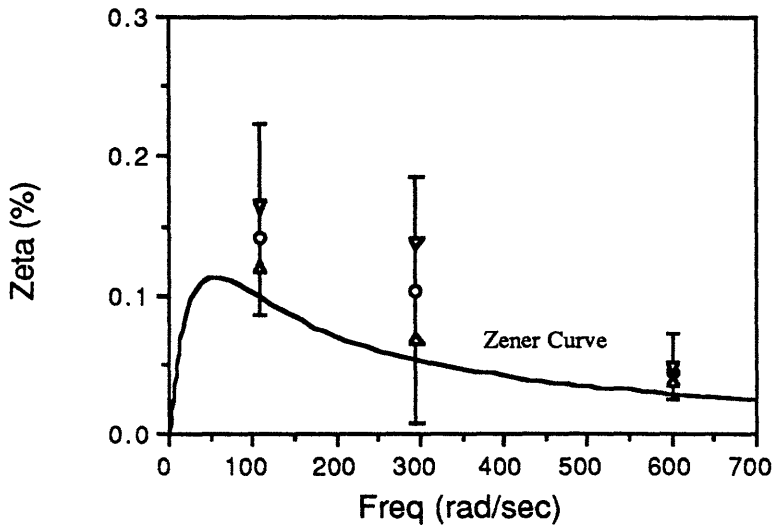

Fitted Damping vs Fitted Frequency
Continuous Unjointed Beam, Beam 2A, All Low Amplitude Tests
Figure 7.13

Table 7.1
Fitted Damping Parameters
Continuous Unjointed Beam, Beam 2A, All Tests

Specimen	Mode 1			Mode 2			Mode 3		
	Frq	Ave	St Dv	Frq	Ave	St Dv	Frq	Ave	St Dv
	r/s	ζ%	ζ%	r/s	ζ%	ζ%	r/s	ζ%	ζ%
Beam 2A	109	.144	.021	294	.105	.039	602	.040	.0072

The mean is indicated in figures by a circle and the standard deviation is indicated by a set of arrows. The maximum to minimum difference in data points, the bars at the ends of the lines, is approximately 0.1% zeta. The scatter in the data is primarily due to different tests of the same specimen showing slightly different damping values. A single test would have a standard deviation of approximately 0.01% zeta. The difference between the tests seems to depend on how level the specimen remained during the test. Some test specimens experienced a slow rotation which may have effected the damping measurement. The amplitude of the vibration of the mode appears to have had very little effect on the damping ratio. The mean amplitude of the fitted data is plotted against the fitted damping ratio and no clear pattern of amplitude dependence appears, figure 7.12.

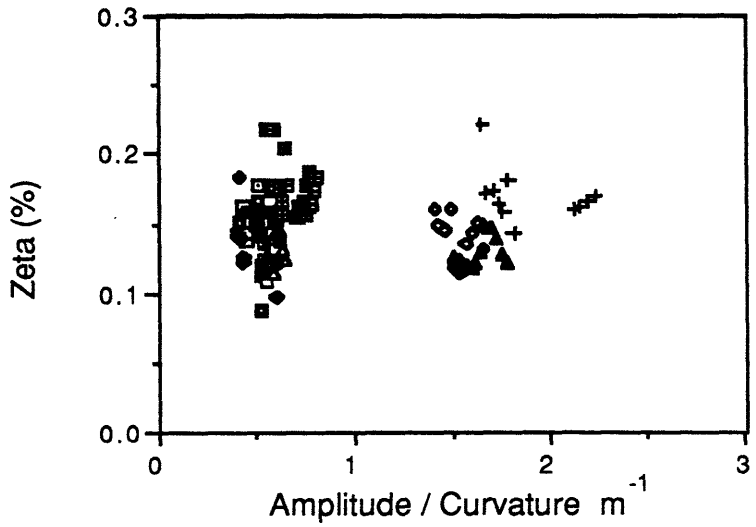

Fitted Damping vs Fitted Amplitude / Curvature
Continuous Unjointed Beam, Beam 2A, All Tests
Figure 7.14

As was discussed above the linear constituent system representing the second sub-system where the linking of the one third points is included could not be directly experimentally tested for sub-system modal damping ratios. Information on the damping ratios was inferred from a low amplitude test on the asymmetrically stiff joint where the short thin plate failed to buckle, (see section 7.3). The inferred information indicates that the thin plates attached to the uprights contribute less than 0.06% internal damping.

The modal damping information experimentally determined and shown in figure 7.13 shows that the modal damping rates of the modes are all very close to one another. This is due to the characteristic material damping, partially described by the Zener theory. The specimen used in these experiments, Beam 2A, had all of its modes to the right of the Zener curve and they tended to follow the Zener curve although about a factor of 1.5 times higher. This is described in more detail in reference 4. The right side of the Zener curve predicts a damping ratio roughly proportional to the inverse of the frequency. The damping rate of the modes are roughly the same but the modes above the fifth mode seem to have an increasing damping rate.

The internal material damping rates of the two linear sub-systems used in the analytic simulation are listed in table 7.2, (derived from the experiments with linear joints). The damping rates are the only property determined from the tests and used in the simulations. All other beam properties are determined directly from the specimen material properties and geometry. The modal frequencies from the simulations are, therefore, not exactly the same as in the experiments due to model inaccuracies and limitations.

Table 7.2
Wire Braced Beam, Beam 2B
Simulation Modal Frequencies and Assumed Damping Parameters

Sub-System	Mode 1			Mode 2			Mode 3			4→
	Frq	ζ%	DR	Frq	ζ%	DR	Frq	ζ%	DR	DR
	r/s		1/s	r/s		1/s	r/s		1/s	1/s
Flex Joint	109	.15	.16	292	.11	.32	607	.045	.27	.23
Stiff Joint	160	.18	.29	292	.11	.32	754	.036	.27	.23

Nonlinear Tests:

The nonlinear specimen, a continuous beam with a thin plate linking its one third points (figure 7.11), was tested and a typical trace of the strain gauge data is shown in figure 7.16. Significant coupling and beating between the modes of the structure is evident in the data and can be observed in the filtered data showing the individual modes, figures 7.17 and 7.18. The curve fitting routines were applied to the filtered data and the resulting damping data is shown in figure 7.15.

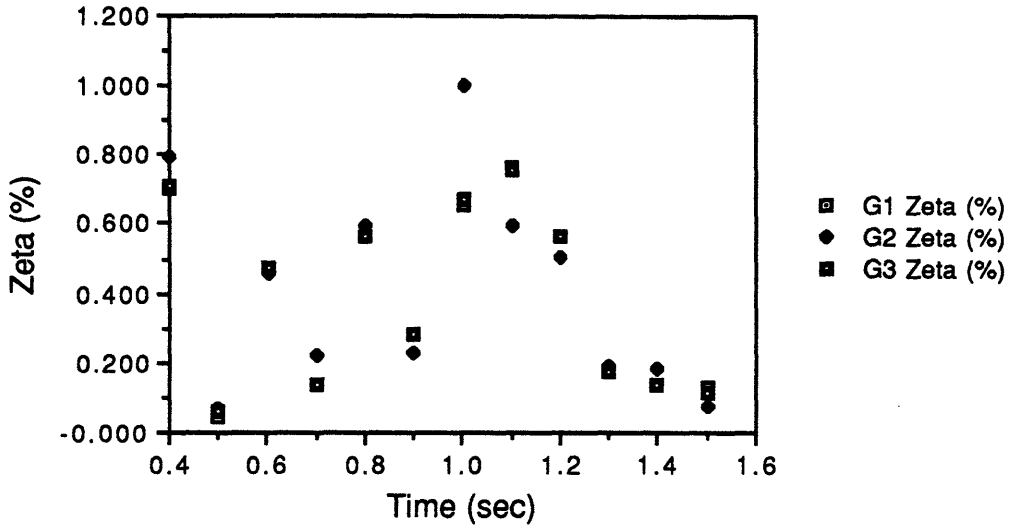

First Mode Fitted Damping Ratio vs Median Time
Wire Braced Beam, Beam 2B, Test AP2501
Figure 7.15

The scatter in the damping data is related to the modal beating seen in the data. The strain gauge (G2) located at the center of the center beam section exhibited a worse fit to the data than the outer strain gauges (G1 and G3). This was observed from the least squares residuals of the curve fits. As can be seen in figure 7.15, the resultant damping data was not effected but this indicates that something else is occurring at the center beam section.

The modal amplitudes and the experimentally determined internal damping rates, table 7.2, were used to generate a simulation of the structure and a simulated strain gauge output, figure 7.19. The frequency and damping rates of the experimental and simulated structures are listed in table 7.3.

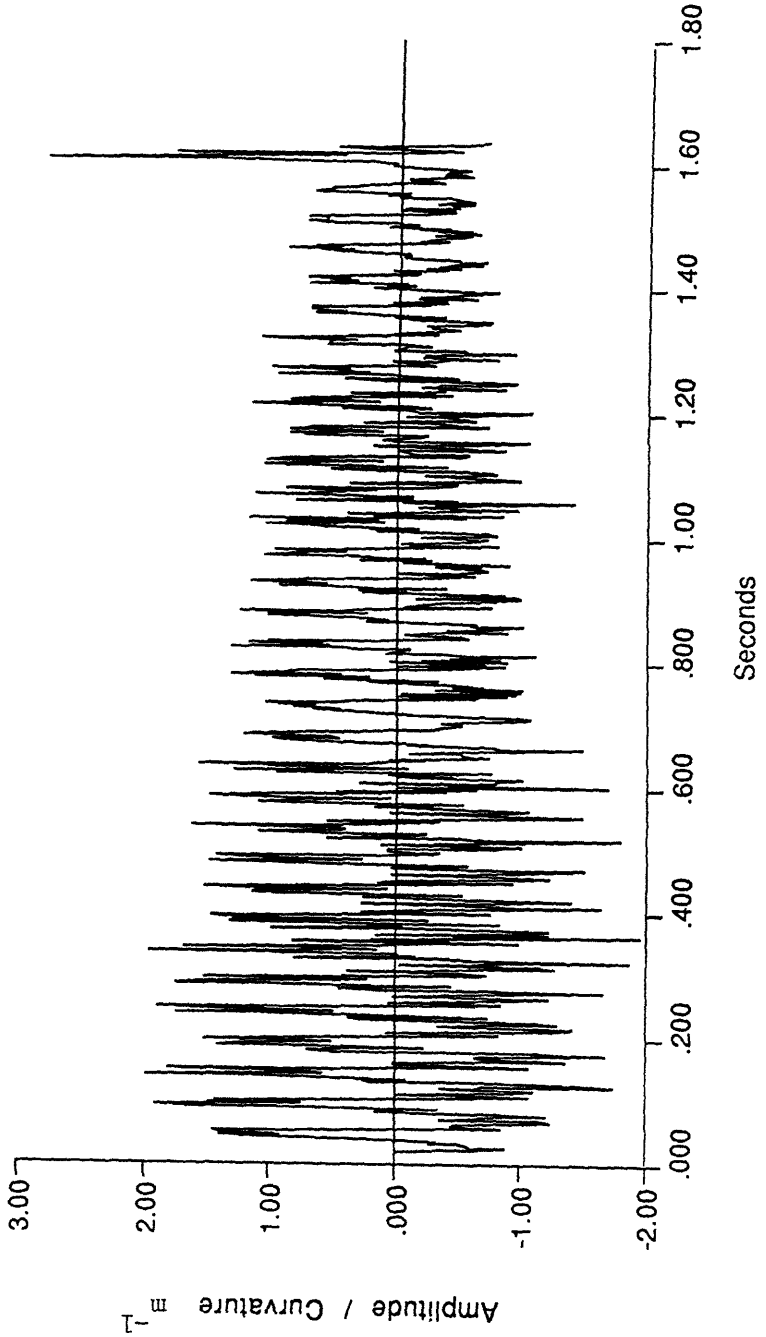

Experimental Strain Gauge Data, Amplitude / Curvature
Wire Braced Beam, Beam 2B, Test AP2501 Gauge 1
Figure 7.16

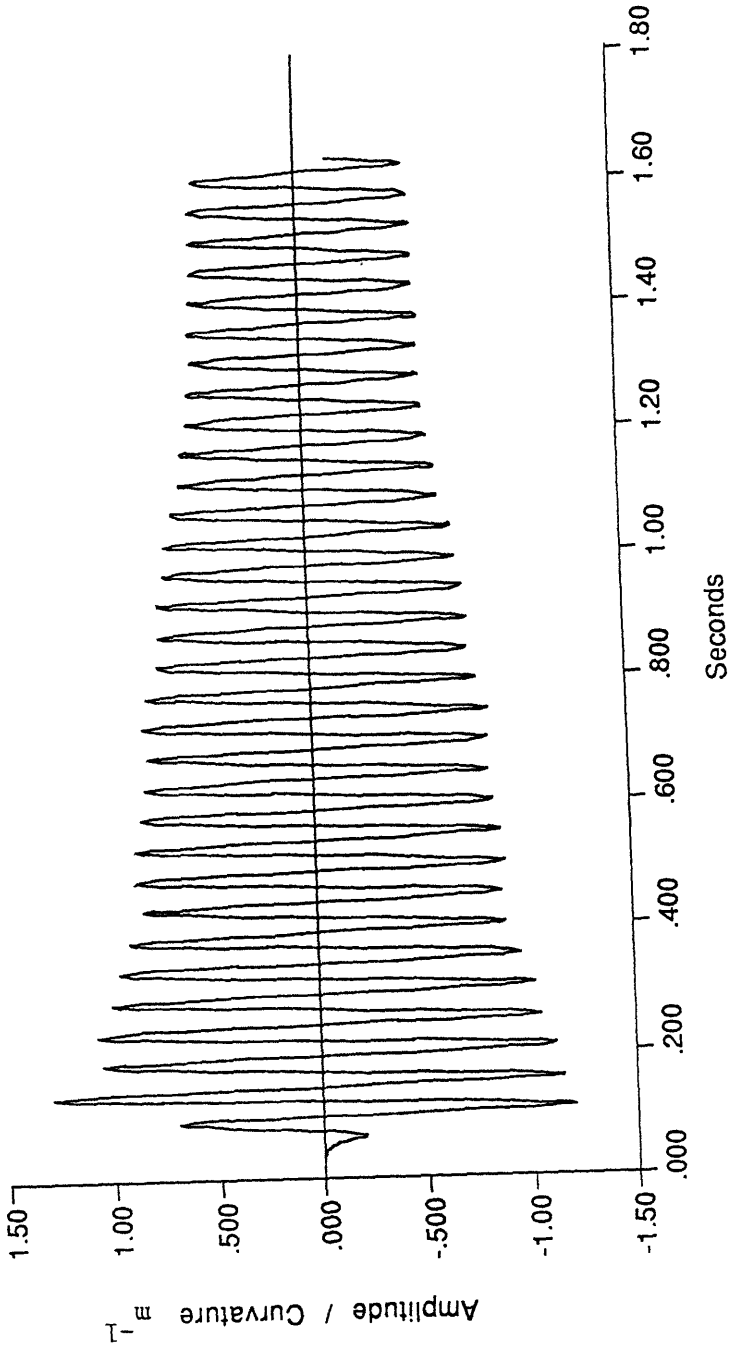

Mode 1 of Experimental Strain Gauge Data, Amplitude / Curvature
Filtered With Band-Pass Filter, Center = 22 Hz, Width = 10 Hz
Wire Braced Beam, Beam 2B, Test AP2501 Gauge 1
Figure 7.17

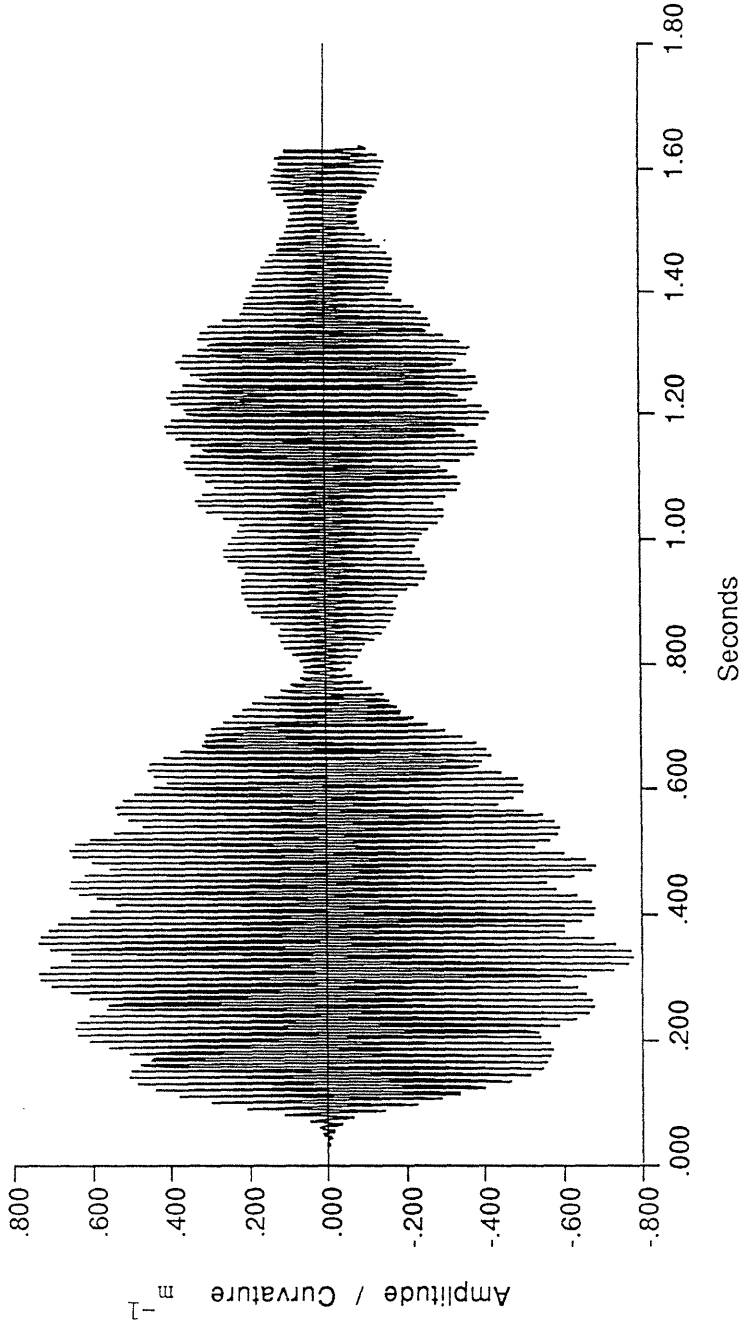

Mode 3 of Experimental Strain Gauge Data, Amplitude / Curvature
Filtered With Band-Pass Filter, Center = 103 Hz, Width = 10 Hz
Wire Braced Beam, Beam 2B, Test AP2501 Gauge 1
Figure 7.18

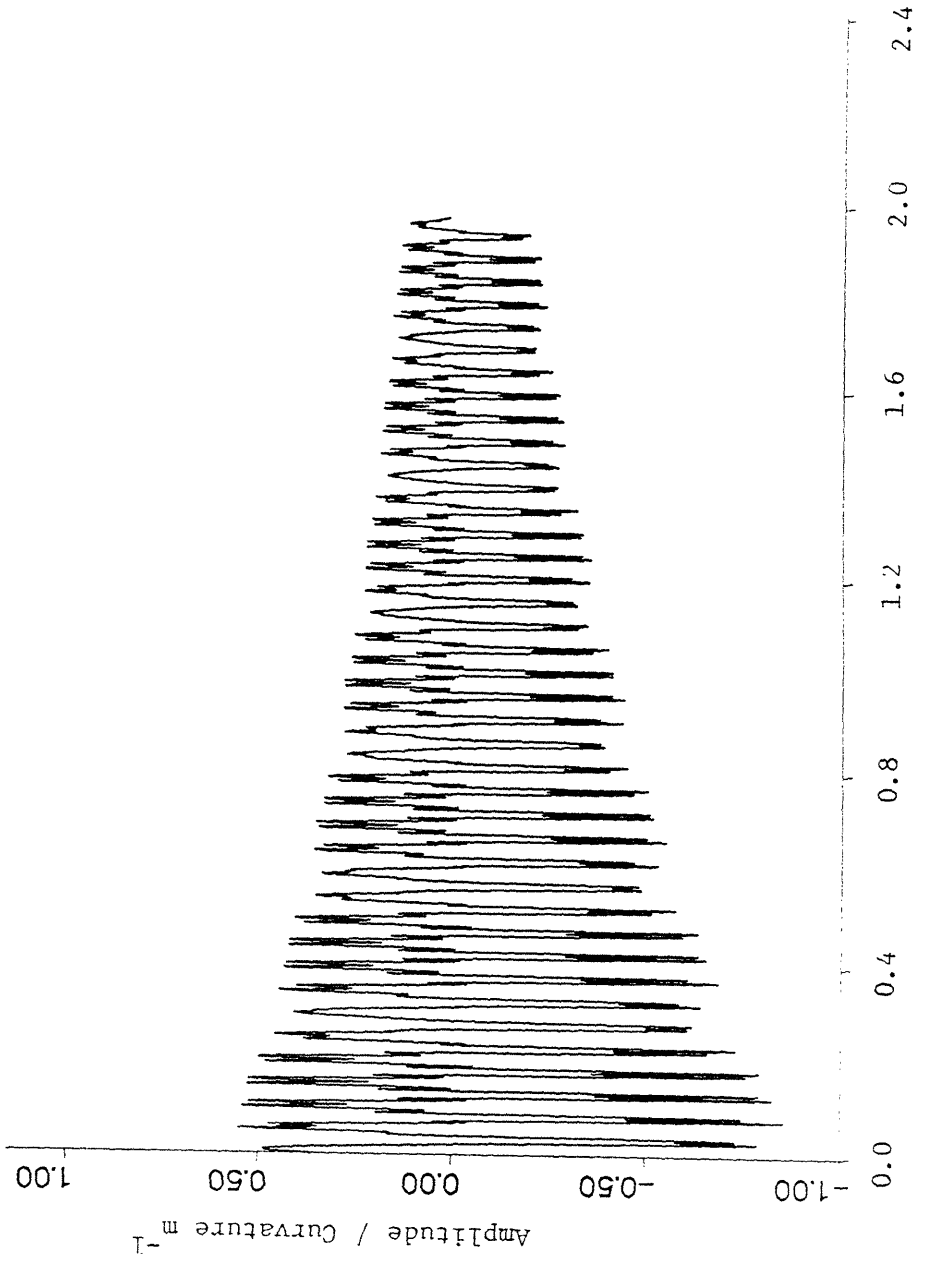

Simulated Strain Gauge Data, Amplitude / Curvature
Wire Braced Beam, Beam 2A, Gauge 1
Figure 7.19

Table 7.3
Wire Braced Beam
Experimental and Simulated Damping Parameters and Frequencies

Mode	Experiment			Simulation		
	Frq	Ave	St Dv	Frq	ζ%	DR
	r/s	ζ%	ζ%	r/s		1/s
Mode 1	129	.455	.2	134	.165	.34
Mode 2	261	—	—	292	—	—
Mode 3	647	—	—	680	—	—
Mode 4	979	—	—	905	—	—

The modal frequencies of the experimental beam were within five percent of those of the simulated beam. A damping ratio was established for the first mode only due to the beating nature of the other modes.

The damping rates of the upper modes of the wire braced structure are approximately the same or lower than the first mode's damping rate. As was established in chapter 5, when the damping rates of the coupled modes are the same or less than that of the primary mode, the increase in damping due to modal coupling was unclear since the simulations showed scattered results but indications were that little or no increased damping occurred and modal beating would be evident. The experimental tests show a marked increase in the first mode's damping rate (see figure 7.15) and significant beating of the modes. There is considerable scatter in the damping data because of the beating.

The experimental data, figures 7.16 to 7.18, show different coupling characteristics than the simulation, primarily a longer beat frequency and a more extensive coupling of all the symmetric modes. The beating frequency of the experiment is 9 rad. / sec. compared to the simulations 21 rad. / sec. Beating of the first mode is larger in the experiment than in the simulations, causing a 10% rise and fall in the first modes amplitude. The extent of modal coupling is also greater in the experiment than in the simulation. The simulation, figure 7.19, shows a coupling primarily with the third mode while the experiment indicates coupling with the upper modes to a much greater extent.

Two explanations for the difference in the coupling are postulated. They both involve unmodeled effects associated with the center beam section and the thin plate linking its ends. The strain gauge data from the strain gage

located at the center of this beam section (G2) indicates that something different is occurring at its position as compared to the outer strain gauges (G1 and G3). One possible explanation is related to the compressive loads applied to the center beam section of the specimen by the thin plate linking the uprights at the ends of the center beam section. The center beam section is actually serving as a beam column and the compressive loads may be causing the dynamics of the specimen to differ from the simulation where the compressive loads are ignored. The compressive loads on the center beam section have been estimated to be from 1/100th to 1/10th of the center beam's pinned-pinned column buckling load, depending on the amplitude of the particular test.

A second possibility comes from the observation that the thin plate linking the uprights is 12 inches long and in air exhibits translational vibrations excited by the structure's motion causing the plate to go slack then taught very quickly. The mass of the thin plate is quite low, it is 0.001 inches thick, and has been assumed to be negligible in the analysis as has its translational vibrations. It is possible that this assumption is incorrect and these vibrations may become large enough to influence the structures dynamics and cause modal coupling and internal damping of its own.

The modal damping of the specimen is hard to estimate for the higher modes but there are indications from the data that the damping rate does rise in the higher modes, ie; the damping ratio, zeta, levels off at a finite value rather than approaching zero as the Zener curve predicts. This is especially true of the contribution to the damping by the thin plates attached to the uprights. Assuming that the modal coupling is more extensive than expected and the internal damping rate of the upper modes is increasing it is not unreasonable that the first mode's damping ratio would rise 0.3% as it does in the experiments.

The design of this specimen was to encourage as much modal coupling as could be accomplished with a single continuous beam. This objective seems to have been satisfied. The increased damping observed in the specimen is most likely due to the modal coupling but some damping may be due to internal damping provided by the attached plate since no direct measurement of this was possible.

7.3 Asymmetrically Stiff Jointed Beam

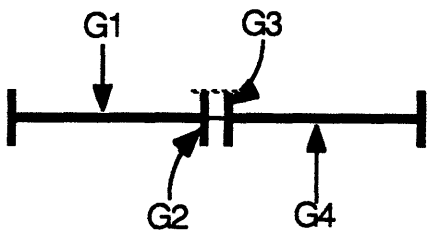

Schematic Asymmetrically Stiff Jointed Beam, Beam 3B
Figure 7.20

A second beam structure, Beam 3, was made to experimentally test jointed structures, the asymmetrically jointed beam and the dead-band jointed beam. The sub-systems of the two joint assemblies are the same so the experimentally determined internal damping rates are the same, (chapter 2). It was possible to test all of the sub-systems since the thin plate used in the joint could be made to not buckle at low amplitudes.

Linear Tests:

The asymmetrically stiff jointed beam is divided into two sub-systems, a flexible jointed beam and a stiff jointed beam. The flexible jointed beam is created by removing the thin plate attached to the uprights, figure 7.21, (see figure 6.9).

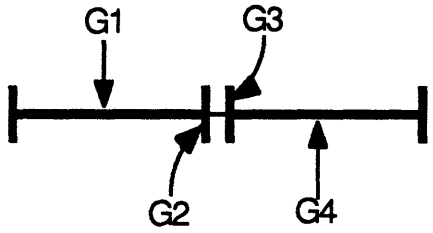

Schematic Flexible Jointed Beam, Beam 3A
Figure 7.21

The internal damping rates were determined for the flexible sub-system, Beam 3A, and are shown in figure 7.18 and table 7.4. The standard deviation of the first mode is up to 0.09% zeta for all five tests but the standard deviation for individual tests is still low, between 0.01% zeta and 0.06% zeta. The modal damping ratio and the standard deviation of the first asymmetric mode, with a

natural frequency near 600 radians per second, remains the same as in the unjointed beams. This illustrates that the joint flexures, the 0.02 inch thick plates glued and bolted to join the beam sections (see figure 6.9), contribute as much as 0.6% damping in the first mode and 0.2% damping in the third mode. Since the joint is located in the middle of the beam, asymmetric modes do not flex the joint and therefore are not affected by the joint damping.

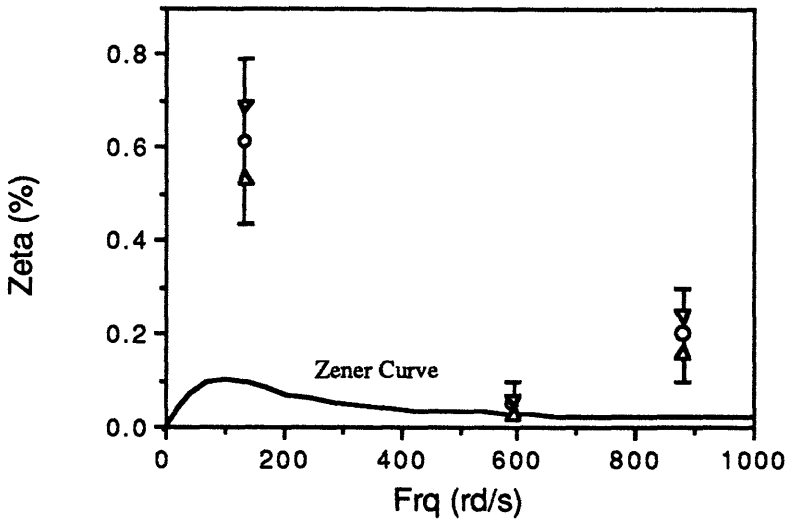

Fitted Damping Ratio vs Fitted Frequency
Jointed Beam, Beam 3A, All Tests
Figure 7.22

The internal damping rates were measured for the flexible sub-system, Beam 3A, and are shown in figure 7.22 and table 7.4. The standard deviation of the first mode is up to 0.09% zeta for all five tests but the standard deviation for individual tests is still low, between 0.01% zeta and 0.06% zeta. The modal damping ratio and the standard deviation of the first asymmetric mode, with a natural frequency near 600 radians per second, remains the same as in the unjointed beams. This illustrates that the joint flexures, the 0.02 inch thick plates glued and bolted to join the beam sections (see figure 6.9), contribute as much as 0.6% damping in the first mode and 0.1% damping in the third mode. Since the joint is located in the middle of the beam, asymmetric modes do not flex the joint and therefore are not affected by the joint damping.

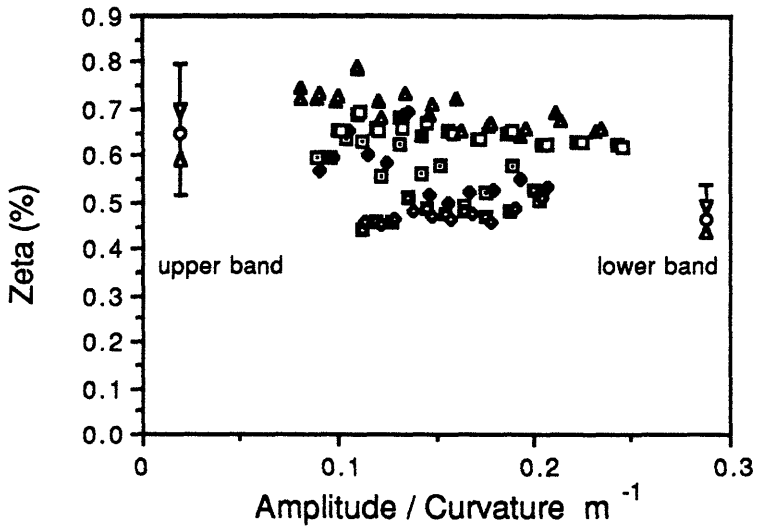

Fitted Damping Ratio vs Fitted Amplitude / Curvature
Jointed Beam, Beam 3A
Figure 7.23

As in the previous case, the amplitude of the vibration does not affect the damping rate in any consistent manner. The large variance of the symmetric modes is not caused by the specimen rotations because if it were the asymmetric mode data would exhibit the same scatter, which it does not. It is more likely that the joints themselves are changing their damping properties from test to test. The tests were not conducted on the same days and the specimens were disassembled and reassembled between some of the tests. As can be seen in figure 7.23, there are distinct bands of damping data. The specimen was assembled twice. The two bands of data correspond to the two specimen assemblies. It is apparent that different assemblies of the same joint can double the standard deviation of the structural damping data.

The individual assemblies of the joint can be associated with individual experiments. The lower band of data represent the first assembly and set of experiments performed on the specimen. The asymmetrically stiff jointed beam was tested with only the first joint assembly. The dead-band jointed beam was also tested primarily with the first assembly. Two tests of the dead-band jointed structure were conducted with the second assembly but these tests were an attempt to measure the internal damping of a sub-system of the structure by assembling the thin plates pulled very tight so that they would not go slack under low excitation. The results of these test were inconclusive partially due to

the changes in the joint damping illustrated in figure 7.23. Only the lower band of data is the pertinent internal damping data used in the analysis.

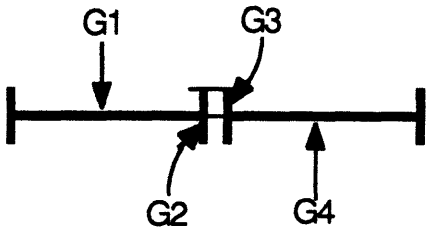

Schematic Stiff Jointed Beam
Figure 7.24

The stiff jointed sub-system, figure 7.24, of the asymmetrically stiff jointed and the dead-band jointed beam could be tested for modal damping ratios. In the case of the asymmetrically stiff and dead-band joints the thin plate was only 1/2 inch long and even though it was 0.001 inch thick, in some cases, where the loads were low, it could take the compressive loads applied to it. This phenomenon was more an error than an intended experiment. When the thin plate was bolted to the uprights, it would occasionally not be perfectly flat, slight ripples would appear. In the first tests of the asymmetrically stiff joint, the strain gauge at the joint indicated that the plate was not buckling as was expected. It was found that simply smoothing the plate with a thin rod solved the problem and the plate would buckle under very low compressive load. The data gathered during the tests where the plate did not buckle became very useful because they established the modal damping rates of the linear system including the plate. The internal damping rates of the linear system including the stiffened joint is shown in figure 7.25 and table 7.4.

The damping rates of the beam with the stiffened joint are not near as great as those of the beam without the thin plates attached to the joints, but approaches that of the unjointed beam, Beam 2A. Considering that the 0.02 inch thick plate joining the two beams together is still contributing to the damping of the joint, the damping data indicates that the thin plates bolted to the stand-offs contribute less than 0.06% internal damping to the system. The added stiffness of the joint prevents the internal damping of the 0.02 inch thick plate joining the beam sections from contributing more to the damping.

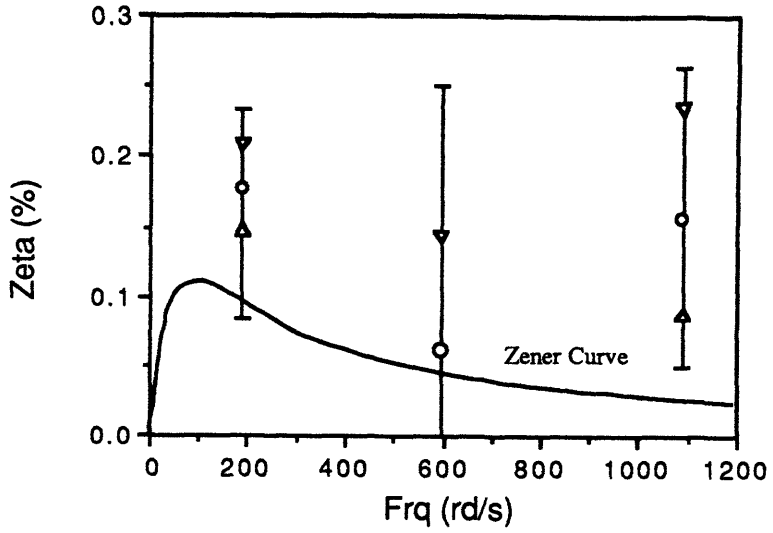

Fitted Damping Ratio vs Fitted Frequency
Stiffened Jointed Beam
Figure 7.25

The modal frequency and damping parameters determined from the linear beam tests are listed in table 7.4.

Table 7.4
Fitted Damping Parameters
Jointed Beam, Beam 3A

Specimen	Mode 1			Mode 2			Mode 3		
	Frq r/s	Ave ζ%	St Dv ζ%	Frq r/s	Ave ζ%	St Dv ζ%	Frq r/s	Ave ζ%	St Dv ζ%
Beam 3A all tests	134	.607	.092	595	.054	.01	880	.208	.04
Beam 3A upper band	134	.642	.068						
Beam 3A lower band	134	.474	.026	594	.053	.0036	879	.167	.029
Beam 3B stiff joint	192	.178	.04	595	.065	.08	1080	.157	.071

Nonlinear Tests:

The asymmetrically stiff jointed beam was tested and the resulting strain gauge data filtered and curve fit to determine the modal frequencies and

damping parameters. The results of the three consecutive tests are listed in table 7.5.

Table 7.5
Asymmetrically Stiff Jointed Beam, Beam 3B
Experimental Fitted Frequency and Damping Parameters

Joint	Test	Fitted Experimental Parameters			
		Ave Frq r/s	St Dv Frq r/s	ζ%	St Dv ζ%
Flexible	Test 1	134	.13	.456	.057
Stiff	Test 2	193	0.5	.178	.04
Asymmetric	Test 3	166	3.2	.572	.22

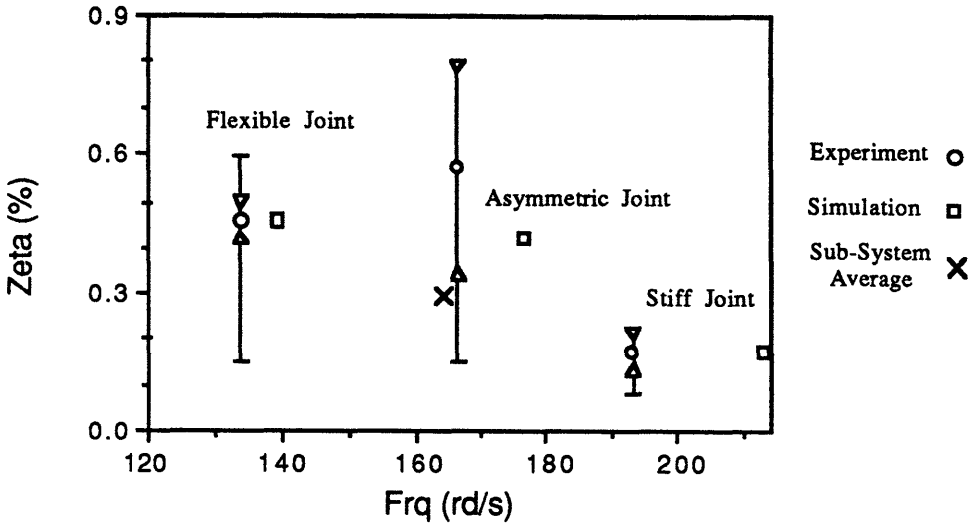

Fitted Damping Ratio vs Fitted Frequency
Asymmetrically Stiff Jointed Beam Tests
Figure 7.26

The frequency and damping data are shown in figure 7.26. In test 1, the off-set was so high that the joint remained linear throughout the test. This established the lower end of the frequency region and the damping ratio of the flexible sub-system. In test 2, as was discused earlier, the thin plate did not buckle, establishing the upper end of the frequency region and the damping

ratio of the stiff sub-system. Test 3, the asymmetrically stiff jointed beam, showed that the damping is greater than that expected from the component sub-system damping rates, indicating that damping due to modal coupling may be present. The larger scatter in the data is due to the beating present in the data. A comparison is also made between the experiment and a simulation of the structure.

The asymmetrically stiff jointed beam, specimen Beam 3B, is simulated by the asymmetrically stiff jointed simulation described in chapter 5 with the joint parameters set at K_N=.033 and K_S=26. The damping parameters and the resulting modal frequencies used in the simulation are listed in table 7.6. The simulated strain gauge data is shown in figure 7.27.

Table 7.6
Simulation Modal Frequencies and Assumed Damping Parameters
Asymmetrically Stiff Jointed Beam, Beam 3B

Sub-System	Mode 1			Mode 2			Mode 3		
	Frq	ζ%	DR	Frq	ζ%	DR	Frq	ζ%	DR
	r/s		1/s	r/s		1/s	r/s		1/s
Flex Joint	139	.47	.65	659	.05	.33	937	.17	1.59
Stiff Joint	213	.18	.38	659	.05	.33	1174	.16	1.90

The modal frequencies of the sub-systems compare well between experiment and simulation. The modal damping rates of the linear sub-systems were established from the experimental data shown in table 7.4. All other beam properties used in the simulations were obtained from the beam material properties and geometry. The internal damping of the joint is not proportional to the rest of the system but a proportional system is assumed so that individual modal damping rates could be assigned.

The simulation's frequency and damping data are listed with the experimental data in table 7.7 and shown in figure 7.26.

Table 7.7
Asymmetrically Stiff Jointed Beam, Beam 3B
Experimental and Simulated Frequency and Damping Parameters

Test	Experimental and Simulated Parameters		
	Ave	ζ%	DR
	Frq r/s		1/s
Simulation	176	.42	.74
Test 3	166	.57	.95

The modal frequencies of the simulation are similar but are consistently higher than those of the experiment. This is most likely due to the joint assembly which allows some flexibility due to its fasteners which is not modeled in the simulation. The first mode damping of the experiment is generally higher than the simulated damping value but within the standard deviation of the measurement. The large standard deviation in the experimental damping data indicates that the measurement is not accurate enough to precisely measure the damping due to modal coupling but within the accuracy of the measurements, do agree with the simulation.

Other characteristics of the oscillations can be identified correlating the nature of the modal coupling of the structure. The simulated strain gauge output is shown in figure 7.27. The experimental data is also shown in figure 7.27. Besides the obvious similarities in the signal traces the individual modal components of the first three modes are shown in figures 7.28 to 7.30. The modal components of the experimental data were created by filtering the data. The primary relationship between the two systems is in the third mode, in which they both exhibit the same beating phenomenon. Similar beating is observable in the first modes, a beating frequency of 5.9 rad. / sec. in the experiment and 4.0 rad./ sec. in the simulation.

The beating is not as sharp in the experiment as it is in the simulation. This is probably due to the nonlinear joints in the experiments not acting as perfectly discontinuous piecewise linear joints, as is assumed in the simulation. The second mode is not effected by the joint and shows the same exponential decay in both the experiment and the simulation. The correlation between the experimental test and the simulation is not exact but it is clear that the same modal coupling is occurring.

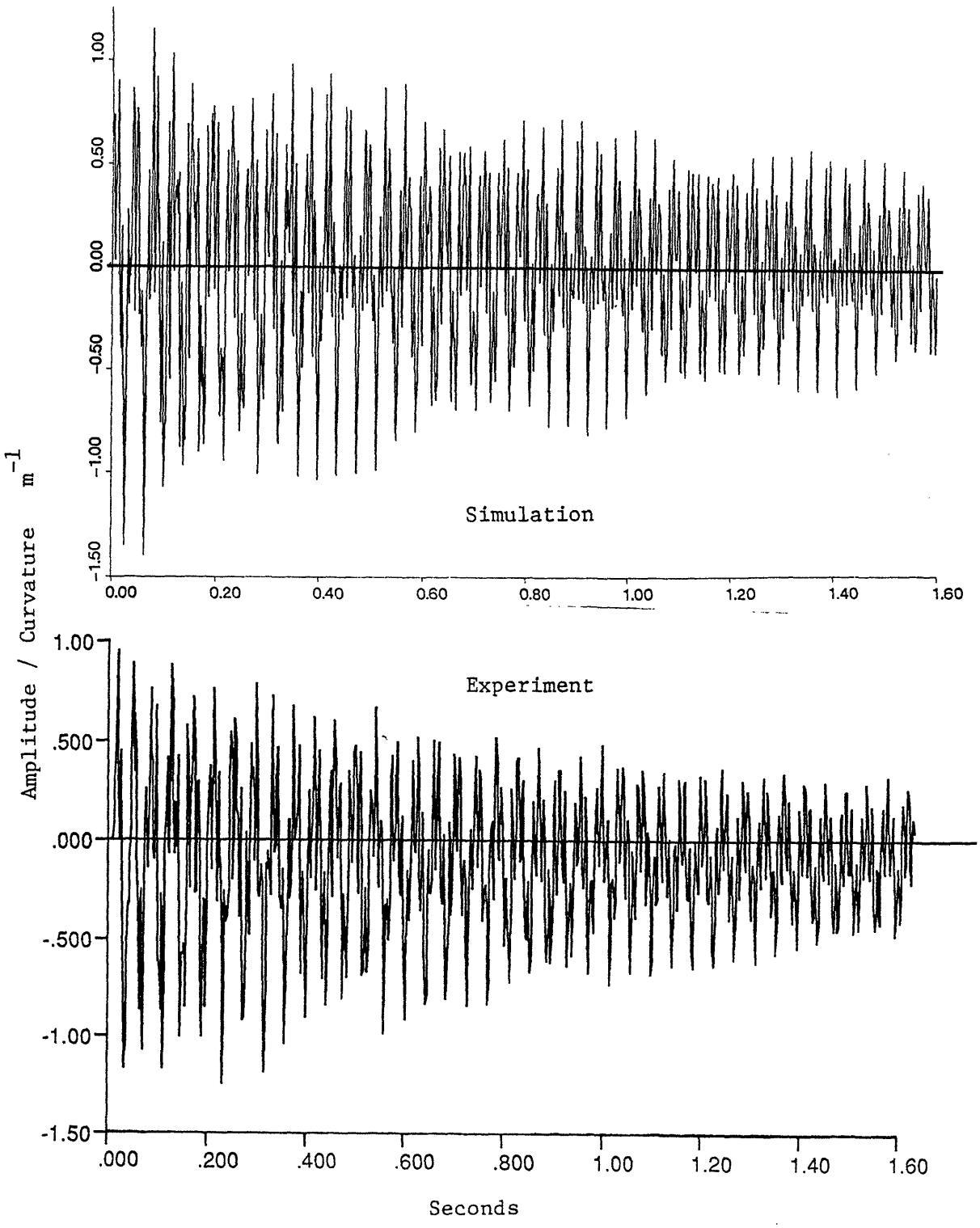

Experiment and Simulation of Asymmetrically Stiff Jointed Beam
Strain Gauge Data, Amplitude / Curvature, All Modes
Figure 7.27

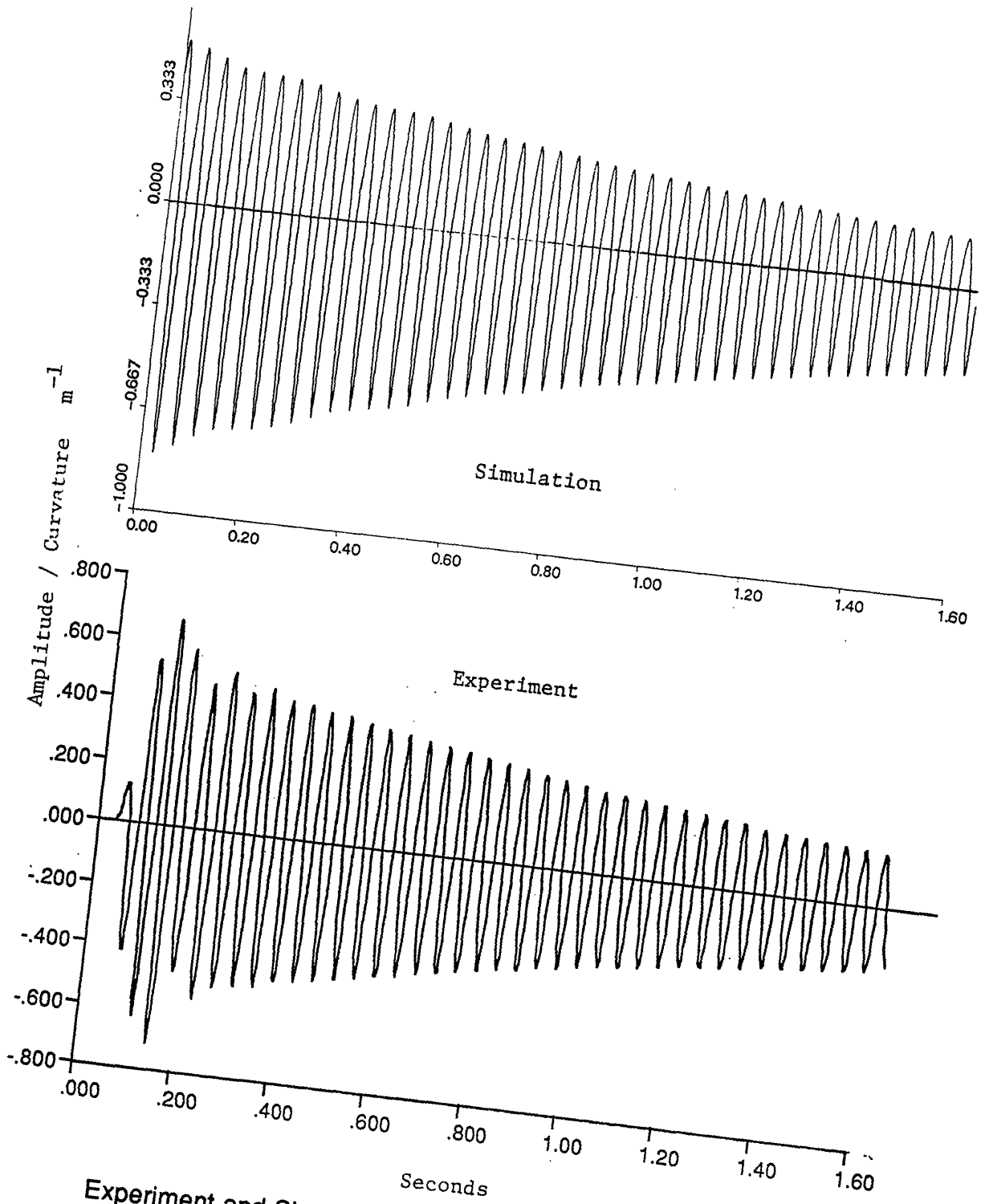

Experiment and Simulation of Asymmetrically Stiff Jointed Beam
Strain Gauge Data, Amplitude / Curvature, Mode 1
Figure 7.28

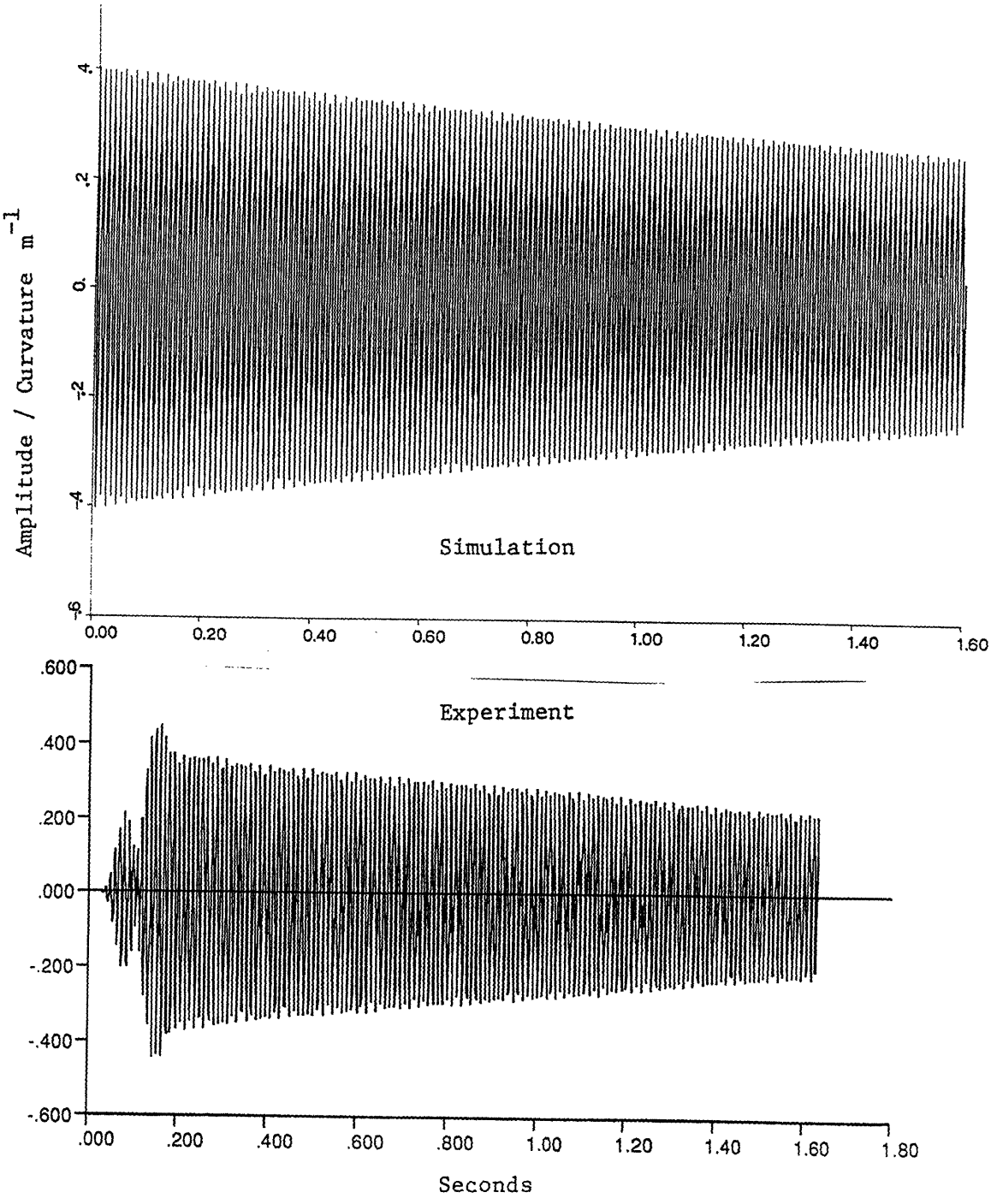

Experiment and Simulation of Asymmetrically Stiff Jointed Beam
Strain Gauge Data, Amplitude / Curvature, Mode 2
Figure 7.29

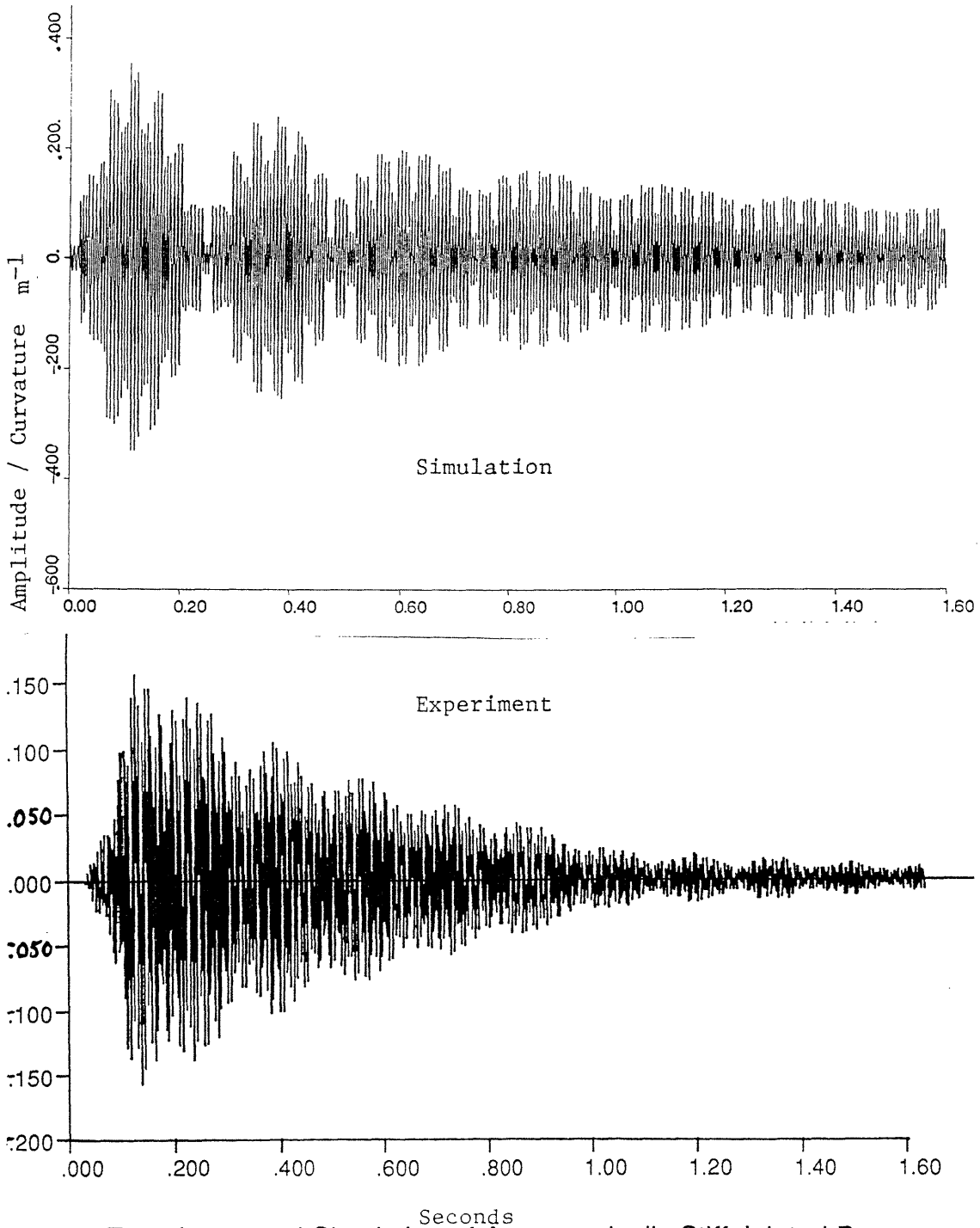

Experiment and Simulation of Asymmetrically Stiff Jointed Beam
Strain Gauge Data, Amplitude / Curvature, Mode 3
Figure 7.30

7.4 Dead-Band Jointed Beam

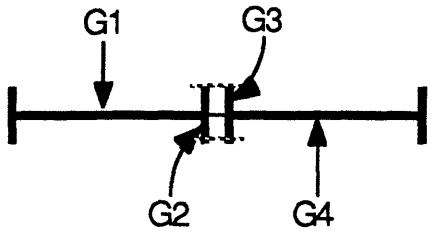

Schematic Dead-Band Jointed Beam
Figure 7.31

A beam structure, Beam 3, was made to be a dead-band jointed beam by adding another thin plate onto the other side of the joint and allowing a small amount of free-play in the joint, figure 7.31 (see figure 6.10).

Linear Tests:

The linear jointed sub-systems of the dead-band jointed beam are the same as the asymmetrically stiff jointed beam. The measured and assumed damping ratios of the asymmetrically stiff jointed beam are also used in this analysis, table 7.6.

Nonlinear Tests:

The dead band joint presented an amplitude dependent nonlinear joint. Several tests were conducted to establish the damping ratio as a function of the amplitude of the vibration. A typical strain gauge data trace is shown in figure 7.32. The amplitude of vibration of the structure was varied by adjusting the launch platform configuration. The results of the fitted data of all of the pertinent tests are presented in figure 7.33. As can be seen there is an increase in damping as the vibration amplitude decreases. There are two reasons for this behavior, the relative damping of the constituent sub-systems and the additional damping due to modal coupling.

As the amplitude of the dead-band jointed beam's vibration grows very large it is expected that the damping rate of the structure would approach that of the stiff jointed beam, table 7.5. This is because the dead-band joint is pulling the thin plate tight over more and more of the cycle as the vibration amplitude increases, therefore, the stiff jointed sub-system dominates the damping of the

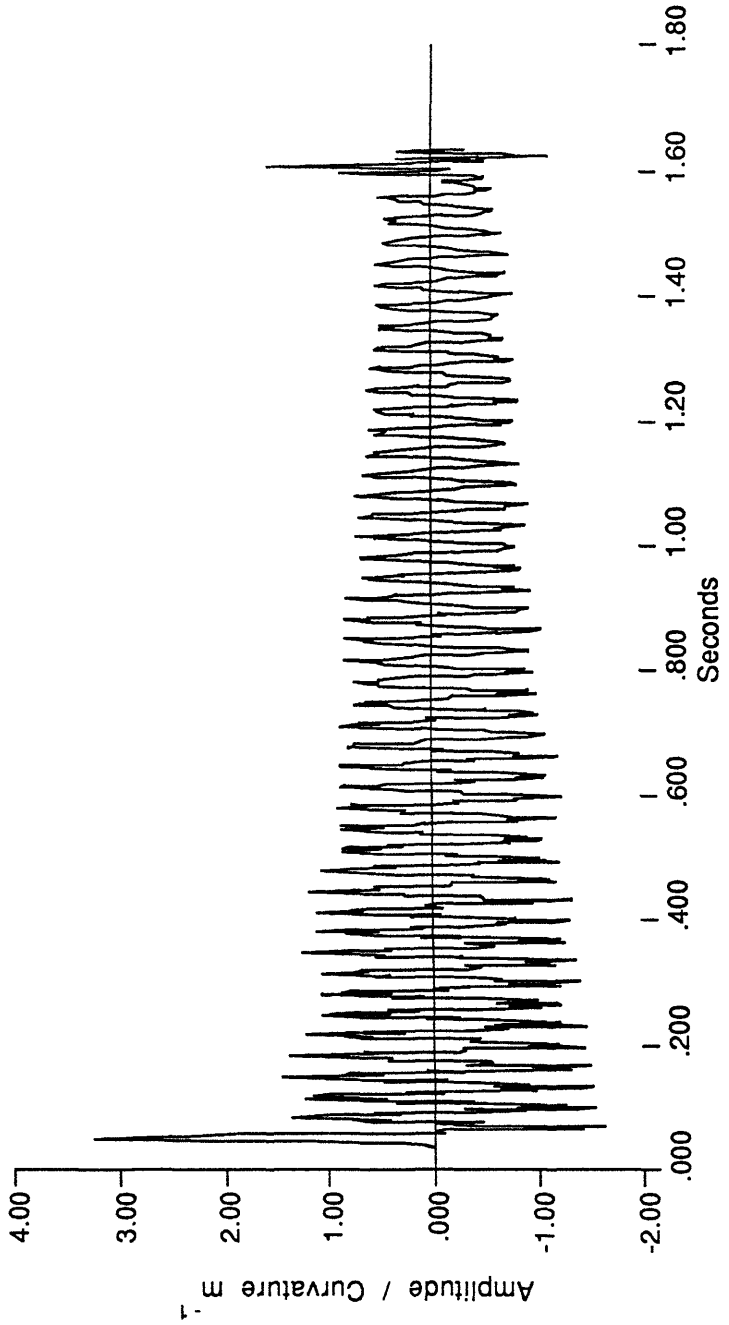

Experimental Strain Gauge Data of Dead-Band Jointed Beam
Amplitude / Curvature vs Time
Figure 7.32

system. As can be seen in figure 7.33, as the vibration amplitude of the tests increase the fitted damping data does approach the stiff jointed beams damping ratio. The opposite is also true, as the beam's vibration amplitude decreases, its fitted damping ratio increases. At the limit where the vibration amplitude drops to a point where the joint stays in its center linear region (see chapter 2), the damping of the system approaches the damping ratio of the flexible sub-system. Where the vibration amplitude is very low there are many tests because it was difficult getting the vibration amplitude as low as was desired. There was much scatter in the data in this amplitude region but it is evident that the damping ratio of the dead-band jointed beam is exceeding that of the flexible jointed sub-system.

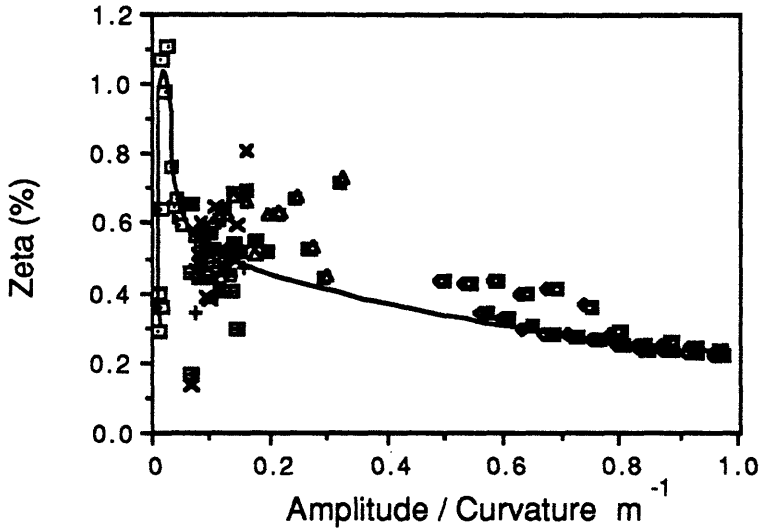

Fitted Damping Ratio vs Fitted Amplitude / Curvature
Dead-Band Jointed Beam, All Tests
Figure 7.33

The second cause of increasing damping at the lower vibration amplitudes is due to modal coupling caused by the dead-band joint. As was discussed in chapter 5, section 5.7, the dead-band beam simulation showed that the effect of the dead-band joint was to cause an increasing contribution to damping as the modal vibration amplitude decreased, (see figures 5.16 through 5.17). The simulation showed an almost linear decay rather than an exponential decay. The simulation also predicted that the increase in damping

due to modal coupling would quickly drop to zero as the vibration amplitude of the first mode dropped below the dead-band gap dimension.

To observe the damping due to modal coupling the experimental specimen was lofted with very low modal excitation. Several attempts at a low enough vibration amplitude were made. Most of the test's vibration amplitudes were too high to observe the drop in damping but one test did achieve an especially low vibration amplitude. The damping information of this test is shown in figure 7.34.

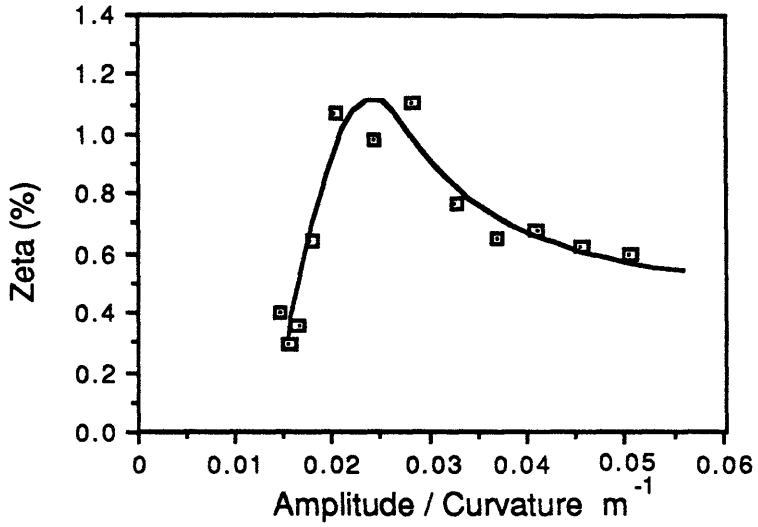

Dead-Band Jointed Beam, Test MY270701
Fitted Damping Ratio vs Fitted Amplitude / Curvature
Figure 7.34

The damping does decrease at very low vibration amplitude as predicted by the simulation. This test followed those of the asymmetrically stiff jointed beam and the damping ratio of the flexible sub-system determined in that analysis agrees well with the damping observed at low vibration amplitude, figure 7.34. The drop is approximately 0.6% which correlates well with figure 5.18 considering that the simulation assumes very high damping in the upper modes which is not the case in the experiment.

Figure 7.33 shows the first mode damping data versus the modal vibration amplitude for all of the tests conducted on the dead-band jointed beam, Beam 3C. The curve shows a continuous rise in damping as the modal vibration amplitude decreases over a wide range of amplitudes. The scatter in

the data is high, especially at the low vibration amplitudes and may indicate that the rapid rise and fall of the damping data in figure 7.34 is attributable to scatter in the data. This is not believed to be the case, however, for three reasons. First, the vibration amplitude data of the low amplitude test shows a linear decay to a point where the rate of decay quickly changes to a lower value. This matches the simulation's decay pattern very well, figures 5.17 and 7.35. Second, the least squares residuals of the curve fitting routine, SSQ, are quite low indicating that the curve fitting routine is working well, figure 7.36. Third, the peak damping of the specimen is greater than would be expected with just linear damping, experimentally determined in tests on specimen Beam 3A, table 7.4 and 7.5.

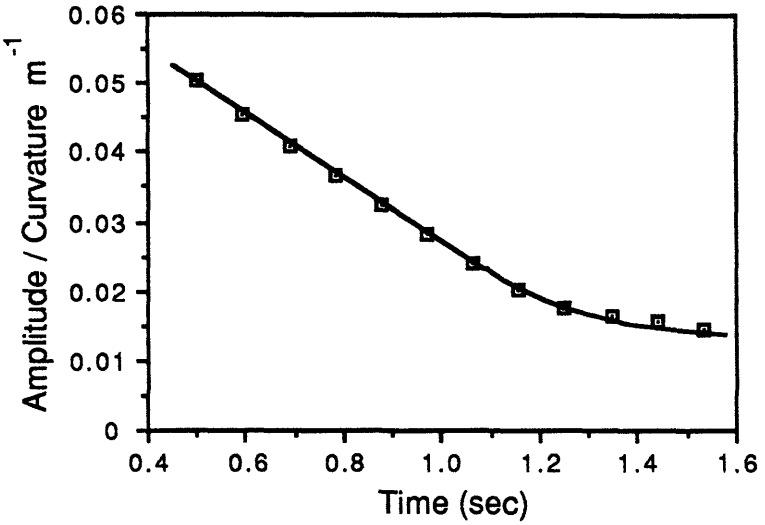

Dead-Band Jointed Beam, Test MY270701
Fitted Amplitude / Curvature vs Median Time
Figure 7.35

A set of experiments, derived from the specimens tested above, were designed to increase the complexity and the modal coupling over the previously tested specimens. This was done by increasing the number of joints or wires in the structure and by varying the orientation and parameters of the joints. The general results of these tests were that the new specimens performed in the same general manner as the specimens described above. The modal coupling, in general, was more extensive and the dynamics of the structures became more complex. The effective damping generally increased as the modal

coupling increased. No analytical analysis was performed due to the complexity of the structures but it appears that the general rules developed in this analysis hold for more complex structures.

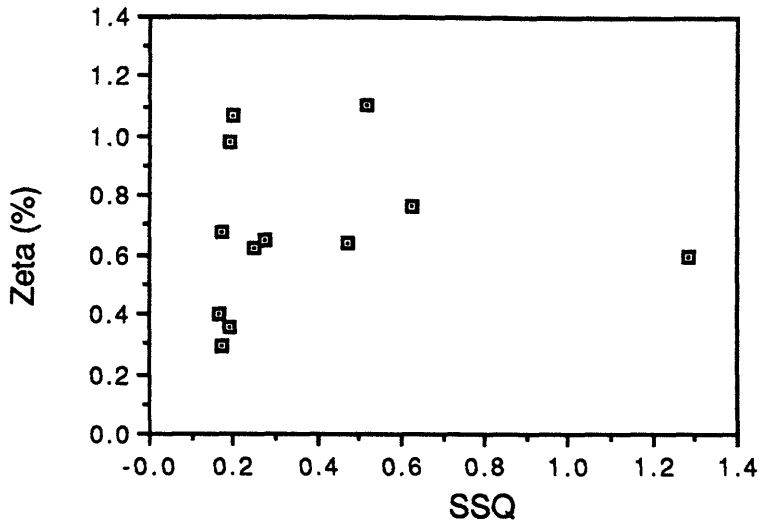

Dead-Band Jointed Beam, Test MY270701
Fitted Damping Ratio vs Least Squares Residuals
Figure 7.36

7.5 Summary

The experimental results and the correlation of the experiments and the analytical simulations was presented in this chapter. Both correlation of modal coupling dynamics and the damping due to the modal coupling is observed. The experimental wire braced structure exhibited unmodeled dynamics and a more extensive coupling of the modes than predicted and it also exhibited a increase in effective damping. The asymmetrically stiff jointed beams and the dead-band jointed beams showed good correlation with theory. In the case of both the asymmetrically stiff jointed beam and the dead-band jointed beam the internal damping and the experimental error in the calculation of the effective modal damping obscured the measurement of damping due to modal coupling. Both experimental beams did show damping due to modal coupling even with relatively high scatter in the measurement.

Chapter 8

Conclusions and Recommendations

8.0 Conclusions

A analytical model of continuous engineering beams linked by piecewise linear rotational spring joints was developed. The beam equations included strain rate or strain velocity damping and the joints included rotational rate damping. The piecewise linear nature of the joints allowed the solution of the equations with the use of linear sub-systems. A special condition of proportional damping was used to separate the individual modes of the sub-systems into individual equations allowing the selection of independent modal damping rates. The modal energy of the structure and the transfer functions between sub-systems were also developed.

Three analytical models of piecewise linear systems were analyzed:

- A asymmetrically stiff jointed beam,
- A wire braced beam,
- A dead-band jointed beam.

The computational technique developed was useful in analyzing damping due to modal coupling because of its implicit incorporation of an infinite number of modes. Seven modes of the analytic models were explicitly calculated and found to be sufficient. The relative increase in damping due to modal coupling was found to be a function of the difference in the modal damping rates of the primary mode in motion and the damping rates of the modes being coupled. When the coupled modes have a higher damping rate than the primary mode then the effective damping rate of the primary mode would increase approaching an asymptotic limit. The asymptotic limit indicates that, given a set of structural parameters, there is a maximum increase in damping due to modal coupling. When the damping rate of the coupled modes was less than the damping rate of the primary mode then the primary mode and the coupled modes would start a beating phenomenon where energy is transferred back and forth between the modes. Damping effects were unclear but the onset of large continuous beating of the modes is evident.

It was also shown that the increase in damping due to modal coupling was a function of the degree of nonlinearity of the joints. It was found that the

joints must be significantly nonlinear before any damping due to modal coupling was evident. The nature of the models used in the analysis allowed the estimation of the maximum damping due to modal coupling by the calculation of a single mode. This simplified the analysis by estimating the maximum amount of damping due to modal coupling, the asymptotic limit of the difference in the modal damping rates, by the inclusion of only a single mode in the model.

The estimation of modal coupling and the associated damping can be extended to finite element models of sufficient order where the nonlinearities are modeled as piecewise linear. The technique of estimating the maximum damping the coupling can provide will be useful in determining whether damping due to modal coupling need be incorporated in the analysis or advocated as a damping enhancement.

An experiment was performed on specimens resembling those in the analysis. The specimens were launched in a vacuum chamber where zero-g and the vacuum of space is simulated for approximately 1.75 seconds. Material damping of the specimens was measured and compared well with other theoretical and experimental analysis. Nonlinear joints were added to the specimens and the changes in the dynamics and the effective damping were observed. Coupling phenomenon and damping phenomenon similar to that which occurred in the simulations was observed.

The experimental technique of lofting a structure in a vacuum has proven to be successful in isolating the structure from all environmental and gravitational effects. This is limited to short duration tests and fragile structures can be tested only once, but it has provided damping data on a wide variety of structures with damping ratios as low as 0.03%. Small, high frequency structures are best suited for this type of testing. The MIT/ASTROVAC can accommodate structures up to three meters long which can be lofted for up to 1.75 seconds of free-fall.

The models used in this investigation to examine damping due to modal coupling are relatively simple compared to the space structures being considered but some general rules of thumb can be established which may, with some careful consideration of the limits of this analysis, be applied to more complex structures.

1) Damping due to modal coupling is fairly small in structures even where the nonlinearities dominate the dynamics of the structure. If the internal

damping of the primary modes of the system is high then damping due to modal coupling will most likely be small in comparison. The internal damping of the primary modes of the system should be small for damping due to modal coupling to be important.

2) The structural nonlinearities of the system must cause sufficient coupling of the modes to induce damping. The structures examined in this analysis show that little damping is induced until the nonlinear joint significantly affects the structure. In order to not violate condition one, the structural nonlinearities are required to induce little or no hysteretic damping of their own. The nonlinearities should be significant and non-hysteretic for damping due to modal coupling to be important.

3) The relative modal time rates of decay have proven to be important in whether or not the damping due to modal coupling can occur. If the primary mode of vibration has a comparable or higher time rate of decay than the modes to which it couples, then indications are that no increase in damping will occur. The modal coupling will cause beating of the coupled modes with similar but opposite beating in the primary mode. When the primary mode has a lower time rate of decay than the coupled modes then the damping due to modal coupling becomes apparent and the modal beating caused by the coupling becomes a steady state oscillation. The time rate of decay of the coupled modes should be greater than that of the primary mode for damping due to modal coupling to occur.

8.1 Recommendations

Recommendations for future research center around the expansion of the analysis to forced response and more complex structures. The analysis in this paper used free decay of the structure to measure its damping. The technique can be extended to that of forced response. The type of analysis presented in this paper should provide useful information on the coupling and effective damping of forced nonlinear structures.

This paper has used continuous engineering beams in order to avoid the possibility of trapping energy within modes due to limitations of other analytical model's degrees of freedom. The technique of separating the structure into piecewise linear sub-systems can be extended to more complex finite element models if sufficient degrees of freedom are included. Complex structures such

as trusses afford the opportunity to couple, via nonlinear joints of the structure, the global motions and the internal motions of the truss. For example, the global motions of a truss typically involve the bending of the complete truss where the individual beam members primarily undergo extension and compression. Internal motions involve bending of the individual beams members. It is more difficult to enhance the damping of individual beams undergoing extension and compression than those undergoing bending. It may be possible to enhance the damping of a truss structure by allowing the joints in the structure to couple the global and internal modes and by constructing the beams to have high bending damping. The energy of the global modes of the truss structure will thus be transferred to the internal modes where it will be dissipated.

References

1 Ashley, Holt. "On Passive Damping Mechanisms in Large Space Structures." AIAA 23 Annual Structures and Structural Dynamics and Materials Conference. AIAA Paper No. 82-0639 (1982).

2 Trudell, R.W., R.C. Curley, and L.C. Rogers. "Passive Damping in Large Precision Space Structures." AIAA/ASME/ASCE/AHS 21st Structures, Structural Dynamics and Materials Conference. 80-0677: pp.124-136 (1980)

3 Nurre, G.S., R.S. Ryan, H.N. Schofield, and J.L. Sims. "Dynamics and Control of Large Space Structures." Journal of Guidance. Vol. 7, No. 5: pp. 514-526 (1982).

4 Ungar, E.E. "The Status of Engineering Knowledge Concerning the Damping of Built-Up Structures." Journal of Sound and Vibration. Vol. 26, No. 1: pp. 141-154 (1973).

5 Crandall, S.H. "The Role of Damping in Vibration Theory." Journal of Sound and Vibration. Vol. 11, No. 1: pp. 3-18 (1970).

6 Rabinowicz, E. FRICTION AND WEAR OF MATERIALS, John Wiley and Sons, New York: pp. 24 and 232-233 (1965).

7 Gaul, L. "Wave Transmission and Energy Dissipation at Structural and Machine Joints." Journal of Vibration, Acoustics, Stress, and Reliability in Design. Vol.105: pp. 489-496 (1983).

8 Wada, B.K., C.P. Kuo, and R.J. Glaser. "Extension of Ground-Bassed Testing for Large Space Systems." AIAA 26 Annual Structures and Structural Dynamics and Materials Conference. AIAA Paper No. 85-0757: pp. 477-483 (1985).

9 Crawley, Edward F., George L. Sarver, and David G. Mohr. "Experimental Measurement of Passive Material and Structural Damping for Flexible Space Structures." Acta Astronautica, Vol. 10, No. 5-6: pp. 381-393 (1983).

10 Marchetti, M., F. Morganti, L. Mucciante, and A.D. Novellino. "Influence of the Lamination and of Some Environmental Effects on Damping Characteristics of Advanced Composites for Space Structures." 35th Congress of the International Astronautical Federation IAF-84-405 (1984)

11 Scanlan, R.H. "Linear Damping Models and Causality in Vibrations." Journal of Sound and Vibration. Vol. 13, No. 4: pp. 499-509 (1970).

12 Naylor, V.D. "Some Fallacies in Modern Damping Theory." Journal of Sound and Vibration. Vol 11, No. 2: pp. 278-280 (1970).

13 Beards, C.F. and J.L. Williams. "The Damping of Structural Vibration by Rotational Slip in Joints." Journal of Sound and Vibration. Vol. 53, No. 3: pp. 333-340 (1977).

14 Rosenberg R.M. and Cheng-Ching Chi. "On Damped Non-Linear Dynamic Systems with Many Degrees of Freedom." International Journal of Non-Linear Mechanics. Vol. 20, No. 5/6: pp. 371-384 (1985).

15 Beucke, Karl E. and James M. Kelly. "Equivalent Linearizations for Practical Hysteretic Systems." International Journal of Non-Linear Mechanics. Vol. 20 , No. 4: pp. 211-238 (1985).

16 Thompson, J.M.T. and L.N. Virgin. "Predicting a Jump to Resonance Using Transient Maps and Beats." International Journal of Non-Linear Mechanics. Vol. 21, No. 3: pp. 205-216 (1986).

17 Pian, T.H. "Structural Damping of a Simple Built-Up Beam With Riveted Joints in Bending." Journal of Applied Mechanics. Vol. 24, No. 1: pp. 35-38 (1957).

18 Williams, D. "Method of Damping Out Bending Vibrations of Beam-Like Structures by Dry (or Coulomb) Friction." Journal of Mechanical Engineering Science. Vol. 2, No. 2: pp. 77-87 (1960).

19 Tait, R.J. and J.B. Haddow. "Multiple Scales Analysis of pointing Effect for Torsional Oscillator with Neo-Hookean Spring." International Journal of Non-Linear Mechanics. Vol. 21, No. 2: pp. 157-164 (1986).

20 Moon, Francis C. and Steven W. Shaw. "Chaotic Vibrations of a Beam with Non-Linear Boundary Conditions." International Journal of Non-Linear Mechanics. Vol. 18, No. 6: pp. 465-477 (1983).

21 Szemplinska-Stupnicka, W. and J. Bajkowski. "Multi-Harmonic Response in the Regions of Instability of Harmonic Solution in Multi-Degree-of-Freedom Non-Linear Systems." International Journal of Non-Linear Mechanics. Vol. 15: pp. 1-11 (1980).

22 Srinivasan, A.V. and D.G. Cutts. "Dry Friction Damping Mechanisms in Engine Blades, " Paper, United Technologies Research Center, East Hartford, Connecticut.

23 Gaul, L. "Analytical and Experimental Study of Dynamics of Structures with Joints and Attached Substructures." American Society of Mechanical Engineers publication 85-DET-164 (1985).

24 Crawley, Edward and Kevin O'Donnell. "Incorporation of the Effects of Material Damping and Nonlinearities on the Dynamics of Space Structures," Paper, Department of Aeronautics and Astronautics, Massachusetts Institute of Technology (1986).

25 Beucke, Karl E. and James M. Kelly. "Equivalent Linearizations for Practical Hysteretic Systems." International Journal of Non-Linear Mechanics. Vol. 23 , No. 4: pp. 211-238 (1985).

26 O'Donnell, Kevin J. and Edward F. Crawley. "The Use of Equivalent Linearization and Eigenvalue Perturbation Methods in Space Structure Design," Paper, Department of Aeronautics and Astronautics, Massachusetts Institute of Technology, Cambridge, Massachusetts (1986).

27 Belvin, W. Keith. "Modeling of Joints for the Dynamic Analysis of Truss Structures," Master's Thesis, School of Engineering and Applied Sciences, George Washington University (1985).

28 Fahy, F.J. "Damping in Plates." Journal of Sound and Vibration. Vol. 9, No. 3: pp. 501-508 (1969).

29 Morley, T.A. and C.J.H. Williams. "A Theoretical and Experimental Study of Mode Coupling due to Non-Linearity in the Vibration of Thin Panels." In Symposium on Non-Linear Dynamics at Loughborough University: Paper E.2: pp. 1 - 14 (1972).

30 van Schoor, M.C. "Modeling of a Free Sliding Mass on a Vibrating Free-Free Beam," Term Project for 16.94 (1987).

31 Chapman, J.M., F.H. Shaw, and W.C. Russell. "Nonlinear Transient Analysis of Joint Dominated Structures." AIAA 28 Annual Structures and Structural Dynamics and Materials Conference. AIAA Paper No.87-0892 (1987).

32 Uhrig, R. "The Transfer Matrix Method Seen as One Method of Structural Analysis among Others." Journal of Sound and Vibration. Vol. 4, No. 2: pp. 136-148 (1966).

33 Clough, R. W. and Penzien, J. DYNAMICS OF STRUCTURES, McGraw Hill Book Company, New York: pp. 301-302 (1975)

APPENDIX

Appendix A

Engineering Beam Equations

A.0 Derivation of Engineering Beam Equation

The structures analyzed in this paper consist of long thin beams linked by piecewise linear joints. The linear systems making up the piecewise linear structure are modeled as a set of proportionally damped engineering beam equations where each equation represents a mode of the structure. Each equation is concerned with a set of uniform beam sections linked by rotational springs. The assumption of proportional damping allows each mode to be modelled by separate but similar beam equations while maintaining mode and modal energy orthogonality. Chapter two describes the computational procedure used to solve the engineering beam equations and the piecewise linear nature of the structures. Appendix A describes in detail the derivation of the modelling technique used in this analysis.

A.1 Damped Engineering Beam

The equation of motion used to model a mode of the long thin structures used in this analysis is assumed to take the form, assuming constant mass,

$$m\ddot{W} + (EIW'' + CI\dot{W}'')'' = f(x,t) \qquad (A.1)$$

A superscript dot indicates differentiation with respect to time and a superscript prime indicates differentiation with respect to space, (x). Equation A.1 is a damped form of the engineering beam equation

$$m\ddot{W} + (EIW'')'' = f(x,t) \qquad (A.2)$$

where damping is provided by the term

$$(CI\dot{W}'')'' \qquad (A.3)$$

The damping term provides a moment force as a function of the rate of change of the beam curvature which can also be described as a material strain velocity or strain rate damping, consistent with the engineering beam assumptions.

The undamped beam equation, equation (A.2), is used to describe the mode shapes of the structures used in this analysis and damping is applied on a mode by mode basis. In effect each mode of the structure is modelled by a separate equation of motion represented by equation (A.1) where each mode is assigned its own damping coefficient. This technique is valid only when the set of modal equations describing the structure are proportional. Equation proportionality allows the energy of the structure to be calculated in terms of modes. The modal characteristic of the vibrational energy is used as justification of this technique of modeling a structural system with uncoupled damping.

This appendix first solves for the general solution, the orthogonality equations, the transfer equations and the energy equations of the damped engineering beam equation, equation (A.1). Proportionality conditions and the effects proportionality has on the solutions, orthogonality equations, and the energy equations are discused. The relationship with the undamped beam equation, equation (A.2), is discused and how damping can be assigned on a mode by mode basis is described.

A.2 Beam Section Solution

The structural beam analyzed is not assumed to be uniform over its length. In order to take advantage of the readily available solution of the uniform beam, the beam is divided into uniform beam sections linked by invoking their boundary conditions. Each beam section is assumed to have uniform mass, stiffness, and damping, over its length, and constant with respect to time.

$$m = E = I = C = \text{Constant} \qquad (A.4)$$

The solution of the complete beam is obtained by deriving the general solution of each beam section and the boundary conditions used to link the beam sections. The beam section solutions are placed into the boundary conditions to form a set of equations describing the forces and motions at the boundaries

as a function of the time and spatial coefficients of the beam sections. The simultaneous solution of these equations results in a transcendental equation. The eigen-values and eigen-vectors of the transcendental equation represent the frequencies and modes of the damped engineering beam.

The solution to a individual beam section is divided into homogeneous and particular parts.

$$W = W_H + W_P \tag{A.5}$$

The particular solution is ignored here to simplify the analysis but is described in detail in chapter 3, section 3.4. The homogeneous equation takes the form

$$m\ddot{W} + (EI\acute{W} + CI\dot{\acute{W}})\acute{} = 0 \tag{A.6}$$

which can also be expressed as the operator

$$L(u) = 0 \tag{A.7}$$

or

$$L(u) = m\frac{d^2}{dt^2}(u) + \frac{d^2}{dx^2}\left(EI\frac{d^2}{dx^2}(u) + CI\frac{d^3}{dx^2 dt}(u)\right) = 0 \tag{A.8}$$

A solution is assumed of the form

$$W = Be^{\Omega t + ax} + B^{*}e^{\Omega^{*} t + a^{*} x} = u + u^{*} \tag{A.9}$$

The complex solutions, u, and, u*, are complex conjugates of one another and must have a non-zero real part if the displacement, W, is to be non-zero. The complex conjugate form of equation (A.9) insures that the displacements ,W, are always real, a requirement of a real system. Inputting equation (A.9) into

(A.8) and noting equation (A.4) the characteristic equation of the operator L becomes

$$u[m\Omega^2 + a^4(EI + CI\Omega)] + u^*[m\Omega^{*2} + a^{*4}(EI + CI\Omega^*)] = 0 \tag{A.10}$$

The equations inside the brackets are also complex conjugates of one another and in general have a non-zero real part. In order for equation (A.10) to be satisfied and the solution be non-trivial the two terms in the brackets must go to zero. The characteristic equation is reduced to

$$m\Omega^2 + a^4(EI + CI\Omega) = 0 \tag{A.11}$$

The second term of equation (A.10) is the complex conjugate of the first and also goes to zero. The complex frequency, Ω, and the complex shape factor, a, are functions of one another and can be written as a solution for either the complex frequency or the complex shape factor.

$$\Omega = \frac{-a^4 CI \pm \sqrt{a^8 C^2 I^2 - 4 m a^4 EI}}{2m} \tag{A.12}$$

$$a = \sqrt[4]{\frac{-m\Omega^2}{EI + CI\Omega}} \tag{A.13}$$

The equivalent complex conjugate equations are not shown here. For each valid value of Ω there are four valid values of a, (ia, -ia, a, -a). Combining this with their complex conjugates a total of eight terms are needed to describe the solution of equation (A.9), (a single mode).

$$W = B_1 e^{\Omega t + iax} + B_2 e^{\Omega t - iax} + B_3 e^{\Omega t + ax} + B_4 e^{\Omega t - ax} + B_1^* e^{\Omega^* t + ia^* x} + B_2^* e^{\Omega^* t - ia^* x} + B_3^* e^{\Omega^* t + a^* x} + B_4^* e^{\Omega^* t - ia^* x} \tag{A.14}$$

These terms can be separated into time, (Y), and spatial, (ϕ), components.

$$W = \phi\ Y + \phi^{*} Y^{*} \tag{A.15}$$

where

$$\phi = c_1\ e^{i a x} + c_2\ e^{-i a x} + c_3\ e^{a x} + c_4\ e^{-a x} \tag{A.16}$$

$$Y = A\ e^{\Omega t} \tag{A.17}$$

In general there are multiple solutions to the homogeneous equation. The subscripts j and k are used to distinguish between the different solutions. The entire solution to equation (A.6) takes the form

$$W_H = \sum_j W_j \tag{A.18}$$

where there are an undefined number of solutions or modes represented in the sum. The modal displacements can be separated into their complex conjugate parts or complex conjugate pair modes.

$$W_j = w_j + w_j^{*} \tag{A.19}$$

The complex conjugate pair modes (w+w*) insure that the system remains real. They behave in the analysis much like modes in their own right. It is found in the analysis to be computationally advantages to consider the complex conjugates separate modes. The number of complex modes is double the real modes or solutions. There are two types of notation used in this analysis, complex conjugate notation and complex mode notation. The indication of the notation type is by the subscript variables. Complex conjugate notation uses j and k as subscript variables while complex mode notation uses n and m as

subscript variables. Complex conjugate notation is illustrated in equation (A.19). The complex conjugate pair modes are given the same mode number and the same subscript variable, j or k. The complex mode notation designates the complex conjugate pair modes as even and odd and have different subscripts, n or m, identifying the complex conjugate modes. There are twice as many complex modes as there are real modes or solutions.

$$W_H = \sum_{j} (w_j + w_j^*) = \sum_{2n} (w_n + w_{n+1}^*) \Rightarrow \sum_{n} w_n \qquad \text{(A.20)}$$

The individual complex modes can be separated into their spatial (mode shape), and time components.

$$w_n = \phi_n Y_n \qquad \text{(A.21)}$$

The spatial components are written as

$$\phi_n = c_{1n} e^{i a_n x} + c_{2n} e^{-i a_n x} + c_{3n} e^{a_n x} + c_{4n} e^{-a_n x} \qquad \text{(A.22)}$$

and the time components are written as

$$Y_n = A_n e^{\Omega_n t} \qquad \text{(A.23)}$$

A.3 Boundary Conditions

Equation (A.14) is applied to a uniform beam section with constant m, E, I, and C. The models used in this analysis link a number of uniform beams together and place the entire system in a free-free environment. These linkages are applied through the boundary conditions at the ends of the beam sections. The boundary conditions used in this analysis are illustrated in the following example.

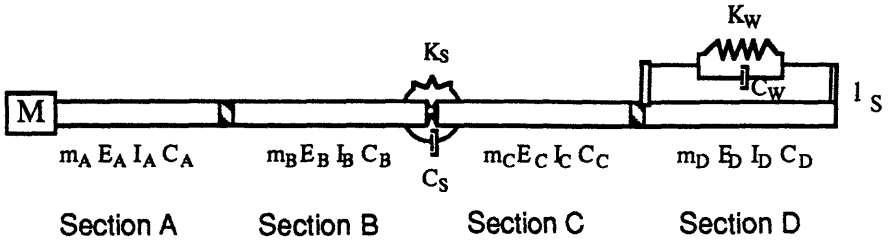

Sample Beam Assembly
Figure A.1

A.3.1 Tip Mass

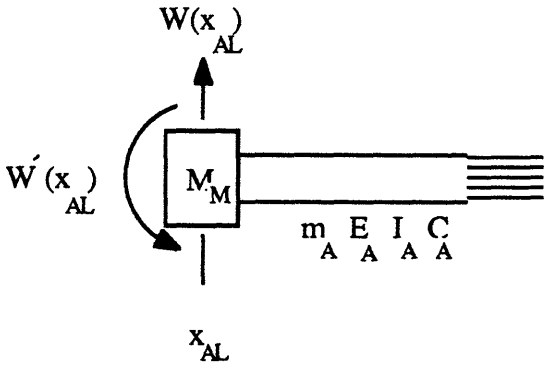

Attached Mass Boundary Condition
Figure A.2

A tip mass at a free end, (the far left end of the example), applies no moments but does apply a inertial shear force, therefore the two boundary conditions are

$$E_A I_A W_A''(x_{AL}) + C_A I_A \dot{W}_A''(x_{AL}) = 0 \qquad (A.24)$$

$$[E_A I_A W_A''(x_{AL}) + C_A I_A \dot{W}_A''(x_{AL})]' = - M \ddot{W}_A(x_{AL}) \qquad (A.25)$$

Had no tip mass been present the right side of equation (A.25) would have been equal to zero.

A.3.2 Straight Link

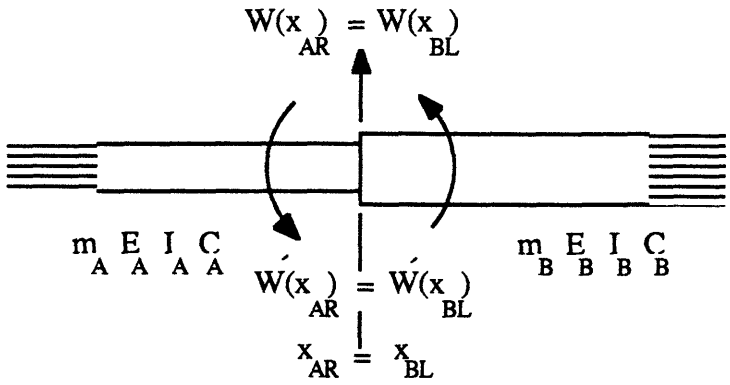

Direct Coupling Boundary Conditions
Figure A.3

A straight link between two beam segments, (the first joint in from the left on the example), has four boundary conditions. The displacements, the angles, the moments, and the shear forces at the boundary between the beams must be the same.

$$x_{AR} = x_{BL} \tag{A.26}$$

$$W_A(x_{AR}) = W_B(x_{BL}) \tag{A.27}$$

$$W_A'(x_{AR}) = W_B'(x_{BL}) \tag{A.28}$$

$$E_A I_A W_A''(x_{AR}) + C_A I_A \dot{W}_A''(x_{AR}) = E_B I_B W_B''(x_{BL}) + C_B I_B \dot{W}_B''(x_{BL}) \tag{A.29}$$

$$[E_A I_A W_A''(x_{AR}) + C_A I_A \dot{W}_A''(x_{AR})]' = [E_B I_B W_B''(x_{BL}) + C_B I_B \dot{W}_B''(x_{BL})]' \tag{A.30}$$

A.3.3 Rotational Spring-Damper

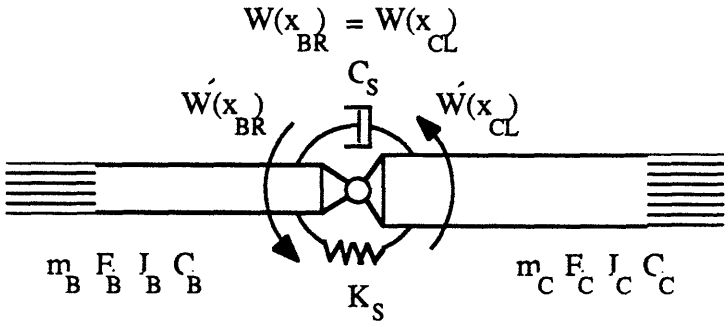

Rotational Spring Damper Boundary Condition
Figure A.4

A rotational spring-damper between two beam segments, (the second joint in from the left on the example), also has four boundary conditions. The displacements, the shear forces, and the moments at the boundary between the beams must be the same. The fourth is a relationship between the angles (and their rates) of the two beam segments at their boundary and the moment forces between them.

$$x_{BR} = x_{CL} \tag{A.31}$$

$$W_B(x_{BR}) = W_C(x_{CL}) \tag{A.32}$$

$$E_B I_B W_B''(x_{BR}) + C_B I_B \dot{W}_B''(x_{BR}) = E_C I_C W_C''(x_{CL}) + C_C I_C \dot{W}_C''(x_{CL}) \tag{A.33}$$

$$[E_B I_B W_B''(x_{BR}) + C_B I_B \dot{W}_B''(x_{BR})]' = [E_C I_C W_C''(x_{CL}) + C_C I_C \dot{W}_C''(x_{CL})]' \tag{A.34}$$

$$K_S [W_C'(x_{CL}) - W_B'(x_{BR})] + C_S [\dot{W}_C'(x_{CL}) - \dot{W}_B'(x_{BR})]$$

$$= E_C I_C W_C''(x_{CL}) + C_C I_C \dot{W}_C''(x_{CL}) \qquad \text{(A.35)}$$

A.3.4 General Rotational Spring Coupling

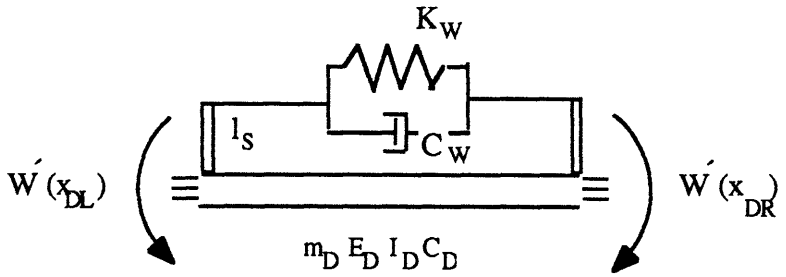

General Rotational Spring Boundary Condition
Figure A.5

The rotational spring damper linking two beams together can be generalized to link any two beam section boundaries together by a rotational spring-damper. The general spring damper coupling is used to model wire bracing of a beam. Wire bracing assumes that two standoffs are linked by a linear spring-damper. The spring-damper linking the ends of the beam section, (the far right beam section on the example), is modeled the same as the rotational spring-damper with the exception that extensional forces are induced by the linear spring and are ignored in the analysis. The equivalent spring stiffness is a function of the length of the standoffs and the stiffness of the linear spring.

$$K_S = l_s K_W \qquad \text{(A.36)}$$

The free-end conditions are included in the boundary conditions.

$$x_{CR} = x_{DL} \qquad \text{(A.37)}$$

$$W_C(x_{CR}) = W_D(x_{DL}) \qquad \text{(A.38)}$$

$$W_C'(x_{CR}) = W_D'(x_{DL}) \tag{A.39}$$

$$E_C I_C W_C''(x_{CR}) + C_C I_C \dot{W}_C''(x_{CR}) = E_D I_D W_D''(x_{DL}) + C_D I_D \dot{W}_D''(x_{DL})$$

$$- K_S [W_D'(x_{DR}) - W_D'(x_{DL})] - C_S [\dot{W}_D'(x_{DR}) - \dot{W}_D'(x_{DL})]$$

$$[E_C I_C W_C''(x_{CR}) + C_C I_C \dot{W}_C''(x_{CR})]' = [E_D I_D W_D''(x_{DL}) + C_D I_D \dot{W}_D''(x_{DL})]' \tag{A.40}$$

$$K_S [W_D'(x_{DR}) - W_D'(x_{DL})] + C_S [\dot{W}_D'(x_{DR}) - \dot{W}_D'(x_{DL})]$$

$$= E_D I_D W_D''(x_{DR}) + C_D I_D \dot{W}_D''(x_{DR}) \tag{A.41}$$

$$[E_D I_D W_D''(x_{DR}) + C_D I_D \dot{W}_D''(x_{DR})]' = 0 \tag{A.42}$$

A.3.5 Transcendental Equation

For the entire system to have a single set of modes each segment must have identical complex frequencies (Ω). The complex shape factors (a) of each beam section (indicated by the sub- or super-script A), in general, are different. Inputting equations (A.13) and the solutions associated with equation (A.20) into the boundary conditions and factoring out the time terms results in a set of equations, when put into matrix form, is similar to equation (A.43). Equation (A.43) is the transcendental matrix equation for a single free-free beam section. The matrix equations for the beam simulations used in this analysis are not shown due to their size and comlexity but follow directly from the boundary condition equations shown.

$$A_n e^{\Omega_n t}(E_A I_A+\Omega_n C_A I_A)\begin{bmatrix} -a_n^{A2} e^{i a_n^A x_{AL}} & -a_n^{A2} e^{-i a_n^A x_{AL}} & a_n^{A2} e^{a_n^A x_{AL}} & a_n^{A2} e^{-a_n^A x_{AL}} \\ -i a_n^{A3} e^{i a_n^A x_{AL}} & i a_n^{A3} e^{-i a_n^A x_{AL}} & a_n^{A3} e^{a_n^A x_{AL}} & -a_n^{A3} e^{-a_n^A x_{AL}} \\ -a_n^{A2} e^{i a_n^A x_{AR}} & -a_n^{A2} e^{-i a_n^A x_{AR}} & a_n^{A2} e^{a_n^A x_{AR}} & a_n^{A2} e^{-a_n^A x_{AR}} \\ -i a_n^{A3} e^{i a_n^A x_{AR}} & i a_n^{A3} e^{-i a_n^A x_{AR}} & a_n^{A3} e^{a_n^A x_{AR}} & -a_n^{A3} e^{-a_n^A x_{AR}} \end{bmatrix}\begin{bmatrix} c_{1n}^A \\ c_{2n}^A \\ c_{3n}^A \\ c_{4n}^A \end{bmatrix}$$

$$= [0] \qquad \text{(A.43)}$$

Simultaneously solving all of the boundary conditions typically results in a transcendental equation, giving a infinite number of mode solutions. The general solution is then the sum of these modes. The transcendental nature of the matrix equation requires a iterative solution technique. The computational technique used to solve the matrix equation is described in detail in Chapter 4, section 4.2.

A.4 Orthogonality Conditions

Orthogonality equations are used to distinguish between the modes. The orthogonality equations allow the modes to be solved for separately and are necessary in the solution of the initial condition problem. The orthogonality equations are derived by placing a single complex mode into the operator defined by the homogeneous equation of motion and multiplying it by another complex mode, subtracting the same equation where the complex modes have switched positions. Integrating by parts and substituting in the boundary conditions an orthogonality relationship is derived which can be shown to exhibit the properties of being non-zero for like modes and zero for unlike modes.

A.4.1 Integral Operator Equation

A single complex mode is inputted into the operator, L , the operator multiplied by a different complex mode and the entire equation integrated results in equation (A.44).

$$\int_{x_1}^{x_2} w_m L\,(w_n)\,dx = 0 \tag{A.44}$$

A similar equation can be written by switching the modes,

$$\int_{x_1}^{x_2} w_n L\,(w_m)\,dx = 0 \tag{A.45}$$

Subtracting equation (A.45) from (A.44) an integral operator is defined by the equation

$$\int_{x_1}^{x_2} \{ w_m L\,(w_n) - w_n L\,(w_m) \}\,dx = 0 \tag{A.46}$$

Inputting equation (A.21) into equation (A.46) and separating the time and spatial terms equation (A.47) results.

$$Y_n Y_m \int_{x_1}^{x_2} \{ \Omega_n^2 m \phi_n \phi_m + (E I \phi_n'' + \Omega_n C I \phi_n'')'' \phi_m$$

$$- \Omega_m^2 m \phi_m \phi_n - (E I \phi_m'' + \Omega_m C I \phi_m'')'' \phi_n \} dx = 0 \qquad \text{(A.47)}$$

Integrating by parts

$$Y_n Y_m \Big[\int_{x_1}^{x_2} \{ (\Omega_n^2 - \Omega_m^2) m \phi_n \phi_m + (\Omega_n - \Omega_m) C I \ \phi_n'' \phi_m'' \} dx$$

$$+ \{ (E I \phi_n'' + \Omega_n C I \phi_n'')' \phi_m - (E I + \Omega_n C I) \phi_n'' \phi_m'$$

$$- (E I \phi_m'' + \Omega_m C I \phi_m'')' \phi_n + (E I + \Omega_m C I) \phi_m'' \phi_n' \} \Big|_{x_1}^{x_2} \Big] = 0$$

(A.48)

The beam section limits and the boundary conditions described in equations (A.24) to (A.42) are inputted into equation (A.48).

A.4.2 Tip Mass

Inputting the tip mass boundary conditions, equations (A.24) and (A.25), assuming the tip mass is a constant, into the relevant portion of equation (A.48),

$$\ldots - Y_n Y_m \Big\{ \Big\{ (E_A I_A \phi_{An}'' + \Omega_n C_A I_A \phi_{An}'')' \phi_{Am} - (E_A I_A + \Omega_n C_A I_A) \phi_{An}'' \phi_{Am}' - (E_A I_A \phi_{Am}'' + \Omega_m C_A I_A \phi_{Am}'')' \phi_{An} + (E_A I_A + \Omega_m C_A I_A) \phi_{Am}'' \phi_{An}' \Big\} \Big|_{x_{AL}} \Big\} + \ldots \tag{A.49}$$

results in the terms at the tip mass boundary going to

$$\ldots + Y_n Y_m \Big\{ \Big\{ M_M (\Omega_n^2 - \Omega_m^2) \phi_{An} \phi_{Am} \Big\} \Big|_{x_{AL}} \Big\} + \ldots \tag{A.50}$$

A.4.3 Straight link

Inputting the boundary conditions for the straight link, equations (A.26)-(A.30), into equation (A.48), results in the terms at the straight link boundary to go to zero. The relevant terms of equation (A.48) are

$$\begin{aligned} &\ldots + Y_n Y_m \Big\{ \Big\{ \phi_{Am} (E_A I_A \phi_{An}'' + \Omega_n C_A I_A \phi_{An}'')' - \phi_{Am}' (E_A I_A \phi_{An}'' + \Omega_n C_A I_A \phi_{An}'') \\ &- \phi_{An} (E_A I_A \phi_{Am}'' + \Omega_m C_A I_A \phi_{Am}'')' + \phi_{An}' (E_A I_A \phi_{Am}'' + \Omega_m C_A I_A \phi_{Am}'') \Big\} \Big|_{x_{AR}} \\ &- \Big\{ \phi_{Bm} (E_B I_B \phi_{Bn}'' + \Omega_n C_B I_B \phi_{Bn}'')' - \phi_{Bm}' (E_B I_B \phi_{Bn}'' + \Omega_n C_B I_B \phi_{Bn}'') \\ &- \phi_{Bn} (E_B I_B \phi_{Bm}'' + \Omega_m C_B I_B \phi_{Bm}'')' + \phi_{Bn}' (E_B I_B \phi_{Bm}'' + \Omega_m C_B I_B \phi_{Bm}'') \Big\} \Big|_{x_{BL}} \Big\} + \ldots \end{aligned} \tag{A.51}$$

Rearranging and inputting equations (A.26)-(A.30) results in equation (A.51) equaling zero.

A.4.4 Rotational Spring Damper

Inputting the boundary conditions for the rotational spring damper, equations (A.31)-(A.35), into equation (A.48), results in some terms not going to zero. The relevant terms of equation (A.48) are

$$\ldots + Y_n Y_m \Big\{ \{ \phi_{Bm}(E_B I_B \phi''_{Bn} + \Omega_n C_B I_B \phi''_{Bn})' - \phi'_{Bm}(E_B I_B \phi''_{Bn} + \Omega_n C_B I_B \phi''_{Bn})$$
$$- \phi_{Bn} (E_B I_B \phi''_{Bm} + \Omega_m C_B I_B \phi''_{Bm})' + \phi'_{Bn}(E_B I_B \phi''_{Bm} + \Omega_m C_B I_B \phi''_{Bm}) \Big\}\Big|_{x_{BR}}$$
$$- \{ \phi_{Cm}(E_C I_C \phi''_{Cn} + \Omega_n C_C I_C \phi''_{Cn})' - \phi'_{Cm}(E_C I_C \phi''_{Cn} + \Omega_n C_C I_C \phi''_{Cn})$$
$$- \phi_{Cn} (E_C I_C \phi''_{Cm} + \Omega_m C_C I_C \phi''_{Cm})' + \phi'_{Cn}(E_C I_C \phi''_{Cm} + \Omega_m C_C I_C \phi''_{Cm}) \Big\}\Big|_{x_{CL}} \Big\} + \ldots \quad \text{(A.51)}$$

Inputting equations (A.31)-(A.35) into equation (A.48) and rearranging gives

$$\ldots + Y_n Y_m \Big\{ (\Omega_n - \Omega_m) C_S (\phi'_{Cn} - \phi'_{Bn}) (\phi'_{Cm} - \phi'_{Bm}) \Big\}\Big|_{x_{CL}} + \ldots \quad \text{(A.52)}$$

A.4.5 General Rotational Spring Coupling of Boundaries

Rotational spring dampers can couple different ends of a beam section by using wires linking standoffs at the beam ends. Inputting the boundary conditions for the spring-damper linking the beam sections, equations (A.36)-(A.42), into equation (A.48), also results in some terms not going to zero. The relevant terms of equation (A.48) are

$$\ldots + Y_n Y_m \Big\{ \Big\{ \phi_{Cm}(E_C I_C \phi''_{Cn} + \Omega_n C_C I_C \phi''_{Cn})' - \phi'_{Cm}(E_C I_C \phi''_{Cn} + \Omega_n C_C I_C \phi''_{Cn})$$

$$- \phi_{Cn} (E_C I_C \phi''_{Cm} + \Omega_m C_C I_C \phi''_{Cm})' + \phi'_{Cn}(E_C I_C \phi''_{Cm} + \Omega \ C_C I_C \phi''_{Cm}) \Big\}\Big|_{x_{CR}}$$

$$\Big\{ \phi_{Dm}(E_D I_D \phi''_{Dn} + \Omega_n C_D I_D \phi''_{Dn})' - \phi'_{Dm}(E_D I_D \phi''_{Dn} + \Omega_n C_D I_D \phi''_{Dn})$$

$$- \phi_{Dn} (E_D I_D \phi''_{Dm} + \Omega_m C_D I_D \phi''_{Dm})' + \phi'_{Dn}(E_D I_D \phi''_{Dm} + \Omega \ C_D I_D \phi''_{Dm}) \Big\}\Big|_{x_{DL}}$$

$$+ \ \Big\{ \phi_{Dm}(E_D I_D \phi''_{Dn} + \Omega \ C_D I_D \phi''_{Dn})' - \phi'_{Dm}(E_D I_D \phi''_{Dn} + \Omega_n C_D I_D \phi''_{Dn})$$

$$- \phi_{Dn} (E_D I_D \phi''_{Dm} + \Omega_m C_D I_D \phi''_{Dm})' + \phi'_{Dn}(E_D I_D \phi''_{Dm} + \Omega_m C_D I_D \phi''_{Dm}) \Big\}\Big|_{x_{DR}} \Big\}$$

(A.53)

After some manipulation, equation (A.53) reduces to equation (A.54).

$$\ldots + Y_n Y_m \Big\{ \ (\Omega_n - \Omega_m) \ C_S \ [\phi'_{Dn}(x_{DR}) - \phi'_{Dn}(x_{DL})][\phi'_{Dm}(x_{DR}) - \phi'_{Dm}(x_{DL})] \Big\}$$

(A.54)

A.4.6 First Orthogonality Equation

Adding the component terms of equation (A.48) together

$$Y_n Y_m (\Omega_n - \Omega_m) \left[\int_{x_{AL}}^{x_{AR}} \{ (\Omega_n + \Omega_m) m_A \phi_{An} \phi_{Am} + C_A I_A \phi''_{An} \phi''_{Am} \} \, dx \right.$$

$$+ \int_{x_{BL}}^{x_{BR}} \{ (\Omega_n + \Omega_m) m_B \phi_{Bn} \phi_{Bm} + C_B I_B \phi''_{Bn} \phi''_{Bm} \} \, dx$$

$$+ \int_{x_{CL}}^{x_{CR}} \{ (\Omega_n + \Omega_m) m_C \phi_{Cn} \phi_{Cm} + C_C I_C \phi''_{Cn} \phi''_{Cm} \} \, dx$$

$$+ \int_{x_{DL}}^{x_{DR}} \{ (\Omega_n + \Omega_m) m_D \phi_{Dn} \phi_{Dm} + C_D I_D \phi''_{Dn} \phi''_{Dm} \} \, dx$$

$$+ \{ \{ M_M (\Omega_n + \Omega_m) \phi_{An} \phi_{Am} \} |_{x_{AL}} \}$$

$$+ \{ C_S (\phi'_{Cn} - \phi'_{Bn}) (\phi'_{Cm} - \phi'_{Bm}) \} |_{x_{CL}}$$

$$\left. + \{ C_S [\phi'_{Dn}(x_{DR}) - \phi'_{Dn}(x_{DL})][\phi'_{Dm}(x_{DR}) - \phi'_{Dm}(x_{DL})] \} \right] = 0 \qquad \text{(A.55)}$$

Equation (A.55) can be cast in more general terms by condensing the beam, mass, and spring terms into summations.

$$Y_n Y_m (\Omega_n - \Omega_m) \Bigg[\sum_{B}^{\text{all beams}} \int_{x_{BL}}^{x_{BR}} \{ (\Omega_n + \Omega_m) m_B \phi_{Bn} \phi_{Bm} + C_B I_B \phi''_{Bn} \phi''_{Bm} \} \, dx + \sum_{M}^{\text{all masses}} \{ \{ M_M (\Omega_n + \Omega_m) \phi_{Mn}(x_M) \phi_{Mm}(x_M) \} \} + \sum_{S}^{\text{all springs}} \{ C_S [\phi'_{Dn}(x_{DR}) - \phi'_{Dn}(x_{DL})][\phi'_{Dm}(x_{DR}) - \phi'_{Dm}(x_{DL})] \} \Bigg] = 0 \quad \text{(A.56)}$$

Since the frequency term at the left of equation (A.56) is zero when n = m the equation can be put in terms of complex modal orthogonality.

$$\sum_{B}^{\text{all beams}} \int_{x_{BL}}^{x_{BR}} \{ (\Omega_n + \Omega_m) m_B \phi_{Bn} \phi_{Bm} + C_B I_B \phi''_{Bn} \phi''_{Bm} \} \, dx + \sum_{M}^{\text{all masses}} \{ \{ M_M (\Omega_n + \Omega_m) \phi_{Mn}(x_M) \phi_{Mm}(x_M) \} \} + \sum_{S}^{\text{all springs}} \{ C_S [\phi'_{Dn}(x_{DR}) - \phi'_{Dn}(x_{DL})][\phi'_{Dm}(x_{DR}) - \phi'_{Dm}(x_{DL})] \} = \delta_{nm} \nu_{nm} \quad \text{(A.57)}$$

This is designated the first orthogonality equation. A second orthogonality equation can be derived by inputting the first orthogonality equation into a relationship derived from the homogeneous equation of motion and its solution.

A.4.7 Second Orthogonality Equation

Inputting a single complex mode solution into the homogeneous equation of motion, equation (A.1), equation (A.58) results.

$$Y_n \left\{ \Omega_n^2 m \phi_n + (E I \phi_n'' + \Omega_n C I \phi_n'')'' \right\} = 0 \tag{A.58}$$

Multiplying by a second complex mode solution and integrating over the length of the beam equation (A.59) results.

$$Y_n Y_m \int_{x_1}^{x_2} \left\{ \Omega_n^2 m \phi_n \phi_m + (E I \phi_n'' + \Omega_n C I \phi_n'')'' \phi_m \right\} dx = 0 \tag{A.59}$$

Integrating by parts

$$Y_n Y_m \int_{x_1}^{x_2} \left\{ \Omega_n^2 m \phi_n \phi_m + (E I + \Omega_n C I) \phi_n'' \phi_m'' \right\}$$

$$+ \left\{ (E I \phi_n'' + \Omega_n C I \phi_n'')' \phi_m - (E I + \Omega_n C I) \phi_n'' \phi_m' \right\} \Big|_{x_1}^{x_2} = 0 \tag{A.60}$$

Separating the beam sections and inputting the boundary conditions into equation (A.60), equation (A.61) results.

$$\sum_{B}^{\text{all beams}} \int_{x_{BL}}^{x_{BR}} \{ \Omega_n^2 m_B \phi_{Bn} \phi_{Bm} + (E_B I_B + \Omega_n C_B I_B) \phi''_{Bn} \phi''_{Bm} \}$$

$$+ \sum_{M}^{\text{all masses}} \{ \Omega_n^2 M_M \phi_{Mn}(x_M) \phi_{Mm}(x_M) \}$$

$$+ \sum_{S}^{\text{all springs}} \{ K_S [\phi'_{SRm}(x_{SR}) - \phi'_{SLm}(x_{SL})][\phi'_{SRn}(x_{SR}) - \phi'_{SLn}(x_{SL})] \}$$

$$+ \sum_{S}^{\text{all springs}} \{ \Omega_n C_S [\phi'_{SRm}(x_{SR}) - \phi'_{SLm}(x_{SL})][\phi'_{SRn}(x_{SR}) - \phi'_{SLn}(x_{SL})] \} = 0 \qquad \text{(A.61)}$$

Multiplying equation (A.57) by the complex frequency (Ω) and subtracting it from equation (A.61) gives the second orthogonality equation, equation (A.62).

$$\sum_{B}^{\text{all beams}} \int_{x_{BL}}^{x_{BR}} \{ - \Omega_n \Omega_m m_B \phi_{Bn} \phi_{Bm} + E_B I_B \phi''_{Bn} \phi''_{Bm} \}$$

$$+ \sum_{M}^{\text{all masses}} \{ - \Omega_n \Omega_m M_M \phi_{Mn}(x_M) \phi_{Mm}(x_M) \}$$

$$+ \sum_{S}^{\text{all springs}} \{ K_S [\phi'_{SRm}(x_{SR}) - \phi'_{SLm}(x_{SL})][\phi'_{SRn}(x_{SR}) - \phi'_{SLn}(x_{SL})] \} = - \Omega_n \delta_{mn} \nu_{mn}$$

(A.62)

A.5 Initial Condition Problem

The initial condition is a known real displacement and rate distribution at the initial time, indicated by the subscript T.

$$W_T = W(t_T) \qquad \dot{W}_T = \dot{W}(t_T) \qquad \text{(A.63)}$$

The initial conditions establish the initial complex modal amplitudes of the solution. The orthogonality equation is used to decouple the modes making it possible to calculate each mode individually.

A.5.1 Orthogonal Initial Condition Equation

Dividing equation (A.56) by the square of the time function Y, of the complex mode m, integrating with respect to time and summing over all modes n and m

$$\sum_{n}\sum_{m}\int_{T}^{t}\left\{\frac{Y_n}{Y_m}\,(\Omega_n-\Omega_m)\right\}dt\,\Bigg[$$

$$\sum_{B}^{\text{all beams}}\int_{x_{BL}}^{x_{BR}}\left\{(\Omega_n+\Omega_m)m_B\,\phi_{Bn}\,\phi_{Bm}+C_B\,I_B\,\phi''_{Bn}\,\phi''_{Bm}\right\}\,dx$$

$$+\sum_{M}^{\text{all masses}}\left\{\left\{M_M\,(\Omega_n+\Omega_m)\,\phi_{Mn}\,\phi_{Mm}\right\}\Big|_{x_M}\right\}$$

$$+\sum_{S}^{\text{all springs}}\left\{C_S\,[\phi'_{Dn}(x_{DR})-\phi'_{Dn}(x_{DL})][\phi'_{Dm}(x_{DR})-\phi'_{Dm}(x_{DL})]\right\}\Bigg]=0 \qquad \text{(A.64)}$$

results in an equation where the limits of integration can be put on different sides of the equation. Equation (A.64) becomes

$$\sum_{n}\sum_{m}\left\{\frac{Y_n}{Y_m}\right\}\Big|_{T}\,\Bigg[$$

$$\sum_{B}^{\text{all beams}}\int_{x_{BL}}^{x_{BR}}\left\{(\Omega_n+\Omega_m)m_B\,\phi_{Bn}\,\phi_{Bm}+C_B\,I_B\,\phi''_{Bn}\,\phi''_{Bm}\right\}\,dx$$

$$+\sum_{M}^{\text{all masses}}\left\{\left\{M_M\,(\Omega_n+\Omega_m)\,\phi_{Mn}\,\phi_{Mm}\right\}\Big|_{x_M}\right\}$$

$$+\sum_{S}^{\text{all springs}}\left\{C_S\,[\phi'_{Dn}(x_{DR})-\phi'_{Dn}(x_{DL})][\phi'_{Dm}(x_{DR})-\phi'_{Dm}(x_{DL})]\right\}\Bigg]=$$

$$= \sum_n \sum_m \left\{ \frac{Y_n}{Y_m} \right\} \Big|_t \Bigg[$$

$$\sum_{B}^{\text{all beams}} \int_{x_{BL}}^{x_{BR}} \left\{ (\Omega_n + \Omega_m) m_B \phi_{Bn} \phi_{Bm} + C_B I_B \phi''_{Bn} \phi''_{Bm} \right\} dx$$

$$+ \sum_{M}^{\text{all masses}} \left\{ \left\{ M_M (\Omega_n + \Omega_m) \phi_{Mn} \phi_{Mm} \right\} \Big|_{x_M} \right\}$$

$$+ \sum_{S}^{\text{all springs}} \left\{ C_S \left[\phi'_{Dn}(x_{DR}) - \phi'_{Dn}(x_{DL}) \right] \left[\phi'_{Dm}(x_{DR}) - \phi'_{Dm}(x_{DL}) \right] \right\} \Bigg]$$

(A.65)

The complex frequency terms evaluated at the initial time, T, can be reassembled with the time and mode shape terms to form the initial conditions and the terms evaluated at the final time, t, can be reduced by the orthogonality condition, equation (A.57). The left side of equation (A.65) is reduced to a single summation, equation (A.66) and the time functions are replaced by the equation (A.23).

$$\sum_m \Bigg[\left\{ A_m e^{(-\Omega_m) t_T} \right\}$$

$$\left\{ \sum_{B}^{\text{all beams}} \left\{ \int_{x_{BL}}^{x_{BR}} \left\{ \Omega_m \phi_{Bm} W_{B_0} m_B + \phi_{Bm} \dot{W}_{B_T} m_B + \phi''_{Bm} W''_{B_T} C_B I_B \right\} dx \right\} \right.$$

$$+ \sum_{M}^{\text{all masses}} \left\{ \left\{ M_M (\Omega_m \phi_{Mm} W_{M_T} + \phi_{Mm} \dot{W}_{M_T}) \right\} \Big|_{x_M} \right\}$$

$$\left. + \sum_{S}^{\text{all springs}} \left\{ C_S \left[\phi'_{SRm}(x_{SR}) - \phi'_{SLm}(x_{SL}) \right] \left[W'_{SR_T}(x_{SR}) - W'_{SL_T}(x_{SL}) \right] \right\} \right\} \Bigg] =$$

$$= \sum_m \sum_n \left[\left\{ A_m A_n e^{(-\Omega_m + \Omega_n)t} \right\} \delta_{mn} \nu_{mn} \right]$$

(A.66)

The right hand side of equation (A.66) can be reduced to a single sum since it is non-zero only when m equals n

$$\sum_m \left[\left\{ A_m e^{(-\Omega_m)t_T} \right\} \right.$$

$$\left\{ \sum_B^{\text{all beams}} \left\{ \int_{x_{BL}}^{x_{BR}} \left\{ \Omega_m \phi_{Bm} W_{B_0} m_B + \phi_{Bm} \dot{W}_{B_T} m_B + \phi''_{Bm} W''_{B_T} C_B I_B \right\} dx \right\} \right.$$

$$+ \sum_M^{\text{all masses}} \left\{ \left\{ M_M (\Omega_m \phi_{Mm} W_{M_T} + \phi_{Mm} \dot{W}_{M_T}) \right\} \Big|_{x_M} \right\}$$

$$\left. + \sum_S^{\text{all springs}} \left\{ C_S [\phi'_{SRm}(x_{SR}) - \phi'_{SLm}(x_{SL})][W'_{SR_T}(x_{SR}) - W'_{SL_T}(x_{SL})] \right\} \right\} \left. \right]$$

$$= \sum_m \left\{ A_m^2 \nu_{mm} \right\}$$

(A.67)

The general initial value equation can therefore be reduced to solving for each mode independently.

$$\frac{e^{-\Omega_m t_T}}{\nu_{mm}} \left\{ \sum_B^{\text{all beams}} \left\{ \int_{x_{BL}}^{x_{BR}} \left\{ \Omega_m \phi_{Bm} W_{B_T} m_B + \phi_{Bm} \dot{W}_{B_T} m_B + \phi''_{Bm} W''_{B_T} C_B I_B \right\} dx \right\} \right.$$

$$+ \sum_M^{\text{all masses}} \left\{ \left\{ M_M (\Omega_m \phi_{Mm} W_{M_T} + \phi_{Mm} \dot{W}_{M_T}) \right\} \Big|_{x_M} \right\}$$

$$\left. + \sum_S^{\text{all springs}} \left\{ C_S [\phi'_{SRm}(x_{SR}) - \phi'_{SLm}(x_{SL})][W'_{SR_T}(x_{SR}) - W'_{SL_T}(x_{SL})] \right\} \right\} = A_m$$

(A.68)

A.5.2 System Transfer Equation

The technique used in this analysis models piece-wise linear structures. As the structure oscillates different but similar structural models are used to describe its motion. When a first or initial structural modal transfers to a second or final structural modal the final state of the initial system, the position and velocity, is used as the initial condition of the final structural model. The structures are identical except the damping and stiffness coefficients are allowed to vary. This allows the complex modal amplitudes of the final system to be solved for in terms of the complex modal amplitudes of the initial system. The computational technique is described in more detail in chapter 4. It must be emphasized that the transfer from one system to another must be accomplished with emphasis on the conservation of energy, momentum, and mass from one system to another.

An initial structure is assumed to take the form of equation (A.69).

$$m\ddot{V} + (EI V'' + CI \dot{V}'')'' = 0 \tag{A.69}$$

and the assumed solution is shown in equation (A.70).

$$v = B e^{\omega t + bx} + B^{*} e^{\omega^{*} t + b^{*} x} \tag{A.70}$$

The characteristic equation is therefore

$$m\omega^{2} + b^{4}(EI + CI\omega) = 0 \tag{A.71}$$

and the time and spatial modal components are shown in equations (A.72) to (A.76).

$$V = \sum_{n} V_{n} \tag{A.72}$$

$$V_{n} = v_{n} + v_{n}^{*} \tag{A.73}$$

$$v_n = \psi_n Z_n \tag{A.74}$$

$$\psi_n = d_{1n} e^{i b_n x} + d_{2n} e^{-i b_n x} + d_{3n} e^{b_n x} + d_{4n} e^{-b_n x} \tag{A.75}$$

$$Z_n = B_n e^{\omega_n t} \tag{A.76}$$

In this analysis the assumption is made that the component beam dimensions are the same for the initial system as the final system. The system transfer equation can then be written as

$$\frac{e^{-\Omega_m t_T}}{v_{mm}} \left\{ \sum_{B}^{\text{all beams}} \left\{ \int_{x_{BL}}^{x_{BR}} \left\{ \Omega_m \phi_{Bm} V_{B_T} m_B + \phi_{Bm} \dot{V}_{B_T} m_B + \phi''_{Bm} V''_{B_T} C_B I_B \right\} dx \right\} \right.$$

$$+ \sum_{M}^{\text{all masses}} \left\{ \left\{ M_M (\Omega_m \phi_{Mm} V_{M_T} + \phi_{Mm} \dot{V}_{M_T}) \right\} \Big|_{x_M} \right\}$$

$$\left. + \sum_{S}^{\text{all springs}} \left\{ C_S [\phi'_{SRm}(x_{SR}) - \phi'_{SLm}(x_{SL})][V'_{SR_T}(x_{SR}) - V'_{SL_T}(x_{SL})] \right\} \right\} = A_m \tag{A.77}$$

Inputting equations associated with equation (A.72) into equation (A.77) gives equation (A.78).

$$\sum_{n} \left[B_n \frac{e^{(\omega_n - \Omega_m) t_T}}{v_{mm}} \left\{ \sum_{B}^{\text{all beams}} \left\{ \int_{x_{BL}}^{x_{BR}} \left\{ (\Omega_m + \omega_n) \phi_{Bm} \psi_{Bn} m_B + \phi''_{Bm} \psi''_{Bn} C_B I_B \right\} dx \right\} \right. \right.$$

$$+ \sum_{M}^{\text{all masses}} \left\{ \left\{ M_M (\Omega_m + \omega_n) \phi_{Mm} \psi_{Mn} \right\} \Big|_{x_M} \right\}$$

$$\left. \left. + \sum_{S}^{\text{all springs}} \left\{ C_S [\phi'_{SRm}(x_{SR}) - \phi'_{SLm}(x_{SL})][\psi'_{SRn}(x_{SR}) - \psi'_{SLn}(x_{SL})] \right\} \right\} \right] = A_m \tag{A.78}$$

The transfer coefficient (τ) is defined in equation (A.79) as the portion of equation (A.78) which is similar to the orthogonality equation, equation (A.57).

$$\left\{ \sum_{B}^{\text{all beams}} \left\{ \int_{x_{BL}}^{x_{BR}} \left\{ (\Omega_m + \omega_n)\, \phi_{Bm} \psi_{Bn}\, m_B + \phi''_{Bm} \psi''_{Bn} C_B\, I_B \right\} dx \right\} \right.$$

$$+ \sum_{M}^{\text{all masses}} \left\{ \left\{ M_M (\Omega_m + \omega_n)\, \phi_{Mm}\, \psi_{Mn} \right\} \Big|_{x_M} \right\}$$

$$\left. + \sum_{S}^{\text{all springs}} \left\{ C_S \left[\phi'_{SRm}(x_{SR}) - \phi'_{SLm}(x_{SL}) \right] \left[\psi'_{SRn}(x_{SR}) - \psi'_{SLn}(x_{SL}) \right] \right\} \right\} = \tau_{mn} \qquad \text{(A.79)}$$

The transfer equation can therefore be written as

$$\sum_{n} \left\{ B_n e^{(\omega_n - \Omega_m) t_T} \frac{\tau_{mn}}{\nu_{mm}} \right\} = A_m \qquad \text{(A.80)}$$

The individual contribution of each complex mode of the initial system to each complex mode of the final system is written as equation (A.81).

$$B_n e^{(\omega_n - \Omega_m) t_T} \frac{\tau_{mn}}{\nu_{mm}} = A_{mn} \qquad \text{(A.81)}$$

Equation (A.81) establishes a computationally direct correlation between the complex modes of the initial system and the complex modes of the final system. If the initial system is identical to the final system the transfer coefficient (τ) reduces to the orthogonality coefficient (ν). Equation (A.81) then reduces to the statement of the complex modes of the initial system being equal to the complex modes of the final system.

A.6 Energy Equation

The energy of the engineering beam structures used in this analysis is defined as the sum of the potential energy (strain energy) and the kinetic energy.

$$\underline{E} = \int_{x_1}^{x_2} \frac{1}{2} m \dot{W}^2 + \frac{1}{2} E I W''^2 \, dx \tag{A.82}$$

Placing the beam section limits and the boundary conditions, section A.3, into equation (A.82), the energy equation becomes a sum of the constituent parts of the beam.

$$\underline{E} = \sum_{B}^{\text{all beams}} \frac{1}{2} \int_{x_{BL}}^{x_{BR}} m_B \dot{W}_B^2 + E_B I_B W_B''^2 \, dx$$

$$+ \sum_{M}^{\text{all masses}} \frac{1}{2} M_M \dot{W}_M^2(x_M)$$

$$+ \sum_{S}^{\text{all springs}} \frac{1}{2} K_S [W_S'(x_{SR}) - W_S'(x_{SL})]^2 \tag{A.83}$$

Inputting the complex mode solution, equation (A.20)-(A.23), the energy equation can be separated into its time and spatial components.

$$\underline{E} = \frac{1}{2} \sum_{m} \sum_{n} Y_m Y_n \Big[$$

$$\sum_{B}^{\text{all beams}} \int_{x_{BL}}^{x_{BR}} \{ \Omega_m \Omega_n m_B \phi_{Bm} \phi_{Bn} + E_B I_B \phi_{Bm}'' \phi_{Bn}'' \} \, dx$$

$$+ \sum_{M}^{\text{all masses}} \{ \Omega_m \Omega_n M_M \phi_{Mm}(x_M) \phi_{Mn}(x_M) \}$$

$$+ \sum_{S}^{\text{all springs}} \{ K_S [\phi'_{Sm}(x_{SR}) - \phi'_{Sm}(x_{SL})] [\phi'_{Sn}(x_{SR}) - \phi'_{Sn}(x_{SL})] \} \Big]$$

(A.84)

Using the second orthogonality equation, equation (A.62), to remove the stiffness terms, equation (A.84) becomes

$$\underline{E} = \sum_{m} \sum_{n} Y_m Y_n \Big[-\frac{1}{2} \Omega_n \delta_{mn} \nu_{mn}$$

$$+ \sum_{B}^{\text{all beams}} \int_{x_{BL}}^{x_{BR}} \{ \Omega_m \Omega_n m_B \phi_{Bm} \phi_{Bn} \} dx$$

$$+ \sum_{M}^{\text{all masses}} \{ \Omega_m \Omega_n M_M \phi_{Mm}(x_M) \phi_{Mn}(x_M) \} \Big]$$

(A.85)

Defining the modal mass, μ, as

$$\mu_{mn} = \Big[\sum_{B}^{\text{all beams}} \int_{x_{BL}}^{x_{BR}} \{ m_B \phi_{Bm} \phi_{Bn} \} dx$$

$$+ \sum_{M}^{\text{all masses}} \{ M_M \phi_{Mm}(x_M) \phi_{Mn}(x_M) \} \Big]$$

(A.86)

The energy equation reduces to

$$\underline{E} = \sum_{m} \sum_{n} Y_m Y_n \Omega_n \Big[\Omega_m \mu_{mn} - \frac{1}{2} \delta_{mn} \nu_{mn} \Big]$$

(A.87)

Energy terms involving different modes are present. In general the energy equation does not decouple into modal form. Transferring equation (A.87) into complex conjugate form, equation (A.20),

$$\underline{E} = \sum_j \sum_k \Big[Y_j Y_k \, \Omega_k \, \{ \, \Omega_j \, \mu_{jk} - \frac{1}{2} \, \delta_{jk} \nu_{jk} \, \} + Y_j^* \, Y_k \, \Omega_j^* \, \Omega_k \, \mu_{j^*k} + \text{c. c.} \Big] \tag{A.88}$$

where the * superscript of the mode subscript indicates the complex conjugate mode is inputted into the modal mass function. Further separating equation (A.88) into like and unlike terms the energy equation can be written as equation (A.89).

$$\underline{E} = \sum_j \Big[Y_j^2 \, \Omega_j \, \{ \, \Omega_j \mu_{jj} - \frac{1}{2} \, \nu_{jj} \, \} + Y_j^* \, Y_j \, \Omega_j^* \, \Omega_j \mu_{j^*j} + \text{c. c.} \Big] + \sum_{j \neq k} \sum \Big[Y_j Y_k \, \Omega_j \, \Omega_k \mu_{jk} + Y_j^* \, Y_k \, \Omega_j^* \, \Omega_k \mu_{j^*k} + \text{c. c.} \Big] \tag{A.89}$$

The first summation in equation (A.89) consists of complex energy terms which are each related to a single mode. These terms are dubbed the modal energy terms. There are two types of modal energy terms present, oscillatory terms and non-oscillatory terms. The oscillatory terms oscillate at twice the frequency and decay at twice the rate of the relevant modal amplitudes. The non-oscillatory terms are always real and decay at twice the rate the relevant modal amplitude decays.

The second summation in equation (A.89) consists of terms which are dependent on two separate modes and represent modal coupling of the energy equation. These terms are dubbed coupled complex energy terms. Generally

the coupled energy terms are non-zero and are oscillatory with frequencies and decay rates which are combinations of frequencies and decay rates of pairs of modes. There are special cases where energy does decouple into modal form, the coupled complex energy terms become zero. The two special cases examined in this analysis are the cases of undamped beams and of proportionally damped beams. The proportionally damped beam is examined first since the undamped beam can be derived from the proportionally damped beam.

A.6.1 Condition of Proportionality

The condition of proportionality is defined as

$$\frac{C_B}{E_B} = \frac{C_S}{K_S} = K \qquad \text{(A.90)}$$

Equation (A.90) states that the ratio of the damping coefficient and the stiffness coefficient is the same for all beam sections and boundary conditions.

The first observation is that a proportionally damped beam has identical mode shapes as the same beam without damping. This can be shown most readily by examining the boundary conditions, section A.3. By inputting into the boundary conditions an assumed solution, equation(A.20)-(A.23), performing the time differentiations, and applying the proportionality conditions, a factor of $(1+ K \Omega)$ can be factored out and cancelled, reducing the boundary condition to the same boundary condition as the undamped beam. For example, equation (A.35) becomes

$$(1 + K \Omega) \; K_S \; [\phi_C'(x_{CL}) - \phi_B'(x_{BR})]$$

$$= \; (1 + K \Omega) \; E_C I_C \; \phi_C''(x_{CL}) \qquad \text{(A.90)}$$

The single exception to this is the attached mass boundary condition, equation (A.25). It can also be shown to reduce to the undamped system's boundary condition by performing the same operation and using the

characteristic equation to eliminate the complex frequency terms. Equation (A.25) then reduces to the same boundary condition as in the undamped system.

$$[E_A I_A \phi_A''(x_{AL})]' = -\frac{a_A^4 E_A I_A}{m_A} M \phi_A(x_{AL}) \tag{A.91}$$

Since the boundary condition equations for the proportionally damped and undamped beams are identical the matrix equation formed by the boundary conditions is the same matrix equation for the proportionally damped beam as for the undamped beam. The mode shapes (the complex shape factors, and shape coefficients) of the proportionally damped system and the undamped system are therefore identical. A result of this observation is that the complex shape factor (a) is real for a proportionally damped beam. The characteristic equation can therefore be used to define a relationship between the proportionality coefficient (K) and the complex frequency (Ω).

$$K = \frac{\Omega_j + \Omega_j^*}{-\Omega_j \Omega_j^*} \tag{A.92}$$

This relationship is useful when calculating the energy of a proportionally damped system.

A.6.2 Energy of Proportionally Damped System

The first and second orthogonality equations can be combined with the conditions of proportionality to show modal energy decoupling of a proportionally damped system. This is accomplished by multiplying the second orthogonality equation, equation (A.62), by the proportionality coefficient, (K), and subtracting it from the first orthogonality equation, equation (A.57). Since the proportionality coefficient is identical for all beam sections and boundary conditions the resultant equation takes the form

$$\sum_{B}^{\text{all beams}} \left\{ \int_{x_{BL}}^{x_{BR}} \left\{ \frac{(\Omega_m + \Omega_n + \Omega_m \Omega_n K)}{(1 + \Omega_n K)} \phi_{Bm} \phi_{Bn} m_B \right\} dx \right\}$$

$$+ \sum_{B}^{\text{all masses}} \left\{ \frac{(\Omega_m + \Omega_n + \Omega_m \Omega_n K)}{(1 + \Omega_n K)} \phi_{Mm}(x_M)\ \phi_{Mn}(x_M)\ M_M \right\} = \delta_{mn} \nu_{mn}$$

(A.93)

Substituting for the modal mass, equation (A.86), equation (A.93) reduces to equation (A.94).

$$\frac{(\Omega_m + \Omega_n + \Omega_m \Omega_n K)}{(1 + \Omega_n K)} \mu_{mn} = \delta_{mn} \nu_{mn} \tag{A.94}$$

Converting to complex conjugate notation, equation (A.94) becomes equations (A.5) and (A.6).

$$\frac{(\Omega_j + \Omega_k + \Omega_j \Omega_k K)}{(1 + \Omega_k K)} \mu_{jk} = \delta_{jk} \nu_{jk} \tag{A.95}$$

$$\frac{(\Omega_j^* + \Omega_k + \Omega_j^* \Omega_k K)}{(1 + \Omega_k K)} \mu_{j^*k} = 0 \tag{A.96}$$

When equation (A.92) is substituted for the proportionality coefficient (K) in equation (A.96), equation (A.96) becomes

$$\frac{(\Omega_j^* + \Omega_k) - \dfrac{\Omega_j^* \Omega_k}{\Omega_k^* \Omega_k} (\Omega_k^* + \Omega_k)}{- \dfrac{\Omega_k^2}{\Omega_k^* \Omega_k}} \mu_{jk}^* = 0 \tag{A.97}$$

When j=k the numerator in equation (A.97) goes to zero. Equation (A.97) can therefore be written as an orthogonality condition. Equations (A.95) and (A.96) can be written as

$$\mu_{jk} = \delta_{jk}\,\mu_{jk} \tag{A.98}$$

$$\mu^{*}_{jk} = \delta^{*}_{jk}\,\mu^{*}_{jk} \tag{A.99}$$

where

$$\frac{(1+\Omega_k K)}{(\Omega_j+\Omega_k+\Omega_j\Omega_k K)}\;\mu_{jk} = \nu_{jk} \tag{A.100}$$

but the mixed terms can only be written as

$$\mu_{j^{*}k} = \left[\sum_{B}^{\text{all beams}} \int_{x_{BL}}^{x_{BR}} \{ m_B\,\phi^{*}_{Bj}\;\phi_{Bk} \}\,dx + \sum_{M}^{\text{all masses}} \{ M_M \phi^{*}_{Mj}(x_M)\,\phi_{Mk}(x_M) \} \right] \tag{A.101}$$

Inputting equations (A.98) and (A.99) into the energy equation, equation (A.88) becomes

$$\underline{E} = \sum_j \sum_k \left[Y_j Y_k\;\Omega_k \left\{ \Omega_j\,\delta_{jk}\,\mu_{jk} - \frac{1}{2}\,\delta_{jk}\,\nu_{jk} \right\} + Y^{*}_j\,Y_k\,\Omega^{*}_j\,\Omega_k\;\delta_{j^{*}k}\;\mu_{j^{*}k} + \text{c. c.} \right] \tag{A.102}$$

Equation (A.102) can be reduced to a single summation.

$$\underline{E} = \sum_m \left[Y_m^{2}\;\Omega_m \left\{ \Omega_m \mu_{mm} - \frac{1}{2}\nu_{mm} \right\} + Y^{*}_m\,Y_m\;\Omega^{*}_m \Omega_m \mu_{m^{*}m} + \text{c. c.} \right] \tag{A.103}$$

Equation (A.103) shows that the energy of a proportionally damped system is decoupled. The energy of a known mode can therefore be calculated without prior knowledge of other modes of the structure.

A.6.3 Energy of Undamped System

The undamped beam equation, equation (A.2), is the case where the damping coefficient, (C), is zero. This is equivalent to the case where the proportionality coefficient, (K), is zero. The characteristic equation reduces to

$$m\,\Omega^2 + a^4\,EI = 0 \tag{A.104}$$

and the complex frequency becomes purely imaginary.

$$\Omega_j = i\,\underline{\omega}_j \tag{A.105}$$

Where $\underline{\omega}$ is a real number. Equation (A.100) reduces to

$$\frac{1}{(\Omega_j + \Omega_k)}\mu_{jk} = \nu_{jk} \tag{A.106}$$

and inputting equation (A.100) into the energy equation, equation (A.103), the energy equation reduces to,

$$\underline{E} = \sum_j \left[Y_j^* Y_j\, \Omega_j^* \Omega_j\ \mu_{jj}^* + \text{c. c.} \right] \tag{A.107}$$

Noting that the terms in equation (A.107) are always real the energy of the undamped beam is real, constant and uncoupled.

$$\underline{E} = \sum_{j} 2\,\underline{\omega}_j^2\,\mu_{j^*j} \qquad \text{(A.108)}$$

A.7 Modal Damping

To this point in the analysis a single equation of motion has been used to describe the motion of the beam. The model, the engineering beam equation with strain rate damping, is solved along with the initial condition equation, system transfer equation, and the energy equation. The general solution exhibits modal characteristics but will posses modal energy characteristics only when the beam is proportionally damped. A proportionally damped beam possesses the same mode shapes as the same beam with no damping, provided the solution remains oscillatory. As can be surmised from the orthogonality equations, the energy equations, and the modal mass equations for the proportionally damped beam, the orthogonality equations and the energy equations hold for any two modes of any two beams where the beams are identical except for the damping coefficient. This property allows each mode of a beam, both complex conjugate parts, to be modeled by a separate equation without loosing modal or energy orthogonality.

The technique of a system of proportionally damped beam equations modeling a structure provides a model which has orthogonal modes, modal energy, and exponential decay of the modes which can be set. The allowable equations are the proportionally damped equation where the proportionality coefficient is variable. This technique is valuable because it allows the decay rate of each mode to be set and the energy of each mode to be calculated. The single drawbacks to this technique is its inability to model localized damping. Localized damping is in general non-proportional and is not applicable to this technique. Such localized damping can only be modelled by a single beam equation and is limited, assuming strain rate damping, to the modal damping distribution inherent in the model. The non-proportionally damped model is also limited in that energy can not be calculated on a modal bases.

This paper uses the technique of separate proportionally damped beam equations to model the beam structure's modes for three reasons. First, the damping mechanism being modeled is that of material damping which follows a frequency distribution different than that of strain rate damping. Second, it is

assumed that the material damping is small, uncoupled and induces exponential decay. Third, it is required of the analysis that the beam's energy is uncoupled and calculable.

Appendix B

List of Experiments

Beam 2, System A (Beam 2A): 3 Section, Continuous Unjointed Beam, Linear

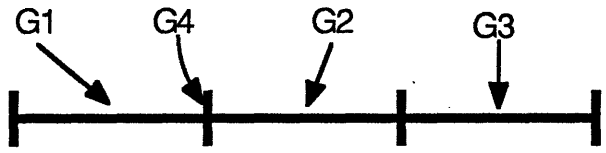

Feb. 13, Test 1 (FB1301): tapped ceiling	high amp.
Feb. 13, Test 2 (FB1302): Not used	high amp.
Feb. 25, Test 1 (FB2501): Rotation	high amp.
Feb. 25, Test 2 (FB2502): Rotation?	high amp.
July 2, Test 1 (JY0201): Signal Problems	low amp.
July 2, Test 2 (JY0202): Tapped Ceiling	low amp.
Apr. 24, Test 1 (AP2401): Good test	low amp.
Apr. 24, Test 2 (AP2402): Good test	low amp.

Beam 2, System B (Beam 2B): 3 Section, Continuous Unjointed Beam, Thin Plate Across Middle Section

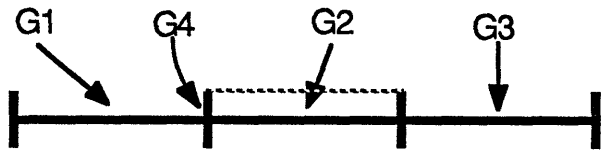

March 3, Test 1 (MR0301): Not used	high amp.
March 3, Test 2 (MR0302): Not used	high amp.
March 4, Test 1 (MR0401): Short	high amp.
March 4, Test 2 (MR0402): Short	high amp.
March 4, Test 3 (MR0403): Short	high amp.
March 4, Test 4 (MR0404): Not used	high amp.
March 5, Test 1 (MR0501): Not used	high amp.
March 5, Test 2 (MR0502): Not used	high amp.

March 5, Test 3 (MR0503): Not used	high amp.
April 22, Test 1 (AP2201): Hit ceiling	low amp.
April 22, Test 2 (AP2202): Good test	low amp.
April 23, Test 1 (AP2301): Spinning	low amp.
April 24, Test 3 (AP2403): Good test	low amp.
April 24, Test 4 (AP2404): Good test	low amp.
April 25, Test 1 (AP2501): Good test	low amp.
April 25, Test 2 (AP2502): Good test	low amp.

Beam 2, System C (Beam 2 C): 3 Section, Continuous Unjointed Beam, Thin Plate on Each Side of Center Section

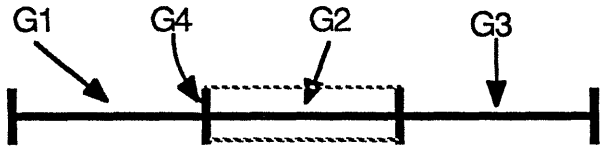

July 14, Test 1 (JY1401): hit ceiling hard	low amp.
July 14, Test 2 (JY1402): Good test	low amp.

Beam 3, System A (Beam 3A): 2 Section, Linear Jointed Beam

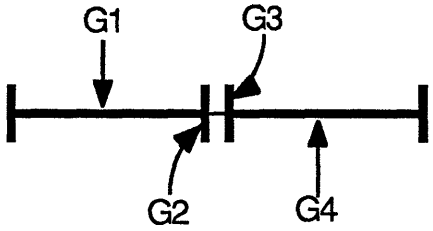

May 26, Test 1 (MY2601): Good test	low amp.
May 26, Test 2 (MY2602): Hit ceiling	low amp.
May 26, Test 3 (MY2603): Good test	low amp.
July 7, Test 1 (JY0701): Good test	very low amp.
July 7, Test 2 (JY0702): Good test	very low amp.

Beam 3, System B (Beam 3B): 2 Section, Asymmetrically Stiff Jointed Beam

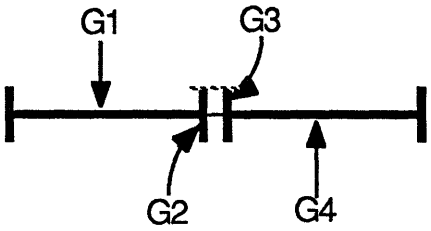

May 27, Test 1 (MY2701): Thin plate did not go tight	low amp.
May 27, Test 2 (MY2702): Thin plate did not buckle	low amp.
May 27, Test 3 (MY2703): Good test	low amp.
May 27, Test 4 (MY2704): Good test	low amp.

Beam 3, System C (Beam 3C): 2 Section, Dead-Band Jointed Beam

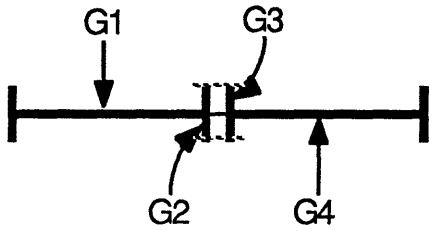

May 27, Test 5 (MY2705): low	low amp.
May 27, Test 6 (MY2706): Good test	low amp.
May 27, Test 7 (MY2707): Good test	low amp.
May 28, Test 1 (MY2801): Good test	low amp.
May 28, Test 2 (MY2802): Good test	low amp.
May 28, Test 3 (MY2803): very low	low amp.
May 28, Test 4 (MY2804): slow spin	low amp.
July 7, Test 3 (JY0703): ceiling?	very low amp.
July 9, Test 1 (JY0901): low	very low amp.

Beam 3, System D (Beam 3D): 2 Section, Bolted Beam

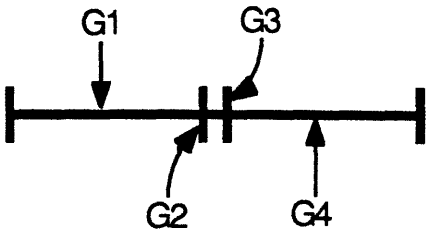

July 9, Test 2 (JY0902): Good test	very low amp.
July 12, Test 1 (JY1201): Good test	very low amp.

Beam 4, System A (Beam 4A): 3 Section, Linear Jointed Beam,

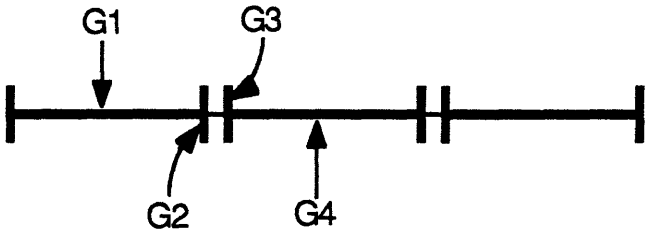

May 30, Test 1 (MY3001): hit ceiling	low amp.
May 30, Test 2 (MY3002): Good test	low amp.
July 2, Test 3 (JY0203): Good test	low amp.
July 2, Test 4 (JY0204): ceiling	low amp.
July 6, Test 1 (JY0601): Good test	very low amp.
July 6, Test 2 (JY0602): low	very low amp.

Beam 4, System B (Beam 4B): 3 Section, Asymmetrically Jointed Beam,
Asymmetry on Same Side of Beam

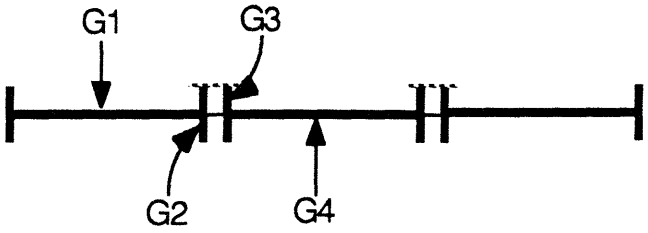

July 17, Test 1 (JY1701): Short low amp.
July 17, Test 2 (JY1702): Good test low amp.
July 17, Test 3 (JY1703): Good test low amp.

Beam 4, System C (Beam 4C): 3 Section, Asymmetrically Jointed Beam,
Asymmetry on Opposite Sides of Beam

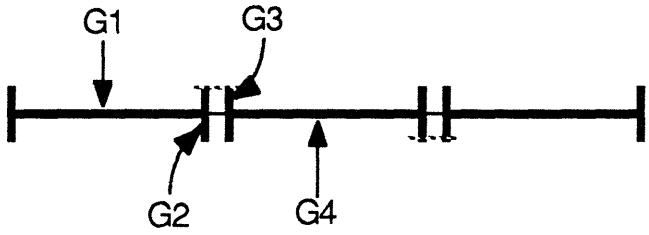

July 17, Test 4 (JY1704): hit ceiling shim low amp.
July 17, Test 5 (JY1705): Good test low amp.

Beam 4, System D (Beam 4D): 3 Section, Dead-Band Jointed Beam

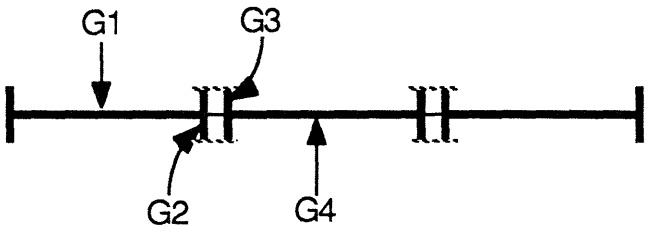

May 29, Test 1 (MY2901): hit ceiling low amp.
May 29, Test 2 (MY2902): Good test low amp.

May 29, Test 3 (MY2903): hit ceiling — low amp.
May 29, Test 4 (MY2904): Good test — low amp.
May 29, Test 5 (MY2905): Good test — low amp.

Beam 4, System E (Beam 4E): 3 Section, Bolted Beam

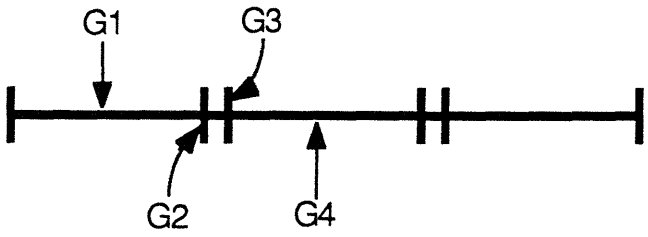

July 12, Test 2 (JY1202): hit ceiling — very low amp.
July 12, Test 3 (JY1203): Good test — very low amp.

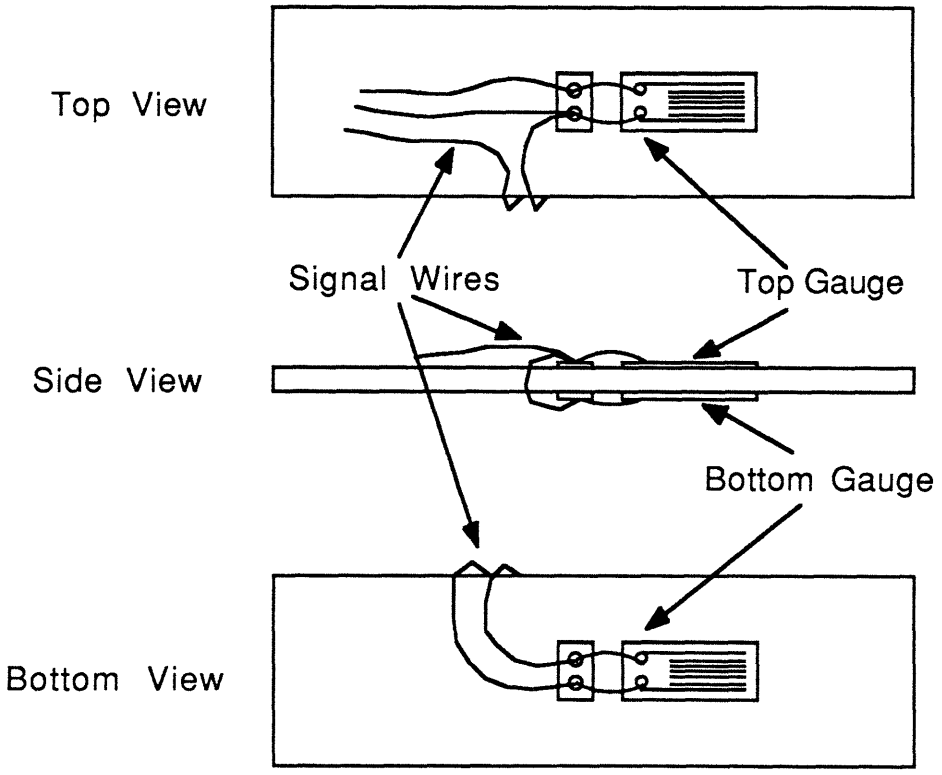

Strain Gauge Set-up
Half Bridge
Figure B.1

Appendix C

List of Simulations

Dead-Band Jointed Beam Simulation

	DBR	Z_{1eff}%	DR_{1eff}	DR_{1int}	Z_{1int}%	DR_1	Z_1%
1	10.6	.6122	1.306	1	.4686	0.306	0.144
2	10.2	.6367	1.359	1	.4686	0.359	0.168
3	9.8	.6632	1.415	1	.4686	0.415	0.195
4	9.4	.6039	1.289	1	.4686	0.289	0.135
5	9.05	.7195	1.535	1	.4686	0.535	0.251
6	8.65	.6191	1.321	1	.4686	0.321	0.150
7	8.32	.6840	1.460	1	.4686	0.460	0.215
8	7.97	.7166	1.529	1	.4686	0.529	0.248
9	7.6	.7566	1.615	1	.4686	0.615	0.288
10	7.3	.7820	1.669	1	.4686	0.669	0.313
11	6.95	.8224	1.755	1	.4686	0.755	0.354
12	6.6	.7404	1.580	1	.4686	0.580	0.272
13	6.3	.8297	1.770	1	.4686	0.770	0.361
14	5.98	.7632	1.629	1	.4686	0.629	0.295
15	5.7	.9196	1.962	1	.4686	0.962	0.451
16	5.38	1.0075	2.150	1	.4686	1.150	0.539
17	5.05	.8745	1.866	1	.4686	0.866	0.406
18	4.78	1.2050	2.571	1	.4686	1.571	0.736
19	4.45	1.1385	2.429	1	.4686	1.429	0.670
20	4.15	1.4023	2.992	1	.4686	1.992	0.934
21	3.8	1.3089	2.793	1	.4686	1.793	0.840
22	3.5	1.9315	4.122	1	.4686	3.122	1.463
23	3.1	2.1987	4.692	1	.4686	3.692	1.730
24	1	.4686	1	1	.4686	0	0

Table C.1

Table C.1

Table C.2

Wire Braced Beam Simulation

	K_2	Mode 1 Hz	DR_{int}	DR_{2-7}	DR_{leff}	Z_{lint}%	Z_{leff}%	ΔDR_M	ΔZ_M%	ΔZ_l%
1	5	18.04	.5	1000	.508	0.446	.448	999.500	879.444	2.000e-3
2	20	19.37	.5	1000	.582	0.414	.4779	999.500	819.048	0.064
3	60	20.58	.5	1000	.807	0.382	.624	999.500	770.905	0.242
4	100	21.01	.5	1000	1.029	0.382	.7793	999.500	755.127	0.397
5	60	20.58	.5	0	.4934	0.382	.3815	-0.500	-0.381	-5.000e-4
6	60	20.58	.5	.5	.504	0.382	.39065	0.000	0.000	8.650e-3
7	60	20.53	.5	1	.522	0.382	.405	0.500	0.381	0.023
8	60	20.53	.5	5	.5747	0.382	.4456	4.500	3.476	0.064
9	60	20.53	.5	10	.6465	0.382	.5012	9.500	7.349	1.084
10	60	20.52	1	0	.9576	0.780	.743	-1.000	-0.778	-0.037
11	60	20.53	1	.5	.9945	0.780	.771	-0.500	-0.381	-9.000e-3
12	60	20.53	1	1	1.002	0.780	.777	0.000	0.000	-3.000e-3
13	60	20.53	1	5	1.0765	0.780	.8346	4.000	3.095	0.055
14	60	20.53	1	10	1.1325	0.780	.878	9.000	6.952	0.098
15	60	20.56	2	0	2.0078	1.544	1.5542	-2.000	-1.540	0.010
16	60	20.56	2	.5	2.0078	1.544	1.5542	-1.500	-1.159	0.010
17	60	20.56	2	1	2.0078	1.544	1.5542	-1.000	-0.778	0.010
18	60	20.56	2	5	2.0516	1.544	1.588	3.000	2.317	0.044
19	60	20.56	2	10	2.116	1.544	1.638	8.000	6.175	0.094

Table C.2

Table C.3 Asymmetrically Stiff Jointed Beam Simulation

	K_N/K_2	K_2	Mode 1 Hz	DR_{1int}	DR_{2-7}	DR_{1eff}	Z_{1int}%	Z_{1eff}%	ΔDR_M	ΔZ_M%	ΔZ_1%	K_2/K_1	ΔDR_1
1	.033	42.4	13.3	.5	1000	.67	0.038	.816	999.500	1192.857	0.778	30.303	0.170
2	.05	42.4	15.37	.5	1000	.695	0.033	.695	999.500	1032.206	0.662	20.000	0.195
3	.1	42.4	19.0	.5	1000	.70	0.026	.587	999.500	835.000	0.561	10.000	0.200
4	.2	42.4	22.6	.5	1000	.64	0.022	.449	999.500	702.000	0.427	5.000	0.140
5	.3	42.4	24.4	.5	1000	.58	0.020	.38	999.500	650.206	0.360	3.333	0.080
6	.5	42.4	26.44	.5	1000	.525	0.019	.316	999.500	600.048	0.297	2.000	0.025
7	.7	42.4	27.6	.5	1000	.508	0.018	.29	999.500	574.825	0.272	1.429	8.000e-3
8	.967	42.4	28.4	.5	1000	.5	0.018	.28	999.500	558.635	0.262	1.034	0.000
9	.033	212	22.86	.5	1000	.911	0.350	.634	999.500	695.873	0.284	30.303	0.411
10	.05	212	25.1	.5	1000	.843	0.318	.534	999.500	633.770	0.216	20.000	0.343
11	.1	212	28.3	.5	1000	.696	0.286	.39	999.500	562.103	0.104	10.000	0.196
12	.2	212	30.68	.5	1000	.573	0.255	.2975	999.500	518.495	0.042	5.000	0.073
13	.3	212	31.57	.5	1000	.532	0.255	.268	999.500	503.884	0.013	3.333	0.032
14	.5	212	32.4	.5	1000	.507	0.239	.249	999.500	490.977	0.01	2.000	7.000e-3
15	.7	212	32.8	.5	1000	.501	0.239	.243	999.500	484.992	4.000e-3	1.429	1.000e-3
16	.967	212	33.1	.5	1000	.5023	0.239	.2415	999.500	480.584	2.500e-3	1.034	2.300e-3
17	.033	424	26.7	.5	1000	.85	0.302	.503	999.500	595.780	0.201	30.303	0.350
18	.05	424	28.56	.5	1000	.73	0.286	.407	999.500	556.978	0.121	20.000	0.230
19	.1	424	30.93	.5	1000	.607	0.255	.312	999.500	514.309	0.057	10.000	0.107
20	.2	424	32.4	.5	1000	.53	0.239	.26	999.500	490.977	0.021	5.000	0.030
21	.3	424	32.89	.5	1000	.509	0.239	.246	999.500	483.656	0.007	3.333	9.000e-3
22	.5	424	33.55	.5	1000	.499	0.239	.24	999.500	474.138	1.000e-3	2.000	-1.000e-3
23	.7	424	33.67	.5	1000	.498	0.239	.235	999.500	472.451	-4.000e-3	1.429	-2.000e-3
24	.967	424	33.8	.5	1000	.499	0.239	.235	999.500	470.637	-4.000e-3	1.034	-1.000e-3
25	.033	424	26.7	.1	.5	.126	0.060	.075	0.400	0.239	0.015	30.303	0.026
26	.033	424	26.7	.1	1	.141	0.060	.084	0.900	0.541	0.024	30.303	0.041
27	.033	424	26.7	.1	5	.25	0.060	.147	4.900	2.928	0.087	30.303	0.150
28	.033	424	26.7	.1	10	.35	0.060	.21	9.900	5.905	0.150	30.303	0.250
29	.033	424	26.7	.1	1000	.444	0.060	.265	999.900	596.019	0.205	30.303	0.344
30	.033	424	26.7	.5	0	.494	0.302	.294	-0.500	-0.302	-8.000e-3	30.303	-6.000e-3
31	.033	424	26.7	.5	.5	.51	0.302	.31	0.000	0.000	8.000e-3	30.303	0.010
32	.033	424	26.7	.5	1	.529	0.302	.32	0.500	0.302	0.018	30.303	0.029
33	.033	424	26.7	.5	5	.63	0.302	.376	4.500	2.690	0.074	30.303	0.130
34	.033	424	26.7	.5	10	.74	0.302	.44	9.500	5.666	0,138	30.303	0.240
35	.033	424	26.7	1	0	.998	0.589	.59	-1.000	-0.589	1.000e-3	30.303	-2.000e-3
36	.033	424	26.8	1	.01	1.017	0.589	.6	-0.990	-0.589	0.011	30.303	0.017
37	.033	424	26.8	1	.1	1.024	0.589	.61	-0.900	-0.541	0.021	30.303	0.024
38	.033	424	26.76	1	.5	.982	0.589	.58	-0.500	-0.302	-9.000e-3	30.303	-0.018
39	.033	424	26.76	1	1	.997	0.589	.593	0.000	0.000	4.000e-3	30.303	-3.000e-3
40	.033	424	26.76	1	2	1.11	0.589	.66	1.000	0.589	0.071	30.303	0.110
41	.033	424	26.76	1	10	1.23	0.589	.73	9.000	5.348	0.141	30.303	0.230
42	.033	424	26.8	1	100	1.35	0.589	.804	99.000	58.792	0.215	30.303	0.350
43	.033	424	26.75	2	0	2.12	1.194	1.26	-2.000	-1.194	0.066	30.303	0.120
44	.033	424	26.75	2	.5	2.02	1.194	1.2	-1.500	-0.891	6.000e-3	30.303	0.020
45	.033	424	26.75	2	1	2.02	1.194	1.2	-1.000	-0.589	6.000e-3	30.303	0.020
46	.033	424	26.75	2	5	2.09	1.194	1.24	3.000	1.783	0.046	30.303	0.090
47	.033	424	26.75	2	10	2.22	1.194	1.32	8.000	4.759	0.126	30.303	0.220
48	.033	424	26.75	2	1000	2.29	1.194	1.36	998.000	593.775	0.166	30.303	0.290
49	.033	424	26.9	5	0	5.03	2.960	3	-5.000	-2.960	0.040	30.303	0.030
50	.033	424	26.5	5	.5	5.14	3.008	3.08	-4.500	-2.706	0.072	30.303	0.140
51	.033	424	26.7	5	1	5.03	2.976	3	-4.000	-2.367	0.024	30.303	0.030
52	.033	424	26.6	5	5	5.0	2.992	3	0.000	0.000	8.000e-3	30.303	0.000
53	.033	424	26.7	5	10	5.07	2.976	3	5.000	2.976	0.024	30.303	0.070
54	.033	424	26.7	5	1000	5.27	2.976	3.15	995.000	593.106	0.174	30.303	0.270